JAEA-Conf 2023-001
INDC(JPN)-0209
DOI:10.11484/jaea-conf-2023-001

JAEA-Conf

Proceedings of the 2022 Symposium on Nuclear Data
November 17-18, 2022,
BLOSSOM CAFÉ, Main Campus, Kindai University,
Higashiosaka City, Osaka, Japan

(Eds.) Nobuhiro SHIGYO, Atsushi KIMURA and Tadafumi SANO

Nuclear Science and Engineering Center
Sector of Nuclear Science Research

February 2024

Japan Atomic Energy Agency

日本原子力研究開発機構

国立研究開発法人日本原子力研究開発機構　JAEA イノベーションハブ　研究成果利活用課
〒 319-1112　茨城県那珂郡東海村大字村松 4 番地 49
E-mail: ird-support@jaea.go.jp

JAEA-Conf 2023-001
INDC(JPN)-0209

Proceedings of the 2022 Symposium on Nuclear Data
November 17-18, 2022,
BLOSSOM CAFÉ, Main Campus, Kindai University,
Higashiosaka City, Osaka, Japan

(Eds.) Nobuhiro SHIGYO*[1], Atsushi KIMURA and Tadafumi SANO*[2]

Nuclear Science and Engineering Center, Sector of Nuclear Science Research,
Japan Atomic Energy Agency,
Tokai-mura, Naka-gun, Ibaraki-ken

(Received November 6, 2023)

The 2022 Symposium on Nuclear Data was held at BLOSSOM CAFÉ in Main Campus of Kindai University on November 17-18, 2022. The symposium was organized by the Nuclear Data Division of the Atomic Energy Society of Japan (AESJ) in cooperation with Investigation Committee on Nuclear Data in AESJ, Nuclear Science and Engineering Center of Japan Atomic Energy Agency, and High Energy Accelerator Research Organization.

In the symposium, tutorials " The Future of Nuclear Reactor Physics Experimental Research in Japan" was proposed and held. two sessions of lectures and discussions were held: "Recent Topics on Nuclear Data". In addition, recent research progress on experiments, nuclear theory, evaluation, benchmark, and applications were presented in the poster session. The total number of participants was 76 participants. Each oral and poster presentation was followed by an active question and answer session. This report consists of a total of 22 papers including 4 oral and 18 poster presentations.

Keywords: Nuclear Data Symposium 2022, Experiments, Nuclear Theory, Nuclear Data Evaluation, Benchmark Test, Nuclear Data Applications

---

*[1] Kyushu University

*[2] Kindai University

Organizers: Tadafumi SANO (Chair, Kindai Univ.), Yosuke IWAMOTO (Vice-chair, JAEA), Tatsuya KATABUCHI (Tokyo Tech.), Toshiya SANAMI (KEK), Atsushi KIMURA (JAEA), Katsuhisa NISHIO (JAEA), Nobuhiro SHIGYO (Kyushu Univ.), Jun-ichi HORI (Kyoto Univ.), Osamu IWAMOTO (JAEA), Yuji YAMAGUCHI (JAEA), Kazushi TERADA (Kyoto Univ.)

JAEA-Conf 2023-001
INDC(JPN)-0209

2022 年度核データ研究会報告集

2022 年 11 月 17 日～18 日

近畿大学 東大阪キャンパス ブロッサムカフェ
大阪府東大阪市

日本原子力研究開発機構　原子力科学研究部門　原子力基礎工学研究センター

（編）執行　信寛*1、木村　敦、佐野　忠史*2

(2023 年 11 月 6 日受理)

2022 年度核データ研究会は、2022 年 11 月 17 日～18 日に、大阪府東大阪市にある近畿大学東大阪キャンパスの BLOSSOM CAFÉ 多目的ホールにて開催された。本研究会は、日本原子力学会核データ部会が主催、日本原子力学会「シグマ」調査専門委員会、日本原子力研究開発機構原子力基礎工学研究センター、高エネルギー加速器研究機構が共催した。

チュートリアルとして、「我が国の原子炉物理学実験的研究の歴史」を、講演・議論のセッションとして、「核データに関する最近の話題」2 セッションを実施した。さらにポスターセッションでは実験、理論、評価、ベンチマーク、応用など幅広い内容について発表が行われた。参加者数は 76 名で、それぞれの口頭発表およびポスター発表では活発な質疑応答が行われた。本報告書は、本研究会における口頭発表 4 件、ポスター発表 18 件の合計 22 の論文を掲載している。

キーワード: 2022 年度核データ研究会、実験、原子核理論、核データ評価、ベンチマークテスト、核データ応用

原子力科学研究所：〒319-1195　茨城県那珂郡東海村大字白方 2-4
*1 九州大学
*2 近畿大学

Contents

Papers presented at Poster Session

目次

ポスター発表論文

1. 2022 Symposium on Nuclear Data - Programme

November 17 - 18, 2022

Thursday, November 17

Opening Address (13:30 - 13:40)

Convener: Tadafumi SANO (Kindai Univ.)

Retirement Memorial Lecture (13:40 - 15:00)

Convener: Osamu IWAMOTO (JAEA)

13:40 Some memories of relationship with Nuclear Data
Ken NAKAJIMA (Kyoto Univ.)

14:20 40-year experience in nuclear data
Satoshi CHIBA (Tokyo Tech.)

Break (15:00 - 15:30)

Poster Session (15:30 - 17:00)

Measurement and evaluation of DD neutron field characteristics for OKTAVIAN
Hikaru MATSUNAGA (Osaka Univ.)

Production cross sections of ^{198g}Au in proton-induced reactions on natural platinum
Gantumur DAMDINSUREN (Hokkaido Univ.)

Preliminary experiment for measurement of radionuclide yield from nuclear capture reaction of negative muon
Yuji YAMAGUCHI (JAEA)

Measurement of sample reactivity worth of calcium hydride in UTR-KINKI
Takashi KANDA (Kindai Univ.)

Cross comparison on neutron spectra with Liquid scintillator and Bonner Sphere Spectrometry
Eunji LEE (KEK)

New analytical model for momentum distribution on the spallation reaction in inverse kinematics
Riku MATSUMURA (Saitama Univ.)

Neutron Capture Cross Section Measurement of ^{129}I and ^{127}I using ANNRI at MLF/J-PARC
Gerard ROVIRA (JAEA)

Measurement of heavy nuclide production cross section via the reaction between GeV proton and ^{nat}Pb
Kenta SUGIHARA (KEK)

Experimental examination of activation detector for long-term DT neutron irradiation
Ryota EGUCHI (Osaka Univ.)

Friday, November 18, 2022

Tutorial (09:00 - 10:00)

Convener: Tadafumi SANO (Kindai Univ.)

09:00 The Future of Nuclear Reactor Physics Experimental Research in Japan
Kengo HASHIMOTO (Kindai Univ.)

Recent Topic (1) (10:00 - 11:30)

Convener: Jun-ichi HORI (Kyoto Univ.)

10:00 Conceptual Design Study of New Research Reactor at the Monju Site
Kazufumi TSUJIMOTO (JAEA)

10:30 Measurement of 100 MeV-range nuclear reaction data using the fixed field alternating gradient accelerator at Kyoto University
Hiroki IWAMOTO (JAEA)

11:00 About Kindai Research Reactor
Tadafumi SANO (Kindai Univ.)

Lunch (11:30 - 13:00)

Recent Topic (2) (13:00 - 14:30)

Convener: Atsushi KIMURA (JAEA)

13:00 Research and development of alpha radiation nuclear medicine treatment using ^{211}At
Takashi NAKANO (RCNP)

13:30 Production of medical radionuclides using electron linear accelerators
Takahiro TADOKORO (Hitachi)

14:00 Half-life change of orbital electron capture modified nuclide ^{7}Be
Tsutomu OHTSUKI (Kyoto Univ.)

Break (14:30 - 15:00)

Nuclear Data Section Award in 2022 (15:00 - 16:30)

Convener: Katsuhisa NISHIO (JAEA)

15:00 Measurement of neutron energy spectrum by 345 MeV/u ^{238}U incident on a copper target
Kenta SUGIHARA (KEK)

15:20 Excitation energy dependence of total kinetic energy of fission fragments
Kazuya SHIMADA (Tokyo Tech.)

15:40 Measurement of fast neutron capture reaction of ^{243}Am
Yu KODAMA (Tokyo Tech.)

16:00 Incident neutron energy dependent calculation of fission yield and prompt/delayed neutron yield of ^{235}U, ^{238}U and ^{239}Pu

Shin OKUMURA (IAEA)

Closing Address (16:30 - 17:00)

Tadafumi SANO (Kindai Univ.), Yosuke IWAMOTO (JAEA)

2. Some memories of relationship with Nuclear Data

Ken NAKAJIMA
Institute for Integrated Radiation and Nuclear Science, Kyoto University
Asashiro-Nishi 2-1010, Kumatori-cho, Sennan-gun, Osaka 590-0494, Japan
Email: nakajima.ken.5m@kyoto-u.ac.jp

I have had some involvement with nuclear data for 45 years, ever since I heard the term "Nuclear Data" in the lecture of Nuclear Reactor Physics in my junior year of university. This paper describes some of my memories of relationship with nuclear data.

1. First contact with Nuclear Data (1978-)

I think the first time I became aware of “Nuclear Data” was in the lecture of Nuclear Reactor Physics in university. There, nuclear data was used mainly as the neutron induced nuclear reaction cross sections. I didn't understand much about it at the time, but anyway, the nuclear reaction rate could be calculated by multiplying the neutron flux by the nuclear data (the cross section). The nuclear data were evaluated by experts, which meant that users of the nuclear data could obtain the reaction rate without knowing the details of the nuclear reaction. Although it may be difficult for those who evaluate nuclear data, I had the impression that it is very convenient for the users because they do not have to perform difficult calculations.

Later, when I started to use nuclear data in my work, I found that I needed to put in a lot of effort in their use, but my initial impression has not changed much. As one of the users, I cannot help but admire the experts who measure and evaluate nuclear data and maintain nuclear data libraries.

2. Use of Nuclear Data at JAERI (1982-)

2.1. NUCEF Design Work

In 1982, I joined the Japan Atomic Energy Research Institute (JAERI) and was assigned to the Criticality Safety Laboratory. At that time, the laboratory was designing a new experimental facility for criticality safety (now called NUCEF [1]), which was to have two critical experimental facilities: the steady-state critical experimental facility (STACY) to measure the nuclear characteristics such as critical mass using solution fuel, and the transient critical experimental facility (TRACY) to conduct dynamic experiments simulating a criticality accident. I was mainly in charge of the TRACY design (Fig. 1).

In the design of those facilities, the critical mass, reactivity coefficient, and kinetic parameters (the effective delayed neutron fraction and prompt neutron lifetime) were calculated for various fuel conditions, and the core shapes and dimensions and the operation control system were investigated. For this purpose, it was necessary to perform nuclear calculations, and the SRAC code system, which was under development at the time and was also used in the design of the modified JRR-3 reactor, was used

as the nuclear calculation tool. In addition, the KENO-IV code, which was widely used as a Monte Carlo code, was used for criticality calculations for complex geometries. For these nuclear calculations, the JENDL-2 nuclear data library, which was the latest version at that time, was used. The nuclear calculations require the atomic number density of the target material. Since there was no accurate atomic number density evaluation formula for uranyl nitrate and/or plutonium solution, the fuel used in the calculations, the Chemical Process Research Group of the Criticality Safety Laboratory conducted experimental research and developed a new evaluation formula. In parallel with the nuclear calculations, a new kinetic code for solution fuel systems, AGNES [2] was developed to evaluate the kinetic experiments to be conducted using TRACY. The reactivity coefficients and kinetic parameters used in the code were calculated by SRAC.

In the process of these design works, the NUCEF Construction Office was separated from the Criticality Safety Laboratory, and the facility licensing and construction works were carried out mainly by the NUCEF Construction Office. As a result, STACY and TRACY went critical for the first time in February and December 1995, respectively. I have heard that the conceptual design work of NUCEF started in 1981, so it took almost 15 years from the conception to the start of operation. During this period, in addition to the update of the SRAC code, nuclear data were updated from JENDL-2 (1982: 82 nuclides → revised in 1985: 181 nuclides) to JENDL-3 (1989: 171 nuclides), JENDL-3.1 (1990: 324 nuclides) and JENDL-3.2 (1994: 340 nuclides). In principle, it is better to use the new data which reflects the latest findings, but if the calculation results change during the licensing process, it is necessary to recheck the validity of the safety review. Then the calculation environment should be maintained so that the results obtained in the past can be reproduced. At the same time, it is also necessary to check the impact of employing the latest findings in the safety review. Even if there is no significant impact, it is required to keep quality control of past calculations.

2.2. TCA critical experiments

In parallel with the design and construction of NUCEF, various experiments on criticality safety and nuclear characteristics of light water reactors were conducted in the Criticality Safety Laboratory using the Tank-type Critical Assembly TCA [3] (Fig. 2), which simulates light water reactor cores. These experimental data are used as benchmark data for nuclear data and contribute to improving the accuracy of nuclear data.

In the late 1980s, a new reactor concept, the high-conversion light water reactor (HCLWR), attracted worldwide attention. To improve the efficiency of nuclear fuel use, a high conversion ratio was achieved by hardening the neutron spectrum with a tight-lattice core. In TCA, a series of critical experiments were performed with several different tight-lattice cores. In these experiments, a new nondestructive method of measuring a new spectral index called the modified conversion ratio was developed to investigate spectral changes caused by the tightness of the lattice [4]. Later, this technique was used to measure the modified conversion ratios of a series of fuel lattices in TCA to obtain spectral indices for a wide range of spectral changes [5]. Other critical assemblies in Japan and abroad began to measure modified conversion ratios using the same method, and the results were used as benchmark data for nuclear data.

Almost at this time, the continuous energy Monte Carlo code MVP, which had been under development at JAERI, was released, allowing as build analysis of critical experiment systems. As a result, direct verification (benchmarking) of nuclear data using critical experiment data became possible, and the distance between reactor physics (experiment) and nuclear data (evaluation) seemed to become

very close. Through benchmark calculations, I also began to participate in the nuclear data evaluation activities conducted by the Japanese Nuclear Data Committee (JNDC). In this committee activity, I also participated in the evaluation of the effective delayed neutron fraction (β_{eff}), which is a quantity that serves as a scale for converting the numerically calculated reactivity (in dk/k) to the experimentally calculated reactivity (in $). If the value of β_{eff} is inaccurate, a certain deviation (bias) will occur between the numerical calculation and the experimental value. The TCA reactivity value also showed a certain bias from the numerical calculation results. Therefore, we re-evaluated the β_{eff} of TCA [6] and proposed a new value for delayed neutron fraction, which was considered appropriate from the reactor physics side, together with other experimental data [7]. The result was reflected in the revision of the nuclear data library JENDL (JENDL-3.3). Although there was no tool to calculate β_{eff} in continuous energy at that time, and the multigroup approximation was necessary, but MVP was later improved, and this problem was solved.

Besides above experiments, a series of MOX critical experiments conducted in the past at TCA, which have measured critical mass in the same core geometry for about seven years. Since Pu-241 in MOX fuel decays to Am-241 with a half-life of about 14 years, this long-term critical experiment data is valuable for verifying the accuracy of Pu-241 or Am-241 nuclear data. Benchmark evaluations using this critical experiment data show a trend of increasing effective multiplication factor (which should be constant) with time [8] indicating that there is some problem with either (or both) of the above two nuclides.

This trend was also observed in the MOX critical experiments in France, and is not a bias effect due to the experimental setup. The latest nuclear data are expected to improve the situation.

3. Use of Nuclear Data at Kyoto University (2003-)

3.1. KUR Core Conversion to LEU

In 2003, I started to work at the Kyoto University Research Reactor Institute (now the Institute for Integrated Radiation and Nuclear Science). My laboratory has been conducting the nuclear data measurement using an electron linear accelerator (LINAC) and, it has been also in charge of the safety management of the Kyoto University Research Reactor, KUR (Fig. 3). At that time, there was a news report that KUR might be decommissioned due to the problem of its spent fuel treatment. However, it was later officially decided to continue its operation, and the core would be converted from highly enriched uranium (HEU) core to low enriched uranium (LEU) one. I was assigned to work on the licensing process for the conversion of the KUR core.

Changing the fuel enrichment of a reactor means configuring a completely new core, and all descriptions involving the core (and fuel) must be changed in its safety review. In the low-enriched fuel design, instead of reducing the fuel enrichment, the fuel concentration is increased by employing the silicide material, and then the nuclear characteristics, such as critical mass, does not change significantly. But even so, the impact of the enrichment change cannot be ignored. In addition, the content of the KUR installation application at that time only partially complied to the safety review guidelines for the water-cooled test and research reactors established by the Nuclear Safety Commission. Therefore, the main part of the installation application had to be completely revised.

In this safety review, nuclear characteristics of the new core were evaluated. In this evaluation, the SRAC code system was used as the main calculation code, and JENDL-3.3, the latest nuclear data library at that time, was used. As mentioned before, the new value was used for the delayed neutron fraction of

JENDL-3.3, the calculated result of effective delayed neutron fraction was approximately 10% smaller than that used in the previous version (highly enriched uranium system, ENDF-B/IV was used for the nuclear data library). The smaller effective delayed neutron fraction means that the reactivity in $ unit becomes 10% larger when the reactivity is input in dk/k unit, and as a result, the analytical results of control rod mis-withdrawal events did not meet the limit value. Therefore, it became necessary to set a new limit for control rod operation. Although the accuracy was improved by revising the delayed neutron fraction, I experienced the magnitude of the impact of revising the nuclear data myself.

3.2. LINAC Experiments

As mentioned above, our laboratory has an electron linear accelerator, LINAC, and nuclear data are measured using the time-of-flight neutron method. By using LINAC, we have started the project of "Development of Nondestructive Methods Adopted for Integrity Test of Next Generation Nuclear Fuels" with other organizations in 2014 [9]. This project was funded by the Ministry of Education, Culture, Sports, Science and Technology of Japan (MEXT) for 4 years.

In the nondestructive measurement, we use the neutron resonance absorption reaction of the target nuclide, and we can identify the nuclide and its concentration in the fuel rod. To obtain the accurate results, the highly accurate nuclear data are indispensable. If we apply this measurement technique to the advanced fuel, which will be used to transmute the high-level radioactive waste in fast reactor systems, accurate nuclear data for various minor actinides and long-lived fission products are required. Therefore, the improving of the nuclear data library should be continuously carried out.

4. Activities in the Japanese Nuclear Data Committee

When I started experiments on high conversion LWRs (around 1992) using TCA, I was asked to introduce the experimental data in the Integral Test Working Group (WG) of the Japanese Nuclear Data Committee (JNDC), which led me to become a member of this WG and to participate in benchmarking activities for a wide range of critical experiments. Here, we provided experimental data on critical masses and reaction rate ratios of various core at TCA, and they were used to validate JENDL. In addition to this WG, there are many other technical subcommittees, WGs, and so on in JNDC. I also participated in some of those groups as follows.

The Delayed Neutron WG was established in 1997 to review delayed neutron data and has been re-evaluating the delayed neutron fraction based on experimental data from JAERI's critical assemblies, FCA (Fast Critical Assembly), TCA, and VHTRC (High Temperature Gas Reactor Critical Assembly). The results of the reevaluation are reflected in JENDL-3.3, as mentioned earlier. The WG also considered a proposal from a U.S. researcher to increase the number of delayed neutron groups to nine, but in consideration of the impact of this change, it was decided to maintain the existing six groups.

Furthermore, in 2006, the Quality Assurance Study Group was established to examine the quality assurance of nuclear data, and after about three years of activities, the basic concept of quality assurance for JENDL was compiled [10]. For JENDL to be widely used internationally in the future, it is necessary not only to ensure the accuracy of nuclear data and the number of nuclides and reactions, but also to ensure the quality assurance of nuclear data, and this activity is a pioneering step in this direction.

The Japanese Nuclear Data Committee was initially a generic name for the committee of JAERI and that of the Atomic Energy Society of Japan (AESJ), called as SIGMA special committee. The activities of the above-mentioned technical subcommittees, working groups, etc. were basically supported by

JAERI. However, after the Japan Atomic Energy Agency (JAEA) was established as the result of organizational reform of JAEA in 2005, a clear distinction between academic activities and JAEA's activity was required, and then the committee independent of the Society was established, which was also called as JNDC. In 2010, the name of the committee was changed to the current "JENDL Committee" and has continued its activities.

On the other hand, AESJ's SIGMA special (ad-hoc) committee, which was established in in 1963, (SIGMA special committee since 1965), has continued its activities to this day as the SIGMA investigation committee (Investigation Committee on Nuclear Data) since 2019.

I am not an expert in nuclear data as mentioned so far, but since I have been participating in the activity of JNDC for a long time, I have been chairing the JENDL committee since FY2017. JAEA released JENDL-5 in December 2021, and since then, we have been conducting data validation and dissemination activities, as well as studying the next revision of JENDL.

5. At the end

I have looked back on some memories that have something to do with nuclear data. Please forgive me if some of them seem to have nothing to do with nuclear data.

In principle, nuclear data should converge to a single value at some point, but in reality this is not the case, and nuclear data are reviewed and updated on a daily basis. It is necessary to continue this activity to build a nuclear data library with higher accuracy in the future. For this purpose, the development of research infrastructure and human resources necessary for nuclear data measurement and evaluation are urgent issues.

References

[1] Takeshita I. et al., Safety design of the NUCEF critical facilities, Proc. of the 3rd Int. Conf. on Nuclear Fuel Reprocessing and Waste Management, Sendai, 1991, vol.1, pp.510-515.

[2] Nakajima K. et al., A Kinetics Code for Criticality Accident Analysis of Fissile Solution Systems: AGNES2, JAERI-Data/Code 2002-004, 2002 [in Japanese].

[3] Tsuruta H. et al., Critical Sizes of Light-Water Moderated UO_2 and PuO_2-UO_2 Lattices, JAERI 1254, 1978.

[4] Nakajima K. et al., Measurements of the Modified Conversion Ratio by Gamma-Ray Spectrometry of Fuel Rods for Water-Moderated $U0_2$ Cores, Nucl. Sci. Eng., vol.116, 1994, pp.138-146.

[5] Nakajima K. et al., Modified Conversion Ratio Measurement in Light Water-Moderated UO2 Lattices, Nucl. Technol., vol.113, 1996, pp.375-379.

[6] Nakajima K., Re-evaluation of the Effective Delayed Neutron Fraction Measured by the Substitution Technique for a Light Water Moderated Low-Enriched Uranium Core, J. Nucl. Sci. Technol., vol.38, no.12, 2001, pp.1120-1125.

[7] Yoshida T., et al., Evaluation of Delayed Neutron Data for JENDL-3.3, J. Nucl. Sci. Technol., Supplement 2, 2002, pp.136-139.

[8] Nakajima K., et al., Validation of ^{241}Am Capture Cross Section through Integral Test using Criticality Data of Light-water Moderated MOX Cores, Energy Procedia, vol.71, 2015, pp.237-243.

[9] Nakajima K., Outline of the Development of Nondestructive Methods Adopted for Integrity

Test of Next Generation Nuclear Fuels (N-DeMAIN), JPS Conf. Proc, vol.24, 011019, 2019, pp. 1-6. (Proc. 2nd Int. Symp. on Radiation Detectors and Their Uses (ISRD2018))

[10] Yamano N., et al., Quality Management System Proposed to JENDL Evaluation Project, J. Korean Physical Soc., vol.59, no.2, 2011, pp.1298-1302.

Acknowledgements

I would like to thank all the people who have been very helpful to me in the nuclear data-related activities.

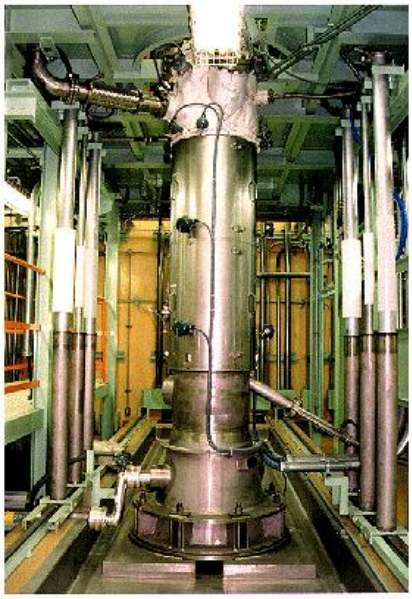

Fig. 1 Core tank of TRACY
Source:
https://rdreview.jaea.go.jp/tayu/ACT96J/04/0404.htm

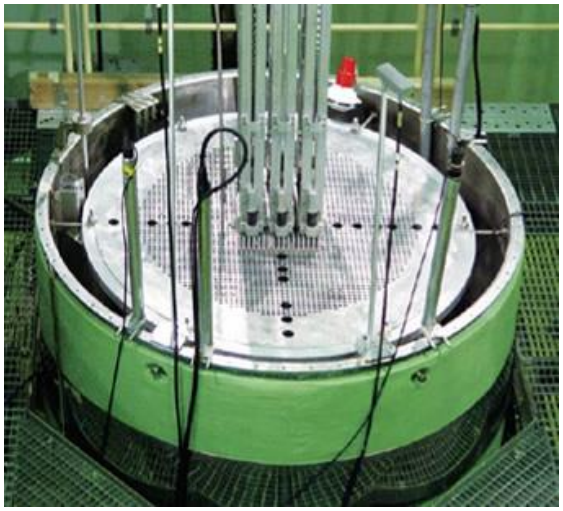

Fig.2 Core tank of TCA
Source:
https://www.jaea.go.jp/english/04/ntokai/anzen/anzen_04.html

Fig.3 Reactor building of KUR

3. 40-year experience in nuclear data

Satoshi CHIBA
Tokyo Institute of Technology
2-12-1 Ookayama, Meguro, Tokyo 152-8550, Japan

*Email: chiba.s.ae@m.titech.ac.jp

A part of my experiences during my career of about 40 years will be reviewed briefly. I have involved in researches such as neutron scattering experiments and analysis in terms of dispersive optical model, analysis of nucleon scattering data by the soft-rotator model, solution of a puzzle in statistical treatment of nuclear data referred to as “Peelle’s Pertinent Puzzle”, development of JENDL Fusion File and JENDL-3, 4 and 5, development of Quantum Molecular Dynamics (QMD), providing nuclear data to nucleosynthesis such as neutrino cross sections and fission fragment yields, developing surrogate reaction method with heavy-ion beams, theoretical treatment of nuclear fission with a set of variety of theories to cover the whole process of nuclear fission, development of a transmutation system of LLFP with fast reactors, and uncertainty qualification based on total Monte-Carlo method. In the reference section, papers published in scientific and/or engineering journals in my whole career have been listed in the inversely chronological order [1-214], excluding review articles and proceedings.

1. Introduction

Nuclear data is one of the most fundamental and therefore important fields in research and development of nuclear energy systems. The field of nuclear data contains actually variety of subjects such as 1) experimental activities, 2) theoretical activities, 3) statistical analysis including machine learning, 4) compilation of knowledge and database, 5) evaluation, and 6) benchmark and studies on impact to reactor properties. I have involved in researches in some of these subjects for almost 40 years. Some of my recent activities will be briefly reviewed in this manuscript, but, unfortunately not all of them.

Nuclear fission, which proceeds as shown in Fig. 1, is the most fundamental physics process underlying nuclear energy, which is recognized widely as an important source of zero-carbon energy. Nuclear fission makes the stable operation of nuclear reactors possible through a chain reaction mediated by fission neutrons, generating heat at the same time due to its huge positive Q-value. Furthermore, nuclear fission populates a number of radioactive fission products, and the treatment of the radioactive wastes is one of the key issues in the utilization of nuclear energy. On the other hand, some of the fission products like ^{99}Tc have been used as important radioactive materials for, e.g., medical applications. Moreover, nuclear fission takes place in r-process nucleosynthesis in merger events of 2 neutron stars or between a neutron star and a blackhole, which determines the abundance of medium to heavy nuclei through fission recycling. Therefore, information on nuclear fission is crucial in accurate design of nuclear systems, medical applications and in understanding origin of matter in the cosmos. Recently, it is also pointed out that antineutrinos emitted by the β^- decay of fission products can be used for precise understanding of the neutrino oscillation, verification of sterile neutrinos, and also for remote monitoring of reactor status for nuclear safeguards.

Nuclear fission has been studied for more than eighty years since its discovery. However, fundamental

aspects of nuclear fission still remain to be a mystery due to its sophisticated nature as a large-amplitude collective motion of systems including finite number of nucleons [16]. Indeed, we still cannot explain the whole property of nuclear fission even for the n+^{235}U reaction with sufficient predictive power, although experimental data and/or empirical models have been applied for practical use. Such practical methods may work properly in the case of well examined neutron-induce fission of ^{235}U and ^{239}Pu. In order to develop a new system such as Accelerator-driven Systems (ADS) and Fast Reactors (FR) which may act also as a transmuter of the TRU wastes, we need high quality nuclear data of minor actinides (MA), which are fissile or fissionable nuclei. Experiments to obtain fission data for MA and long-lived fission products (LLFP) have been performed in various facilities. However, it is still difficult to cover wide-variety of fission data, such as fission fragment mass distributions (FFMDs), total kinetic energy (TKE), number of prompt and delayed neutrons, decay heat, and emission of antielectron neutrinos from the fission products. We have developed a comprehensive set of nuclear models which can reproduce and predict these physical quantities related to nuclear fission.

In addition to the above fundamental approaches, we have worked also on the reduction of long-lived fission products, research on the effects of uncertainty of nuclear data on properties of nuclear systems, and the influence of nuclear data on the clearance problem of decommissioning by developing a computational scheme of high-quality nuclear data. The aim of my work has been improvement of nuclear data starting from fundamental researches to application, placing emphasis on fission-related nuclear data.

2. Fundamental studies for nuclear fission

Nuclear fission we consider is initiated by absorption of neutrons by heavy nuclei like ^{235}U and ^{239}Pu, the process ① in Fig. 1, which can be described by a standard method like the optical model or the coupled-channels theory. However, it is still difficult to describe the whole feature of a nuclear fission process starting at ② and after with a single model due to the fact that nuclear force is still unclear owing to its complexity as a relativistic many-body problem consisting of quarks and gluons, as well as a fact that it consists of several parts which have completely different time scales ranging from ～ 10^{-20} second (process ②to ④) to ～10^{6} years for process ⑥. Indeed, there is no theoretical model which can simulate the whole process of nuclear fission shown in Fig. 1. Therefore, we have developed different models depending on our purpose. We have studied the fundamental mechanism of nuclear fission at low excitation energies with models such as a 4-dimensional Langevin model, the Anti-symmetrized Molecular Dynamics, relativistic and non-relativistic density functional theories to describe the process ② to ④ in Fig. 1. As a result of this process, about 1,300 different primary fission fragments are formed at stage ④ even from a single fissioning system, and we need to specify the yield, distributions of kinetic energy, excitation energy and spin-parity to each of the

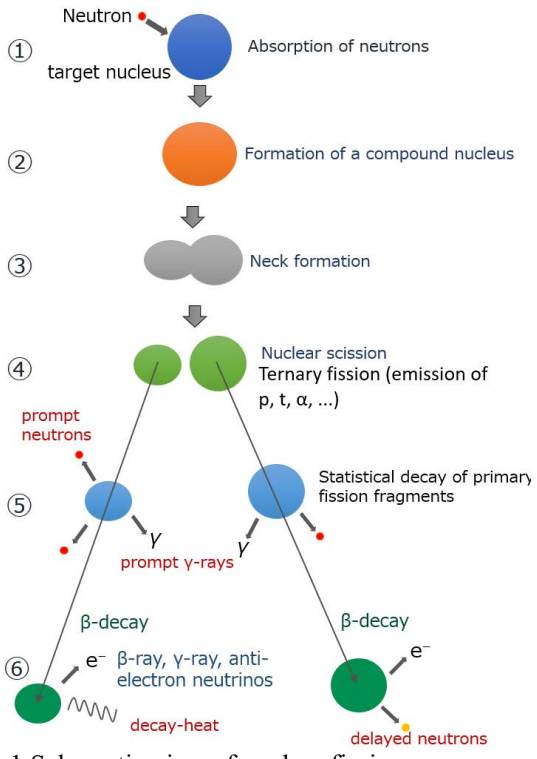

Fig. 1 Schematic view of nuclear fission process.

populated fragment, which is a formidable task. Furthermore, we have used the Hauser-Feshbach theory to describe the statistical decay of the primary fission fragments (process ⑤) to lead to the population of independent fission products and emission of prompt neutrons and γ-rays, and the gross theory of beta-decay and summation method to investigate the final β-decay part (process ⑥) which leads to the generation of delayed neutrons, decay heat, and emission of anti-electron neutrinos.

2.1. Fission properties studied by the Langevin equation

Langevin dynamical model can reproduce and predict not only the fission fragment mass yields but also the total kinetic energies of the fission fragments of various actinides very accurately. In the Langevin model, a nuclear fission process is regarded as a time-evolution of the nuclear shape of a compound nucleus, which is formed via neutron absorption by a target in a neutron-induced reaction, following the equation of motion under the friction force and the random force (so called the Langevin equation). The Langevin equations are formulated as a set of coupled stochastic differential equations. We have developed a 4-dimensinal Langevin model [27, 29, 30] by extending degree of freedom to describe a realistic nuclear-shape leading to nuclear scission, and by introduction of quantal effects to the free energy, the zero-point energy correction to each of the collective coordinate, and also by introducing microscopic transport coefficients based on the linear response theory [46].

Figure 2 shows calculated mass distributions of fission fragments (black histograms) compared with experimental data (red circles) at excitation of 20 MeV as representatives of compound nuclei populated by neutrons. In contrast, Fig. 3 compares calculated mass-TKE correlation of fission fragments (left panel) with experimental data (right panel). The gray histogram in the upper-left panel of Fig. 2 shows a calculation without quantal effects yielding only 1-peak in mass distribution. These figures show how our 4D Langevin model can describe known properties of nuclear fission by taking account of the quantal effects properly into the thermodynamic approach represented by the Langevin equation. Verified by this quantitative agreement, we have made a systematic calculation of fragments-mass vs. TKE correlation for actinides as shown in Fig. 4 [19]. We notice that, starting from the left-bottom to the right-upper panel, the TKE of the symmetric component makes a sudden jump to higher values at mass number of 250 to 254 which is an indication of transition of the symmetric mode from superlong to supershort mode.

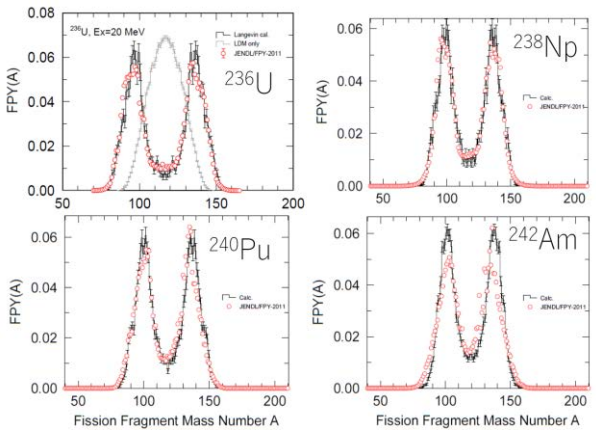

Fig. 2 Calculated mass distribution of fission fragments (black histograms) compared to experimental information (right circles).

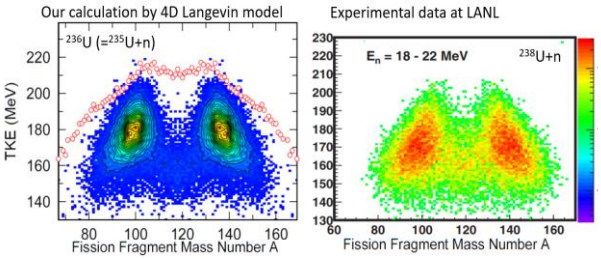

Fig. 3 Mass-TKE correlation of fission fragments (left: our calculation, right: experimental data).

Furthermore, the dominant mode, shown by red dots, moves from the asymmetric mode to the symmetric mode at A=257 to 258, then moves back to the asymmetric mode at ^{260}Md to ^{256}No, making mass distribution to change from 2-peak structure to 1-peak, then to 2-peak again. Such a "correlated transition" of 2 physical quantities were effective in understanding systematical and anomalous trends in the fission mechanisms of actinide nuclei in a unified manner.

Then, based on this success, we have extended our calculation to superheavy nuclei [13]. A result is shown in Fig. 5 for the fragment-mass vs. TKE correlation of ^{294}Og (Z=118). We can notice that this correlation pattern is much more complicated than that of the actinide region shown in Figs. 3 and 4. We have found that the shell of ^{208}Pb plays a dominant role in the fission mechanisms of superheavy nuclei to form the "superaymmetric" component.

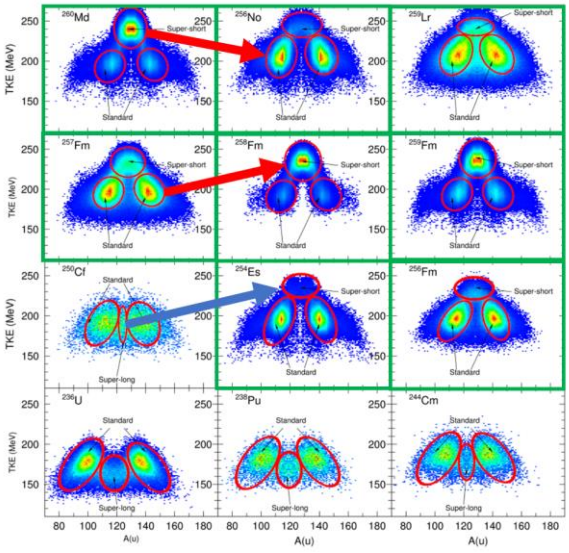

Fig. 4 Mass-TKE correlation of fission fragments for a series of actinide nuclei arranged in increasing order of $Z^2/A^{1/3}$ of fissioning nucleus starting from the leftmost-bottom to the rightmost upper panel.

2.2. Application of Antisymmetrized Molecular Dynamics (AMD) to study of nuclear fission

While we understood that Langevin model gives rather accurate results to describe various properties of nuclear fission, it is based on a macroscopic approach, and it lacks full microscopic description of the fission process, which is becoming a major trends in this field. Then, we also have investigated the fission reaction based on the Antisymmetrized Molecular Dynamics (hereafter AMD). In AMD, a nucleus can be microscopically described by a Slater determinant consisting of Gaussian wave packets chosen as variational functions to represent single-particle states. AMD has been widely used to study nuclear reactions and nuclear structures for light nuclei, but we are the only one group to apply AMD to fission study. From this study, we expect to get aspects of nuclear fission that cannot be obtained from the Langevin model.

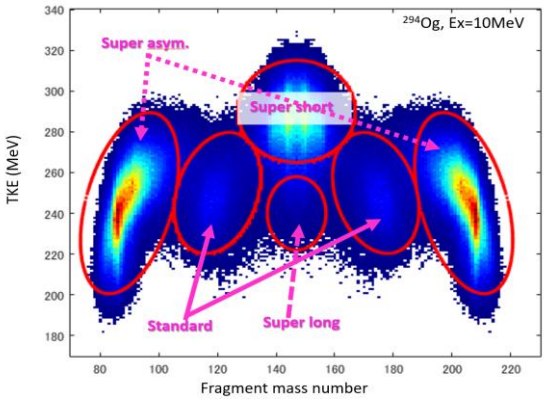

Fig. 5 Predicted mass-TKE correlation of fission fragments for ^{294}Og at Ex=10 MeV.

In Fig. 6, we show snapshots of nucleon density distributions during the fission of ^{236}U (= compound nucleus of n + ^{235}U reaction), where degree-of-freedom of 92 protons and 144 neutrons are explicitly considered. We have adopted SLy4 effective interaction acting among nucleons, NN collision by Li-Machleit parameterization, and the fission was initiated by a technique called "symmetric boost mechanism". By repeating such calculations, we can obtain distributions of isotopes, TKE and spin of fission fragments.

In Fig. 7, we plotted mass-TKE correlation of fission fragments originated from ^{236}U compound nucleus. The color contour shows data estimated from experimental information, while circles are the results of AMD calculation, which corresponds to symmetric fission mode. We notice that the AMD calculation can describe the TKEs of symmetric fission components quite accurately. Through such simulations, we could draw conclusions on the spin distribution and mechanisms of ternary fission in quantitative manner.

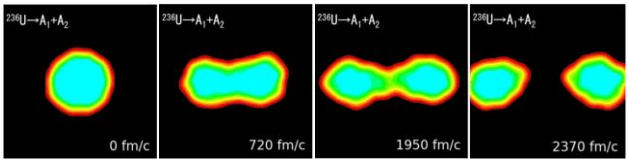

Fig. 6 Snapshots of time evolution of nucleon density during fission of ^{236}U.

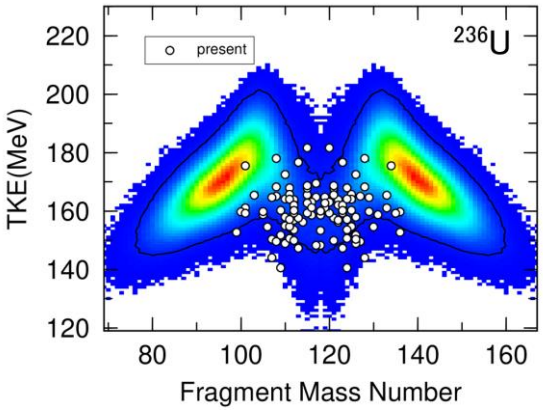

Fig. 7 Fragment mass-TKE correlation of ^{236}U. Color contour: experimental data, white circles: AMD calculation.

2.3 Relativistic and non-relativistic density functional theories

Other microscopic approaches used in our laboratory are relativistic and non-relativistic density functional theories. These models can provide detailed information on potential energy surfaces as a function of nuclear deformations and on fission barrier height. Nevertheless, there is no effective interaction designed for nuclear fission itself. In our laboratory, we have investigated how the pairing interaction affects the fission barrier height in both models, and found that about 20% increase in the pairing strength drastically improves reproduction of fission barrier heights [3,5,7]. Our study on the pairing interaction is based on a consideration including the pairing rotational energy, which confirms the validity of our conclusions. Furthermore, we found that triaxiality has a dominant role in the height of outer fission barrier.

3. Beta decay of fission products [22, 33, 42]

After prompt neutrons and gammas emitted from the fission fragments, the beta-decays of these nuclei will occur. Anti-electron neutrinos (abbreviated as neutrinos for simplicity) produced by the beta-decay process play a significant role in the surveillance and in-service inspection of nuclear power plants, which can serve as a novel method of nuclear safeguards. They are also used to establish neutrino oscillations, and such a study eventually leads to discovery of exotic particles such as sterile neutrinos.

We have studied the antineutrino spectrum from aggregate beta-decay of fission products based on summation calculation and the gross theory. Figure 8 shows a comparison of antineutrino spectra emitted from β-decay of ^{92}Rb calculated by Gross Theory 2 (red line) and experimental data (triangles). We have performed such calculations for about 1,000 FP nuclei, and constructed an original database. Then, Fig. 9 compares aggregate and independent antineutrino spectra emitted from fission products populated in the fission of thermal neutron + ^{235}U system. The aggregate spectra are made by superposition of about 1,000 fission products. The calculation was done by using JENDL Decay Data Library 2011 and FPY (Fission Product Yield) from FPY2011 and that in JENDL-5 (FPY2020). We notice that the difference of the FPY data makes a difference in the neutrino spectra above 8 MeV, where only several nuclei like ^{92,95}Rb and ^{96}Y, having large Q_β values, contribute. Even though the calculation seems to reproduce the

measured data, the accuracy of such a computational method must be further improved for practical applications. Anyhow, we have established the basis of such a computational method.

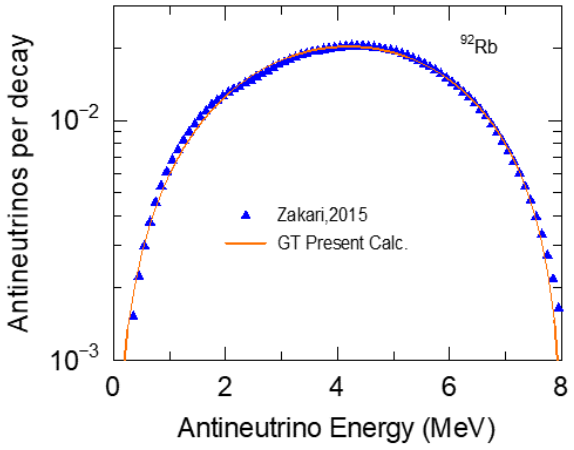

Fig. 8 Comparison of antineutrino energy spectra emitted from β-decay of ^{92}Rb calculated by Gross Theory 2 (red line) and experimental data (triangles).

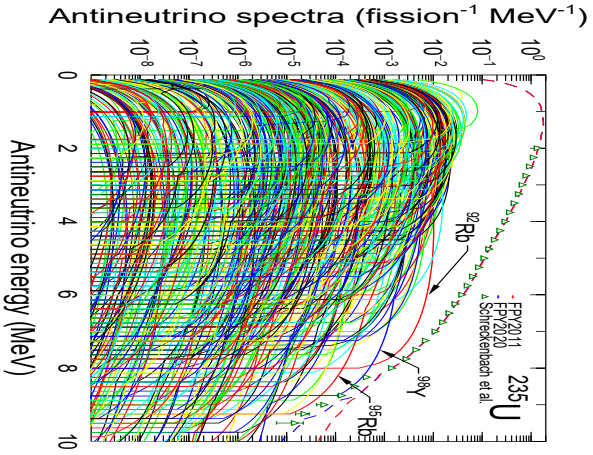

Fig. 9 Aggregate and independent neutrino spectra emitted from fission products populated in fission of n + ^{235}U system. The triangles are experimental data, while the total and independent neutrino spectra are shown by lines.

4. Evaluation of nuclear data and its impact on integral system

4.1. Development of fission yield data library for various applications

High precision nuclear data on the fission product yield (FPY) is necessary to evaluate the inventory of radioactive materials in spent nuclear fuel, total decay heat from the fission products and their toxicity. Historically, FPY data in JENDL have been borrowed from U.S. evaluation ENDF. Fortunately, a number of measurements of fission product yields (FPYs) have been accumulated since the last major evaluation was performed in ENDF library.

We have developed a FPY library based on the original evaluation method of experimental data, guided by all the fundamental research on nuclear fission we have carried out [24]. Our FPY library contains not only yields such as independent yields and cumulative yields, but also the covariance information on uncertainty in each data. Recently, such covariance data has been necessitated significantly for V&V (Validation and Verification) purposes. To develop the new library, we first gathered and evaluated experimental data from EXFOR database, and then developed a semi-phenomenological FPY model based on the recent knowledge of the shell effects including the even-odd staggering. The semi-phenomenological model is necessary to estimate the FPYs where no measured data exist. Hauser-Fechbach theory [28] was also applied to estimate unknown isomer ratios. The covariance was obtained by a generalized least-squares analysis containing minimal physics constraints. In this manner, we constructed a brand-new FPY library for the first time in Japan [12]. Our FPY library was adopted in JENDL-5 as a national nuclear database.

4.2. Impact of uncertainty of nuclear data on integral system

The uncertainty in various quantities relating to nuclear reactors becomes necessary information. Especially, the uncertainty in the evaluation for radioactivity due to neutron irradiation is strongly

required by nuclear regulation procedures.

We have evaluated the uncertainty of the cross sections of some LLFP nuclides in JENDL-4.0 by use of T6 code which evaluates the nuclear data employing the Bayesian Monte Carlo calculations [14]. Using these methods, we have investigated the uncertainty of the neutron spectra after deep penetration and found that the correlation of the total cross section and forward elastic angular distribution plays a crucial role [9].

Acknowledgment

I appreciate all my collaborators. Unfortunately, not all my activities could not be covered in this manuscript. Here, I wish to post summaries of them taken from Google Scholar citations and ResearchGate:

Google Scholar citations:
https://scholar.google.com/citations?hl=en&user=bBpCh60AAAAJ&view_op=list_works&sortby=pubdate
ResearchGate: https://www.researchgate.net/profile/Satoshi-Chiba/stats

I hope this field will evolve steadily in the future.

References

1) Chikako Ishizuka, Xuan Zhang, Kazuya Shimada, Mark Usang, Fedir Ivanyuk and Satoshi Chiba, “Nuclear Fission Properties of Super Heavy Nuclei described within the four-dimensional Langevin model”, Frontiers in Physics, Vol. 11, 2023.
2) Jeong-YeonLee, Yeongduk Kim and Satoshi Chiba, “New targets for relic antineutrino capture”, Nuclear Physics A, Vol. 1031, 122594, 2023, (DOI 10.1016/j.nuclphysa.2022.122594).
3) Kazuki Fujio, Shuichiro Ebata, Tsunenori Inakura, Chikako Ishizuka, Satoshi Chiba. "Energy competition and pairing effect for the fission path with a microscopic model", Frontiers in Physics, Vol. 10, (DOI 10.3389/fphy.2022.986488, Sep 2022).
4) Yoshihisa Tahara, Peng-hong Liem, Naoyuki Takaki, Satoshi Chiba. "Design of Cesium target assembly with YH_2 moderator and Gd thermal neutron shielding to produce ^{135}Cs for LLFP transmutation study using the experimental fast reactor Joyo", Annals of Nuclear Energy, Vol. 166, 108830, Elsevier, Jan 2022.
5) Taiki Kouno, Chikako Ishizuka, Kazuki Fujio, Tsunenori Inakura, Satoshi Chiba. "Effects of triaxiality and pairing interaction on fission barriers of actinide nuclei", International Journal of Modern Physics E, 2250080, Sep 2022.
6) F.A.Ivanyuk, S.V.Radionov, C.Ishizuka and S.Chiba. "The memory effects in the Langevin description of nuclear fission", Nuclear Physics A, Vol. 1028, p. 122526, Jul 2022.
7) Taiki Kouno, Chikako Ishizuka, Tsunenori Inakura, Satoshi Chiba. "Pairing strength in the relativistic mean-field theory determined from the fission barrier heights of actinide nuclei and verified by pairing rotation and binding energies", Progress of Theoretical and Experimental Physics, Vol. 2022, Issue 2, Oxford University Press, Dec 2021.
8) Takehito Hayakawa, Yosuke Toh, Atsushi Kimura, Shoji Nakamura, Toshiyuki Shizuma, Nobuyuki Iwamoto, Satoshi Chiba, Toshitaka Kajino. "Isomer production ratio of the $^{112}Cd(n, \gamma)$ ^{113}Cd reaction in an s-process branching point", Physical Review C, Vol. 103, p. 045801, Apr 2021.

9) Naoki Yamano, Tsunenori Inakura, Chikako Ishizuka, Satoshi Chiba. "Crucial importance of correlation between cross sections and angular distributions in nuclear data of ^{28}Si on estimation of uncertainty of neutron dose penetrating a thick concrete", Journal of Nuclear Science and Technology, Vol. 59, No. 5, pp. 641-646, Taylor and Francis, Nov 2021.
10) Kazuya Shimada, Chikako Ishizuka, Fedir Ivanyuk, Satoshi Chiba. "Dependence of total kinetic energy of fission fragments on the excitation energy of fissioning systems", Physical Review C - Nuclear Physics, Vol. 104, 054609, American Institute of Physics, Nov 2021.
11) P. Dimitriou, I. Dillmann, B. Singh, V. Piksaikin, K.P. Rykaczewski, J.L. Tain, A. Algora, K. Banerjee, I.N. Borzov, D. Cano-Ott, S. Chiba, M. Fallot, D. Foligno, R. Grzywacz, X. Huang, T. Marketin, F. Minato, G. Mukherjee, B.C. Rasco, A. Sonzogni, M. Verpelli, A. Egorov, M. Estienne, L. Giot, D. Gremyachkin, M. Madurga, E.A. McCutchan, E. Mendoza, K.V. Mitrofanov, M. Narbonne, P. Romojaro, A. Sanchez-Caballero, N.D. Scielzo. "Development of a Reference Database for Beta-Delayed Neutron Emission", Nuclear Data Sheets, Vol. 173, pp. 144-238, Elsevier, May 2021.
12) Kohsuke Tsubakihara, Shin Okumura, Chikako Ishizuka, Tadashi Yoshida, Futoshi Minato, Satoshi Chiba. "Evaluation of fission product yields and associated covariance matrices", Journal of Nuclear Science and Technology, Sep 2020.
13) C. Ishizuka, X. Zhang, M. D. Usang, F. A. Ivanyuk, S. Chiba. "Effect of the doubly magic shell closures in ^{132}Sn and ^{208}Pb on the mass distributions of fission fragments of superheavy nuclei", Physical Review C - Nuclear Physics, Vol. 101, 011601(R), Jan 2020.
14) Naoki Yamano, Tsunenori Inakura, Chikako Ishizuka, Satoshi Chiba. "Estimation of uncertainty in transmutation rates of LLFPs in a fast reactor transmutation system via an estimation of the cross-section covariances", Journal of Nuclear Science and Technology, Vol. 58, No. 5, pp. 567-578, Taylor & Francis, Nov 2020.
15) Heamin Ko, Myung-Ki Cheoun, Eunja Ha, Motohiko Kusakabe, Takehito Hayakawa, Hirokazu Sasaki, Toshitaka Kajino, Masa-aki Hashimoto, Masaomi Ono, Mark D. Usang, Satoshi Chiba, Ko Nakamura, Alexey Tolstov, Ken'ichi Nomoto, Toshihiko Kawano, Grant J. Mathews. "Neutrino Process in Core-collapse Supernovae with Neutrino Self-interaction and MSW Effects", The Astrophysical Journal Letters, Vol. 891, Mar 2020.
16) Michael Bender, Remi Bernard, George Bertsch, Satoshi Chiba, Jacek Dobaczewski, Noel Dubray, Samuel A. Giuliani, Kouichi Hagino, Denis Lacroix, Zhipan Li, Piotr Magierski, Joachim Maruhn, Witold Nazarewicz, Junchen Pei, Sophie Peru, Nathalie Pillet, Jorgen Randrup, David Regnier, Paul-Gerhard Reinhard, Luis M. Robledo, Wouter Ryssens, Jhilam Sadhukhan, Guillaume Scamps, Nicolas Schunck, Cedric Simenel, Janusz Skalski, Ionel Stetcu, Paul Stevenson, Sait Umar, Marc Verriere, Dario Vretenar, Michaa Warda, Sven Aberg. "Future of Nuclear Fission Theory", Journal of Physics G: Nuclear and Particle Physics, Vol. 47, No. 11, 113002, Oct 2020.
17) Toshio Wakabayashi, Makoto Takahashi, Satoshi Chiba, Naoyuki Takaki, Yoshiaki Tachi. "A fast reactor transmutation system for 6 LLFP nuclides", Nuclear Engineering and Design, Vol. 363, 110667, Jul 2020.
18) Toshio Wakabayashi, Yoshiaki Tachi, Makoto Takahashi, Satoshi Chiba, Naoyuki Takaki. "Study on method to achieve high transmutation of LLFP using fast reactor", Scientific Reports, 9, 19156 (2019), Dec 2019.
19) Mark Dennis Usang, Fedir A. Ivanyuk, Chikako Ishizuka, Satoshi Chiba. "Correlated transitions in TKE and mass distributions of fission fragments described by 4-D Langevin equation", Scientific

Reports, Vol. 9, Page 1525, Springer Nature, Feb 2019.

20) K. R. Kean, K. Nishio, K. Hirose, M. J. Vermeulen, H. Makii, R. Orlandi, K. Tsukada, A. N. Andreyev, I. Tsekhanovich, S. Chiba. "Validation of the multinucleon transfer method for the determination of the fission barrier height", Physical Review C, Vol. 100, 014611, Jul 2019.
21) V. L. Litnevsky, F. A. Ivanyuk, G. I. Kosenko, S. Chiba. "Description of the mass-asymmetric fission of the Pt isotopes, obtained in the reaction ^{36}Ar+^{142}Nd within the two-stage fusion-fission model", Physical Review C, Vol. 99, 054624, May 2019.
22) Tadashi Yoshida, Takahiro Tachibana, Shin Okumura, Satoshi Chiba. "Spectral anomaly of reactor antineutrinos based on theoretical energy spectra", Physical Review C, Vol. 98, 041303(R), Oct 2018.
23) Yuma Kikuchi, Kazuyuki Ogata, Takehito Hayakawa, Satoshi Chiba. "Azimuthal angle distributions of neutrons emitted from the ^{9}Be(γ, n) reaction", Physical Review C, Vol. 98, Dec 2018.
24) Takehito Hayakawa, Heamin Ko, Myung-Ki Cheoun, Motohiko Kusakabe, Toshitaka Kajino, Mark D. Usang, Satoshi Chiba, Ko Nakamura, Alexey Tolstov, Ken'ichi Nomoto, Masa-aki Hashimoto, Masaomi Ono, Toshihiko Kawano, Grant J. Mathews. "Short-Lived Radioisotope ^{98}Tc Synthesized by the Supernova Neutrino Process", Physical Review Letters, vol. 121, page 102701, Sep 2018.
25) F.A. Ivanyuk, C. Ishizuka, M.D. Usang, S. Chiba. "The 4-dimensional Langevin approach to low energy nuclear fission", EPJ Web of Conferences, vol. 169, page 00005, Mar 2018.
26) Toshio Suzuki, Satoshi Chiba, Takashi Yoshida, Koh Takahashi, Hideyuki Umeda. "Neutrino-nucleus reactions on ^{16}O based on new shell-model Hamiltonians", Physical Review C, Vol. 98, Page 034613, Sep 2018.
27) Fedir A. Ivanyuk, C. Ishizuka, M.D. Usang, S. Chiba. "Temperature dependence of shell corrections", Phys. Rev. C, vol. 97, page 054331, May 2018.
28) Shin Okumura, Toshihiko Kawano, Patrick Jaffke, Patrick Talou, Satoshi Chiba. "^{235}U(n,f) Independent Fission Product Yield and Isomeric Ratio Calculated with the Statistical Hauser-Feshbach Theory", Journal of Nuclear Science and Technology, Volume 55, Issue 9, pp. 1009-1023, Taylor & Francis, Jun 2018.
29) M. D. Usang, F. A. Ivanyuk, C. Ishizuka, S. Chiba. "Analysis of the total kinetic energy of fission fragments with the Langevin equation", Phys. Rev. C, vol. 96, page 064617-1-13, Dec 2017.
30) Chikako Ishizuka, Mark D. Usang, Fedir A. Ivanyuk, Joachim A. Maruhn, Katsuhisa Nishio, Satoshi Chiba. "Four-dimensional Langevin approach to low-energy nuclear fission of ^{236}U", Physical Review C - Nuclear Physics, Volume 96, 6, 064616, Dec 2017.
31) K. Hirose, K. Nishio, S. Tanaka, R. L´eguillon, H. Makii, I. Nishinaka, R. Orlandi, K. Tsukada, J. Smallcombe, M. J. Vermeulen, S. Chiba, Y. Aritomo, T. Ohtsuki, K. Nakano, S. Araki, Y. Watanabe, R. Tatsuzawa, N. Takaki, N. Tamura, S. Goto, I. Tsekhanovich, A. N. Andreyev. "Role of Multichance Fission in the Description of Fission-Fragment Mass Distributions at High Energies", Phys. Rev. Lett, vol. 119, 222501, Nov 2017.
32) C. Ishizuka, S. Chiba, N. Carjan. "Charge polarization and the elongation of the fissioning nucleus at scission", Romanian Reports in Physics, vol. 70, page 202, Sep 2017.
33) Hiroyuki Koura, Satoshi Chiba. "Improvement to the gross theory of β decay by inclusion of change in parity", Physical Review C, vol. 95, 064304-1-6, Jun 2017.
34) Rei Kimura, Hiroshi Sagara, Satoshi Chiba. "Applicability Study of the Photofission Based Nuclear Material Isotopic Composition Measurement Method on the Thorium Uranium System", Energy Procedia, pp. 264-273, Dec 2017.

35) D.S. Martyanov, E.Sh. Soukhovitski˜ı, R. Capote, J.M. Quesada, S. Chiba. "Predicting the optical observables for nucleon scattering on even-even actinides", Chinese Physics C, Vol. 41, No. 9, 094105-1-6, Sep 2017.
36) Usang, M.D., Ivanyuk, F., Chikako Ishizuka, Satoshi Chiba. "Systematic Analysis of Fission Fragment Mass Distribution and TKE for Actinides by Langevin Equation", Energy Procedia, Vol. 131, pp. 299-305, 2017.
37) Satoshi Chiba, Toshio Wakabayashi, Yoshiaki Tachi, Naoyuki Takaki, Atsunori Terashima, Shin Okumura, Tadashi Yoshida. "Method to Reduce Long-lived Fission Products by Nuclear Transmutations with Fast Spectrum Reactors", Scientific Reports, Vol. 7, Springer Nature, Oct 2017.
38) Chikako Ishizuka, Hiroki Jojima, Mark D. Usang, Satoshi Chiba, Nicolae Carjan. "The charge polarization and its impact on prompt fission neutron multiplicity", Energy Procedia, Vol. 131, pp. 285-291, Dec 2017.
39) Kentaro Hirose, K. Nishio, Hiroyuki Makii, Ichiro Nishinaka, S. Ota, T. Nagayama, N. Tamura, S. Goto, A.N. Andreyev, M.J. Vermeulen, S. Gilespie, C. Barton, A. Kimura, H. Harada, S. Meigo, S. Chiba, T. Ohtsuki. "Simultaneous measurement of neutron-induced fission and capture cross sections for ^{241}Am at neutron energies below", Nuclear Instruments and Methods in Physics Research Section A, vol. 856, pp. 133-138, 2017.
40) E. Sh. Soukhovitski, R. Capote, J. M. Quesada, S. Chiba, D. S. Martyanov. "Nucleon scattering on actinides using a dispersive optical model with extended couplings", Physical Review C, Vol. 94, 064605, Dec 2016.
41) Tanaka, K.-I., Ueno, J., Satoshi Chiba. "Estimation of a boundary to distinguish between radioactive materials and non-radioactive materials around a Main Steam line and a Feed Water line in a Biological Shielding Wall of a BWR for decommissioning", Progress in Nuclear Energy, Vol. 93, pp. 371-385, 2016.
42) Tadashi Yoshida, Takahiro Tachibana, Naoto Hagura, Satoshi Chiba. "Composition, decomposition and analysis of reactor antineutrino and electron spectra based on gross theory of β-decay and summation method", Progress in Nuclear Energy, Vol. 88, pp. 175-182, Apr 2016.
43) Rei Kimura, Hiroshi Sagara, Satoshi Chiba. "Principle validation of nuclear fuel material isotopic composition measurement method based on photofission reactions", Journal of Nuclear Science and Technology, Vol. 53, Issue 12, pp. 1978-1987, May 2016.
44) R. Léguillon, K. Nishio, K. Hirose, H. Makii, I. Nishinaka, R. Orlandi, K. Tsukada, J. Smallcombe, S. Chiba, Y. Aritomo, T. Ohtsuki, R. Tatsuzawa, N. Takaki, N. Tamura, S. Goto, I. Tsekhanovich, C. M. Petrache, A. N. Andreyev. "Fission fragments mass distributions of nuclei populated by the multinucleon transfer channels of the ^{18}O + ^{232}Th reaction", Physics Letters B, Vol. 761, pp. 125-130, Oct 2016.
45) D. Ichinkhorloo, M. Aikawa, S. Chiba, Y. Hirabayashi, K. Katō. "Low energy scattering cross sections for n + ^{6,7}Li reactions using the continuum-discretized coupled-channels method", Physical Review C, Vol. 93, 064612, Jun 2016.
46) M. D. Usang, F. A. Ivanyuk, C. Ishizuka, S. Chiba. "Effects of microscopic transport coefficients on fission observables calculated by the Langevin equation", Physical Review C, Vol. 94, No. 4, Page 044602, Oct 2016.
47) T. Hayakawa, T. Shizuma, S. Miyamoto, S. Amano, A. Takemoto, M. Yamaguchi, K. Horikawa, H. Akimune, S. Chiba, K. Ogata, M. Fujiwara. "Spatial anisotropy of neutrons emitted from the

^{56}Fe(γ,n)^{55}Fe reaction with a linearly polarized γ-ray beam", Physical Review C, Vol. 93, 044313, Apr 2016.

48) Takehito Hayakawa, Shuji Miyamoto, Takayasu Mochizuki, Ken Horikawa, Sho Amano, Dazhi Li, Kazuo Imazaki, Yasukazu Izawa, Kazuyuki Ogata, Satoshi Chiba. "Laser Compton Scattering Gamma-Ray Experiments for Supernova Neutrino Process", Plasma and Fusion Research, Vol. 11, Page 3406066, Jun 2016.
49) T. Hayakawa, Y. Toh, M. Huang, T. Shizuma, A. Kimura, S. Nakamura, H. Harada, N. Iwamoto, S. Chiba, T. Kajino. "Measurement of the isomer production ratio for the ^{112}Cd(n, γ)^{113}Cd reaction using neutron beams at J-PARC", Physical Review C, Vol. 94, No. 5, 055803, Nov 2016.
50) S. Shibagaki, T. Kajino, G. J. Mathews, S. Chiba, S. Nishimura, G. Lorusso. "Relative contributions of the weak, main and fission-recycling r-process", The Astrophysical journal, Vol. 816, No. 2, Jan 2016.
51) R. Capote, N. Carjan, S. Chiba. "Scission neutrons for U, Pu, Cm, and Cf isotopes: Relative multiplicities calculated in the sudden limit", Physical Review C, Vol. 93, 024609, Feb 2016.
52) T. Sato, K. Niita, N. Matsuda, S. Hashimoto, Y. Iwamoto, T. Furuta, S. Noda, T. Ogawa, H. Iwase, H. Nakashima, T. Fukahori, K. Okumura, T. Kai, S. Chiba, L. Sihver. "Overview of particle and heavy ion transport code system PHITS", Annals of Nuclear Energy, Vol. 82, pp. 110-115, Aug 2015.
53) Koura, H., Satoshi Chiba. "Theoretical Study of Beta Decay for Delayed Neutron", Energy Procedia, Vol. 71, pp. 228-236, 2015.
54) H. Makii, S. Ota, T. Ishii, Y. Wakabayashi, K. Furutaka, K. Nishio, I. Nishinaka, S.Chiba, M. Igashira, A. Czeszumska. "Development of a measurement system for the determination of (n, γ) cross-sections using multi-nucleon transfer reactions", Nuclear Instruments and Methods in Physics Research Section A: Accelerators, Spectrometers, Detectors and Associated Equipment, Vol. 797, pp. 83-93, Oct 2015.
55) Ken-ichi Tanaka, Jun Ueno, Masataka Adachi, Satoshi Chiba. "Improvement of a calculation procedure of neutron-flux distribution for radioactivity inventory estimation for decommissioning of nuclear power plants", Progress in Nuclear Energy, Vol. 85, pp. 254-270, Nov 2015.
56) Satoshi Chiba, Nishio, K., Aritomo, Y., Koura, H., Iwamoto, O., Kugo, T., "A Comprehensive Approach to Estimate Delayed-neutron Data of Actinides and Minor-actinides", Energy Procedia, Vol. 71, pp. 205-212, 2015.
57) Yoshihiro Aritomo, Satoshi Chiba, Katsuhisa Nishio. "Independent fission yields studied based on Langevin equation", Progress in Nuclear Energy, Vol. 85, pp. 568-572, Nov 2015.
58) Fedir Ivanyuk, Satoshi Chiba, Yoshihiro Aritomo. "The transport coefficient of collective motion within the two-center shell model shape parameterization", Journal of Nuclear Science and Technology, Vol. 53, 6, pp. 737-748, Aug 2015.
59) Toshiki Maruyama, Toshitaka Tatsumi, Dmitri N. Voskresensky, Tomonori Tanigawa, Satoshi Chiba. "Nuclear “pasta” structures and the charge screening effect", Physical Review C - Nuclear Physics, Vol. 72, 015802, Jul 2005.
60) K. Horikawa, S. Miyamoto, T. Mochizuki, S. Amano, D. Li, K. Imasaki, Y. Izawa, K. Ogata, S. Chiba, T. Hayakawa. "Neutron angular distribution in (γ, n) reactions with linearly polarized γ-ray beam generated by laser Compton scattering", Physics Letters B, Vol. 737, pp. 109-113, Oct 2014.
61) Yuji Fukaya, Minoru Goto, Hirofumi Ohashi, Yukio Tachibana, Kazuhiko Kunitomi, Satoshi Chiba. "Proposal of a plutonium burner system based on HTGR with high proliferation resistance", Journal

of Nuclear Science and Technology, Vol. 51, 6, pp. 818-831, Apr 2014.

62) Shusaku Noda, Shintaro Hashimoto, Tatsuhiko Sato, Tokio Fukahori, Satoshi Chiba, Koji Niita. "Improvement of photonuclear reaction model below 140 MeV in the PHITS code", Journal of Nuclear Science and Technology, Vol. 52, 1, pp. 57-62, Jun 2014.
63) S. Chiba, K. Nishio, H. Makii, Y. Aritomo, I. Nishinaka, T. Ishii, K. Tsukada, M. Asai, K. Furutaka, S. Hashimoto, H. Koura, K. Ogata, T. Otsuki, T. Nagayama. "Surrogate Reactions Research at JAEA/Tokyo Tech", Nuclear Data Sheets, Vol. 119, pp. 229-232, May 2014.
64) Y. Aritomo, S. Chiba, F. Ivanyuk. "Fission dynamics at low excitation energy", Physical Review C, Vol. 90, 054609, Nov 2014.
65) F. A. Ivanyuk, S. Chiba, Y. Aritomo. "Scission-point configuration within the two-center shell model shape parameterization", Physical Review C, Vol. 90, 054607, Nov 2014.
66) H. Makii, S. Ota, T. Ishii, K. Nishio, I. Nishinaka, K. Furutaka, Y. Wakabayashi, S. Chiba, M. Igashira. "Development of Anti-Compton LaBr3(Ce) Spectrometer for Measurement of Surrogate Reactions", NUCLEAR DATA SHEETS, Vol. 119, pp. 361-364, May 2014.
67) J.M. Quesada, R. Capote, E.Sh. Soukhovitskij, S. Chiba. "Rotational-vibrational Description of Nucleon Scattering on Actinide Nuclei Using a Dispersive Coupled-channel Optical Model", Nuclear Data Sheets, Vol. 118, Page 270-272, Apr 2014.
68) Tatsuhiko Sato, Koji Niita, Norihiro Matsuda, Shintaro Hashimoto, Yosuke Iwamoto, Shusaku Noda, Hiroshi Iwase, Hiroshi Nakashima, Tokio Fukahori, Satoshi Chiba, Lembit Sihver. "Overview of the PHITS code and its application to medical physics", Progress in Nuclear Science and Technology, Vol. 4, pp. 879-882, 2014.
69) Hiroyuki Koura, Satoshi Chiba. "Single-Particle Levels of Spherical Nuclei in the Superheavy and Extremely Superheavy Mass Region", Journal of the Physical Society of Japan, Vol. 82, No. 1, 2013.
70) Tatsuhiko Sato, Koji Niita, Norihiro Matsuda, Shintaro Hashimoto, Yosuke Iwamoto, Shusaku Noda, Tatsuhiko Ogawa, Hiroshi Iwase, Hiroshi Nakashima, Tokio Fukahori, Keisuke Okumura, Tetsuya Kai, Satoshi Chiba, Takuya Furuta, Lembit Sihver. "Particle and Heavy Ion Transport code System, PHITS, version 2.52", Journal of Nuclear Science and Technology, Vol. 50, No. 9, Jul 2013.
71) Y. Aritomo, S. Chiba. "Fission process of low excited nuclei with Langevin approach", PHYSICAL REVIEW C, 88, 044614, Oct 2013.
72) T. Hayakawa, K. Nakamura, T. Kajino, S. Chiba, N. Iwamoto, M. K. Cheoun, G. J. Mathews. "Supernova neutrino nucleosynthesis of the radioactive ^{92}Nb observed in primitive meteorites", The Astrophysical Journal, 779, 1, L9-1-5, Dec 2013.
73) S. Hashimoto, K. Niita, N. Matsuda, Y. Iwamoto, H. Iwase, T. Sato, S. Noda, T. Ogawa, H. Nakashima, T. Fukahori, T. Furuta, S. Chiba, "Features of PHITS and its Application to Medical Physics", Japanese Journal of Medical Physics (Igakubutsuri), Vol. 33, No. 2, pp. 88–95,2013.
74) Y. Aritomo, K. Hagino, K. Nishio, S. Chiba. "Dynamical approach to heavy-ion induced fission using actinide target nuclei at energies around the Coulomb barrier", Physical Review C - Nuclear Physics, Vol. 85, No. 4, Apr 2012.
75) D. Ichinkhorloo, Y. Hirabayashi, K. Kato, M. Aikawa, T. Matsumoto, S. Chiba. "Analysis of ^{7}Li(n, n')^{7}Li* reactions using the continuum-discretized coupled-channels method", Physical Review C, Vol. 86, 064604, Dec 2012.
76) Myung-Ki Cheoun, Eunja Ha, T. Hayakawa, Satoshi Chiba, Ko Nakamura, Toshitaka Kajino, Grant J. Mathews. "Neutrino induced reactions for -process nucleosynthesis of ^{92}Nb and ^{98}Tc", Physical

Review C, Vol. 85, No. 6, 065807, American Physical Society, Jun 2012.

77) D. Ichinkhorloo, Y. Hirabayashi, K. Kato, M. Aikawa, T. Matsumoto, S. Chiba. "Analysis of 7Li(n,n′)7Li* reactions using the continuum-discretized coupled-channels method", Physical Review C - Nuclear Physics, Vol. 86, No. 6, 2012.
78) Toshiki Maruyama, Gentaro Watanabe, S. Chiba. "Molecular Dynamics for Dense Matter", Prog. Theor. Exp. Phys., 01A201, 1-27, 2012.
79) T. Matsumoto, D. Ichinkhorloo, Y. Hirabayashi, K. Katō, S. Chiba. "Systematic description of ^{6}Li(n, n')^{6}Li* → d + α reactions with the microscopic coupled-channels method", Physical Review C, Vol. 83, 064611, Jun 2011.
80) S. Oryu, Y. Hiratsuka, S. Nishinohara, S. Chiba. "Proton-proton phase shifts calculations in momentum space by a rigorous Coulomb treatment", Journal of Physics G: Nuclear and Particle Physics, Vol. 39, No. 4, pp. 0451011 - 04510112, Feb 2012.
81) Keiichi Shibata, Osamu Iwamoto, Tsuneo Nakagawa, Nobuyuki Iwamoto, Akira Ichihara, Satoshi Kunieda, Satoshi Chiba, Kazuyoshi Furutaka, Naohiko Otuka, Takaaki Ohsawa, Toru Murata, Hiroyuki Matsunobu, Atsushi Zukeran, So Kamada, Jun-ichi Katakura. "JENDL-4.0: A New Library for Nuclear Science and Engineering", Journal of Nuclear Science and Technology, Vol. 48, 1, pp. 1-30, 2011.
82) Kazuyuki OGATA, Shintaro HASHIMOTO, Satoshi CHIBA. "Three-Body Model Calculation of Spin Distribution in Two-Nucleon Transfer Reaction for the System of ^{238}U(^{18}O,^{16}O)^{240}U Reaction", Journal of Nuclear Science and Technology, Vol. 48, No. 10, pp. 1337-1342, Jan 2011.
83) Dagvadorj ICHINKHORLOO, Takuma MATSUMOTO, Yoshiharu HIRABAYASHI, Kiyoshi KATO, Satoshi CHIBA. "Analysis of n + ^{6}Li Reactions Using the Continuum-Discretized Coupled-Channels Method", Journal of Nuclear Science and Technology, Vol. 48, No. 11, pp. 1357-1360, Nov 2011.
84) Shintaro Hashimoto, Masanobu Yahiro, Kazuyuki Ogata, Kosho Minomo, Satoshi Chiba. "Effective radii of deuteron induced reactions", Physical Review C, Vol. 83, No. 5, 054617, Apr 2011.
85) Yutaka Utsuno, Satoshi Chiba. "Multiparticle-multihole states around ^{16}O and correlation-energy effect on the shell gap", Physical Review C - Nuclear Physics, Vol. 83, 021301(R), Feb 2011.
86) Satoshi Chiba, Osamu Iwamoto, Yoshihiro Aritomo. "Spin-dependent observables in surrogate reactions", Physical Review C, Vol. 84, 054602, Nov 2011.
87) F. Minato, S. Chiba. "Fission barrier of actinide nuclei with double-Λ particles within the Skyrme–Hartree–Fock method", Nuclear Physics A, Vol. 856, 1, Apr 2011.
88) T. Matsumoto, D. Ichinkhorloo, Y. Hirabayashi, K. Katō, S. Chiba. "Systematic description of ^{6}Li(n,n')dα reactions with the microscopic coupled-channels method", Physical Review C - Nuclear Physics, Vol. 83, 064611, Jun 2011.
89) Y. Aritomo, S. Chiba, K. Nishio. "Dynamical model of surrogate reactions", Physical Review C - Nuclear Physics, Vol. 84, No. 2, pp. 024602, American Physical Society, Aug 2011.
90) T. Hayakawa, T. Kajino, S. Chiba, G. J. Mathews. "New estimate for the time-dependent thermal nucleosynthesis of ^{180}Ta^{m}", Physical Review C - Nuclear Physics, Vol. 81, 5, 052801(R), May 2010.
91) T. Hayakawa, P. Mohr, T Kajino, S. Chiba, G. J. Mathews. "Re-analysis of the (J= 5) state at 592 keV in ^{180}Ta and its role in the ν-process nucleosynthesis of 180Ta in supernovae", Physical Review C - Nuclear Physics, Vol. 82, 058801, Nov 2010.
92) Toshiki Maruyama, Toshitaka Tatsumi, Satoshi Chiba. "Liquid-gas phase transition in asymmetric nuclear matter at finite temperature", Nuclear Physics A, Vol. 834, 1-4, 561c-563c, Mar 2010.

93) Myung-Ki Cheoun, Eunja Ha, T. Hayakawa, Toshitaka Kajino, Satoshi Chiba. "Neutrino reactions on ^{138}La and ^{180}Ta via charged and neutral currents by the quasiparticle random-phase approximation", Physical Review C - Nuclear Physics, Vol. 82, 035504, Sep 2010.
94) Satoshi Chiba, Osamu Iwamoto. "Verification of the Surrogate Ratio Method", Physical Review C - Nuclear Physics, Vol. 81, 044604, Apr 2010.
95) Osamu Iwamoto, Tsuneo Nakagawa, Naohiko Otuka, Satoshi Chiba, Keisuke Okumura, Go Chiba, Takaaki Ohsawa, Kazuyoshi Furutaka. "JENDL Actinoid File 2008", Journal of Nuclear Science and Technology, Vol. 46, 5, pp. 510-528, 2009.
96) Satoshi Kunieda, Satoshi Chiba, Keiichi Shibata, Akira Ichihara, Osamu Iwamoto, Nobuyuki Iwamoto, Tokio Fukahori, Efrem Sh. SukhovitskiĬ. "Extensive Study of the Soft-Rotator Model Hamiltonian Parameters for Medium and Heavy Even-Even Nuclei", Journal of Nuclear Science and Technology, Vol. 46, No. 9, pp. 914-924, 2009.
97) Jeong-Yeon Lee, Insik Hahn, Yeongduk Kim, Seung-Woo Hong, Satoshi Chiba, Efrem Sh. Soukhovitskii. "Optical potentials for nuclear level structures and nucleon interactions data of tin isotopes based on the soft-rotator model", Physical Review C - Nuclear Physics, Vol. 79, 064612, Jun 2009.
98) F. Minato, S. Chiba, K. Hagino. "Fission of heavy Λ hypernuclei with the Skyrme–Hartree–Fock approach", Nuclear Physics A, Vol. 831, 3-4, pp. 150-162, Dec 2009.
99) Shintaro Hashimoto, Kazuyuki Ogata, Satoshi Chiba, Masanobu Yahiro. "New Approach for Evaluating Incomplete and Complete Fusion Cross Sections with", Progress of Theoretical Physics, Vol. 122, 5, pp. 1291–1300, Nov 2009.
100) Toshio Suzuki, Satoshi Chiba, Takashi Yoshida, Koji Higashiyama, Michio Honma, Toshitaka Kajino, Takaharu Otsuka. "Neutrino-nucleus reactions based on recent advances in shell-model calcuations", Nuclear Physics A, Vol. 805, pp. 579-581, 2008.
101) S. Chiba, H. Koura, T. Hayakawa, T. Maruyama, T. Kawano, T. Kajino. "Direct and semi-direct capture in low-energy (n , γ) reactions of neutron-rich tin isotopes and its implications for r -process nucleosynthesis", Physical Review C - Nuclear Physics, Vol. 77, 015809, Jan 2008.
102) M. Ohta, S. Tatsuda, K. Yamamoto, T. Asano, T. Wada, K. Hashizume, K. Sumiyoshi, K. Otsuki, T. Kajino, H. Koura, S. Chiba, T. Tachibana. "Systematic study for the shell effect in the fission fragment mass distribution ruptured from neutron rich nuclei", Nuclear Physics A, Vol. 805, pp. 558-560, 2008.
103) Tao Ye, Yukinobu Watanabe, Kazuyuki Ogata, Satoshi Chiba. "Analysis of deuteron elastic scattering from ^{6,7}Li using the continuum discretized coupled channels method", Physical Review C - Nuclear Physics, Vol. 78, 024611, Aug 2008.
104) Toshiki Maruyama, Satoshi Chiba, Hans-Josef Schulze, Toshitaka Tatsumi. "Quark deconfinement transition in hyperonic matter", Physics Letters B, Vol. 659, 1-2, Jan 2008.
105) R. Capote, S. Chiba, E. Sh. Soukhovitskiĭ, J. M. Quesada, E. Bauge. "A Global Dispersive Coupled-Channel Optical Model Potential for Actinides", Journal of Nuclear Science and Technology, Vol. 45, 4, 333-340, 2008.
106) Takashi Yoshida, Toshio Suzuki, Satoshi Chiba, Toshitaka Kajino, Hidekazu Yokomakura, Keiichi Kimura, Akira Takamura, Dieter H. Hartmann. "Neutrino-Nucleus Reaction Cross Sections for Light Element Synthesis in Supernova Explosions", The Astrophysical journal, Vol. 686, No. 1, pp. 448–466, Oct 2008.

107) N. T. Okumuşoğlu, F. Korkmaz Gorur, J. Birchall, E. Sh. Soukhovitskii, R. Capote, J. M. Quesada, S. Chiba. "Angular distributions of protons scattered by ^{40}Ar nuclei with excitation of the 2^+ (1.46 MeV) and 3^- (3.68 MeV) collective levels for incident energies of 25.1, 32.5, and 40.7 MeV", Physical Review C - Nuclear Physics, Vol. 75, 034616, Mar 2007.

108) S. Oryu, S. Nishinohara, N. Shiiki, S. Chiba. "Coulomb phase shift calculation in momentum space", Physical Review C - Nuclear Physics, Vol. 75, 021001(R), Feb 2007.

109) L. Bonneau, T. Kawano, T. Watanabe, S. Chiba. "Nucleon direct-semidirect radiative capture with Skyrme-Hartree-Fock-BCS bound states", Physical Review C - Nuclear Physics, Vol. 75, 054618, May 2007.

110) Satoshi Kunieda, Satoshi Chiba, Keiichi Shibata, Akira Ichihara, Efrem Sh. SukhovitskĬ. "Coupled-channels Optical Model Analyses of Nucleon-induced Reactions for Medium and Heavy Nuclei in the Energy Region from 1 keV to 200 MeV", Journal of Nuclear Science and Technology, Vol. 44, 6, pp. 838-852, 2007.

111) Toshiki Maruyama, Satoshi Chiba, Hans-Josef Schulze, Toshitaka Tatsumi. "Hadron-quark mixed phase in hyperon stars", Physical Review D - Particles, Fields, Gravitation and Cosmology, Vol. 76, 123015, Dec 2007.

112) S. Nishinohara, S. Chiba, S. Oryu. "The Coulomb scattering in momentum space for few-body systems", Nuclear Physics A, Vol. 790, 1-4, pp. 277c-281c, Jun 2007.

113) K. Sumiyoshi, S. Yamada, H. Suzuki, S. Chiba. "Neutrino Signals from the Formation of a Black Hole: A Probe of the Equation of State of Dense Matter", Physical Review Letters, Vol. 97, 091101, Aug 2006.

114) Yuka Akimura, Toshiki Maruyama, Naotaka Yoshinaga, Satoshi Chiba. "Properties of Hadron and Quark Matter Studied with Molecular Dynamics", Acta Physica Hungarica Series A, Heavy Ion Physics, Vol. 27, pp. 355–358, Feb 2006.

115) Toshio Suzuki, Satoshi Chiba, Takashi Yoshida, Toshitaka Kajino, Takaharu Otsuka. "Neutrino-nucleus reactions based on new shell model Hamiltonians", Physical Review C - Nuclear Physics, Vol. 74, 034307, Sep 2006.

116) Satoshi Chiba, Mamoru Baba, Hiroshi Nakashima, Masahiro Ono, Naohiro Yabuta, Shigeru Yukinori, Naohiro Hirakawa. "Interaction of fast neutrons with ^{6,7}Li", Radiation Effects & Defects in Solids, Vol. 92, 1-4, pp. 227-230, Aug 2006.

117) Toshiki Maruyama, Toshitaka Tatsumi, Dmitri N. Voskresensky, Tomonori Tanigawa, Tomoki Endo, Satoshi Chiba. "Finite size effects on kaonic pasta structures", Physical Review C - Nuclear Physics, Vol. 73, 035802, Mar 2006.

118) T. Hayakawa, S. Miyamoto, Y. Hayashi, K. Kawase, K. Horikawa, S. Chiba, K. Nakanishi, H. Hashimoto, T. Ohta, M. Kando, T. Mochizuki, T. Kajino, M. Fujiwara. "Half-life of ^{184}Re populated by the (γ,n) reaction from laser compton scattering γ rays at the electron storage ring New SUBARU", Physical Review C - Nuclear Physics, Vol. 74, 065802, Dec 2006.

119) Tomoyuki Maruyama, Satoshi Chiba. "Nuclear electromagnetic current in the relativistic approach with the momentum-dependent self-energies", Physical Review C - Nuclear Physics, Vol. 74, 1, 014315, Jul 2006.

120) Toshiki Maruyama, Toshitaka Tatsumi, Tomoki Endo, Satoshi Chiba. "Pasta structures in compact stars", Recent Research Developments in Physics, Vol. 7, pp. 1-57, 2006.

121) Toshihiko Kawano, Satoshi Chiba, Hiroyuki Koura. "Phenomenological Nuclear Level Densities

Using the KTUY05 Nuclear Mass Formula for Applications Off-Stability", Journal of Nuclear Science and Technology, Vol. 43, 1, pp. 1-8, 2006.

122) Tomoki Endo, Toshiki Maruyama, Satoshi Chiba, Toshitaka Tatsumi. "Charge Screening Effect in the Hadron-Quark Mixed Phase", Progress of Theoretical Physics, Vol. 115, 2, pp. 337–353, Feb 2006.

123) T. Hayakawa, T. Shizuma, T. Kajino, S. Chiba, N. Shinohara, T. Nakagawa, T. Arima. "New s-Process Path and Its Implications for a ^{187}Re-^{187}Os Nucleo-Cosmochronometer", The Astrophysical journal, Vol. 628, No. 1, pp. 533-540, Jul 2005.

124) T.Nakagawa, S.Chiba, T.Hayakawa, T.Kajino, Satoshi Chiba. "Maxwellian-averaged neutron-induced reaction cross sections and astrophysical reaction rates for kT = 1 keV to 1 MeV calculated from microscopic neutron cross section library JENDL-3.3", Atomic Data and Nuclear Data Tables, Vol. 91, 2, pp. 77-186, Nov 2005.

125) R. Capote, E. Sh. Soukhovitskii, J. M. Quesada, S. Chiba. "Is a global coupled-channel dispersive optical model potential for actinides feasible?", Physical Review C - Nuclear Physics, Vol. 72, 064610, Dec 2005.

126) Y. Akimura, T. Maruyama, N. Yoshinaga, S. Chiba. "Molecular dynamics simulation for the baryon-quark phase transition at finite baryon density", The European Physical Journal A - Hadrons and Nuclei, Vol. 25, pp. 405-411, Sep 2005.

127) E. Sh. Soukhovitskii, R. Capote, J. M. Quesada, S. Chiba. "Dispersive coupled-channel analysis of nucleon scattering from ^{232}Th up to 200 MeV", Physical Review C - Nuclear Physics, Vol. 72, 024604, Aug 2005.

128) K. Sumiyoshi, S. Yamada, H. Suzuki, H. Shen, S. Chiba, H. Toki. "Postbounce Evolution of Core-Collapse Supernovae: Long-Term Effects of the Equation of State", The Astrophysical Journal, Vol. 629, No. 2, 922-932, Aug 2005.

129) Tomonori Tanigawa, Masayuki Matsuzaki, Satoshi Chiba. "1S0 proton superfluidity in neutron star matter: Impact of bulk properties", Physical Review C - Nuclear Physics, Vol. 70, 065801, Dec 2004.

130) Tomoyuki Maruyama, Satoshi Chiba. "In-Medium Effects in Eta Photo-Production through the S11 Resonance in the Relativistic Approach", Progress of Theoretical Physics, Vol. 111, 2, pp. 229–243, Feb 2004.

131) Hiroki Takemoto, Masahiro Fukushima, Satoshi Chiba, Hisashi Horiuchi, Yoshinori Akaishi, Akihiro Tohsaki. "Clustering phenomena in nuclear matter below the saturation density", Physical Review C - Nuclear Physics, Vol. 69, 035802, Mar 2004.

132) Efrem Sh Soukhovitskii, Satoshi Chiba, Jeong-Yeon Lee, Osamu Iwamoto, Tokio Fukahori. "Global coupled-channel optical potential for nucleon-actinide interaction from 1 keV to 200 MeV", Journal of Physics G: Nuclear and Particle Physics, Vol. 30, 7, 905–920, May 2004.

133) T. Matsumoto, E. Hiyama, K. Ogata, Y. Iseri, M. Kamimura, S. Chiba, M. Yahiro. "Continuum-discretized coupled-channels method for four-body nuclear breakup in ^{6}He + ^{12}C scattering", Physical Review C - Nuclear Physics, Vol. 70, 061601(R), Dec 2004.

134) Efrem Sh. SUKHOVITSKIĬ, Satoshi CHIBA, Jeong-Yeon LEE, Byung-taik KIM, Seung-Woo HONG. "Analysis of Nucleon Scattering Data of ^{52}Cr with a Coupling Scheme Built with the Soft-rotator Model", Journal of Nuclear Science and Technology, Vol. 40, 2, pp. 69-76, Feb 2003.

135) Weili Sun, Yukinobu Watanabe, Efrem Sh. SukhovitskiĬ, Osamu Iwamoto, Satoshi Chiba. "Coupled-Channels Analysis of Nucleon Interaction Data of ^{28,30}Si up to 200 MeV Based on the Soft Rotator

Model", Journal of Nuclear Science and Technology, Vol. 40, 9, 635-643, Sep 2003.

136) Tomonori Tanigawa, Masayuki Matsuzaki, Satoshi Chiba. "Possibility of Λ Λ pairing and its dependence on background density in relativistic Hartree-Bogoliubov model", Physical Review C - Nuclear Physics, Vol. 68, 015801, Jul 2003.

137) Yuichi Hirata, Akira Ohnishi, Yasushi Nara, Toshihiko Kido, Toshiki Maruyama, Naohiko Otuka, Koji Niita, Hiroshi Takada, Satoshi Chiba. "Sideward peak of intermediate mass fragments in high energy proton induced reactions", Nucl. Phys. Vol. 707, 1-2, 193-212, Aug 2002.

138) Efrem Sh. Sukhovitskiĭ, Satoshi Chiba, Jeong-Yeon Lee, Young-Ouk Lee, Jonghwa Chang, Toshiki Maruyama, Osamu Iwamoto. "Nuclear Level Structure, B(E2) Gamma-transitions and Nucleon Interaction Data for ^{56}Fe by a Unified Soft-rotator Model and Coupled-Channels Framework", Journal of Nuclear Science and Technology, Vol. 39, 8, pp. 816-826, Aug 2002.

139) Tokio Fukahori, Yukinobu Watanabe, Nobuaki Yoshizawa, Fujio Maekawa, Shin-ichiro Meigo, Chikara Konno, Naoki Yamano, Alexander Yu. Konobeyev, Satoshi Chiba. "JENDL High Energy File", Journal of Nuclear Science and Technology, Vol. 39, No. sup2, pp. 25-30, Aug 2002.

140) Osamu Iwamoto, Jian Rong, Tokio Fukahori, Satoshi Chiba. "Calculation of Fission Reaction in the Framework of QMD+SDM", Journal of Nuclear Science and Technology, Vol. 39, sup2, 128-131, Aug 2002.

141) Toshiki Maruyama, Aldo Bonasera, Massimo Papa, Satoshi Chiba. "Formation and decay of super-heavy systems", The European Physical Journal A - Hadrons and Nuclei, Vol. 14, 191–197, Jun 2002.

142) Toshiki Maruyama, Aldo Bonasera, Massimo Papa, Satoshi Chiba. "Lifetime of Heavy Composite Systems Formed by Fusion between Heavy Nuclei", Journal of Nuclear and Radiochemical Sciences, Vol. 3, 1, 77-80, Jul 2002.

143) Masayoshi Kawai, Takashi Watanabe, Atsushi Zukeran, Hiroyuki Matsunobu, Satoshi Chiba, Tsuneo Nakagawa, Yutaka Nakajima, Teruo Sugi, Klaus Dietze. "Interpretation of Integral Test Results of FP Cross Sections in JENDL-3.2 by Analyzing the STEK Experiments", Journal of Nuclear Science and Technology, Vol. 39, sup2, 982-985, Aug 2002.

144) Keiichi Shibata, Toshihiko Kawano, Tsuneo Nakagawa, Osamu Iwamoto, Jun-ichi Katakura, Tokio Fukahori, Satoshi Chiba, Akira Hasegawa, Toru Murata, Hiroyuki Matsunobu, Takaaki Ohsawa, Yutaka Nakajima, Tadashi Yoshida, Atsushi Zukeran, Masayoshi Kawai, Mamoru Baba, Makoto Ishikawa, Tetsuo Asami, Takashi Watanabe, Yukinobu Watanabe, Masayuki Igashira, Nobuhiro Yamamuro, Hideo Kitazawa, Naoki Yamano, Hideki Takano. "Japanese Evaluated Nuclear Data Library Version 3 Revision-3: JENDL-3.3", Journal of Nuclear Science and Technology, Vol. 39, 11, pp. 1125-1136, Nov 2002.

145) Masahide Harada, Yukinobu Watanabe, Yasuhiro Tanaka, Yasuaki Matsuoka, Kazuo Shin, Shin-ichiro Meigo, Hiroshi Nakashima, Hiroshi Takada, Toshinobu Sasa, Osamu Iwamoto, Tokio Fukahori, Satoshi Chiba, Susumu Tanaka. "Light Charged-Particle Production in Proton-Induced Reactions on ^{12}C, ^{27}Al, ^{58}Ni, ^{90}Zr, ^{197}Au, and ^{209}Bi at 42 and 68 MeV", Journal of Nuclear Science and Technology, Vol. 39, sup2, pp. 393-396, Aug 2002.

146) Masahiro Fukushima, Hideo Suganuma, Satoshi Chiba. "Instanton and Monopole in External Chromomagnetic Fields", Progress of Theoretical Physics, Vol. 107, 6, pp. 1147–1161, Jun 2002.

147) Satoshi Chiba, Tokio Fukahori, Keiichi Shibata, Baosheng Yu, Kazuaki Kosako, Nobuhiro Yamamuro. "JENDL Fusion File 99", Journal of Nuclear Science and Technology, Vol. 39, 2, Feb 2002.

148) Keiichi Shibata, Akira Hasegawa, Osamu Iwamoto, Satoshi Chiba, Masayoshi Sugimoto, Naoteru Odano, Toshihiko Kawano, Yutaka Nakajima, Toru Murata, Hiroyuki Matsunobu, Youl Soo Oh, Kenji Yokoyama, Kazuteru Sugino, Makoto Ishikawa, Kazuaki Kosako, Naoki Yamano, Yukinori Kanda. "JENDL-3.2 Covariance File", Journal of Nuclear Science and Technology, Vol. 39, sup2, pp. 40-43, Aug 2002.

149) Efrem Sh. Soukhovitskiĭ, Satoshi Chiba. "Analyses of Nucleon Interaction with ^{238}U up to 150 MeV Incident Energies Using Coupled-Channels Approach with a Saturated Coupling Scheme Based on Soft-Rotator Nuclear Model Hamiltonian", Journal of Nuclear Science and Technology, Vol. 39, sup2, pp. 144-147, Aug 2002.

150) Efrem Sh. Soukhovitskiĭ, Satoshi Chiba. "Soft-Rotator Model and Coupled-Channels Approach for Consistent Description of the Nuclear Collective Levels and Their Excitation by Nucleons", Journal of Nuclear Science and Technology, Vol. 39, sup2, 697-702, Aug 2002.

151) Weili Sun, Yukinobu Watanabe, Efrem Sh. Sukhovitskiĭ, Osamu Iwamoto, Satoshi Chiba. "Evaluation of Cross Sections for Neutrons and Protons up to 200 MeV on Silicon Isotopes", Journal of Nuclear Science and Technology, Vol. 39, sup2, Aug 2002.

152) Toshiki Maruyama, Aldo Bonasera, Satoshi Chiba. "Nuclear fragmentation by tunneling", Physical Review C, Vol. 63, 057601, Apr 2001.

153) Shinpei Chikazumi, Toshiki Maruyama, Satoshi Chiba, Koji Niita, Akira Iwamoto. "Quantum molecular dynamics simulation of expanding nuclear matter and nuclear multifragmentation", Physical Review C, Vol. 63, 024602, Jan 2001.

154) Masayoshi Kawai, Tsuneo Nakagawa, Takashi Watanabe, Yutaka Nakajima, Atsushi Zukeran, Hiroyuki Matsunobu, Teruo Sugi, Satoshi Chiba. "Re-evaluation of Nuclear Data of Fission Product Nuclides for JENDL-3.2", Journal of Nuclear Science and Technology, Vol. 38, 4, 261-269, Apr 2001.

155) V. N. Kondratyev, Toshiki Maruyama, Satoshi Chiba. "Magnetic Field Effect on Masses of Atomic Nuclei", The Astrophysical Journal, Vol. 546, No. 2, pp. 1137-1148, Jan 2001.

156) T. Maruyama, T. Hatsuda, S. Chiba. "Color molecular dynamics simulation of nuclei and dense matter", Nuclear Physics A, Vol. 681, 1-4, 72-75, Jan 2001.

157) J.Y. Lee, E.S. Sukhovitski, Y.O. Lee, J. Chang, S. Chiba, O. Iwamoto. "Analyses of the Nuclear Level Structure and Nucleon Interaction Data for ^{56}Fe Based on the Soft-rotator Model", Journal of Korean Physics Society, Vol. 38, 2, Feb 2001.

158) Efrem Sh. SukhovitskiĬ, Osamu Iwamoto, Satoshi Chiba, Tokio Fukahori. "Nucleon Optical Potential of ^{238}U up to 150 MeV", Journal of Nuclear Science and Technology, Vol. 37, No. 2, 120-127, Feb 2000.

159) Masahide Harada, Yukinobu Watanabe, Akihisa Yamamoto, Yasuhiro Tanaka, Sun Weili, Kazuo Shin, Shin-ichiro Meigo, Osamu Iwamoto, Hiroshi Nakashima, Hiroshi Takada, Satoshi Chiba, Tokio Fukahori, Toshinobu Sasa, Susumu Tanaka. "Measurement of Double Differential Cross Sections of Secondary Charged-Particles Produced by Proton-Induced Reactions at Several Tens of MeV", Journal of Nuclear Science and Technology, Vol. 37, sup1, 687-691, Mar 2000.

160) Tokio Fukahori, Norio Kishida, Satoshi Chiba, Toru Murata, Tetsuo Asami, Kazuki Hida, Koichi Maki. "Status of JENDL Photonuclear Data File and Intercomparison with Other Libraries", Journal of Nuclear Science and Technology, Vol. 37, sup1, pp. 728-732, Mar 2000.

161) Efrem Sh. Sukhovitskiĭ, Young-Ouk Lee, Jonghwa Chang, Satoshi Chiba, Osamu Iwamoto. "Nucleon interaction with Ni-58 up to 150-MeV studied in the coupled channels approach based on

the soft rotator nuclear structure model", physical review c, Vol. 62, 4, Sep 2000.

162) Satoshi Chiba, Osamu Iwamoto, Efrem Sh. Sukhovitskii, Yukinobu Watanabe, Tokio Fukahori. "Coupled-channels optical potential for interaction of nucleons with ^{12}C up to 150 MeV in the soft-rotator model", Journal of Nuclear Science and Technology, Vol. 37, 6, 498-508, Jun 2000.

163) Tomoyuki Maruyama, Satoshi Chiba. "Isoscalar Giant Quadrupole Resonance State in the Relativistic Approach with the Momentum-Dependent Self-Energies", Physical Review C - Nuclear Physics, Vol. 61, 037301, Feb 2000.

164) G. Mao, S. Chiba, W. Greiner, K. Oyamatsu. "Vacuum Discharge as a Possible Source of Gamma-ray Bursts", International journal of modern physics E, Vol. 09, No. 02, pp. 185-192, Apr 2000.

165) V. N. Kondratyev, T. Maruyama, S. Chiba. "Shell Structure of Nuclei in Strong Magnetic Fields in Neutron Star Crusts", Physical Review Letters, Vol. 84, 1086, Feb 2000.

166) Toshihiko Kido, Toshiki Maruyama, Koji Niita, Satoshi Chiba. "MD simulation study for nuclear matter", Nuclear Physics A, Vol. 663-664, 31, pp. 877c-880c, Jan 2000.

167) Kiminori Iga, Kenji Ishibashi, Nobuhiro Shigyo, Keisuke Maehata, Naruhiro Matsufuji, Tatsushi Nakamoto, Masaharu Numajiri, Shin-ichirou Meigo, Hiroshi Takada, Satoshi CHIBA. "Measurement of Gamma-Ray Production Double-Differential Cross Sections for 1.5 GeVπ+ Meson Incidence on Iron", Journal of Nuclear Science and Technology, Vol. 37, 3, 211-214, Mar 2000.

168) Tomoyuki Maruyama, Satoshi Chiba. "Equation of state of neutron-star matter and the isovector nucleon optical model potential", Journal of Physics G: Nuclear and Particle Physics, Vol. 25, 12, 2361–2369, Dec 1999.

169) Toshiki Maruyama, Koji Niita, Kazuhiro Oyamatsu, Tomoyuki Maruyama, Satoshi Chiba, Akira Iwamoto. "Nuclear matter structure studied with quantum molecular dynamics", Nuclear Physics A, Vol. 654, 1, pp. 908c-911c, Jul 1999.

170) Efrem Sh. Sukhovitskiĭ, Satoshi Chiba, Osamu Iwamoto. "Coupled-channels optical model calculations with account of nuclear volume conservation", Nuclear Physics A, Vol. 646, 1, pp. 19-28, Feb 1999.

171) Shin-ichiro MEIGO, Satoshi CHIBA, Kazuo SHIN. "Analysis of Neutron Spectra from Thick Targets Bombarded with 710-MeV Alpha Particles by Quantum Molecular Dynamics plus Statistical Decay Model", Journal of Nuclear Science and Technology, Vol. 36, 3, pp. 250-255, Mar 1999.

172) M. B. Chadwick, F. S. Dietrich, A. K. Kerman, A. J. Koning, S. M. Grimes, M. Kawai, W. G. Love, M. Herman, F. Petrovich, G. Walker, Y. Watanabe, H. Wolter, M. Avrigeanu, E. Běták, S. Chiba, J. P. Delaroche, E. Gadioli, S. Hilaire, M. S. Hussein, T. Kawano, R. Lindsay, A. Marcinkowski, B. Mariański, M. Mustafa, E. Ramström, G. Reffo, W. A. Richter, M. A. Ross, S. Yoshida. "Open problems in quantum-mechanical approaches to multistep direct nuclear reactions", Acta Physica Slovaca, Vol. 49, 3, pp. 365-379, Jun 1999.

173) Y. Nara, N. Otuka, A. Ohnishi, K. Niita, S. Chiba. "Relativistic nuclear collisions at 10A GeV energies from p+Be to Au+Au with the hadronic cascade model", Physical Review C, Vol. 61, 2, Dec 1999.

174) M.B. Chadwick, P.G. Young, S. Chiba, S.C. Frankle, G.M. Hale, G. Hughes, A.J. Koning, R.C. Little, R.E. MacFarlane, R.E. Prael, L.S. Waters. "Cross Section Evaluations to 150 MeV for Accelerator-Driven Systems and Implementation in MCNPX", Nuclear Science and Engineering, Vol. 131, 3, 293-328, Mar 1999.

175) Masahide Harada, Yukinobu Watanabe, Akihisa Yamamoto, Satoshi Yoshioka, Kazumichi Sato,

Toshiyuki Nakashima, Hidenobu Ijiri, Hiroki Yoshida, Yusuke Uozumi, Norihiko Koori, Shin-ichiro Meigo, Osamu Iwamoto, Tokio Fukahori, Satoshi Chiba. "The ^{12}C(p,p'3α) Breakup Reaction Induced by 14, 18 and 26 MeV Proton", Journal of Nuclear Science and Technology, Vol. 36, 4, pp. 313-325, Apr 1999.

176) S. Meigo, H. Takada, S. Chiba, T. Nakamoto, K. Ishibashi, N. Matsufuji, K. Maehata, N. Shigyo, Y. Watanabe, M. Numajiri. "Measurement of Neutron Spectra Produced from a Thick Lead Target Bombarded with 0.5- and 1.5-GeV Protons", Nuclear Instruments and Methods in Physics Research Section A: Accelerators, Spectrometers, Detectors and Associated Equipment, Vol. 431, 3, pp. 521-530, Jul 1999.

177) S. Chiba, K. Togasaki, M. Ibaraki, M. Baba, S. Matsuyama, N. Hirakawa, K. Shibata, O. Iwamoto, A. J. Koning, G. M. Hale, M. B. Chadwick. "Measurement and theoretical analysis of neutron elastic scattering and inelastic reactions leading to a three-body final state for ^{6}Li at 10 to 20 MeV", Physical Review C - Nuclear Physics, Vol. 58, No. 4, 2205-2216, Erratum Phys. Rev. C 59, 558 (1999), Oct 1998.

178) A B Smith, P T Guenther, J F Whalen, S Chiba. "Fast-neutron total and scattering cross sections of ^{58}Ni and nuclear models", Journal of physics G : nuclear and particle physics, Vol. 18, Number 4, 629, Jan 1999.

179) Young-Ouk Lee, Jonghwa Chang, Tokio Fukahori, Satoshi Chiba. "Evaluation of Neutron- and Proton-induced Nuclear Data on ^{27}Al up to 2 GeV", Journal of Nuclear Science and Technology, Vol. 36, 12, pp. 1125-1134, Dec 1999.

180) Mark B. Chadwick, Phillip G. Young, Satoshi Chiba. "Photonuclear angular distribution systematics in the quasideuteron regime", Journal of Nuclear Science and Technology, Vol. 32, 11, 1154-1158, Nov 1995.

181) Toshiki Maruyama, Koji Niita, Kazuhiro Oyamatsu, Tomoyuki Maruyama, Satoshi Chiba, Akira Iwamoto. "Quantum molecular dynamics approach to the nuclear matter below the saturation density", Physical Review C - Nuclear Physics, Vol. 57, 655, Feb 1998.

182) Kiminori Iga, Kenji Ishibashi, Nobuhiro Shigyo, Naruhiro Matsufuji, Tatsushi Nakamoto, Keisuke Maehata, Masaharu Numajiri, Shin-ichirou Meigo, Hiroshi Takada, Satoshi Chiba, Takashi Nakamura, Yukinobu Watanabe. "Measurement of Gamma-Ray Production Double-Differential Cross Sections for the Spallation Reaction Induced by 0.8, 1.5 and 3.0 GeV Protons", Journal of Nuclear Science and Technology, Vol. 35, No. 5, pp. 329-334, May 1998.

183) Efrem Sh.Sukhovitskiĭ, Satoshi Chiba, Osamu Iwamoto, Yurij V.Porodzinskiĭ. "Nucleon interaction with ^{12}C studied by the soft-rotator model and a limit on the charge-symmetry breaking in the nuclear mean field", Nuclear Physics A, Vol. 640, 2, 147-162, Sep 1998.

184) H. Vonach, A. Pavlik, A. Wallner, M. Drosg, R.C. Haight, D.M. Drake, S. Chiba. "Spallation reactions in ^{27}Al and ^{56}Fe induced by 800 MeV protons", Physical Review C - Nuclear Physics, Vol. 55, No. 5, 2458-2467, May 1997.

185) Satoshi Chiba, Osamu Iwamoto, Yoshimaro Yamanouti, Masayoshi Sugimoto, Motoharu Mizumoto, Kazuo Hasegawa, Efrem Sh. Sukhovitskiĭ, Yurij V.Porodzinskiĭ, Yukinobu Watanabe. "Consistent description of collective level structure and neutron interaction data for 12C in the framework of the soft-rotator model", Nuclear Physics A, Vol. 624, 3, 305-327, Oct 1997.

186) Masahide Harada, Yukinobu Watanabe, Satoshi Chiba, Tokio Fukahori. "Evaluation of Neutron Cross Sections of Carbon-12 for Energies up to 80MeV", Journal of Nuclear Science and Technology,

Vol. 34, 2, pp. 116-127, Feb 1997.

187) Keiichi SHIBATA, Tokio FUKAHORI, Nobuhiro YAMAMURO, Keiichi SHIBATA, Tokio FUKAHORI, Satoshi CHIBA, Nobuhiro YAMAMURO. "Evaluation of Neutron Nuclear Data for Mercury", Journal of Nuclear Science and Technology, Vol. 34, No. 12, Dec 1997.

188) Satoshi Chiba, Tokio Fukahori, Keiichi Shibata, Baosheng Yu, Kazuaki Kosako. "Status and evaluation methods of JENDL Fusion File and JENDL PKA/KERMA File", Fusion Engineering and Design, Vol. 37, 1, pp. 175-183, Aug 1997.

189) Tatsushi Nakamoto, Kenji Ishibashi, Naruhiro Matsufuji, Nobuhiro Shigyo, Keisuke Maehata, Hidehiko Arima, Shin-ichirou Meigo, Hiroshi Takada, Satoshi Chiba, Masaharu Numajiri. "Experimental Neutron-Production Double-Differential Cross Section for the Nuclear Reaction by 1.5-GeV π+ Mesons Incident on Iron", Journal of Nuclear Science and Technology, Vol. 34, 8, 860-862, Aug 1997.

190) Osamu Iwamoto, Satoshi Chiba, Ryousaku Kuwata. "Soft-rotator Model Analysis of Collective Band Structures of Even-even Actinide Nuclei", Journal of Nuclear Science and Technology, Vol. 34, No. 5, May 1997.

191) Kenji Ishibashi, Hiroshi Takada, Tatsushi Nakamoto, Nobuhiro Shigyo, Keisuke Maehata, Naruhiro Matsufuji, Shin-ichiro Meigo, Satoshi Chiba, Masaharu Numajiri, Yukinobu Watanabe, Takashi Nakamura. "Measurement of Neutron-Production Double-Differential Cross Sections for Nuclear Spallation Reaction Induced by 0.8, 1.5 and 3.0 GeV Protons", Journal of Nuclear Science and Technology, Vol. 34, No. 6, pp. 529-537, Jun 1997.

192) Satoshi Chiba, Osamu Iwamoto, Tokio Fukahori, Koji Niita, Toshiki Maruyama, Tomoyuki Maruyama, Akira Iwamoto. "Analysis of proton-induced fragment production cross sections by the quantum molecular dynamics plus statistical decay model", physical review c, Vol. 54, 285, Jul 1996.

193) Satoshi Chiba, Masahide Harada. "Applicability of Optical Model Potentials for Intermediate-Energy Nuclear Data Evaluations in the 1p-shell Mass Region", Journal of Nuclear Science and Technology, Vol. 33, 4, 346-353, Apr 1996.

194) Satoshi Chiba, Mark B. Chadwick, Koji Niita, Toshiki Maruyama, Tomoyuki Maruyama, Akira Iwamoto. "Nucleon-induced preequilibrium reactions in terms of the quantum molecular dynamics", Physical Review C - Nuclear Physics, Vol. 53, 1824, Apr 1996.

195) Satoshi Chiba, Sin-ichi Morioka, Tokio Fukahori. "Evaluation of Neutron Cross Sections of Hydrogen from 20 MeV to 1 GeV", Journal of Nuclear Science and Technology, Vol. 33, 8, pp. 654-662, Aug 1996.

196) A.B. Smith, S. Chiba. "Neutron scattering from elemental uranium and thorium", Annals of Nuclear Energy, Vol. 23, 6, pp. 459-467, Apr 1996.

197) Satoshi Chiba, Koji Niita, Osamu Iwamoto. "Time scale of the preequilibrium process in intermediate-energy nucleon-induced reactions", Physical Review C - Nuclear Physics, Vol. 54, 3302, Dec 1996.

198) Tomoyuki Maruyama, Koji Niita, Toshiki Maruyama, Satoshi Chiba, Yasuaki Nakahara, Akira Iwamoto. "Relativistic Effects in Transverse Flow in the Molecular Dynamics Framework", Progress of Theoretical Physics, Vol. 96, 1, pp. 263–268, Jul 1996.

199) M. Baba, S. Matsuyama, M. Ishikawa, S. Chiba, T. Sakase, N. Hirakawa. "Correction of double-differential neutron emission data for sample-dependent effects", Nuclear Instruments & Methods in Physics Research. Section A, Vol. 366, 2-3, pp. 354-365, Dec 1995.

200) Tsuneo Nakagawa, Keiichi Shibata, Satoshi Chiba, Tokio Fukahori, Yutaka Nakajima, Yasuyuki Kikuchi, Toshihiko Kawano, Yukinori Kanda, Takaaki Ohsawa, Hiroyuki Matsunobu, Masayoshi Kawai, Atsushi Zukeran, Takashi Watanabe, Sin-iti Igarasi, Kazuaki Kosako, Tetsuo Asami. "Japanese Evaluated Nuclear Data Library Version 3 Revision-2: JENDL-3.2", Journal of Nuclear Science and Technology, Vol. 32, No. 12, 1259-1271, Dec 1995.

201) Watanabe Y, Aoto A, Kashimoto H, Chiba S, Fukahori T, Hasegawa K, Mizumoto M, Meigo S, Sugimoto M, Yamanouti Y, Koori N, Chadwick MB, Hodgson PE. "Feshbach-Kerman-Koonin model analysis of preequilibrium (p,p') and (p,n) reactions at 12 to 26 MeV", Physical Review C - Nuclear Physics, Vol. 51, 4, 1891-1907, Apr 1995.

202) M. B. Chadwick, S. Chiba, K. Niita, T. Maruyama, A. Iwamoto. "Quantum molecular dynamics and multistep-direct analyses of multiple preequilibrium emission", Physical Review C - Nuclear Physics, Vol. 52, 2800, Nov 1995.

203) Tatsushi NAKAMOTO, Kenji ISHIBASHI, Naruhiro MATSUFUJI, Nobuhiro SHIGYO, Keisuke MAEHATA, Shin-ichirou MEIGO, Hiroshi TAKADA, Satoshi CHIBA, Masaharu NUMAJIRI, Takashi NAKAMURA, Yukinobu WATANABE. "Spallation Neutron Measurement by the Time-of-Flight Method with a Short Flight Path", Journal of Nuclear Science and Technology, Vol. 32, No. 9, pp. 827-833, Sep 1995.

204) Koji Niita, Satoshi Chiba, Toshiki Maruyama, Tomoyuki Maruyama, Hiroshi Takada, Tokio Fukahori, Yasuaki Nakahara, Akira Iwamoto. "Analysis of the (N,xN') reactions by quantum molecular dynamics plus statistical decay model", Physical Review C - Nuclear Physics, Vol. 52, 2620, Nov 1995.

205) Mamoru Baba, Nobuo Ito, Isamu Matsuyama, Shigeo Matsuyama, Naohiro Hirakawa, Satoshi Chiba, Tokio Fukahori, Motoharu Mizumoto, Kazuo Hasegawa, Shin-ichiro Meigo. "Differential α-Production Cross Sections of Iron and Nickel for 4.3 to 14.1 MeV Neutrons", Journal of Nuclear Science and Technology, Vol. 31, pp. 745-747, Jul 1994.

206) Satoshi CHIBA, Donald L. SMITH. "Impacts of Data Transformations on Least-Squares Solutions and Their Significance in Data Analysis and Evaluation", Journal of Nuclear Science and Technology, Vol. 31, 8, 770-781, Aug 1993.

207) Baosheng Yu, Satoshi Chiba, Tokio Fukahori. "Examination of Various Kinds of Systematics of Double-Differential Particle Emission Cross Sections for Medium-Heavy Nuclei Important to Fusion Neutronics", Journal of Nuclear Science and Technology, Vol. 29, 7, pp. 677-689, Jul 1992.

208) Chiba S, Guenther PT, Smith AB, Sugimoto M, Lawson RD. "Fast-neutron interaction with elemental zirconium, and the dispersive optical model", Physical Review C - Nuclear Physics, Vol. 45, Mar 1992.

209) S. Chiba, P. T. Guenther, R. D. Lawson, A. B. Smith. "Neutron scattering from elemental indium: Optical model and bound-state potential", Physical Review C - Nuclear Physics, Vol. 42, 2487-2496, Dec 1990.

210) S. Chiba, P. T. Guenther, A. B. Smith. "Some remarks on the neutron elastic—And inelastic—Scattering cross sections of palladium", Annals of Nuclear Energy, Vol. 16, No. 12, pp. 637-645, Aug 1989.

211) Satoshi Chiba, Motoharu Mizumoto, Kazuo Hasegawa, Yoshimaro Yamanouti, Masayoshi Sugimoto, Yukinobu Watanabe, Manfred Drosg. "The $^{1}H(^{11}B,n)^{11}C$ reaction as a practical low background monoenergetic neutron source in the 10 MeV region", Nuclear Instruments and Methods in Physics

Research Section A: Accelerators, Spectrometers, Detectors and Associated Equipment, Vol. 281, 3, pp. 581-588, Sep 1989.

212) Satoshi Chiba, Yoshimaro Yamanouti, Masayoshi Sugimoto, Motoharu Mizumoto, Yutaka Furuta, Mikio Hyakutake, Shin Iwasaki. "Fast neutron scattering cross sections of ^{118}Sn at 14.9 and 18.0 MeV", Journal of Nuclear Science and Technology, Vol. 25, 6, pp. 511-519, Jun 1988.

213) Satoshi Chiba, Yoshimaro Yamanouti, Motoharu Mizumoto, Mikio Hyakutake, Shin Iwasaki. "Measurements of Fast Neutron Scattering Cross Sections of Li-7 at 11.0 and 13.0 MeV", Journal of Nuclear Science and Technology, Vol. 25, No. 2, pp. 210-214, Feb 1988.

214) Satoshi Chiba, Mamoru Baba, Hiroshi Nakashima, Masahiro Ono, Naohiro Yabuta, Shigeru Yukinori, Naohiro Hirakawa. "Double-Differential Neutron Emission Cross Sections of ^{6}Li and ^{7}Li at Incident Neutron Energies of 4.2, 5.4, 6.0 and 14.2 MeV", Journal of Nuclear Science and Technology, Vol. 22, No. 10, pp. 771-787, Oct 1985.

4. Conceptual Design Study of New Research Reactor at the Monju Site

Kazufumi TSUJIMOTO

Japan Atomic Energy Agency
2-4, Shirakata, Tokai-mura, Naka-gun, Ibaraki-ken 319-1195, Japan
Email: tsujimoto.kazufumi@jaea.go.jp

In 2016, the Japanese government decided to decommission “MONJU” and to establish a new research reactor by utilizing “MONJU” site. In 2020, the Ministry of Education, Culture, Sports, Science and Technology (MEXT) concluded that a medium-power reactor (thermal power of less than 10 MW) mainly for neutron beam applications would be most appropriate for a new research reactor using the “MONJU” site. The consortium consisted with Japan Atomic Energy Agency, Kyoto University, and the University of Fukui was selected as the core organization for the conceptual design of the new research reactor. The present paper describes the status of conceptual design study of new research reactor at the Monju site that has been conducted mainly by JAEA.

1. Introduction

In December 2016, when the government policy to decommission “MONJU” was decided at the Nuclear Energy Ministerial Meeting, it was decided to establish a new research reactor by utilizing the "MONJU" site in the future. In response, Ministry of Education, Culture, Sports, Science and Technology (MEXT) established a committee of external experts consisting of various stakeholders from FY 2017 to FY 2019 to conduct a survey on a new research reactor, and selected several candidate reactor types in May 2020. Specifically, (1) Medium-power reactor (thermal power of less than 10 MW, mainly for research using neutron beams and highly versatile), (2) Low-power reactor (thermal power of about 500 kW, mainly used for nuclear engineering experiments), (3) Zero-Power critical experiment facility (thermal power of about a few kW, mainly used for basic research and education) were selected as reactor types that could be constructed by incorporating the latest technology based on existing reactors. After hearing to the opinions of Fukui Prefecture and Tsuruga City, and through discussions at the Working Group on Nuclear Research and Development, Infrastructure, and Human Resources of MEXT, in September 2020, the most appropriate reactor type was selected as a medium power reactor (<10 MW) mainly for neutron beam applications, from two perspectives: to realize functions suitable as a core center for nuclear research and development and human resources development in western Japan and to contribute to local development. Moreover, as a way to proceed with the study, it was recommended to establish an organization consisting with research institutes and universities with knowledge, experience,

and ability in the three aspects of "steady design, construction, and operation of the research reactor," "operation of the research reactor so that a wide range of related researchers can use it," and "establishment of cooperation with related local organizations".

In order to effectively implement the study on the conceptual design and operation of the new research reactor from the above recommendation, MEXT issued a public offering ("Study on the conceptual design and operation of the new research reactor at the Monju site") and selected the consortium consisted with Japan Atomic Energy Agency (JAEA), Kyoto University, and the University of Fukui as the core organizations in November 2020. The roles of each organization are

JAEA : Design, construction, and operation of new research reactor,
Kyoto University : Operation of a wide range of utilization, and
University of Fukui : Building partnerships with local institutions.

The present paper describes the status of conceptual design study of new research reactor at the Monju site that has been conducted mainly by JAEA.

2. Conceptual Design Study of Reactor Core

2.1. Design Targets

In the conceptual design study of the new research reactor, it is possible to refer to the knowledge of existing research reactors such as JRR-3 of JAEA and KUR of Kyoto University, which have knowledge and experience in construction and operation management. The goal of this project is to maximize the performance as a medium-power reactor mainly for neutron beam applications. The basic policies of this project are (1) increasing safety performance, (2) improving user convenience, (3) ensuring operation stability, (4) exploring economical design, and (5) securing future potential. Figure 1 shows the relationship between the basic policy and typical items that should be specifically considered when conducting a conceptual design study.

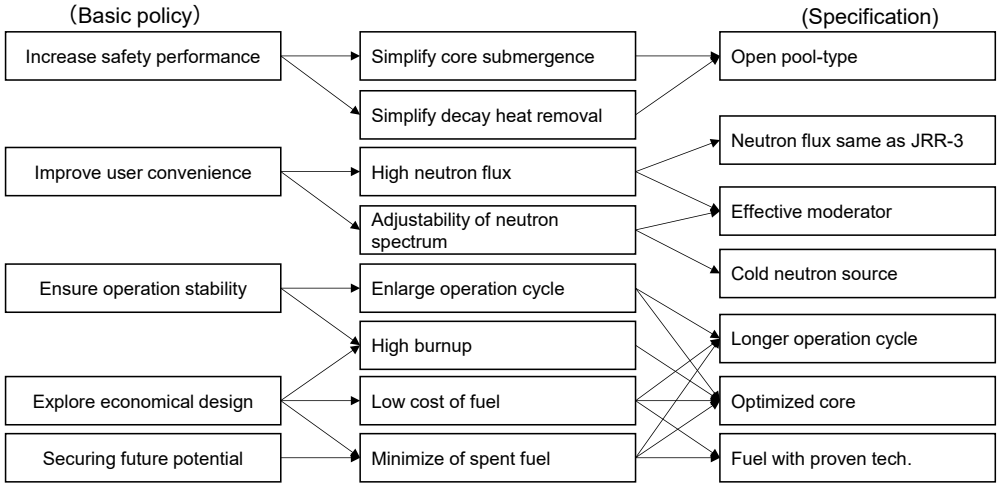

Fig.1 Relationship between the basic policy of the core concept study and specific study items

In order to concretize the core configuration of the new research reactor as a medium power reactor, the maximum thermal neutron flux in the reflector and the available operation days were set as tentative design targets to be achieved as follows.

・Maximum thermal neutron flux：> 10^{14} n/cm^2/s（JRR-3：1.0～2.0×10^{14} n/cm^2/s）

・Available operation days：> 400 days（JRR-3：370 days）

It is desirable to achieve as high thermal neutron flux as possible in the new research reactor whose main purpose is to utilize neutron beams. In addition, since the number of days of sustainable operation is directly related to the availability of the new research reactor, it is desirable to be able to maintain operation for as long as possible without fuel replacement. These design targets were set with reference to the performance of the JRR-3 (20 MW thermal power) currently in operation at JAEA. For the maximum thermal neutron flux, the target was set to equivalent to that of the JRR-3 although the thermal power of the new research reactor is half that of JRR-3. The operation days set here is the number of days until the effective multiplication factor will fall below 1 in the burnup analysis, which is different from the actual available operation days.

2.2. Core Configuration

In the consideration of the core design, core configurations with various fuel element numbers and arrangements were assumed, and their respective neutron fluxes and burnup characteristics were analyzed. The calculations were performed under the assumption using JRR-3 fuel element. Table 1 shows the main parameters of the JRR-3 fuel element which is a typical MTR-type fuel element. Figure 2 shows the schematic drawing of the JRR-3 fuel element. The JRR-3 core consists of standard fuel elements and follower-fueled control rods, but in this study, it was assumed that the core consists entirely of standard fuel elements.

Table 1 Main parameters of JRR-3 fuel element

Size		64×64×880 mm
Nuclear Fuel		U_3Si_2
^{235}U enrichment		20 wt%
^{235}U content		300 g
Uranium density		4.8 g/cm^3
Fuel meat	Thickness	0.51 mm
	Width	49 mm
	Length	750 mm
Cladding		Al alloy
Cladding thickness		0.38 mm
Fuel plate	Thickness	1.27 mm
	Width	60 mm
	Length	770 mm
Number of coolant channel		16
Coolant channel thickness		2.40 mm (×15)

For the core configuration, we analyzed the neutron flux and burnup characteristics for each of the assumed fuel numbers and fuel configuration pairs shown in Figure 3. In setting the core geometry, not only the number of fuels is used as a parameter, but also the core outline is kept the same, as in x16, x17, and Ce20, and the number of fuels constituting the core is adjusted so that only the effect of the number of fuels can be considered. It is assumed that the coolant region of the fuel elements is filled with light

water, and the outside of the core is surrounded by heavy water of sufficient thickness. The continuous energy Monte Carlo codes MVP[1] and MVP-BURN were used for the calculations, and JENDL-4.0[2] was used for the nuclear data.

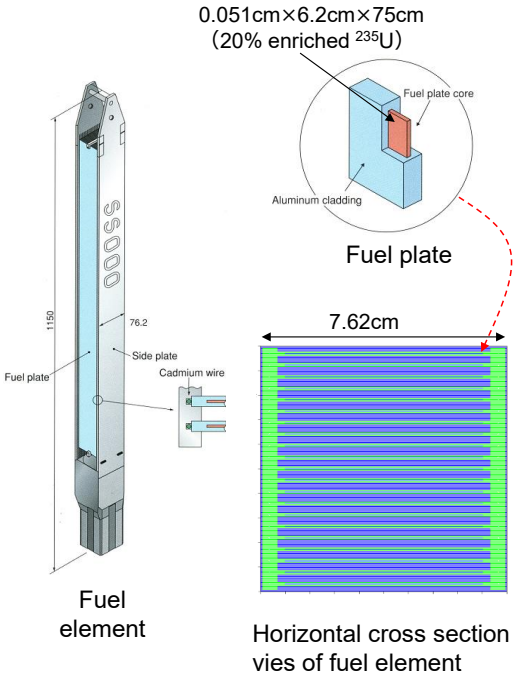

Fig.2 Standard JRR-3 fuel element

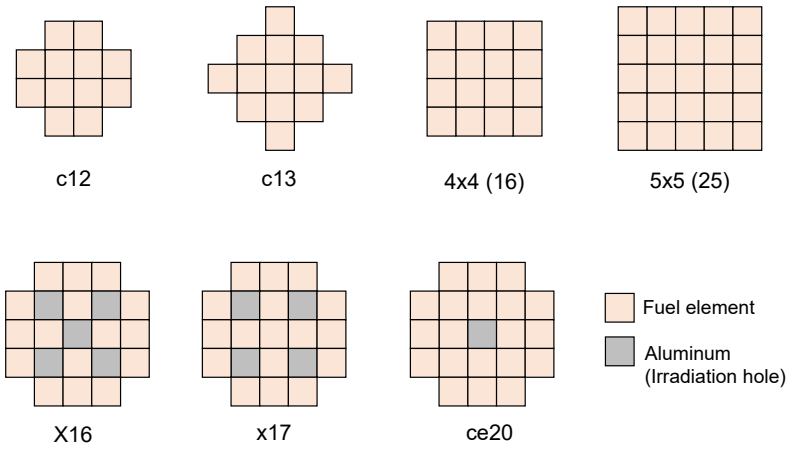

Fig.3 Fuel element arrangement analyzed in the core concept study

The thermal neutron flux in the heavy water tank outside the core and the change of effective multiplication factor due to burnup for each core configuration are shown in Figures 4 and 5, respectively. Although the maximum thermal neutron flux became smaller as the number of fuel elements increased and the core became larger, the maximum thermal neutron flux for all core geometries was found to be about 10 cm from the core edge, which is higher than the target of 10^{14} n/cm^2/s. On the other hand, as for the burnup characteristics, it was also found that as the number of fuel elements increases and the core becomes larger, the period when the effective multiplication factor falls below one increases, the number

of days of operation becomes longer, the burnup rate of ^{235}U increases, and the fuel can be used more efficiently. Among the configured cores, 5x5 cores (25 fuel elements, 588 days of sustainable operation, 61% burnup) and ce20 cores (20 fuel elements, 416 days of sustainable operation, 55% burnup) met the target of 400 days of sustainable operation.

Based on the above results, it was decided that the Ce20 core is the reference configuration which has potential address a wide variety of needs because irradiation utilization will be available at the center and the four corners of the core, and it is relatively more flexible than the 5×5 core.

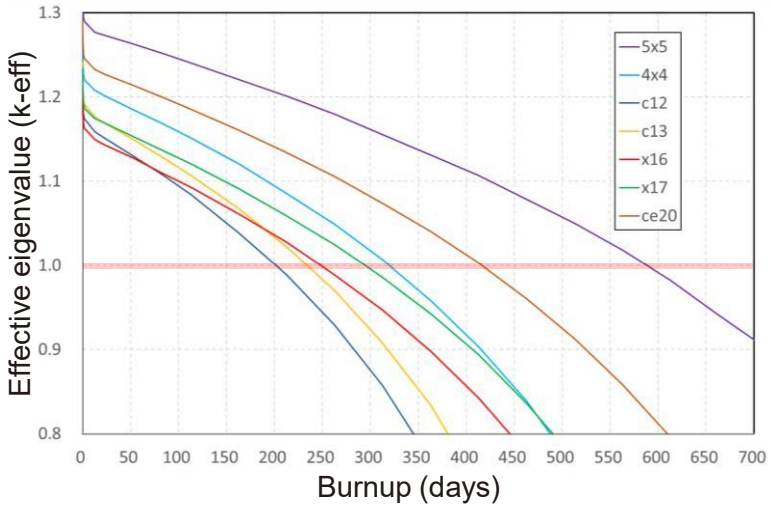

Fig.4 Comparison of calculated thermal neutron flux in heavy water tanks

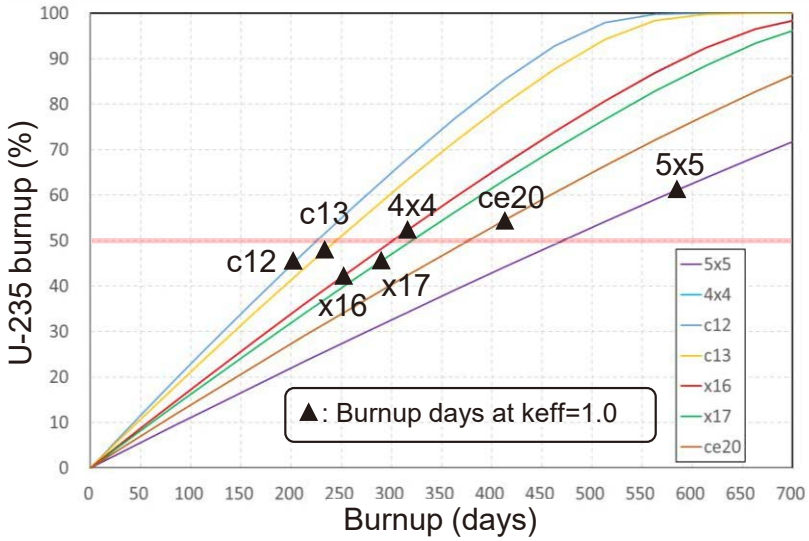

Fig.5 Change of effective multiplication factor (k_{eff}) with burnup

3. Concluding remarks

In the conceptual design study of the reactor core, the maximum thermal neutron flux in the heavy water reflector and the number of days of operation duration were set as the design goals to be achieved, and a core configuration capable of achieving each goal was obtained. Based on these results, the fuel elements, control elements, and reflector will be concretized to determine the basic specifications to

proceed with the detailed design.

On December 23, 2022, JAEA was selected by MEXT as the main entity to implement the new experimental research reactor project at the "MONJU" site from the detailed design stage onward. We will continue to work with Kyoto University and the University of Fukui to steadily proceed with the project, while gathering a wide range of opinions from related organizations and gaining the understanding of the local community, following the schedule as shown in the Fig.6

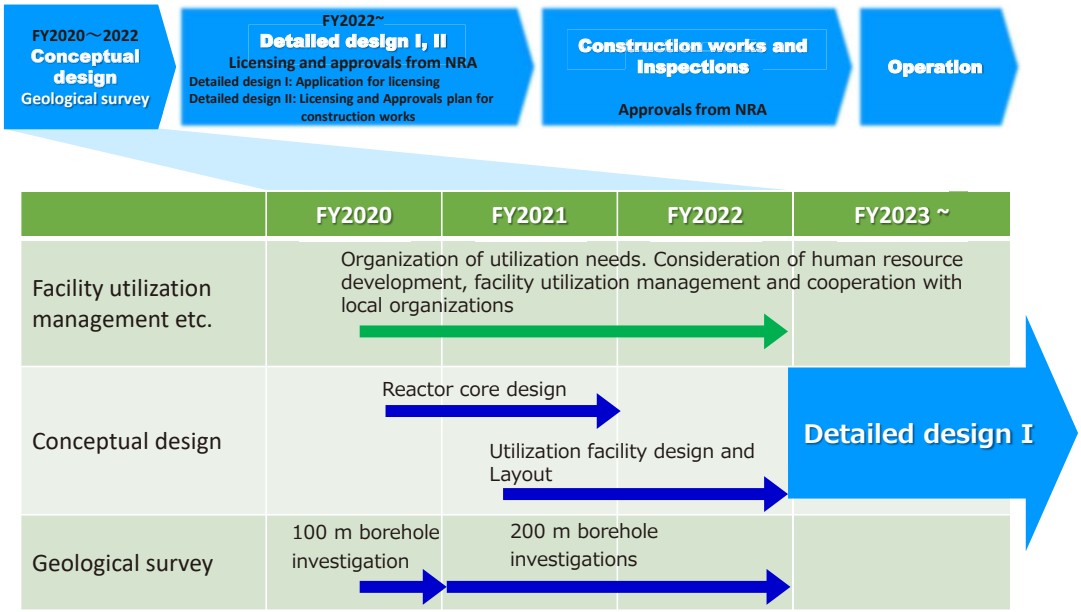

Fig.6 Tentative Schedule for construction and operation of the new research reactor at Monju site

References

1) Nagaya, Y, Okumura, K. Sakurai, T. et al., MVP/GMVP version 3; General purpose Monte Carlo codes for neutron and photon transport calculations based on continuous energy and multigroup methods, Japan Atomic Energy Agency, JAEA-Data/Code 2016-018 (2017).

2) Shibata K., Iwamoto O., Nakagawa T. et al., JENDL-4.0: A New Library for Nuclear Science and Engineering," J. Nucl. Sci. Technol.. 48(1), 1-30 (2011).

5. Measurement of 100 MeV-range nuclear reaction data using the fixed field alternating gradient accelerator at Kyoto University

Hiroki IWAMOTO[1]

[1]Japan Atomic Energy Agency
[†]E-mail: iwamoto.hiroki@jaea.go.jp

Abstract

For the research and development of accelerator-driven systems (ADSs) and fundamental ADS reactor physics research using the Kyoto University Critical Assembly combined with the fixed-field alternating gradient (FFAG) accelerator, we are conducting experiments on 100 MeV-range nuclear reaction data using the FFAG accelerator at Kyoto University. This paper presents an overview of the experiments.

1 Introduction

Spent fuel from nuclear power plants is radioactive and toxic for a long period of time, even tens of thousands of years. From the viewpoint of effective utilization of energy resources, Japan's basic policy is to reprocess the spent fuel to recover plutonium (Pu) and uranium (U) and reuse them as fuel. The high-level radioactive liquid waste (HLW) produced in the reprocessing process will be vitrified and disposed into a stable bedrock formation several hundred meters underground. It is of social significance to reduce the toxicity of HLW as much as reasonably achievable and to reduce the burden of geological disposal. As one of the solutions to this problem, Accelerator-Driven System (ADS) has attracted attention and is being researched and developed around the world.

Figure 1 shows the concept of the ADS proposed by the Japan Atomic Energy Agency (JAEA). This system is a combined reactor system that combines a 1.5 GeV high-intensity proton accelerator and a subcritical core to efficiently perform transmutation while keeping the core subcritical. The core is loaded with nuclear fuel containing minor actinides (MA) such as neptunium (Np) and americium (Am), which have particularly high radio-toxicity among HLW, and is surrounded by a liquid lead-bismuth eutectic (LBE) alloy. The LBE is used as a coolant to extract the heat generated from the nuclear fuel during operation, and also serves as a target or spallation neutron source to supply spallation neutrons generated by nuclear reactions (spallation reactions) using high-energy protons to the core.

Figure 2 shows the time behavior of the potential radiotoxicity of radioactive waste [1]. If Pu and U are recovered from the waste and MA with high potential radiotoxicity are separated and burned in ADS, the toxicity can be reduced to several hundred years, which is expected to make a significant contribution to solving the problem of negative legacy.

In the research and development of ADS using spallation neutrons, it is important to improve nuclear reaction models that describe spallation reactions. In particular, the yield of spallation neutrons, their energy distribution (spectrum), and angular distribution obtained by the nuclear

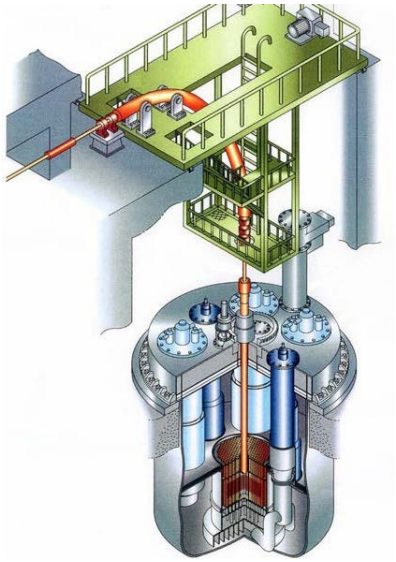

Figure 1: Concept of ADS proposed by JAEA.

reaction model calculation are essential information for evaluating the nuclear performance of the ADS, such as transmutation efficiency and proton beam current. In addition, the beam window, which forms the boundary between the proton injection region and the core region, is irradiated by high-energy protons and produces gases such as helium and hydrogen inside the material. Accurate prediction of gas production and irradiation damage in the beam window, which is exposed to severe thermal conditions, is important to ensure its performance and integrity in the design. In addition, it is necessary to accurately evaluate the induced radioactivity of the spallation target and constituent materials and the shielding performance of neutron shields, and nuclear reaction models that describe these fundamental processes play an extremely important role.

At Kyoto University, a series of experimental studies simulating ADS has been conducted using the Kyoto University Critical Assembly (KUCA) coupled with the FFAG (Fixed Field Alternating Gradient) accelerator; the nuclear reaction model is being verified in this framework [2]. On the other hand, in the actual ADS, which assumes deeper subcriticality than the subcritical regime that can be tested in KUCA, the contribution of spallation reactions to the neutron energy spectrum increases, so that more accurate nuclear reaction model analysis is required for nuclear performance evaluation and demonstration experiments.

Due to the importance of nuclear reaction models in ADS nuclear design, measurements of the double-differential cross section (DDX) of neutrons and charged particles and the neutron yield of neutrons emitted from a thick Pb target (i.e., thick target neutron yield, TTNY) have been measured intensively by research institutes around the world, and the nuclear reaction models have been refined and benchmarked by the International Atomic Energy Agency (IAEA) [3]. However, despite these efforts, the reaction mechanisms of neutron-production DDX and TTNY and high-energy fission in the tens to 100 MeV region have not yet been predicted with satisfactory accuracy even by the latest nuclear reaction models. In this background, we are planning to measure neutron-production DDX and TTNY for ADS components (Fe, Pb, and Bi), fission fragment distribution and fission neutron number in high-energy fission of Pb and Bi using the FFAG accelerator, which can accelerate protons in the 100 MeV region. The experimental data obtained from these measurements will be compared with the nuclear reaction model (theoretical model) in order to improve the statistical accuracy of the nuclear reaction

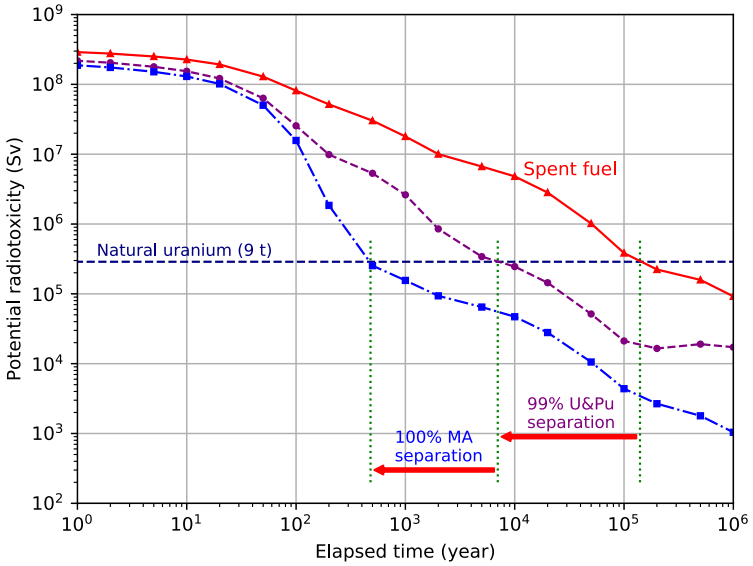

Figure 2: Reduction of potential radiotoxicity of spent fuel by ADS (partitioning and transmutation) technology, plotted based on Ref. [1].

model.

2 Experiment

The experiments were conducted in the experimental hall where the FFAG accelerator is installed in the Innovation Research Laboratory of the Institute for Integrated Radiation and Nuclear Science, Kyoto University. A series of experiments on TTNY and DDX have been completed, and experiments on high-energy fission of Pb and Bi are planned. Figure 3 shows the experimental setup for the TTNY and DDX measurements. In each of these experiments, a disc-shaped target is placed in a vacuum chamber on a different beamline, and a neutron detector is positioned at a specific angle of 5–120 degrees from the proton beam injection axis, about 2–7 m away from the target (Figure 4). After the target and neutron detector were set up, the target was irradiated with a 107-MeV proton beam accelerated by the FFAG accelerator for 1–4 hours to detect neutrons and gamma rays emitted from the target during irradiation.

In the TTNY measurements, Fe (beam window component), Pb, and Bi (spallation target component), which are the main components of ADS, were used as targets, and their thickness was 30 mm so that they were longer than the range for 107-MeV protons (i.e. 16.1 mm, 15.9 mm, and 18.5 mm for Fe, Pb, and Bi, respectively). The target thickness for DDX measurements should be thin from a physical point of view, but for better statistics, 2-mm-thick Pb and 5-mm-thick Bi were used to improve the accuracy. The diameter of the target was 48 mm to ensure that the proton beam would enter the target with sufficient margin based on past beam profiles.

The beam repetition rate was set to the standard FFAG accelerator specification of 30 Hz. The time width of the pulsed beam before the experiment was about 100 ns, but since a time width of less than 10 ns is required to obtain high energy resolution for TTNY and DDX measurements, the pulsed beam was shortened to $\sim$8 ns (1σ) by the bunch rotation method and the kicker method [4]. The beam profile was checked by placing a fluorescent plate near the target and using a CCD camera to observe the scintillation from the proton beam irradiation.

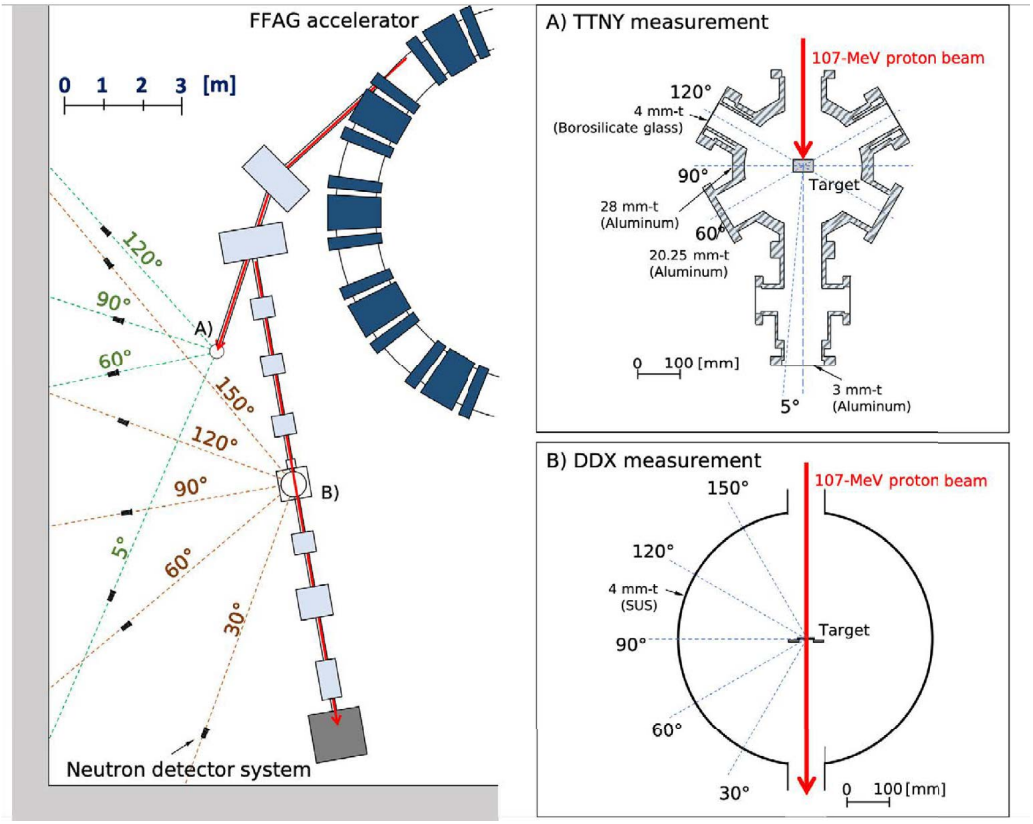

Figure 3: Experimental setup of the TTNY and DDX measurements.

This check was performed before each TTNY and DDX measurement at each measurement angle.

In order to measure neutron energy spectra with high detection efficiency over a wide energy range from several hundred keV to 107 MeV, we used a compact EJ-301 with a diameter of 8 mm and a PMT (HAMAMATSU H3164-12) that can handle a wide luminous flux band. In the TTNY measurement, a 16 mm thick copper block was placed in front of the neutron detector to prevent charged particles such as scattered protons from entering the detector. In the DDX measurement, on the other hand, a VETO detector consisting of a light-guided plastic scintillator and PMT with a thickness of 2 mm and a length and width of 100 mm was placed in front of the neutron detector to eliminate charged particle events detected by the neutron detector.

Data acquisition (DAQ) during the measurement was performed using a multichannel digitizer (Struck Innovative System, model No. SIS3316) with a field-programmable gate array (FPGA). The pulse-shape discrimination (PSD) method was used to discriminate between neutron and gamma-ray events detected by the neutron detectors, where two different gates (fast and slow gates) were set and the integral amount of scintillation at each gate width was recorded as a digital signal. The time-of-flight (TOF) method was used to derive the TOF spectrum of neutrons based on the time information of neutron detection events obtained by removing gamma-ray detection events by the PSD method. The contribution of room-scattering neutrons was removed by the results of measurements using a shadow bar. Furthermore, the neutron TOF spectra were converted to energy spectra based on relativistic kinematics by correcting for detector detection efficiency, target-to-detector neutron attenuation, and other factors based on analysis using the radiation behavior analysis code PHITS [5].

The energy spectra of TTNY and DDX for Fe, Pb, and Bi targets were obtained from

this experiment. As an example, Figure 4 shows a comparison between the experimental data of 107-MeV proton-induced TTNY for Pb and the nuclear reaction model analysis. The results of the analysis using the nuclear reaction models incorporated in PHITS (INCL4.6/GEM, Bertini/GEM, JQMD/GEM, and JQMD/SMM/GEM [6, 7, 8, 9, 10]) and the evaluated nuclear data library JENDL-4.0/HE [11] are described here. The energy distribution at high energies is strongly forward, while at low energies, the distribution is isotropic and Maxwellian. This is because the mechanism of neutron emission from nuclei is very different between the two processes in nuclear reactions, which are described by the intranuclear cascade model and the evaporation model included in nuclear reaction models, respectively. The TTNY and DDX data obtained in this experiment cover a wide energy range from 700 keV to 107 MeV. Comparison with the nuclear reaction models revealed that both models show a characteristic discrepancy trend with respect to the TTNY measurements for Fe, Pb, and Bi (see Ref. [12] for details of the TTNY measurements). The same trend was observed for DDX (see Ref. [13] for preliminary results).

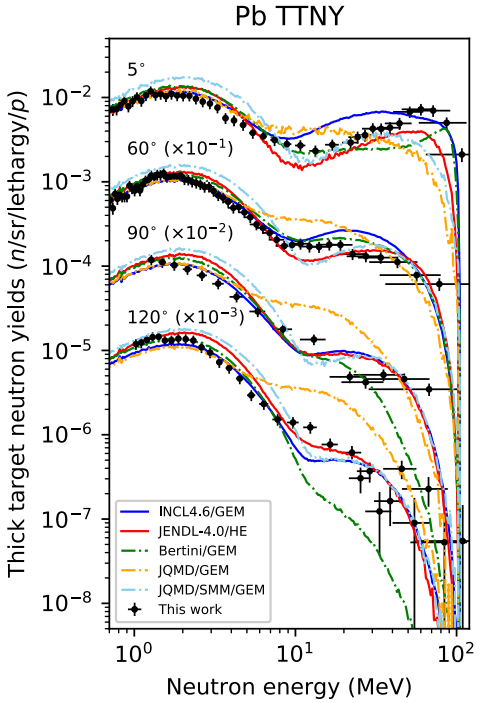

Figure 4: Comparison of energy spectra of 107-MeV proton induced TTNY for Pb. (Ref. [12]).

3 Summary and future work

Experiments on neutron production DDX and TTNY of ADS components and high energy fission have been conducted and planned using the FFAG accelerator at Kyoto University. So far, measurements of TTNY and DDX have been completed, and we have succeeded in obtaining data that will contribute to the advancement of nuclear reaction models. In the future, we plan to conduct experiments on high-energy fission of Pb and Bi.

References

[1] K. Nishihara, "Data for estimating potential radioactivity of spent nuclear fuel", JAEA-Data/Code 2010-012 (2010).

[2] C. Pyeon *et al*., "Reaction rate analyses of accelerator-driven system experiments with 100 MeV protons at Kyoto University Critical Assembly", *J. Nucl. Sci. and Technol.*, vol. 55, no. 2, 2018, pp.190–198, 2009. doi:10.1080/00223131.2017.1389314

[3] D. Filges *et al.*, Joint ICTP-IAEA Advanced Workshop on Model Codes for Spalla-tion Reactions, Trieste, Italy 4–8 Feb. 2008. http://www-nds.iaea.org/reports-new/indc-reports/indc-nds/indc-nds-0530.pdf

[4] T. Uesugi *et al.*, "Short pulsed beam extraction in KURNS FFAG", Proc. the 18th Annual Meeting of Particle Accelerator Society of Japan, QST-Takasaki Online, Japan, Aug. 9–12, 2021; http://www.pasj.jp/web_publish/pasj2021/proceedings/index.html

[5] T. Sato *et al.*, "Features of particle and heavy ion transport code system (PHITS) version 3.02. *J. Nucl. Sci. and Technol.*, vol. 55, no. 6, 2018, pp.684–689, 2018. doi:10.1080/00223131.2017.1419890

[6] A. Boudard *et al.*, "New potentialities of the Liège intranuclear cascade model for reactions induced by nucleonns and light charged particles". *Phys. Rev. C*, vol. 87, p.014606, 2013. doi:10.1103/PhysRevC.87.014606

[7] S. Furihata, "Statistical analysis of light fragment production from medium energy proton-induced reactions", *Nucl. Instrum. Methods Phys. Res. B.*, vol. 171, pp.251–258, 2000. doi:10.1016/S0168-583X(00)00332-3

[8] H. Bertini, "Intranuclear-cascade calculation of the secondary nucleon spectra from nucleon-nucleus interactions in the energy range 340 to 2900 MeV and comparisons with experiment", *Phys. Rev.*, vol. 188, p.1711, 1969. doi:10.1103/PhysRev.188.1711

[9] K. Niita *et al.*, "Analysis of the (N, xN') reactions by quantum molecular dynamics plus sta-tistical decay model", *Phys. Rev. C*, vol. 52, pp.2620–2635, 1995. doi:10.1103/PhysRevC. 52.2620

[10] T. Ogawa *et al.*, "Analysis of multi-fragmentation reactions induced by relativistic heavy ions using the statistical multi-fragmentation model", *Nucl. Instrum. Methods Phys. Res. A.*, vol. 723, pp.36–46, 2013. doi:10.1016/j.nima.2013.04.078

[11] S. Kunieda *et al.*, "Overview of JENDL-4.0/HE and benchmark calculations". *Proc. 2015 Symposium on Nuclear Data*, Tokai, Nov 19–20; JAEA-Conf 2016-004, pp.41–46, 2016.

[12] H. Iwamoto *et al.*, "Measurement of 107-MeV proton-induced double-differential thick target neutron yields for Fe, Pb, and Bi using a fixed field alternating gradient accel-erator at Kyoto University", *J. Nucl. Sci. and Technol.*, published online, 2022. doi: 10.1080/00223131.2022.2115423

[13] H. Iwamoto *et al.*, "Measurement of double-differential neutron yields for iron, lead, and bismuth induced by 107-MeV protons for research and development of accelerator driven systems", *Proc. of 15th International Conference on Nuclear Data for Science and Tech-nology (ND2022)*, 21–29 July 2022, Gather.Town, 2022.

Acknowledgments

This work was supported by MEXT Innovative Nuclear Research and Development Program Grant Number JPMXD0219214562. We would like to express our gratitude to Dr. Daisuke Maki and Prof. Yuichi Oki of Kyoto University for their support.

6. Measurement and evaluation of DD neutron field Characteristics for OKTAVIAN

Hikaru MATSUNAGA[1*], Ryotaro KAWAHATA[1], Shingo TAMAKI[1], Sachie KUSAKA[1],
Fuminobu SATO[1] and Isao MURATA[1]
[1]Graduate school of Engineering, Osaka University
2-1 Yamadaoka, Suita-shi, Osaka-fu 565-0871, Japan
[*]Email: matsunaga21@qr.see.eng.osaka-u.ac.jp

Abstract:

OKTAVIAN is a DT and DD neutron irradiation facility in Osaka University. However, DD neutron source in OKTAVIAN has not been well characterized in terms of angular distribution of neutron intensity and neutron energy distribution, though characterized neutron fields are essential for the applications such as development and calibration of radiation detectors. Therefore, it is necessary to evaluate the DD neutron field in OKTAVIAN.

In this study, we measured the angular distribution of DD neutron from 0° to 150° by 15° intervals, and measured the total neutron production rate of OKTAVIAN by foil activation method with indium. Experimental results were compared with calculated results derived using SRIM, Drosg-2000 and MCNP5, and we discussed about the comparison of the present result with past cross section measurement result, the accuracy of the neutron source term and the validity of the simulation methods. As a result, no significant difference was found less than 135° between experimental and simulation values and at 150°, the simulated intensity was smaller than the experimental result. In conclusion, we confirmed the accuracy of the derived neutron source term and the validity of the simulation method and, revealed the total neutron production rate by OKTAVIAN.

1. Introduction

OKTAVIAN in Osaka University has been used as DT and DD neutron sources for nuclear fusion reactor research since 1981 [1]. Especially the DT neutron source using T(d, n)^{4}He reaction has a strong intensity of 3×10^{12} neutrons per second at maximum and has been primarily used for fusion neutronics studies such as various benchmark experiments including tritium breeding ratio measurements, and in addition for other applications like boron neutron capture therapy (BNCT) and so on [2-3]. On the other hand, DD neutron generated from D(d, n)^{3}He reaction can be utilized for such as oil exploration, active neutron interrogation for fissile materials, neutron imaging and so on [4-6]. However, the DD neutron field in OKTAVIAN has not been well characterized in terms of angular distribution of neutron intensity and neutron energy distribution.

Therefore, it is necessary to evaluate the DD neutron field in OKTAVIAN.

In this study, we measure the angular distribution for DD neutron by activation method using indium-foil, and measure the total neutron production rate by OKTAVIAN. We also characterize the neutron source term for Monte Carlo neutron transport calculation code using SRIM and Drosg-2000, and neutron transport simulation is carried out to calculate the expected angular distribution of neutron flux intensity in real experiment by MCNP5. Finally, we compare the experimental results with the calculation results to confirm whether the calculation results with the past nuclear data reproduce the present experiment.

2. Experimental method

2.1 Measurement method

In this study, DD neutron irradiated by OKTAVIAN was measured by foil activation method using indium foil. The irradiated DD neutron activated indium foils according to nuclear reaction described as Eq. 1,

$$^{115}In + \mathrm{n} \rightarrow {}^{115}In^{*} + \mathrm{n}'$$
$$^{115}In^{*} \rightarrow {}^{115}In + \gamma\ (336\ keV). \qquad \text{(Eq. 1)}$$

After that, radioactivity of indium foil can be derived by measuring the number of 336 keV γ-rays emitted from the activated indium by a germanium detector. The number of measured γ-rays count is expressed in the following equation,

$$C_{\gamma,\theta_\iota} = N_0 \int_0^{t_i} \int_E \sigma(E)\varphi(E,t)_{\theta_i} dE \cdot e^{\lambda t} dt \times e^{-\lambda(t_i+t_c)} \times \left(1 - e^{-\lambda t_m}\right) \times I_\gamma \times f_n \times f_g \times \varepsilon,$$

where C_{γ,θ_ι} is measured count of γ-rays emitted from indium foil placed at θ_ι degrees, N_0 is the number of ^{115}In atoms in the foil, λ is decay constant of $^{115}In^{*}$, t_i is irradiation time, t_c is cooling time, t_m is measurement time, I_γ is γ rays emission ratio, f_n is self-shielding factor, f_g is self-absorption factor, and ε is a detection efficiency of the germanium. We employed JENDL-5 [7] as a nuclear data library for activation cross section $\sigma(E)$. $\varphi(E,t)_{\theta_i}$ is the time-dependent neutron spectrum, described as $\varphi(E,t)_{\theta_i} = \varphi_{\theta_i} \times P(E)_{\theta_i} \times f(t)$, where $P(E)_{\theta_i}$ is neutron energy spectrum normalized as unity, $f(t)$ is time fluctuation factor of neutron production rate normalized as unity, and φ_{θ_i} is neutron fluence during the irradiation at θ_ι degrees. Finally, φ_{θ_i} is derived as following equation (Eq. 2) .

$$\varphi_{\theta_i} = \frac{C_{\gamma,\theta_\iota}}{N_0 \int_E \sigma(E)P(E)_{\theta_i} dE \int_0^{t_i} f(t)e^{\lambda t} dt \times e^{-\lambda(t_i+t_c)} \times (1 - e^{-\lambda t_m}) \times I_r \times f_n \times f_g \times \varepsilon} \qquad \text{(Eq. 2)}$$

Finally, the total produced neutron intensity Φ_{tot} is calculated by integrating experimental neutron flux angular distribution, as Eq. 3,

$$\Phi_{\mathrm{tot}} = \sum_{i=1}^{i=max} \int_{\theta_{i-1}}^{\theta_i} \varphi_{\theta_i} \cdot 2\pi \mathrm{r}^2 \sin\theta \, d\theta\,, \qquad \text{(Eq. 3)}$$

where r is distance between neutron source and measurement point.

2.2 Measurement procedure

The schematic experimental arrangement is shown in Fig. 1. We installed 11 indium foils, which were

10 mm× 10 mm × 0.5 mm, on a polystyrene jig at 10 cm away from the center of the target from 0° to 150° by 15° intervals.

In this experiment, we irradiated with DD neutron for about 8 hours. Accelerated deuteron energy was 250 keV and the deuterons were bombarded the deuterium-loaded titanium target with 1 mA beam current to induce D(d, n)^{3}He reaction. A time fluctuation factor of neutron production rate $f(t)$ was measured by an ^{238}U fission chamber installed during the irradiation. We repeated this irradiation experiment 3 times and measured radio-activities of these activated indium foils with germanium detectors. Finally, we calculated the angular distribution of neutron flux intensity and total neutron production intensity from these measured results.

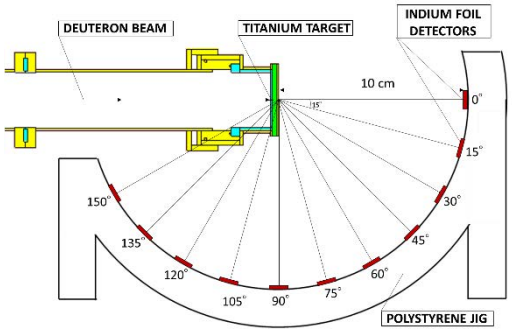

Fig. 1. System of experiments

2.3 Simulation of angular distribution of neutron flux intensity

After the experiment, we carried out a simulation of the real measurement to confirm validity of the present experimental results, and to consider the better simulation methods.

At first, we calculated deuterium ions behavior in a titanium target by using the Stopping and Range of Ions in Matter (SRIM) [8], which can calculate the deuteron path way and energy loss in the materials. Fig.2 shows an example of deuteron path ways calculated by SRIM, with 1000 deuterium ions for the incident energy of 250 keV.

After that, we calculated a neutron source term, i.e., the angular distribution and the neutron spectra for each emission angle, considering the deuterium ions behavior in a titanium target (Fig. 3). D(d, n)^{3}He cross-section and characteristics of produced neutron by the reaction was derived by Drosg-2000 [9]. The DD neutrons emission angle θ from the deuterium beamline direction can be expressed in the following equation.

$$\theta = |\eta - \varphi| \sim \eta + \varphi,$$

where η is the deuterium scattering angle, and φ is the DD neutron emission angle with respect to the incident deuteron beam axis.

Finally, we calculated the angular distribution of neutron flux intensity in the real experiment by A General Monte Carlo N-Particle transport code (MCNP5) [10], and compared the experimental and simulation results. Since the present experimental data cannot be converted to cross section data due to lack of detailed target information such as deuterium density, we normalized the calculated result by average Φ_{tot} value of three experimental results.

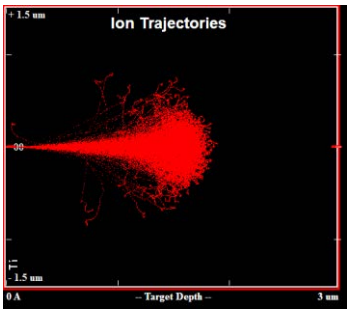

Fig. 2. Path way of deuterium ions (1000pcs.) by SRIM

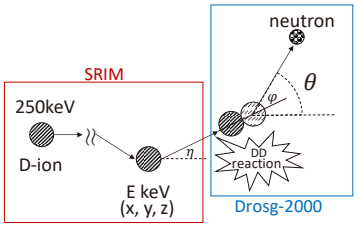

Fig. 3. The simplified diagram of the SRIM and Drosg-2000 combination

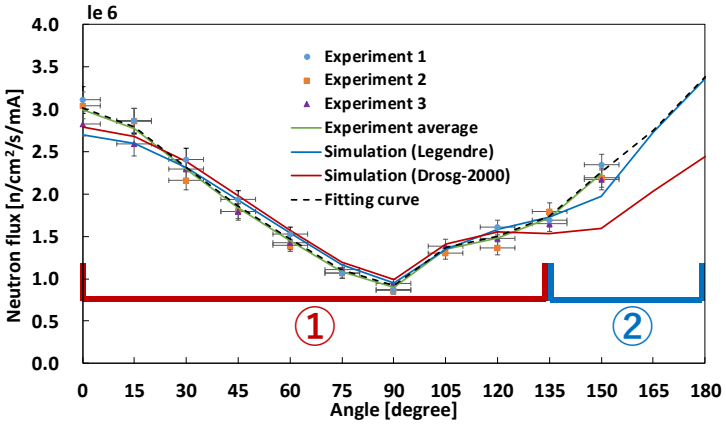

Fig. 4. Angular distribution of neutron flux intensity of experiments and simulation by MCNP5

3. Results and discussion

Measured angular distributions of neutron flux intensity by experimental and simulation results are shown in Fig. 4. The horizontal axis represents the measured angle in the laboratory system. Three dot series with error bars show the experimental values of the neutron flux intensity in the present study. The green solid curve means the average neutron flux of three experimental values, and the red solid curve indicates the calculated values by MCNP5. As a result, no significant difference was found at less than 135° (area ①) between values of experiments and simulation. On the other hand, at 150° (area ②), the simulated intensity was smaller than the experimental result. This discrepancy seemed to be caused by a reason: D(d, n)^{3}He cross-section installed in Drosg-2000.

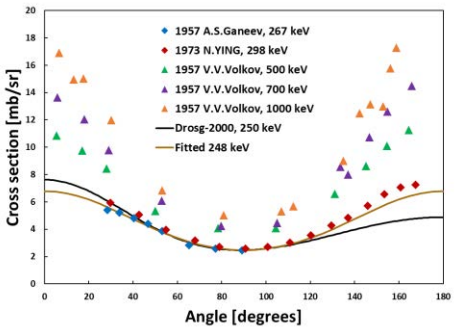

Fig. 5. D(d, n)^{3}He differential cross-sections for each incident deuteron energies in EXFOR, 250 keV in Drosg-2000, and 248 keV fitted.

Fig. 5 shows D(d, n)^{3}He cross-sections in Drosg-2000 (black solid curve) and measured DD cross section in the past studies listed in EXFOR [11-14] (colored plots). This graph shows that measured DD cross sections appears to have a symmetric curve with respect to 90° at lower deuterium beam energies. However, the cross-section data in Drosg-2000 shows higher values in forward angles than in backward angles. Therefore, we calculated new theoretical cross sections and used it to calculate the neutron angular distribution again. In general, the angular distribution of the D(d, n)^{3}He reaction products can be expressed by as an expansion in terms of even Legendre polynomials, as shown in Eq. 4, because the projectile and target are symmetric about the 90° center of mass angle.

$$\frac{d\sigma}{d\cos\theta} = \frac{d\sigma(90°)}{d\cos\theta}[1 + A\cos^2(\theta) + B\cos^4(\theta)], \qquad \text{(Eq. 4)}$$

where A and B are the energy dependent asymmetry coefficients. In case of OKTAVIAN deuteron beam, which has about 250 keV energy, A was 1.32 ± 0.04 and B was 0.43 ± 0.05 [15]. After that, we calculated D(d, n)^{3}He cross sections by using Eq. 4 as shown in Fig. 5, the solid brown curve. Absolute values

of cross section were adjusted so that the 90° value corresponds to D(d, n)^{3}He cross section at 90° in Drosg-2000. The newly derived cross sections with the Legendre polynomials showed smaller value in the forward angle and larger in the backward angle than the cross sections calculated with Drosg-2000, and had good agreement with the experimental results by A.S. Ganeev [12] near the 250 keV of incident deuterium energy.

New-built neutron source term calculated with the new cross-sections is shown as the solid blue curve in Fig. 4, and this result showed a good agreement with present ex perimental values than the previous simulation result at more than 150 degrees. Therefore, we confirmed that the current experimental results are reasonable compared to previous experimental results by using this theoretical cross section data calculated from Legendre polynomials.

Finally, we revealed the DD neutron production intensity of OKTAVIAN. We used the black dotted fitting curve shown in the Fig. 4 as φ_{θ_i}, combining experimental data less than 150° and calculated new values above 150°. Fig. 6 shows the time fluctuation of neutron intensity, $\varphi_{tot} \times f(t)$, for each experiment, and Fig.7 shows the histogram of the generated neutron intensity from these results. We found that OKTAVIAN can generate DD neutrons with $(2.0 \pm 0.1) \times 10^9$ n/mC in average.

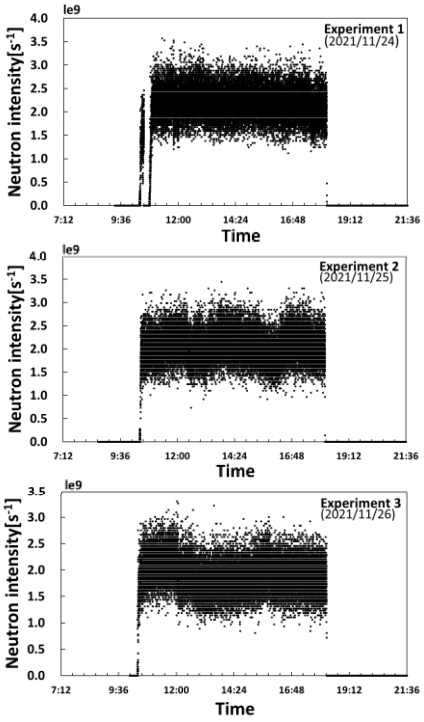

Fig. 6. Time fluctuation of neutron intensity for each of the three experiments

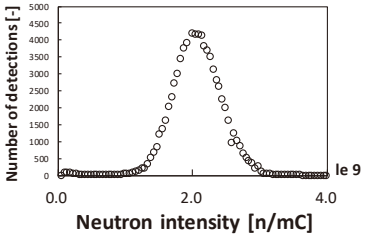

Fig. 7. Histogram of neutron intensity

4. Conclusion

In this study, we measured the angular distribution of DD neutron flux intensity from 0° to 150° by 15° intervals, and compared with numerically calculated result by SRIM, Drosg-2000 and MCNP5 to examine the agreement of the present result with cross section past experimental results, the accuracy of neutron source term and the validity of simulation methods. As a result, no significant difference was found less than 135° between results of experiments and simulation. Also we found that DD neutron intensity was $(2.0 \pm 0.1) \times 10^9$ n/mC by OKTAVIAN. On the other hand, at 150°, the simulated intensity was much smaller than the experimental result and found the probability that cross-section data in Drosg-2000 have some problem. In order to consider this problem, we derived theoretical DD cross-sections from the Legendre polynomials, and performed neutron transport calculation again. As a result, the newly produced cross sections were reasonable in comparison with previous experimental results, and a good agreement was found with the present experimental values. Therefore, we found that the current experimental results were valid compared to past experimental results by using theoretical cross section data calculated from Legendre polynomials.

In the future, we will investigate a new method to measure neutron intensity for angles larger than 150°,

and evaluate the accuracy of DD reaction cross section values in the whole emission angles. And in future we will also investigate the method to measure the DD neutron spectrum.

References

[1] TAMAKI, Shingo, et al. "Radioactivation Analysis of Concrete Wall in OKTAVIAN Facility." *Plasma and Fusion Research* 17 (2022): 1405001-1405001.

[2] Lee, Yi-Kang. "Analysis of the tritium breeding ratio benchmark experiments using the Monte Carlo code TRIPOLI-4. "*Fusion engineering and design* 85.7-9 (2010): 1125-1128.

[3] Asnal, M., T. Liamsuwan, and T. Onjun. "An evaluation on the design of beam shaping assembly based on the DT reaction for BNCT." *Journal of Physics: Conference Series*. Vol. 611. No. 1, 2015.

[4] R.C. Caldwell et al. “Activation analysis in petroleum exploration research”, *Nuclear Instruments and Methods* (1959).

[5] Chichester, D., J. Simpson, and M. Lemchak. "Advanced compact accelerator neutron generator technology for active neutron interrogation field work." *Journal of Radioanalytical and Nuclear Chemistry* 271.3 (2007): 629-637.

[6] Yan, M. F., et al. "Optimization design of a fast neutron imaging collimator by genetic algorithm." *Journal of Instrumentation* 15.12 (2020).

[7] O. Iwamoto, N. Iwamoto, K. Shibata, A. Ichihara, S. Kunieda, F. Minato, and S. Nakayama, "Status of JENDL", *EPJ Web of Conferences,* 239, 09002_1-6 (2020).

[8] Ziegler, James F., Matthias D. Ziegler, and Jochen P. Biersack. "SRIM–The stopping and range of ions in matter (2010)." *Nuclear Instruments and Methods in Physics Research Section B: Beam Interactions with Materials and Atoms* 268.11-12 (2010): 1818-1823.

[9] Drosg, M. DROSG-2000: Neutron source reactions. Data files with computer codes for 56 monoenergetic neutron source reactions. No. IAEA-NDS--87 (REV. 5). International Atomic Energy Agency, 2000.

[10] Brown, F.B., MCNP-A General Monte Carlo N-Particle Transport Code, Oak Ridge(US): Los Alamos National Laboratory; 2003.

[11] Data, Experimental Nuclear Reaction. "EXFOR." CSISRS https://www-nds.iaea.org/exfor (2022).

[12] A.S.Ganeev, “The D-D reaction in the deuteron energy range 100 - 1000 keV.”, *Soviet Atomic Energy*, Supplement, Issue.5, p.21 (1957), USA.

[13] N.Ying, “A Study of the ^{2}H (d, p)^{3}H and ^{2}H (d, n)^{3}He Reactions and the Excited State of ^{4}He at 23.9 MeV”, *Nuclear Physics*, Section A, Vol.206, Issue.3, p.481 (1973), Netherlands.

[14] V.V.Volkov, “Investigation of the D-D reaction in the deuteron energy range 0.20 to 1.75 MeV”, *Soviet Atomic Energy*, Supplement, Issue.5, p.13 (1957), USA.

[15] Theus, R. B., W. I. McGarry, and L. A. Beach. "Angular distributions and cross-section ratios for the reactions ^{2}H (d, n) ^{3}He and ^{2}H (d, p) ^{3}H below 500 keV." *Nuclear Physics* 80.2 (1966): 273-288.

7. Production cross sections of ^{198g}Au in proton-induced reactions on natural platinum

Gantumur DAMDINSUREN[1,2*], Masayuki AIKAWA[1,3,4], Khishigjargal TEGSHJARGAL[2], Norov ERDENE[2], Naoyuki UKON[5], and Hiromitsu HABA[6]

[1] Graduate School of Biomedical Science and Engineering, Hokkaido University, Sapporo 060-8638, Japan
[2] School of Engineering and Applied Sciences, National University of Mongolia, Ulaanbaatar 14201, Mongolia
[3] Faculty of Science, Hokkaido University, Sapporo 060-0810, Japan
[4] Global Center for Biomedical Science and Engineering, Faculty of Medicine, Hokkaido University, Sapporo 060-8648, Japan
[5] Advanced Clinical Research Center, Fukushima Medical University, Fukushima 960-1295, Japan
[6] Nishina Center for Accelerator-Based Science, RIKEN, Wako 351-0198, Japan
[*]Email: damdinsuren@nds.sci.hokudai.ac.jp

The production cross sections of the ^{nat}Pt(p,x)^{198g}Au reaction were measured at the AVF cyclotron of the RIKEN RI Beam Factory. The stacked-foil activation technique and high-resolution γ-ray spectrometry were adopted to derive the cross sections. The derived cross sections were compared with experimental data studied earlier and with the theoretical calculation in the TENDL-2019 library.

1. Introduction

The radionuclide ^{198g}Au has a half-life of 2.6941 d and is a beta emitter (β^-: 100%, $<E_\beta>$ = 312.5 keV) [1]. ^{198g}Au is widely used for therapy in nuclear medicine [2,3]. There are several production routes for ^{198g}Au production. One of the possible production routes is the proton-induced reaction on platinum targets. In this study, we focused on the proton-induced reaction on ^{nat}Pt targets. Two previous experimental studies were found in the literature survey [4,5]. However, their data show large uncertainties and discrepancies. Therefore, we measured the excitation function of the ^{nat}Pt(p,x)^{198g}Au reaction. The result was compared with earlier studies and theoretical calculation in the TENDL-2019 library [6].

2. Experimental method

The experiment was performed at the AVF cyclotron of the RIKEN RI Beam Factory. The stacked-foil activation technique and high-resolution γ-ray spectrometry were adopted to measure the cross sections.

The stacked target consisted of pure metallic foils of ^{nat}Pt (20 μm thick, 99.95% purity, 100×100

mm size), and ^{nat}Ti (5 μm thick, 99.6% purity, 50×100 mm size), which were purchased from Nilaco Corp., Japan. The ^{nat}Ti foil was used for the ^{nat}Ti(p,x)^{48}V monitor reaction to assess beam parameters and target thicknesses. The size and weight of the foils were measured to determine the average thicknesses. The derived thicknesses of the ^{nat}Pt and ^{nat}Ti foils were 39.2 and 2.24 mg/cm^2, respectively. The foils were cut for the size of 10×10 mm to fit a target holder, which served as a Faraday cup. Twenty-five sets of Pt-Pt-Ti-Ti foils were stacked into the target holder.

The stacked target was irradiated with a proton beam for 30 min. The incident beam energy was measured by the time-of-flight method [7] and found to be 30.1±0.1 MeV. The energy degradation in the stacked target was calculated using stopping powers derived from the SRIM code [8]. The average beam intensity was 101 nA, which was measured by the Faraday cup.

γ rays emitted from each irradiated foil were measured by a high-resolution HPGe detector (ORTEC GEM-25185-P). The detector was calibrated by a multiple γ-ray emitting point source. The spectra were analyzed by dedicated software (Gamma Studio, SEIKO EG&G). The dead time was kept less than 4.7% during the measurement.

Cross sections of the ^{nat}Ti(p,x)^{48}V monitor reaction were determined to assess the beam parameters and target thicknesses. The cross sections were derived from measurements of the 983.5-keV γ ray (I_γ = 99.98%) emitted with the ^{48}V decay ($T_{1/2}$ = 15.9735 d). The result was compared with the IAEA recommended values [9,10] in Fig. 1. The derived excitation function of the ^{nat}Ti(d,x)^{48}V reaction was in good agreement with the IAEA-2007 recommended values. The measured beam parameters and target thicknesses without any correction were used to determine the cross sections of the ^{nat}Pt(p,x)^{198g}Au reaction.

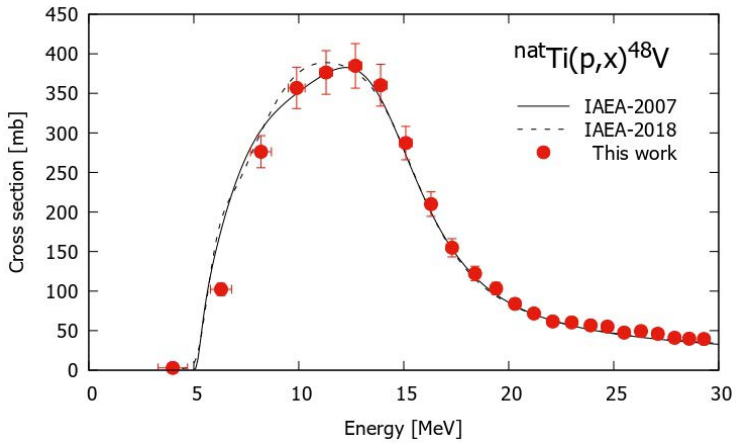

Fig. 1. The excitation function of the ^{nat}Ti(p,x)^{48}V monitor reaction with the recommended values [9,10].

3. Result and discussion

The cross sections of the ^{nat}Pt(p,x)^{198g}Au reaction were derived from the measurement of the 411.80205-keV γ line (I_γ = 95.62%) in the decay of ^{198g}Au. The derived cross sections are shown in Fig. 2 in comparison with the previous experimental data and the theoretical estimation of the TENDL-2019 library. Our result is consistent with the previous experimental data within the uncertainty although the data by Tárkányi et al. (2004) deviated at 17-23 MeV. The TENDL-2019 data show a similar trend to the

experimental cross sections while its peak position is slightly lower.

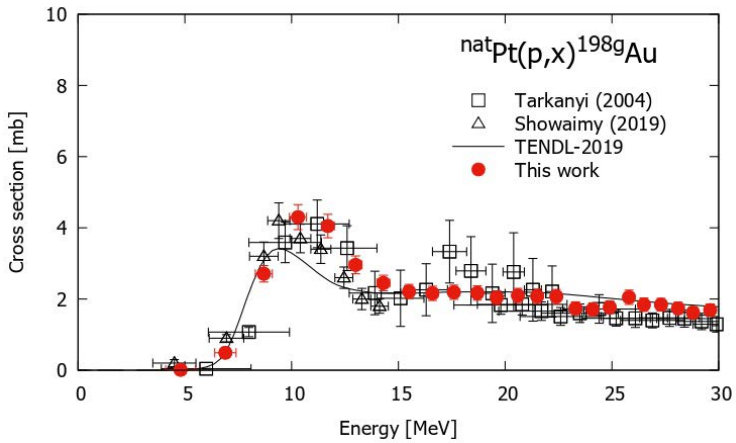

Fig. 2. Excitation function of the ^{nat}Pt(p,x)^{198g}Au reaction with the previous experimental data [4,5] and the TENDL-2019 data [6].

4. Conclusions

The excitation function of the ^{nat}Pt(p,x)^{198g}Au reaction was measured up to 30 MeV. The well-established methods, the stacked-foil activation method and γ-ray spectrometry were used for the cross-section measurement. The derived cross-section data of the ^{nat}Pt(p,x)^{198g}Au reaction is consistent with the data of Tárkányi et al. (2004) [4] and Showaimy et al. (2019) [5] within the uncertainty.

Acknowledgments

The experiment was performed at RI Beam Factory operated by RIKEN Nishina Center and CNS, University of Tokyo, Japan. G. Damdinsuren was granted a scholarship by the M-JEED project (Mongolian-Japan Engineering Education Development Program, J11B16). This work was partially supported by JSPS KAKENHI Grant No. 22H04961.

References

[1] Huang X & Kang M, Nuclear Data Sheets for A = 198, Nucl. Data Sheets, 2016, 133, 221-416.

[2] Konishi M, Fujita M, Takeuchi Y, et al., Treatment outcomes of real-time intraoral sonography-guided implantation technique of ^{198}Au grain brachytherapy for T1 and T2 tongue cancer, J. Radiat. Res., 2021, 62, 871–876.

[3] Chakravarty R, Chakraborty S, Guleria A, et al., Clinical scale synthesis of intrinsically radiolabeled and cyclic RGD peptide functionalized ^{198}Au nanoparticles for targeted cancer therapy, Nucl. Med. Biol., 2019, 72, 1-10.

[4] Tárkányi F, Hermanne A, Takács S, et al., Cross sections for production of the therapeutic radioisotopes ^{198}Au and ^{199}Au in proton and deuteron induced reactions on ^{198}Pt, Radiochim Acta, 2004, 92, 223-228.

[5] Showaimy H, Solieman A.H.M, Hamid A.S.A, et al., Measurements of activation cross sections for proton induced reactions on natural platinum targets leading to the formation of gold radioisotopes, Radiat. Phys. Chem., 2019 157, 97-101.

[6] Koning A.J, Rochman D, Sublet J-C, et al., TENDL: Complete Nuclear Data Library for

Innovative Nuclear Science and Technology, Nucl. Data Sheets, 2019, 155, 1–55.

[7] Watanabe T, Fujimaki M, Fukunishi N, et al., Beam energy and longitudinal beam profile measurement system at the RIBF, Proc. 5th Int. Part. Accel. Conf. (IPAC 2014), 2014, 3566–3568.

[8] Ziegler J.F, Ziegler M.D, Biersack J.P, SRIM - The stopping and range of ions in matter, Nucl. Instrum. Methods. Phys. Res. B, 2010, 268, 1818–1823.

[9] Tárkányi F, Takács S, Gul K, et al., Charged Particle Cross-Section Database for Medical Radioisotope Production: Diagnostic Radioisotopes and Monitor Reactions (updated version), IAEA-TECDOC-1211 [Internet], 2007, Available from: https://www-nds.iaea.org/medical/medical-2020-05/monitor_reactions.html.

[10] Hermanne A, Ignatyuk A.V, Capote R, et al., Reference Cross Sections for Charged-particle Monitor Reactions, Nucl. Data Sheets, 2018, 148, 338–382.

8. Preliminary experiment for measurement of radionuclide yield from nuclear capture reaction of negative muon

Yuji YAMAGUCHI[1*], Masahide HARADA[1], Naritoshi KAWAMURA[2], Izumi UMEGAKI[2], Motonobu TAMPO[2], Soshi TAKESHITA[2], and Katsuhiro HAGA[1]
[1]J-PARC Center, Japan Atomic Energy Agency
2-4 Shirakata, Tokai-mura, Naka-gun, Ibaraki-ken 319-1195, Japan
[2]High Energy Accelerator Research Organization
1-1 Oho, Tsukuba-shi, Ibaraki-ken 305-0801, Japan
[*]Email: yamaguchi.yuji@jaea.go.jp

We have performed a preliminary experiment to check applicability of existing methodology to taking comprehensive data of radionuclide yields from nuclear capture of a negative muon (μ^-) for wide range of target atomic number. The radionuclide yields per stopped μ^- are obtained by spectroscopy of γ-rays and X-rays from targets of ^{27}Al, ^{59}Co, ^{141}Pr, and ^{209}Bi using high-purity germanium detectors. It is confirmed that the methodology can be applied to obtain the comprehensive data.

1. Introduction

A negative muon (μ^-) is known to be captured by a nucleus, ${}^{A}_{Z}\mathrm{N}(\mu^-, \nu_\mu)\,{}^{A}_{Z-1}\mathrm{N}^*$, after the muon cascades down to 1s state of the muonic atom with emitting characteristic X-rays called muonic X-rays and Auger electrons. The nuclear capture reaction competes with the μ^- free decay ($\mu^- \rightarrow e^- + \bar{\nu}_e + \nu_\mu$) and is dominant for the nucleus with atomic number $Z > 12$. After the nuclear capture, a highly excited nucleus is produced because a part of the muon mass of 106 MeV/c^2 is converted to the excitation energy, and is deexcited with emitting neutrons, γ-rays, and sometimes charged particles to reach a stable nucleus or a radionuclide. In this way, an irradiated sample by a large amount of μ^- can be activated.

Materials and Life Science Experimental Facility (MLF), J-PARC provides intense pulsed μ^- beam for various researches such as non-destructive isotopic analysis, negative muon spin rotation and relaxation (μ^-SR), and so on [1-3]. To handle irradiated samples properly at MLF, it is necessary to estimate radioactivity of the irradiated samples accurately for the sake of radiation safety. Recently, an activation calculation code based on particle transport simulation by Particle and Heavy Ion Transport code System (PHITS) [4] has been established to estimate radioactivity of the irradiated samples at MLF. Because reliability of the estimated radioactivity relates to radiation safety of MLF, PHITS calculation needs to be verified for radionuclide production in targets with wide range of *Z*.

To verify the calculation results, comprehensive experimental data of radionuclide production from

nuclear capture of μ^- are required for wide range of target *Z*. However, most of the experiments were performed to take only the data of the target of interest for their specific purposes. It is also known that there exist discrepancies between experimental data and calculation results by PHITS. Therefore, we have started to measure the yield of radionuclide from nuclear capture of μ^- for wide range of target *Z*.

In this paper, we report on the preliminary experiment performed at MLF to check applicability of existing methodology to taking comprehensive data of radionuclide yield for wide range of target *Z*.

2. Experiment

The experiment was performed at D2 area of muon science facility in MLF. The plan view of the experimental setup is shown in Figure 1. A pulsed μ^- beam was generated by a 3-GeV proton beam on a 20-mm-thick graphite target and was provided through decay muon beamline (D-line). Incident negative muons from the D-line were extracted through the thin Kapton beam window at D2 area with momentum of 35 MeV/c. The extracted negative muons flew in the air and stopped in a target.

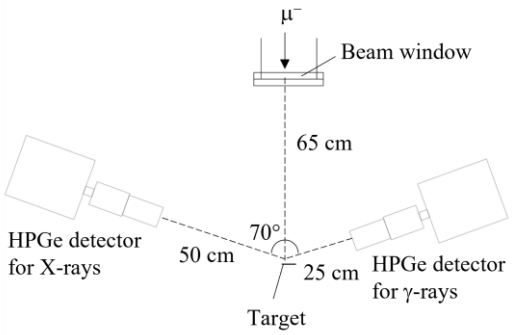

Figure 1. Plan view of experimental setup. Incident negative muons with 35 MeV/c come from the upper side of this view.

The targets used in this experiment are listed in Table 1. They were square-shaped plates thick enough to stop incident negative muons and were selected from monoisotopic elements for simplicity of the measurement and analysis. Each target was irradiated for about 10 hours at μ^- beam intensity of 3×10^3 s^{-1} to measure the radionuclide yield per stopped μ^-.

Table 1. List of targets.

Target	Size [mm]	Thickness [mm]	Purity [%]
^{27}Al	50×50	2.0	99
^{59}Co	50×50	1.0	99.9
^{141}Pr	25×25	1.0	99
^{209}Bi	60×60	1.0	99.9

The yield of radionuclide and the number of stopped μ^- were obtained by γ-ray and X-ray spectroscopy, respectively. The γ-rays from radionuclides and muonic X-rays were measured in-beam using high-purity germanium (HPGe) detectors (ORTEC GMX Series) with a 51-mm diameter window. Two detectors were applied because the detection time distribution was different between γ-rays and muonic X-rays due to the pulsed beam. The HPGe detector for muonic X-rays was placed at 50 cm far from the target to avoid pile-up of the signal. The detector for γ-rays was closer to the target than that for muonic X-rays to obtain γ-ray spectra efficiently. The γ-rays from radionuclides with half-life longer than typically 15 hours were measured off-line using a lead-shielded HPGe detector. To calibrate the absolute energy scales for the HPGe detectors, measurement of γ-rays from ^{152}Eu check source was also performed.

3. Analysis

The energy spectra measured in-beam and off-line γ-spectroscopy for ^{27}Al target are shown in Figure 2 and Figure 3, respectively. In Figure 2, γ-rays from radionuclides produced by μ^- nuclear capture are clearly observed at 844 and 1014 keV (^{27}Mg), and 1809 keV (^{26}Na). Background peaks from

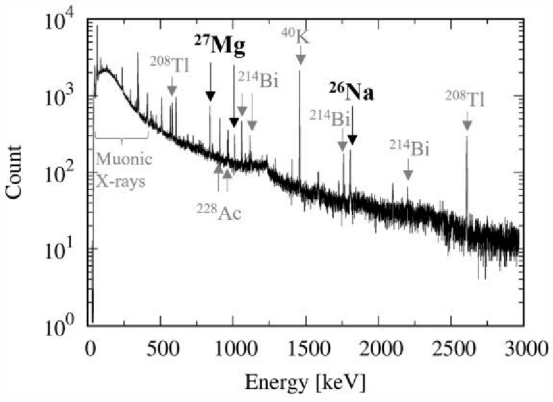

Figure 2. Energy spectrum measured in-beam γ-spectroscopy using ^{27}Al target. The identified radionuclides are shown.

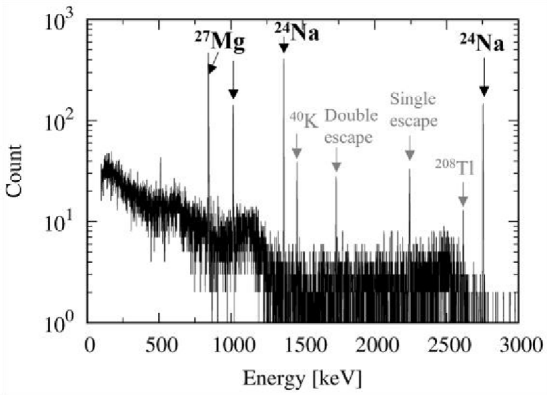

Figure 3. Energy spectrum of γ-rays measured off-line for 1 hour after irradiation of ^{27}Al target. The single and double escape peaks from the 2754-keV γ-rays from ^{24}Na are also shown.

natural radionuclides are also observed such as ^{208}Tl, ^{228}Ac, ^{214}Bi, and ^{40}K because the HPGe detector used in-beam measurement was not shielded. In Figure 3, γ-rays from ^{24}Na are clearly observed at 1369 and 2754 keV in addition to those from ^{27}Mg at 844 and 1014 keV.

The yield of radionuclide produced by μ^- nuclear capture Y was obtained by

$$Y = pT_{\mathrm{irr}} = \begin{cases} (4\pi\Omega^{-1})\varepsilon^{-1}I^{-1}(\mathrm{e}^{-\mu t_{\mathrm{eff}}})^{-1}T_{\mathrm{irr}}^{-1}C_{\gamma}T_{\mathrm{irr}} & \text{for in-beam} \\ (4\pi\Omega^{-1})\varepsilon^{-1}I^{-1}(\mathrm{e}^{-\mu t_{\mathrm{eff}}})^{-1}T_{\mathrm{cor}}^{-1}C_{\gamma}T_{\mathrm{irr}} & \text{for off-line,} \end{cases} \quad (1)$$

where p is production rate, T_{irr} is irradiation time, Ω is solid angle, I is emission rate of the γ-ray of interest, and μ is attenuation coefficient. The effective thickness of the target for photons t_{eff} is expressed by

$$t_{\mathrm{eff}} = \frac{t_{\mathrm{range}}}{\cos 70°}, \quad (2)$$

where t_{range} is range of incident μ^- in the target. The net count of the γ-ray of interest C_{γ} was obtained by fitting using Gaussian functions. A typical example of the fitting is shown in Figure 4. The correction for cooling T_{cor} is written as

$$T_{\mathrm{cor}} = \frac{T}{\ln 2}\left\{1-\left(\frac{1}{2}\right)^{\frac{T_{\mathrm{irr}}}{T}}\right\}\left(\frac{1}{2}\right)^{\frac{T_{\mathrm{off}}}{T}}\left\{1-\left(\frac{1}{2}\right)^{\frac{T_{\mathrm{ms}}}{T}}\right\}, \quad (3)$$

where T is half-life, T_{off} is the period from irradiation stop to measurement start, and T_{ms} is measurement time.

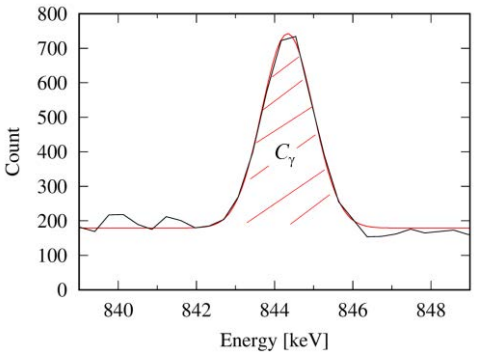

Figure 4. Fitting result for the peak at 844 keV from ^{27}Mg in Figure 2. Black line: Observed spectrum. Red line: fitting curve using Gaussian function. The net count C_{γ} is obtained by integrating the shaded area.

The detection efficiency of the HPGe detector ε was obtained by particle transport simulation using PHITS. The geometry of the system for the simulation is shown in Figure 5. The origin corresponding to the target position is defined as the photon source position. The photon source has Gaussian spatial distribution in x and y directions and is rotated 70° around y-axis. The Gaussian functions for x and y directions are independent each other and are assumed to have σ_x = 6.7 mm and σ_y = 11.7 mm. Photons

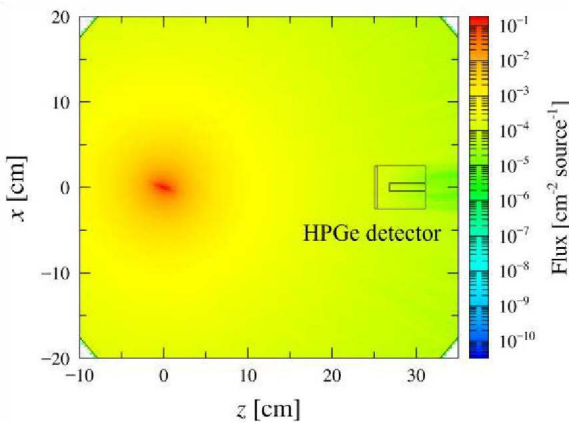

Figure 5. Geometry of the system for the simulation. Photon flux is also drawn with color cluster plot to show the photon source position.

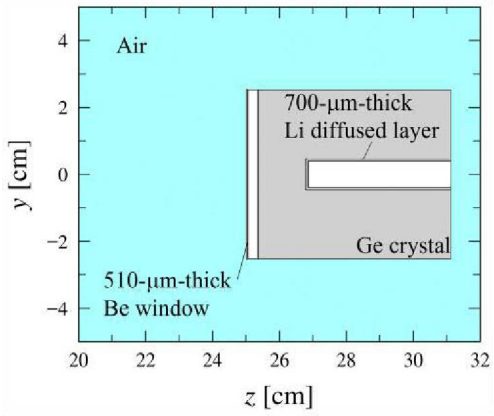

Figure 6. Model of the HPGe detector.

from the source enter the HPGe detector on z-axis through its thin entrance window. The model of the HPGe detector is shown in Figure 6. The HPGe detector is a coaxial detector and has a beryllium window with a diameter of 51 mm and a thickness of 510 μm in front of the crystal. The Ge crystal has 0.3-μm-thick ion implanted and 700-μm-thick lithium diffused dead layers. The obtained efficiency ε is shown in Figure 7 as a function of photon energy. The photon energy range of 25 to 2800 keV was chosen in the calculation according to the energy required for the analysis.

The X-ray energy spectrum from 340 to 460 keV for ^{27}Al target is shown in Figure 8. KX-ray peaks are clearly observed from 2p→1s to 6p→1s in this figure. The number of stopped μ^- I_{μ^-} can be obtained by

$$I_{\mu^-} = (4\pi\Omega^{-1})\varepsilon^{-1}(e^{-\mu t_{\mathrm{eff}}})^{-1}C_{\mathrm{KX}}, \quad (4)$$

where C_{KX} is sum of net count of the KX-rays. However, KX-rays from heavy targets cannot be measured efficiently because they have high energy of several MeV. Thus, I_{μ^-} for ^{141}Pr and ^{209}Bi targets was obtained, assuming that I_{μ^-} is proportional to the number of protons on the graphite target,

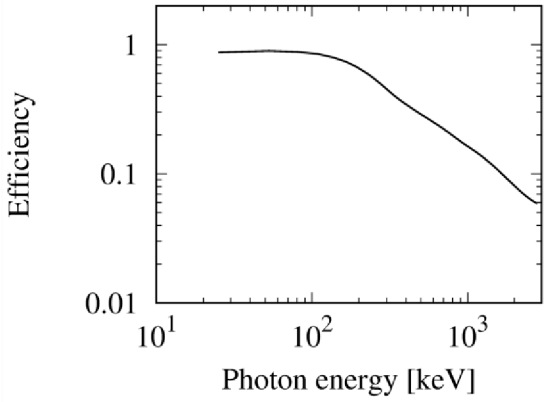

Figure 7. Detection efficiency of the HPGe detector calculated by PHITS. The efficiency in 25 to 2800 keV is shown.

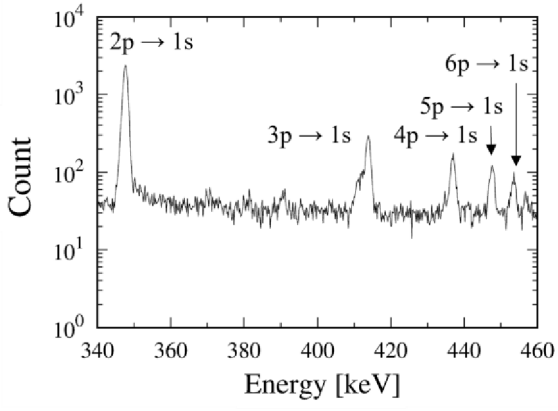

Figure 8. Energy spectrum of X-rays for ^{27}Al target in the range of 340 to 460 keV. KX-ray transitions are shown from 2p→1s to 6p→1s.

by

$$I_{\mu^-} = \frac{\phi}{\phi_C} I_{\mu^-,C} \quad (5)$$

where ϕ is the number of protons on the graphite target. The symbols with the index C are reference values obtained using a 3-mm-thick carbon target. The number of stopped μ^- in the C target $I_{\mu^-, C}$ was obtained from Equation (4).

4. Results and discussion

Typical results of radionuclide yields per stopped μ^- are shown in Figure 9. The present data are consistent with the data by Heisinger et al. [5] within experimental uncertainties.

The present data include not only statistical uncertainty but also systematic uncertainties of solid angle and detection efficiency. The estimated uncertainty of solid angle ranges 8%-16% because the target was set on the detector at zero distance for off-line measurement while was set away from detectors in-beam. The estimated uncertainty of detection efficiency is 8% from the simulation. The uncertainties of solid angle and detection efficiency can be reduced by γ counting using a check source.

In Figure 10, calculation/experiment (C/E) values are shown to compare present data with calculation results by PHITS ver.3.20. Although PHITS results tend to underestimate present data, further data covering wide range of target Z with lower uncertainty are needed to discuss the discrepancy in detail and to verify the calculation results more accurately.

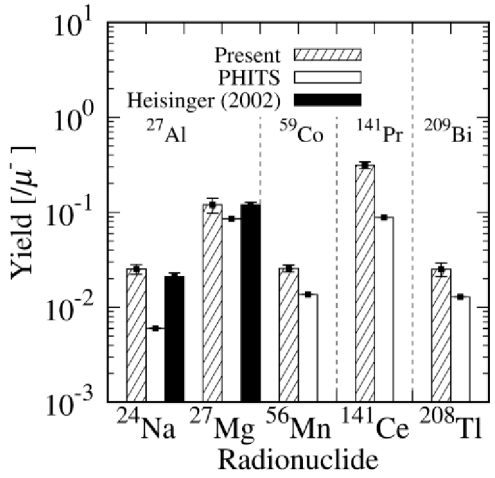

Figure 9. Radionuclide yields per stopped μ^-. Shaded bar: Present data. White bar: PHITS3.20 results. Black bar: Heisinger et al. [5].

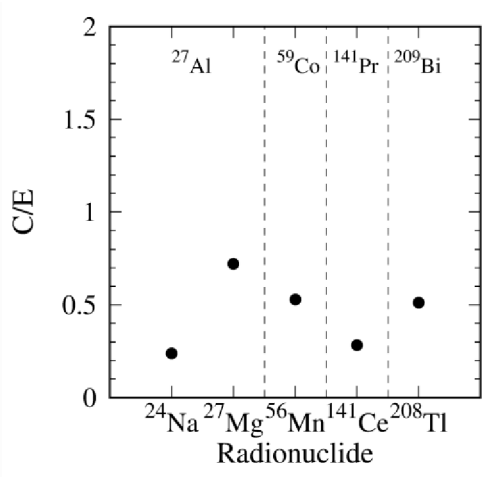

Figure 10. Calculation/experiment (C/E) value of the radionuclide yield in Figure 9. Calculations are PHITS3.20 results and experiments are present data.

5. Summary

We performed the preliminary experiment to check applicability of existing methodology to taking new data set of radionuclide yield for wide range of target Z. It was confirmed that present data obtained using existing methodology were consistent with data by Heisinger et al. Present data were also compared with calculations by PHITS3.20. Although discrepancy between present data and PHITS calculation was observed, further data covering wide range of target Z with lower uncertainty are

needed to discuss the discrepancy in detail and to verify the calculation results more accurately.

References

1) Umegaki, I., et al., Nondestructive High-Sensitivity Detections of Metallic Lithium Deposited on a Battery Anode Using Muonic X-rays, Anal. Chem., vol.92, no.12, 2020, pp.8194-8200.
2) Ninomiya, K., et al., Development of non-destructive isotopic analysis methods using muon beams and their application to the analysis of lead, J. Radioanal Nucl Chem, vol.320, 2019, pp.801-805.
3) Sugiyama, J., Nuclear Magnetic Field in Solids Detected with Negative-Muon Spin Rotation and Relaxation, vol.121, 2018, 087202.
4) Sato, T., et al., Features of Particle and Heavy Ion Transport code System (PHITS) version 3.02, J. Nucl. Sci. Technol., vol.55, 2018, pp.684-690.
5) Heisinger, B., et al., Production of selected cosmogenic radionuclides by muons: 2. Capture of negative muons, Earth and Planetary Science Letters, vol.200, 2002, pp.357-369.

Acknowledgments

The muon experiment at the Materials and Life Science Experimental Facility of the J-PARC was performed under a user program (Proposal No. 2021B0356).

9. Cross Comparison of Neutron Spectra with Liquid Scintillator and Bonner Sphere Spectrometer

Eunji Lee[†1,2], Toshiya Sanami[1,2], Tetsuro Matsumoto[3], Akihiko Masuda[3], Nobuhiro Shigyo[4], Tsuyoshi Kajimoto[5], Noriaki Nakao[6], Robert Froeschl[7], Elpida Iliopoulou[*7] , Angelo Infantino[7], and Stefan Roesler[7]

[1]High Energy Accelerator Research Organization (KEK), Oho, Tsukuba, Ibaraki 305-0801, Japan
[2]The Graduate University for Advanced Studies (SOKENDAI), Hayama, Kanagawa 240-0193, Japan
[3]National Institute of Advanced Industrial Science and Technology, 1-1-1 Umezono, Tsukuba, Ibaraki 305-8560, Japan
[4]Department of Applied Quantum Physics and Nuclear Engineering, Kyushu University, Motooka, Nishi-ku, Fukuoka 819-0395, Japan
[5]Hiroshima University, 1-4-1, Kagamiyama, Higashi-Hiroshima, Hiroshima 739-8527, Japan
[6]Shimizu Corporation, 3-4-17 Etchujima, Koto-ku, Tokyo 135-8530, Japan
[7]CERN, 1211 Geneva 23, Switzerland
[†]Email: eunji.lee@kek.jp

Abstract

Experimental measurements were performed for produced high-energy neutrons when the 24 GeV/c proton beam hit a copper target at the CHARM facility in the East Hall of the CERN proton Synchrotron. Neutron energy spectra after concrete and steel shields were measured with a liquid scintillator and a Bonner sphere spectrometer under an identical shielding configuration. The light output distribution of the liquid scintillator and a set of count rates of the Bonner sphere spectrometer based on the ^{3}He proportional counter was converted into the neutron energy spectrum using the unfolding method with a calculated response matrix for each instrument, respectively. An initial guess of the neutron energy spectrum for unfolding was obtained by the PHITS code. The neutron energy spectra were derived to inter-compare the difference between two measurement methods.

1 Introduction

Production of neutrons is an unavoidable consequence of operating high-energy accelerator facilities. The neutrons have a wide energy range, from thermal to beam energy. From the viewpoint of radiation protection, neutron spectrum after penetrating a shield is important in the shielding design of high-energy accelerator facilities. Monte Carlo codes can provide an estimation of neutron spectrum in accelerator facilities even for complicated shielding structures. However, accuracies of the codes for the high-energy neutrons generated by the high-energy beam, especially above 1 GeV, are not well evaluated since comparable experimental data are

[*]Present address: Hirslanden Private Hospital Group, Radiation Oncology Institute, Lausanne Switzerland

scarce [1]. Therefore, the lack of experimental data in the high-energy region requires new experimental data with a simplified shielding structure.

For high-energy neutrons, a liquid scintillator and a Bonner sphere spectrometer (BSS) are widely used as measurement methods. The scintillator has an energy response of up to a few hundred MeV, but the efficiency decreases with neutron energy. In order to detect high-energy neutron, mostly a larger volume detector is used. This requires to increase the detection threshold to avoid large counting rate, resulting in the rejection of lower energy neutrons. On the other hand, the BSS has a wide energy response from thermal up to 20 MeV. To extend the upper energy range up to a few hundred MeV, concentric spherical shells of copper and lead are used to add (n, xn) reactions in the higher energy region. However, the BSS cannot provide the neutron energy spectrum without an initial guess spectrum.

In this study, with the use of the unfolding method, we experimentally derived the neutron energy spectra, including high-energy neutrons above 10 MeV, obtained by two measurement methods under the identical shielding configuration. The neutron spectra were measured by using different shielding materials of concrete and steel. The initial guess neutron spectra were derived using the Monte Carlo code, PHITS [2], by introducing each shielding condition.

2 Experiment

2.1 CHARM Facility

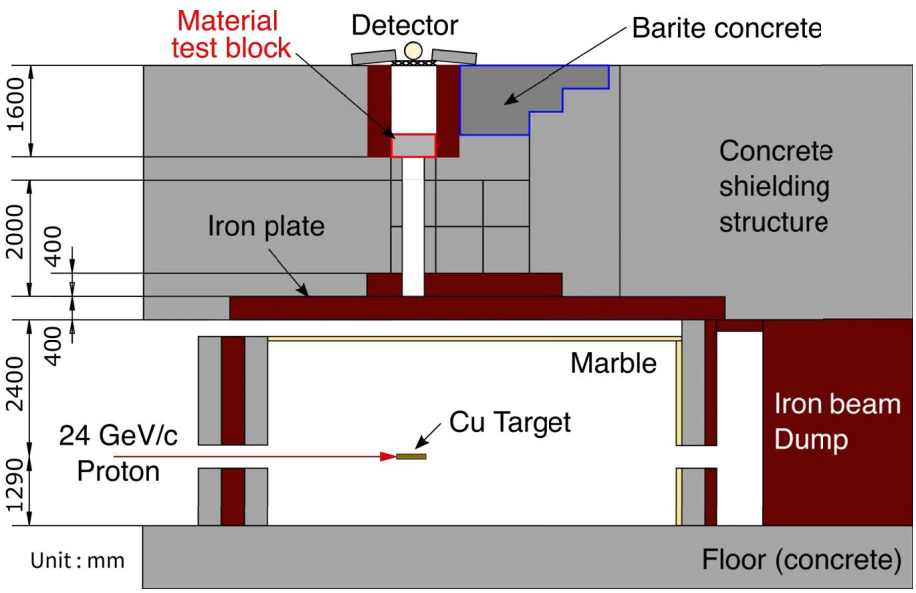

Figure 1: Schematic cross-sectional view of the CHARM facility.

Figure 1 shows an example of the experimental setup for concrete 40 cm in thickness of the CHARM facility in the east hall of CERN.

The facility received pulsed 24 GeV/c proton beam from the CERN proton synchrotron (PS) with an intensity of 1×10^9 to 5×10^{11} protons per pulse and a pulse length of 350 ms. The protons hit a cylindrical copper target of 8 cm in diameter and 50 cm in length in the irradiation room. The protons passing through the target were stopped by an iron beam dump. The irradiation room was surrounded by concrete and iron shield, except for the beam path and the entrance. The beamline was 129 cm in height from the floor. The bulk shielding structure above the ceiling of the irradiation room consisted of a 10-cm-thick marble, a 40-cm-

thick iron slab, and concrete blocks with a total thickness of 360 cm. In the direction above the target, a hole duct called material test location is created (see Fig. 1). Here, one can freely configure any shielding materials made of concrete and steel. The neutron detectors were placed on the top position of the material test location by using metal grating. Densities of concrete, barite concrete, iron, and marble materials are 2.4, 3.35, 7.2, and 2.71 g/cm^3, respectively. The experimental setup for the steel with 40 cm was obtained by replacing concrete blocks shown in figure 1. The concrete and steel blocks have cross-sections with 77.2 cm × 77.2 cm and 78 cm × 78 cm, respectively. The densities of concrete and steel blocks used as material test blocks were 2.23 g/cm^3 and 7.77 g/cm^3.

2.2 Neutron detector

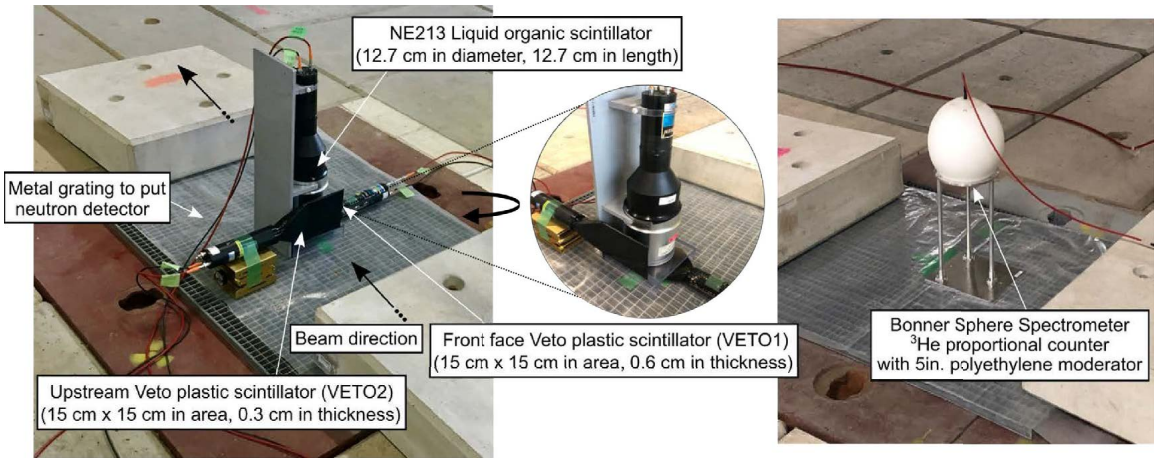

Figure 2: Picture of neutron detector set-up. The liquid scintillator (Left) and the Bonner sphere spectrometer (Right) were installed as the neutron detector. Two concrete blocks with 20-cm-thickness were used to fix the metal grating.

Neutrons were measured using the neutron detectors, an NE213 liquid organic scintillator and a BSS, placed on a metal grating positioned on the top roof. A picture of the detectors is presented in figure 2. The liquid scintillator was filled in a cylindrical-shaped aluminum container 12.7 cm in both diameter and length. The scintillator was supported by an acrylic structure, at 5 cm above the surface of the metal grating. In the 5 cm space beneath the NE213 detector, an NE102A plastic scintillator of dimensions 15 × 15 × 0.6 cm was inserted as a VETO detector (VETO1) to remove charged particle events. Another NE102A plastic scintillator of dimensions 15 × 15 × 0.3 cm surrounded the NE213 detector as an additional VETO detector (VETO2). The BSS consisted of a ^{3}He spherical proportional counter and 7 types of moderator. The moderators were a spherical shape that was made of polyethylene (PE, 0.95 g/cm^3) with diameters of 3 inch, 4 inch, 5 inch, 7 inch, 9.5 inch, and 2 types of polyethylene with inner metal shells. The polyethylene with inner metal shell has 3 layers with 4-inch-diameter PE sphere and 5-inch-diameter inner metal shell (Cu or Pb), and 7-inch-diameter PE shell. The BSS was placed at 40 cm (to the detector center) from the top surface of the metal grating using an aluminum supporting frame.

Output signals from the neutron detectors were fed to a data acquisition system consisting of standard NIM and VME modules. The signals of BSS are passed through a pre-amplifier and an amplifier. The number of ^{3}He(n,p)T reactions was recorded from pulse height spectra for each moderator. On the other hand, data of QDC values of the scintillator, and two veto detectors were recorded event-by-event.

3 Data Analysis - Unfolding method

3.1 Liquid Scintillator

Analysis on the experimental data obtained by the scintillator is basically the same as the previous study [1]. Only a brief data analysis is described in this section. The data were processed by the following procedures prior to spectrum unfolding: 1) extraction of neutron events through event selections; 2) calibration of the channel to light output. After these procedures, the light output distributions for the neutron events could be obtained.

Figure 3(a) shows examples of response functions for the scintillator. The response function was obtained using a SCINFUL-QMD [3], which was modified by Kajimoto et al. [4]. Source neutrons were isotopically emitted to the surface of the scintillator. The neutron energy region between 0 and 1 GeV was divided into 200 steps in a linear interval. A tally with the same shape and size as the scintillator used in the experiment was applied to the calculation. With the response functions, the neutron energy spectra were derived by unfolding method using an iterative Bayesian algorithm [5] in the RooUnfold package [6].

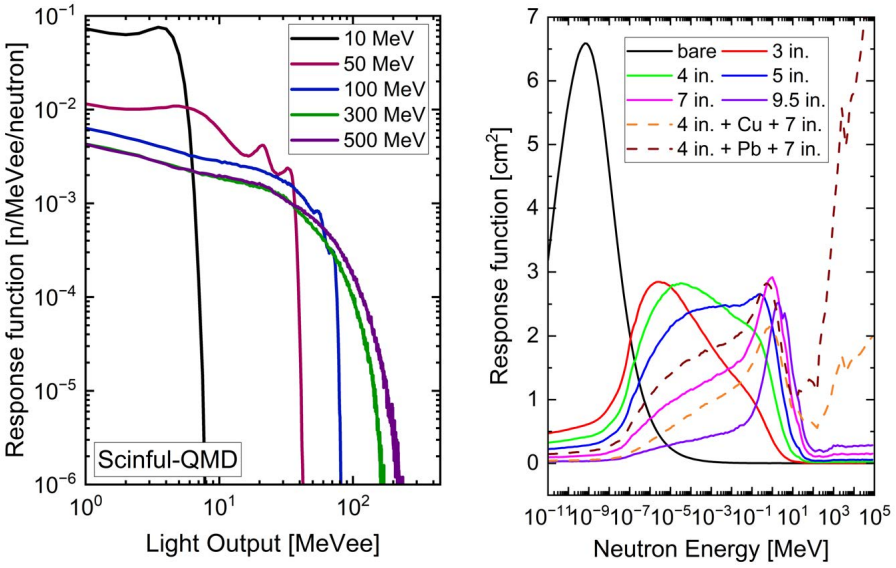

(a) Response functions of the scintillator (b) Response functions of the BSS [7]

Figure 3: Calculated neutron response functions.

3.2 Bonner Sphere Spectrometer

Figure 3(b) shows the response function of BSS for conditions of bare, five polyethylene moderators, and two polyethylene with inner metal shell moderators [7]. The response function was obtained using the MCNP6.2 Monte Carlo code [8] in the energy range from 10^{-11} to 10^{5} MeV. The JENDL4-HE library was used for the neutron energy range below 150 MeV. Above 150 MeV, the MCNP6.2 default physics model was used in the simulation. The geometry was identical to the detailed structure of the facility. Neutron energy spectra were obtained from its response function and initial guesses by using unfolding code, MAXED [9]. Initial guesses of neutron energy spectra for unfolding were calculated by the PHITS code (ver. 3.28) [2] using the default nuclear data library and physical model.

4 Result and Discussion

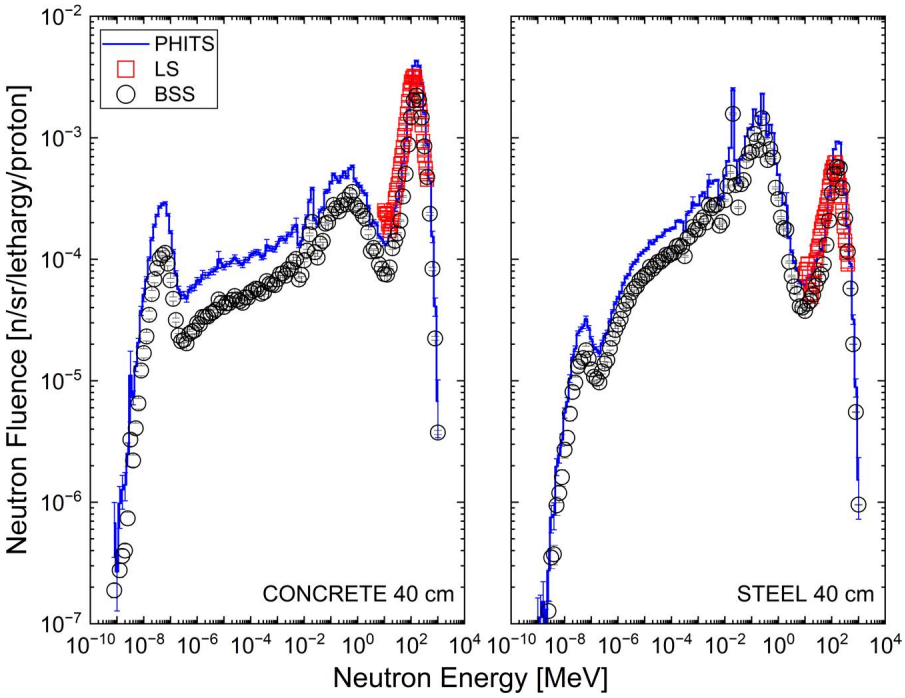

Figure 4: Comparison of experimental results of neutron spectra for same thickness between different materials of concrete and steel and calculations results.

Figure 4 shows the experimental neutron spectra obtained by the liquid scintillator and the BSS. The experimental data from the scintillator were obtained from 10 to 400 MeV. The experimental one from the BSS and calculation results (initial guesses) were obtained in the energy region from 10^{-10} to 10^{4} MeV. Statistical uncertainties were only displayed. The spectra were different for the same thickness of 40-cm-thick between different materials of concrete and steel. For the BSS, the initial guesses, which are the same as calculation results, overestimate the unfolded spectra. However, the shape of unfolded spectra for the BSS has a good agreement with the initial guesses. This means that the initial one is a critical part of the unfolding process and can affect the shape of the final results.

Figure 5 shows the detailed comparison of experimental results and calculation ones. The experimental data from the BSS were interpolated into the same energy interval for the liquid scintillator. The results between the liquid scintillator and the BSS are different within the factors of 3.5 for concrete and 2.5 for steel in the energy region from 10 to 400 MeV. The experimental data from the liquid scintillator tend to overestimate the experimental one from the BSS for the energy region below 150 MeV. Above 150 MeV, this trend is reserved.

5 Summary

In this study, experimental measurements were conducted on the spectra of neutrons that penetrate concrete and steel shields, when a proton beam of 24 GeV/c was incident on a copper target at the CHARM facility in the East Hall of the CERN Proton Synchrotron. The neutron spectra were measured to compare results obtained by the liquid scintillator and the BSS. The neutron spectra were calculated using the PHITS Monte Carlo code with default data library and physics model under a detailed structure of the facility. The results between the liquid

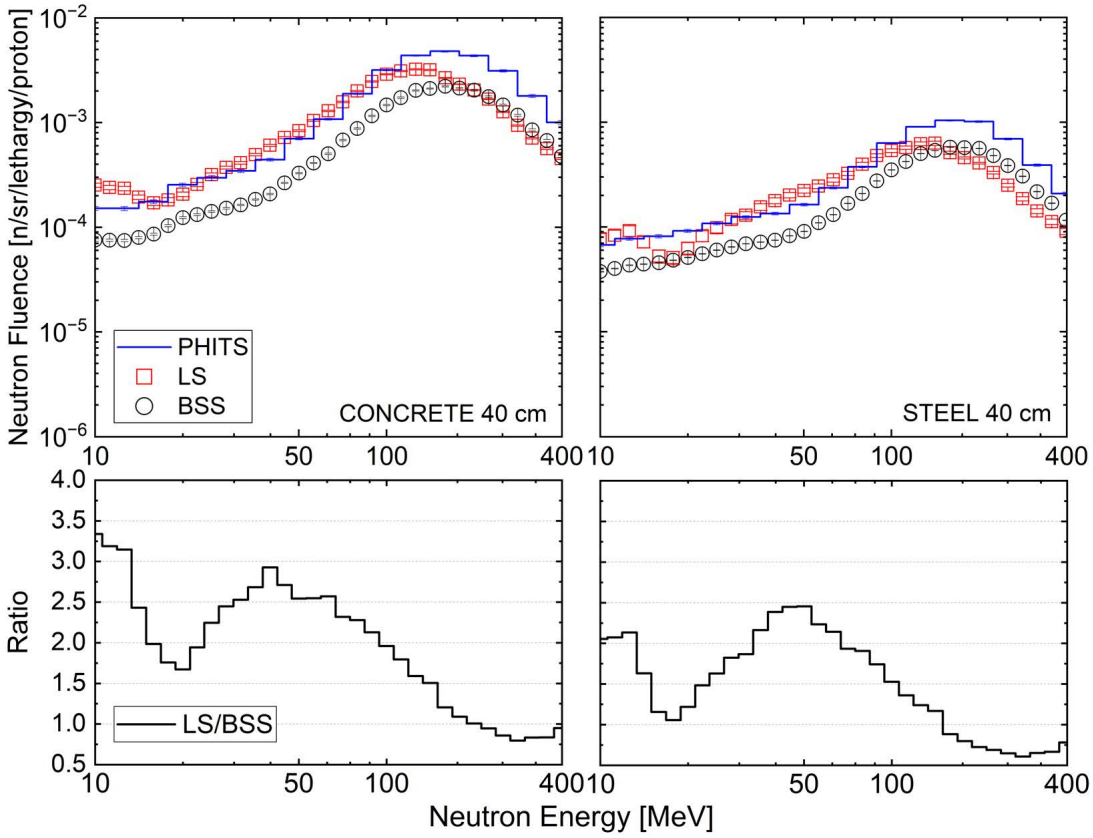

Figure 5: Comparison of experimental results of neutron spectra for the high-energy region above 10 MeV and its ratio.

scintillator and the BSS are different within the factors of 3.5 for concrete and 2.5 for steel in the energy region from 10 to 400 MeV.

References

[1] E. Lee, et al., Nucl. Instrum. Methods Phys. Res. A, 998, 165189 (2021).
[2] Y. Iwamoto, et al., J. Nucl. Sci. Technol. 59, 665-675 (2022).
[3] D. Satoh, et al., J. Nucl. Sci. Technol. 39, 657-660 (2002).
[4] T. Kajimoto, et al., Nucl. Instrum. Methods Phys. Res. A, 665, 80-89 (2011).
[5] G. D'Agostini, Nucl. Instrum. Methods Phys. Res. A, 362(2-3) 487-498 (1995).
[6] T. Adye, Proceedings of the PHYSTAT 2011 workshop on statistical issues related to discovery claims in search experiments and unfolding, 313-318 (2011).
[7] A. Masuda, et al., Nucl. Inst. Methods Phys. Res. A, 849, 94-101 (2017).
[8] C.J. Werner, et al., LA-UR-18-20808 (2018).
[9] M. Reginatto, et al., Nucl. Inst. Methods Phys. Res. A, 476, 242-246 (2002).

Acknowledgments

The authors would like to thank the participants of this experiment, the CERN Transport Group, the operation staff of the IRRAD and CHARM facilities, and the accelerator operators of the CERN Control Centre for their assistance in the experimental study.

10. New analytical model for momentum distribution on the spallation reaction in inverse kinematics

Riku Matsumura[†1, 2], Hideaki Otsu[1], He Wang[3], and Xiaohui Sun[4]

[1]RIKEN Nishina Center for Accelerator-Based Science, Saitama 351-0198, Japan
[2]Department of Physics, Saitama University, Saitama 338-8570, Japan
[3]RIKEN Cluster for Pioneering Research, Saitama 351-0198, Japan
[4]School of Science, Huzhou University, Zhejiang 313000, China
[†]Email: riku@ribf.riken.jp

We proposed a new analytical model that reproduces the momentum distribution of residual nuclei produced by the secondary beam, such as ^{90}Sr at 104 MeV/u, impinging on a target using an inverse reaction kinematics. It is expressed in a simpler form than the conventional ones and is found to reproduce an asymmetric tail that appear at the low momentum side. This will allow us to more precisely evaluate transmission efficiency of the produced residual nucleus through a dedicated in-flight separator, which is important for deriving the production cross sections.

1 Introduction

In general, when measuring reaction cross sections, it is not enough to just measure the yield after the reaction. The final result is obtained after several corrections, such as the beam transmission and the effect of the charge fluctuations when the beam passes through the detectors, and so on. As the beam transmission, i.e., the momentum/angular acceptance of the spectrometer, is evaluated, the momentum distribution on the dispersive focal plane becomes important. The shape of the longitudinal momentum distribution is known to be asymmetric during projectile fragmentation reaction at the lower incident energy as shown in Fig. 1.

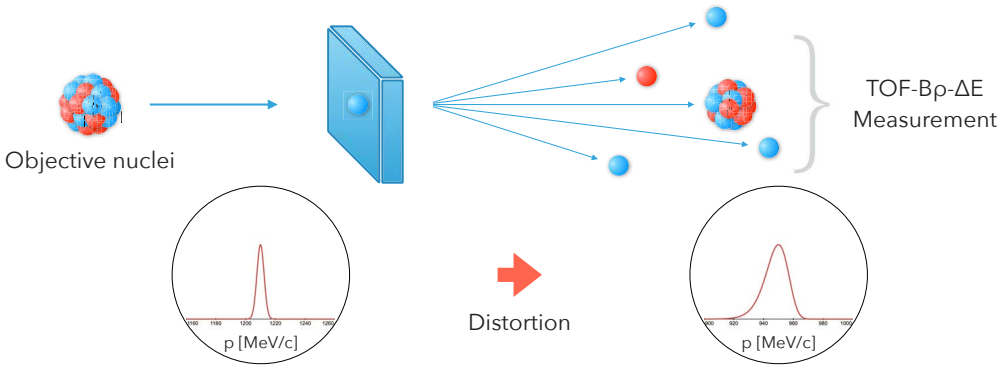

Figure 1: Schematic illustration of the spallation reaction and the associated distorted momentum distribution using the inverse kinematics method.

Reference [1] theoretically considers that the tail on the low momentum side is due to the momentum shift of the outgoing two nucleons inside an attractive potential caused by the residual nucleus. And the cutoff on the high momentum side is due to the phase volume effect reflecting the energy and

momentum conservation. One of the models to reproduce such a momentum distribution is the Goldhaber equation [2]. The width of the momentum distribution σ is defined by

$$\sigma = \sigma_0 \sqrt{\frac{K(A-K)}{A-1}}, \tag{1}$$

where A is the mass number of the projectile, K is the mass number of the spallation-reaction product, and σ_0 is known to be about 90 MeV/c. Refs. [3, 4] states that while the high momentum side is mostly reproduced in Eq. (1), the tail on the low momentum side is a problem.

Therefore, Tarazov [5] introduced the following asymmetric coefficient,

$$\alpha = \frac{\sigma_{\mathrm{low}}}{\sigma} - 1 = 1 - \frac{\sigma_{\mathrm{high}}}{\sigma}, \tag{2}$$

which reproduces the different widths of the left and right sides of the momentum distribution. In LISE^{++} [6], the σ given by the model in Refs. [2, 7, 8] is used. Note that this value has been exper-imentally verified to be acceptable up to 30% according to Ref. [4]. However, it is difficult to understand why the division into cases is required to reproduce a single physical quantity. Thus, we attempted to devise a new analytical model.

2 Experiment

The series of experiments [9–12] were performed at the RIKEN Radioactive Isotope Beam Factory (RIBF) by using the RIKEN Projectile-fragment Separator (BigRIPS) [13] and the ZeroDegree Spectrometer (ZDS) [13]. An experimental setup is shown in Figure 2. The details of the experiment are given in Ref. [10]. The secondary beam, including ^{90}Sr, was produced by in-flight fission of ^{238}U at 345 MeV/nucleon on a 3-mm thick ^{9}Be production target at the BigRIPS first stage. In the following second stage, the beam particles were selected and identified event-by-event using the TOF-$B\rho$-ΔE method [14].

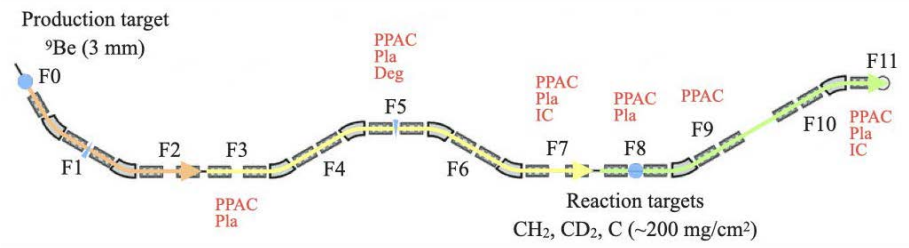

Figure 2: Schematic view of the RIKEN Projectile-fragment Separator (BigRIPS) and the ZeroDegree Spectrometer (ZDS).

The beam particles bombarded at 104 MeV/nucleon to CH_2 (179.2 mg/cm^2), CD_2 (218.2 mg/cm^2), and C (226.0 mg/cm^2) reaction targets, which placed at the entrance of the ZDS. The residual nuclei produced in reactions were identified in the ZDS with the same method as the BigRIPS. Because the momentum acceptance of the ZDS is limited to ±3 %, the experiment was carried out by using five different momentum settings ($\Delta(B\rho)/B\rho = -9$, -6, -3, 0, and $+3$ %) for each target to accept the wide range of mass-to-charge ratio A/Q. Figure 3 shows an example of particle identifications after selecting ^{90}Sr ($Z = 38$, $A/Q = 2.37$) for the projectile and the $\Delta(B\rho)/B\rho = -6$ % setting at the ZDS. The production cross sections for each isotopes were deduced from the number of each residual nuclei normalized by the number of incident secondary ^{90}Sr particles using the thickness of the targets. The backgrounds of carbon from CH_2 and CD_2 targets and beam-line materials were subtracted by using the empty and carbon target runs. Figure 3 right shows that momentum distributions (solid curves) using Eq. (1, 2) with parameters optimized for ^{86}Sr. This expression, however, can not reproduce the data for other residual nuclei. Thus, we need to create a new expression to describe momentum distribution with a simple formula.

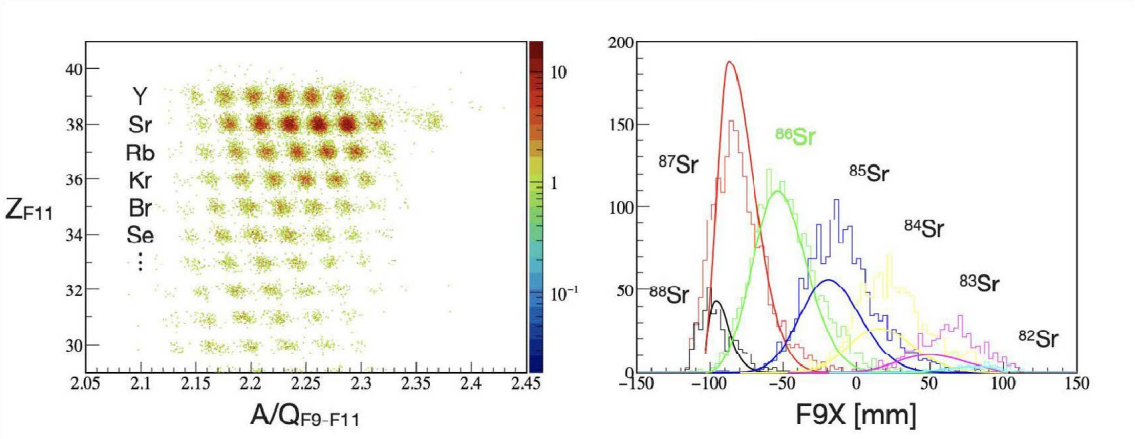

Figure 3: Left) Residual particle identifications at the ZDS. Right) Measured momentum distributions are compared with calculated ones when optimized for the ^{86}Sr spectrum.

3 New analytical model

In order to reproduce the momentum distribution of 104 MeV/u incident energy data, the newly devised model function is introduced as:

$$\sigma(p) = \sigma_0 + \alpha' (p - \mu), \tag{3}$$

where α' is a newly introduced parameter. This changes the σ of the Gaussian and produces asymmetry. The function is intuitive and easy to understand.

Behavior of the model

Figure 4 shows a momentum distribution after the reaction with the CH_2 target and the blue dot line are the fitting results using Eq. (3). It seems to reproduce the asymmetry well for all nuclides. The α' obtained from fitting ranged from 0.056 to 0.093.

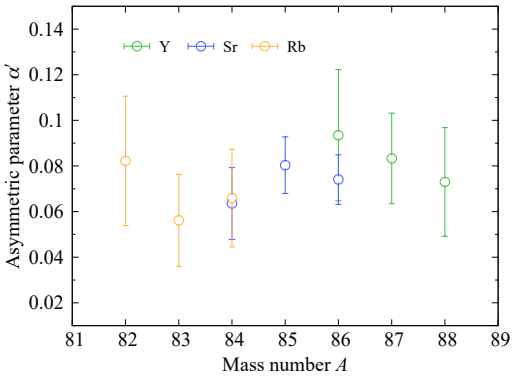

Figure 5: Asymmetric parameter α' obtained from the fitting shown in Fig. 4 plotted against mass number A.

This is actually one value that appears to have the possibility of being reproduced. Although there is some fluctuation for each nuclide, we obtained $\alpha' = 0.0738 \pm 0.0057$ using a weighted average. The result is overlaid on the red line in Fig. 4. The α' value is obtained from the data of CH_2 target, thus the parameter includes the effects of interaction both with carbon and hydrogen. Still, using the data of pure carbon target, we can extract the α' value for hydrogen target. Similarly, α' value for deuteron can be obtained. In addition, we would like to discuss whether this asymmetry is due to the reaction or simply to the energy loss, based on experimental data.

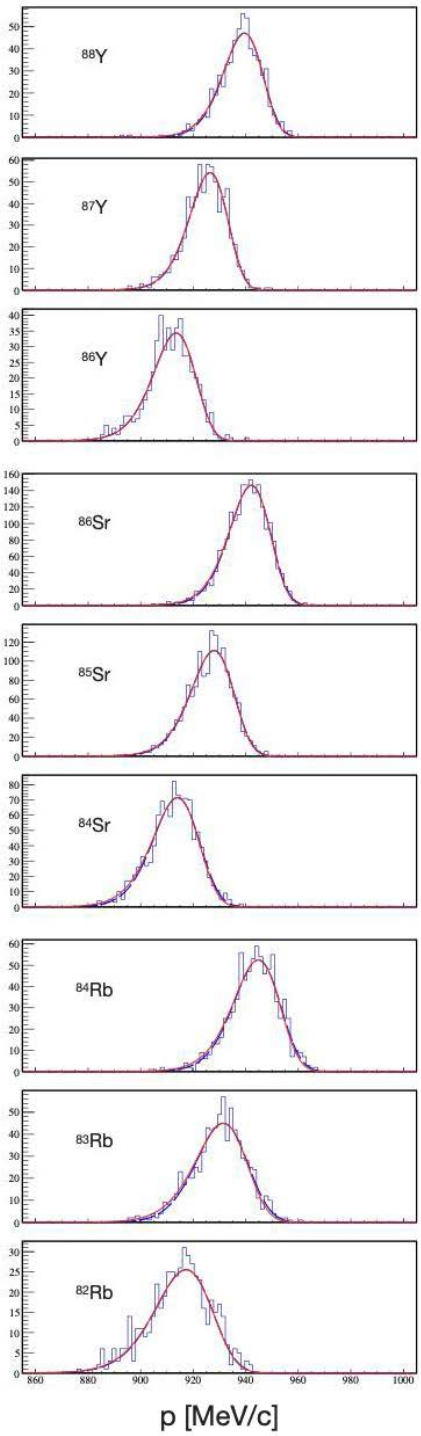

Figure 4: Momentum distributions calculated by Eq. (3) with $\alpha' = 0.0738$ for residual nuclei with $Z = Z_{\mathrm{proj}}(38) \pm 1$.

Advanced approach

Even for particles that are somewhat cutoff by the momentum acceptance of the spectrometer, the central and sigma value of momentum can be inferred from other nuclides with full acceptance because of its linearity, and the yield can be reproduced to a certain extent. If only the rise on one side could be determined, the original momentum distribution might be reproduced. This is measured with five patterns of magnetic field settings as described in Chap. 2, which leads to a reduction of statistical errors for particles in overlapping regions.

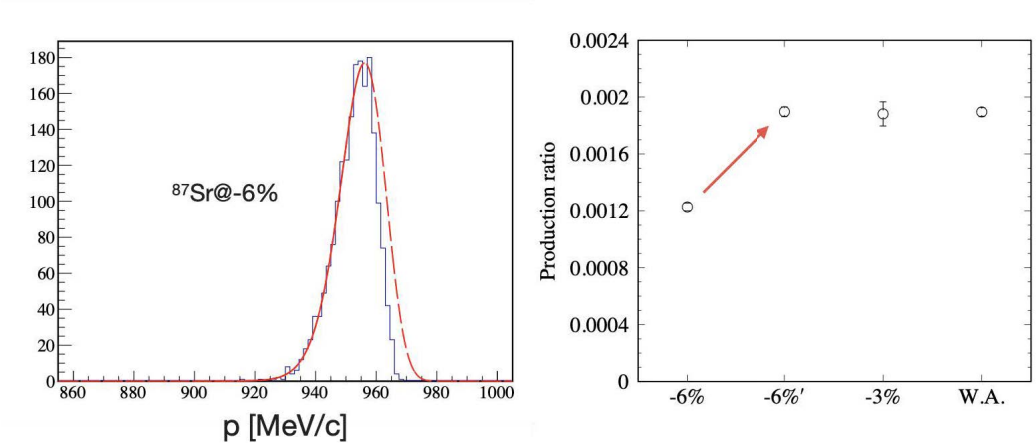

Figure 6: Left) As can be seen from Fig. 3 right, ^{87}Sr deviates slightly from the momentum acceptance, but the model function introduced this time can reproduce the original statistics. Right) The vertical axis is the production ratio, normalized by the number of incident ^{90}Sr beam.

We have counted its yield in the $\Delta(B\rho)/B\rho = -3\,\%$ setting, where ^{87}Sr is definitely within the momentum acceptance, but by using this method, the yield in the $\Delta(B\rho)/B\rho = -6\,\%$ setting is found to agree within the error.

4 Conclusion

We devised a new analytical model to reproduce the momentum distribution. In spite of the simplicity of the function, in contrast to the conventional method, the proposed expression can well reproduce the distribution with higher accuracy. The value of α' is almost constant within the error, and the introduction of one value is sufficient to reproduce the momentum distribution of the isotope in this incident energy region. Note that this value may only be dominant for C within CH_2, so we are considering a method to extract the momentum component of only H by some method such as subtraction. In the future, we plan to analyze the energy dependence of α' at other energies, as it may be an important physical quantity involved in the reaction.

Acknowledgments

We are grateful to the accelerator staff of the RIKEN Nishina Center for providing a high-quality ^{238}U beam. This work was supported by RIKEN Junior Research Associate Program.

References

[1] K. Ogata *et al.*, "Asymmetry of the parallel momentum distribution of (p, pN) reaction residues", Phys. Rev. C **92**, 034616 (2015).

[2] A.S. Goldhaber, "Statistical models of fragmentation processes", Phys. Lett. B **53**, 306 (1974).

[3] M. Notani *et al.*, "Projectile fragmentation reactions and production of nuclei near the neutron drip-line", Phys. Rev. C **76**, 044605 (2007).

[4] S. Momota *et al.*, "Momentum peak shift and width of longitudinal momentum distribution of projectilelike fragments produced at E = 290 MeV/nucleon", Phys. Rev. C **97**, 044604 (2018).

[5] O.B. Tarasov, "Analysis of momentum distributions of projectile fragmentation products", Nucl. Phys. A **734**, 536 (2004).

[6] O.B. Tarasov *et al.*, "LISE++: Radioactive beam production with in-flight separators", Nucl. Instrum. Meth. B **266**, 4657 (2008).

[7] D.J. Morrissey, "Systematics of momentum distributions from reactions with relativistic ions", Phys. Rev. C **39**, 460 (1989).

[8] W.A. Friedman, "Heavy ion projectile fragmentation: A reexamination", Phys. Rev. C **27**, 569 (1983).

[9] H. Wang *et al.*, "Spallation reaction study for fission products in nuclear waste: Cross section measurements for ^{137}Cs and ^{90}Sr on proton and deuteron", Phys. Lett. B **754**, 104 (2016).

[10] S. Kawase *et al.*, "Study of proton and deuteron induced spallation reactions on the long-lived fission product ^{93}Zr at 105 MeV/nucleon in inverse kinematics", Prog. Theor. Exp. Phys. **2017**, 093D03 (2017).

[11] K. Nakano *et al.*, "Isotope production in proton-, deuteron-, and carbon-induced reactions on ^{93}Nb at 113 MeV/nucleon", Phys. Rev. C **100**, 044605 (2019).

[12] X.H. Sun *et al.*, "Spallation and fragmentation cross sections for 168 MeV/nucleon ^{136}Xe ions on proton, deuteron, and carbon targets", Phys. Rev. C **101**, 064623 (2020).

[13] T. Kubo *et al.*, "BigRIPS separator and ZeroDegree spectrometer at RIKEN RI Beam Factory", Prog. Theor. Exp. Phys. **2012**, 03C003 (2012).

[14] N. Fukuda *et al.*, "Identification and separation of radioactive isotope beams by the BigRIPS separator at the RIKEN RI Beam Factory", Nucl. Instrum. Meth. B **317**, 323 (2013).

11. Neutron Capture Cross Section Measurement of ^{129}I and ^{127}I using ANNRI at MLF/J-PARC

Gerard ROVIRA[†1], Atsushi KIMURA[1], Shoji NAKAMURA[1], Shunsuke ENDO[1], Osamu IWAMOTO[1], Nobuyuki IWAMOTO[1], Yosuke TOH[1], Mariko SEGAWA[1], Makoto MAEDA[1], and Tatsuya KATABUCHI[2]

[1]Nuclear Science and Engineering Center, Japan Atomic Energy Agency, Ibaraki, Japan
[2]Laboratory for Zero-Carbon Energy, Tokyo Institute of Technology, Tokyo, Japan
[†]Email: gerard.rovira@jaea.go.jp

Abstract

Neutron capture cross section measurements for ^{129}I and ^{127}I have been conducted at the Accurate Neutron-Nucleus Reaction measurement Instrument (ANNRI) of the Materials and Life science Facility (MLF) in the Japan Proton Accelerator Research Complex (J-PARC). Neutron time-of-flight experiments were performed to determine the cross sections of ^{129}I from 10 eV to 1 keV and of ^{127}I from 0.01 eV to 1 keV. For ^{127}I, the present preliminary results agree within uncertainties with JENDL-5. In the case of ^{129}I, 16 s-wave resonances could be confirmed and their cross sections were found to be comparable with those of JENDL-5.

1 Introduction

Reducing the long-term accumulation of high-level nuclear waste (HLW), mainly constituted by minor actinides (MAs) and long-lived fission products (LLFPs), is one of the most important challenges regarding the management of nuclear waste. To achieve this goal, nuclear transmutation has been proposed to convert the HLW into short-lived nuclei. While the main focus is on the development of Accelerator-Driven Systems (ADS), a transmutation facility for MAs, several solutions have been proposed for LLFPs involving the use of nuclear reactors [1, 2]. For LLFPs, nuclear transmutation can only be achieved through the neutron capture reaction, meaning that an accurate characterization of the neutron capture cross section is of the utmost importance. Moreover, for the majority of LLFPs such as ^{129}I, ^{126}Sn, ^{93}Zr and ^{79}Se, in most of the neutron energy region between thermal to keV energies, neutron capture cross sections have scarcely been measured. Hence, to accurately predict nuclear characteristics in transmutation reactors for LLFPs, further experiments are required to extend the present knowledge of the capture reaction of LLFPs from the thermal to keV neutron energies.

Iodine-129, a LLFP with a 15.7 million years half-life, is one of the targets for transmutation due to the fact that it is soluble and has low absorption to underground materials, which causes problems in long-term geological disposals compared to other LLFPs [2]. Being soluble also makes the handling of ^{129}I complicated, which is one of the main reasons why the experimental data for the neutron capture cross section of ^{129}I is so scarce. Only two experimental data sets using the time-of-flight (TOF) method are available, those of Noguere *et al.* [3] and Macklin [4], which cover the neutron energy range from about 1.6 and 72 eV, respectively. These data are

complemented by several other experimental data at the thermal energy using the activation method [5, 6, 7, 8, 9].

In the present work, preliminary results of the neutron capture cross section of ^{129}I from 10 eV to 1 keV measured at the Accurate Neutron-Nucleus Reaction measurement Instrument (ANNRI) of the Materials and Life science experimental Facility (MLF) in the Japan Proton Accelerator Research Complex (J-PARC) are presented. Moreover, since the ^{129}I sample con-tained about 15.4% in mass concentration of ^{127}I, the neutron capture cross section of ^{127}I was also measured using a separate sample with 100% abundance of ^{127}I and preliminary results are also included.

2 Experimental Setup

The experiments were performed at the ANNRI beamline of the MLF facility in J-PARC. Pulsed neutrons were generated by the Japanese Spallation Neutron Source (JSNS) in MLF using the 3 GeV protons of the J-PARC facility, in which the protons were shot in double-bunch mode every 40 ms and with a beam power of about 700 kW at the time of the experiment. In the experiments, prompt capture γ-rays were detected using a NaI(Tl) detector installed in the experimental area 2 of the ANNRI beamline. The NaI(Tl) detector was situated at a 90° angle with respect to the neutron beam axis and a neutron flight path of 27.9 m. Further information about the time-of-flight experimental setup can be found elsewhere [12].

The ^{129}I sample employed in this experiment amounted to 404(1) mg in mass, with a 20 mm diameter and a 4.1 mm thickness. This sample contained ^{129}I with an isotopic abundance of 84.6% alongside 15.4% of ^{127}I, in the form of sodium iodide (NaI) and encapsulated in a Ti case with a 30 min diameter and 0.4 mm-thick walls. A thorough sample analysis performed by Segawa *et al.* [11] determined that the sample had been damaged and contained an empty space amounting to approximately 17%. Hence, in the present experiment, to avoid irradiating the empty space in the sample, the smaller neutron collimator of 7 mm in diameter was employed. A dummy sample replica of the Ti case was used to derive the sample-dependent background induced by the Ti case. However, the dummy sample contained the same amount of NaI to that in the ^{129}I sample but with a 100% isotopic concentration of ^{127}I, meaning that the dummy sample contained 6.5 times more ^{127}I compared to the ^{129}I sample. Moreover, to measure the neutron capture cross section of ^{127}I and, at the same time, to accurately determine the effects of ^{127}I in both the ^{129}I and dummy samples, an ^{127}I sample with a mass of 562.7(1) mg with a 100% isotopic abundance of ^{127}I was also measured in the present experiments. The incident neutron flux was derived with a boron sample enriched with ^{10}B up to 90% with a diameter of 10 mm and a thickness of 0.5 mm. The ^{10}B(n, α)^{7}Li reaction emits a lone γ-ray with the energy of 478 keV, making events from this reaction easy to isolate. An ^{197}Au sample with a mass of 609.7(1) mg, a diameter of 20 mm and a thickness of 0.1 mm was employed to normalize the neutron capture cross section results using the saturated resonance technique. Finally, the sample-dependent backgrounds due to scattered neutrons for the ^{129}I, ^{127}I, boron and ^{197}Au samples were determined by using a carbon sample.

3 Data Analysis

The experimental results were analyzed offline by means of the pulse-height weighting technique (PHWT) [10]. The ^{129}I and ^{127}I neutron capture yields were derived by applying the PHWT and a weighting function that takes into account the sample characteristics and detector efficiencies. In the present work, the weighting functions for the ^{129}I and ^{127}I samples were obtained with Monte-Carlo simulations with the SG code [13].

3.1 Neutron Flux

The shape of the incident neutron flux was derived by gating the 478 keV γ-rays emitted from the ^{10}B(n, α)^{7}Li reaction measured with the boron sample, after removing the energy-dependent influence of the ^{10}B(n, α)^{7}Li reaction rate using the Monte-Carlo code PHITS [14]. The incident neutron flux from 10 meV to 1 keV determined in the present experiment is shown in Fig. 1.

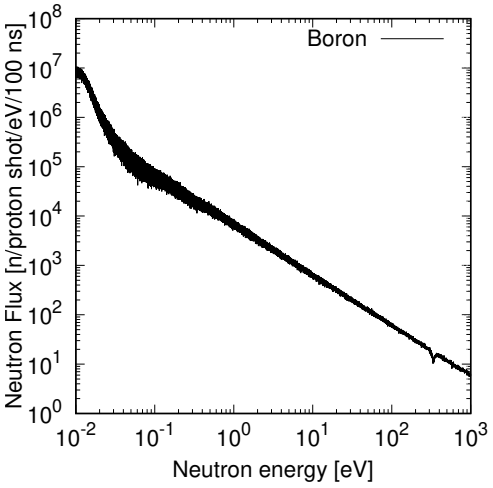

Figure 1: Incident neutron flux from 10 meV to 1 keV.

3.2 Background Subtraction

In order to accurately isolate the quantities of interest in the present experiment, namely the the neutron capture yields of the ^{129}I and ^{127}I samples, several layers of detrimental background and noise had to be removed.

For the case of the ^{127}I sample, the background was constituted by the sample-dependent background, mainly caused by neutrons being scattered at the ^{127}I sample, and the sample-independent background. As mentioned in section 2, the carbon sample was employed to estimate the contribution of the events caused by neutrons scattered at the measured samples. This is a commonly used technique since the neutron elastic scattering is the dominant reaction in carbon and has a flat energy-dependence up to 500 keV. Hence, the neutron capture yield of the ^{127}I sample was obtained by removing the sample-dependent background, using the carbon sample measurement and taking into account the relative differences in both mass and cross section between ^{127}I and carbon, and the sample-independent background with a "blank" measurement in the no-sample condition.

For the ^{129}I sample, however, the situation was much more complicated. Since the amount of ^{127}I in the ^{129}I sample was not equal to that in the dummy sample, the dummy sample could not be directly employed to remove the influence of the Ti case. Thus, the neutron capture yield of ^{127}I sample was utilized to remove the influence of the ^{127}I neutron capture events measured with the dummy sample and isolate the influence of the Ti case. This removal was performed together with corrections using the PHITS code to account for the influence of the Ti case that increased the neutron capture yield of ^{127}I in the resonance region, as can be clearly seen in Fig. 2. The events induced by the Ti case were then removed in the ^{129}I sample measurement using the dummy sample measurements, after removing the neutron capture yield of the ^{127}I sample. Moreover, the influence of ^{127}I, which was contained in the ^{129}I sample with a 15.4% isotopic abundance, was also removed using the neutron capture yield of the ^{127}I sample. Finally, in a

procedure analogous to the analysis of the ^{127}I sample, the sample-dependent background due to neutron scattered at the ^{129}I sample and the sample-independent background were removed using the carbon sample measurement and a no-sample measurement, respectively.

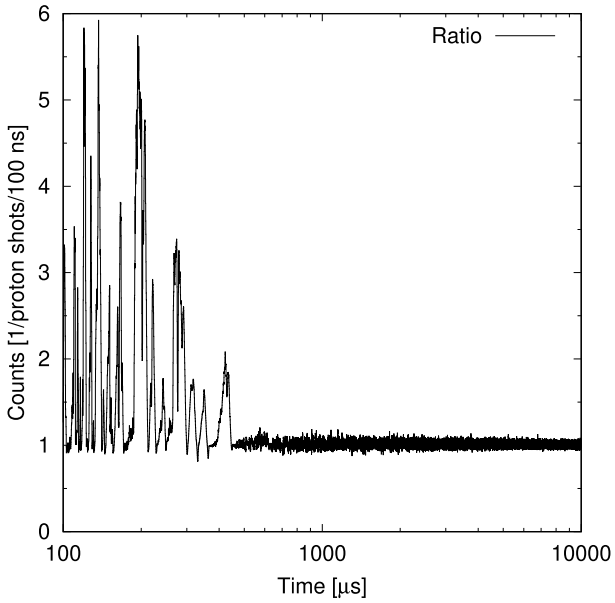

Figure 2: Simulated neutron capture yield ratio between the dummy and the ^{127}I samples in the TOF range between 100 μs and 10 ms, which is from 40 meV to 400 eV in neutron energy.

3.3 Cross Section Calculation

Preliminary results for the neutron capture cross section of ^{129}I and ^{127}I were determined by dividing the neutron capture yields, which were corrected from the self-shielding and multiple scattering effects using the PHITS code, by the incident neutron flux.

For both samples, the results were normalized using the saturate resonance technique with the ^{197}Au sample. The thickness of the ^{197}Au sample was 0.1 mm, enough for the first resonance to be completely saturated. By means of this technique, the neutron capture cross sections were determined as follows:

$$\sigma_I(E_n) = N_{sat}\frac{Y_I(E_n)C_I(E_n)}{\phi_n(E_n)S_I} \tag{1}$$

where $\sigma_I(E_n)$, $Y_I(E_n)$, $C_I(E_n)$, S_I and N_{sat} stand for the neutron capture cross section, neutron capture yield, the correction factor for self-shielding and multiple scattering, the area density, and the normalization factor, for either ^{129}I or ^{127}I, with $\phi_n(E_n)$ as the incident neutron flux. Moreover, for ^{129}I, the area density was corrected using the results found in a thorough analysis by Segawa *et al.* [11]

4 Preliminary Results

Preliminary results for the neutron capture cross sections of ^{129}I and ^{127}I were determined using the formulations explained in section 3.3. The neutron capture cross section of ^{127}I compared to the broadened data of JENDL-5 [15] are shown in Fig. 3. As can be seen, the present results agree within uncertainties with the results from JENDL-5.

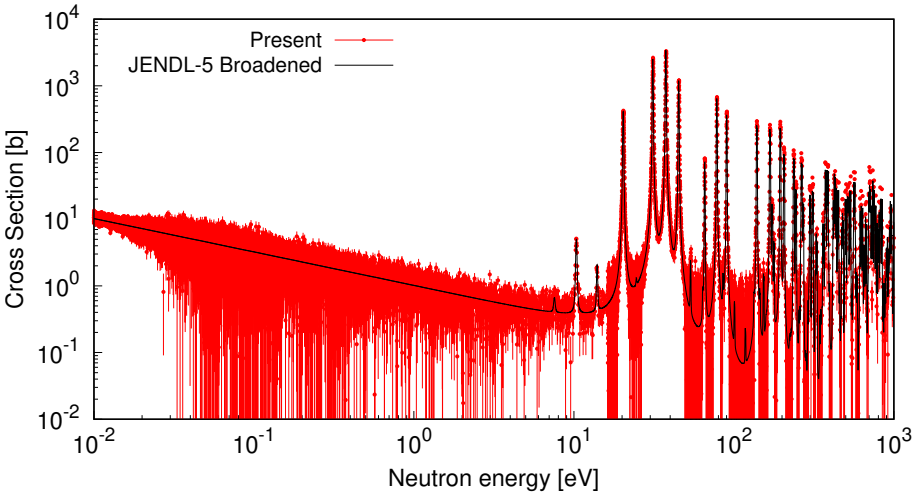

Figure 3: Preliminary results for the ^{127}I neutron capture cross section from 0.01 eV to 1 keV compared to the broadened data of JENDL-5.

For ^{129}I, the preliminary results are displayed in Fig. 4 in comparison to the data from JENDL-5. In the energy region between 10 eV and 1 keV, 16 s-wave resonances could be identified. Since most of the resonances for ^{129}I occur above 100 eV, these resonance appeared in a doublet structure due to the influence of the double-bunch mode. Nonetheless, the present data was found to be comparable with the cross section data of JENDL-5 once corrected with the resolution function of the ANNRI beamline. The resonance parameters of JENDL-5, except for those of negative resonances, were taken from the work of Noguere *et al.* [3], in which the resonance parameters were determined from a combined analysis of neutron capture yields and transmission data measured at the GELINA facility. Such consistency of cross sections between the present experiments and JENDL-5 indicates that the present data are reasonable with the data of Noguere et al., in spite of performing complicated subtractions of components of ^{127}I and Ti case from the yield data of the ^{129}I sample. Unfortunately, small resonances in JENDL-5 could not be confirmed due to a high background level around 5 b.

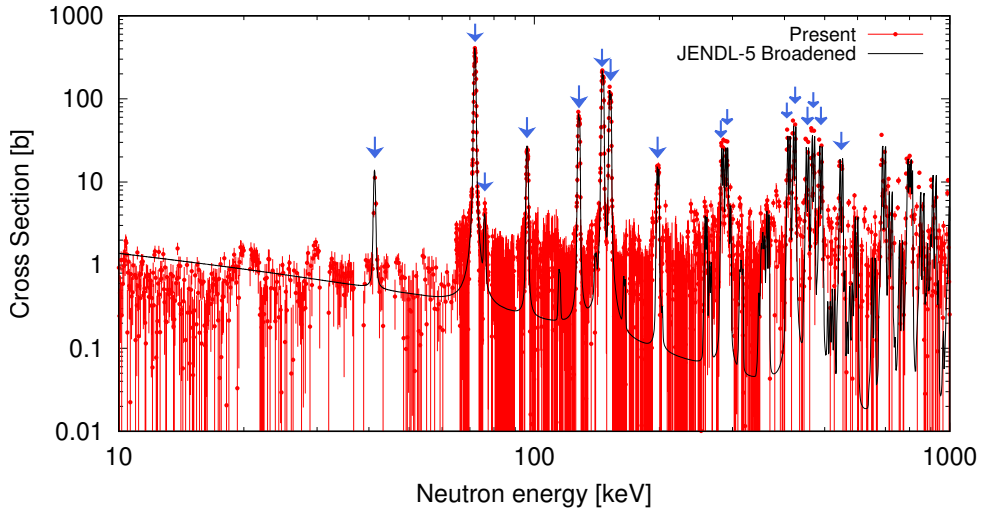

Figure 4: Preliminary results for the ^{129}I neutron capture cross section from 10 eV to 1 keV compared to the broadened data of JENDL-5.

5 Summary

The neutron capture cross sections of ^{129}I and ^{127}I were measured at the ANNRI beamline of MLF in J-PARC from 10 eV to 1 keV and from 0.01 eV to 1 keV, respectively. For ^{127}I, the present preliminary results provide agreement within uncertainties with the data in JENDL-5. In the case of ^{129}I, in the present preliminary results 16 s-wave resonance could be identified that are comparable with those of JENDL-5. The present data are expected to be consistent with the data of Noguere et al., performed at the GELINA experimental facility.

References

[1] Chiba S, Wakabashi T, Yoshiaki T, et al. Method to Reduce Long-lived Fission Products by Nuclear Transmutations with Fast Spectrum Reactors. Sci. Rep., 2017; 7:13961.

[2] Wakabayashi T, Tachi Y, Takahashi M, et al. Study on method to achieve high transmu-tation of LLFP using fast reactor. Sci. Rep., 2019; 9:2-12.

[3] Noguere G, Bouland O, Brusegan A, et al. Neutron capture and total cross sections of ^{127}I and ^{129}I. Phy. Rev. C, 2006; 74:054602.

[4] Macklin RL. Neutron Capture Cross Sections and Resonances of Iodine-127 and Iodine-129. Nucl. Sci. Eng., 1983; 85:350.

[5] Roy J and Wuschke D. Neutron Capture Cross Section of I-129 and I-130. Can. J. Chem., 1958; 36:1424-1430.

[6] Pattenden NJ. Neutron Cross Section Measurements on Fission Product Samarium and Iodine. Nucl. Sci. Eng., 1963; 17:371-380.

[7] Friedmann L and Aumann DC. The Thermal Neutron Cross-Sections and Resonance Inte-grals of ^{127}I, ^{128}I and ^{129}I. Radiochimica Acta, 1983; 33:183-187.

[8] Nakamura S, Harada H, Katoh T, and Ogata Y. Measurement of Thermal Neutron Capture Cross Section and Resonance Integral of the ^{129}I(n,γ)^{130}I Reaction. J. Nucl. Sci. Technol., 1996; 33:283-289.

[9] Belgya T, Bouland O, Noguere G, Plompen A, Schillebeeckx P and Szentmiklósi L. The thermal neutron capture cross section of ^{129}I. Proceedings of the international conference on nuclear data for science and technology, Nice 2007; 631.

[10] Moxon MC et al., A gamma-ray detector for neutron capture cross-section measurements. Nucl. Inst. and Meth., 1963. 24:445-455.

[11] Segawa M, Toh Y, Kai T, et al., Investigation of radioactive samples for neutron capture reaction measurements using energy-resolved neutron imaging, Ann. Nucl. Energ., 2022; 167:108828.

[12] Rovira G et al., Neutron capture cross-section measurement and resolved resonance analysis of ^{237}Np, J. Nucl. Sci. Technol. 2020; 57:24-39.

[13] Ohsaki T et al., An NaI(Tl) spectrometer system for keV neutron radiative-capture reac-tions. Nuc. Ins. and Meth. in Phys., A 1999; 425:302-319

[14] Sato T. et al., Features of Particle and Heavy Ion Transport Code System PHITS Version 3.02, J. Nucl. Sci. Technol. 2018; 55:684-690.

[15] Iwamoto O, Iwamoto N, Kunieda S, et al., Japanese evaluated nuclear data library version 5: JENDL-5, J. Nucl. Sci. Technol., 2023; 60:1-60.

12. Measurement of heavy nuclide production cross-section for ^{nat}Pb irradiated with several GeV protons

Kenta SUGIHARA[†*1], Shin-ichiro MEIGO[1], Hiroki IWAMOTO[1,2], and Fujio MAEKAWA[1]

[1]J-PARC Center, Japan Atomic Energy Agency, 2-4 Shirakata, Tokai-mura, Naka-gun, Ibaraki Pref. 319-1195, Japan

[2]Nuclear Science and Engineering Center, Japan Atomic Energy Agency, 2-4 Shirakata, Tokai-mura, Naka-gun, Ibaraki Pref. 319-1195, Japan

[†]Email: kenta.sugihara@kek.jp

Abstract

Nuclide production cross sections are fundamental to estimate the γ-ray dose rate. Thus, we started the cross section measurement via the reactions of GeV proton incidence on various targets. This paper presents the measured cross sections via the ^{nat}Pb(p,X) reactions. Comparisons among present data, calculated results, and evaluated nuclear data library are also reported.

1 Introduction

These days, various applications with neutrons are paid much attention, e.g., boron neutron capture therapy[1, 2] and accelerator-driven neutron source[3, 4, 5, 6]. Accelerator-Driven System (ADS)[7, 8, 9, 10] for the transmutation of nuclear waste is one example of such applications. In the design of the ADS facility, it is of great importance to ensure safety for radiation workers and neighbors. Thus, precise evaluation of the residual γ-ray dose rate by the reactions among primary protons, target of neutron production (Pb-Bi eutectic), the beam window, and accelerator components is required. The nuclide production cross section is key information to estimate the γ-ray dose rate. These days, nuclear reaction models such as Liège IntraNuclear Cascade (INCL)[11] followed by Generalized Evaporation Model (GEM)[12] in Particle and Heavy Ion Transport code System (PHITS)[13] and evaluated nuclear data libraries such as Japanese Evaluated Nuclear Data Library High Energy file 2007 (JENDL/HE-2007)[14] are utilized to derive the γ-ray dose rate. However, the prediction accuracy of the models should be confirmed in advance because the applicability of the models is not completely understood. There are references for the cross sections via the ^{nat}Pb(p,X) reaction with GeV proton incidence[15, 16]. In previous studies, monitor reactions were utilized to determine the intensity of the incident protons. Because the increase of uncertainty due to the monitor reactions was inevitable in previous studies, more precise measured data are desired currently.

*Present address: High Energy Accelerator Organization (KEK), Oho, Tsukuba, Ibaraki 305-0801, Japan and The Graduate University for Advanced Studies (SOKENDAI), Hayama, Kanagawa 240-0193, Japan

Then, we started a series of experiments at Japan Proton Accelerator Research Complex (J-PARC)[17, 18], where a high-precision current transformer with 2% uncertainty is equipped. In the past, the cross section with smaller uncertainties was successfully obtained using several GeV protons and Al, Ni, Zr, Mn, and Co[19, 20, 21] at J-PARC by means of the activation technique. Here, we measured the nuclide production cross sections with GeV protons and ^{nat}Pb which is used as the target of neutron production. This paper presents the heavy nuclide production cross sections via the ^{nat}Pb(p,X) reaction. In addition, present data were compared with the results by nuclear reaction models and JENDL/HE-2007 to confirm the prediction accuracy.

2 Experiment

Our experiment was carried out at a beam dump line[22, 23] near the extraction port from the 3 GeV Rapid Cycling Synchrotron (RCS)[22] at J-PARC. The vertical plane view is illustrated in Fig. 1. The experimental procedure, such as sample setting, proton beam irradiation, and γ-ray measurement of the activated samples, were followed in previous studies[19, 20, 21]. Due to the limited space, a procedure is explained briefly.

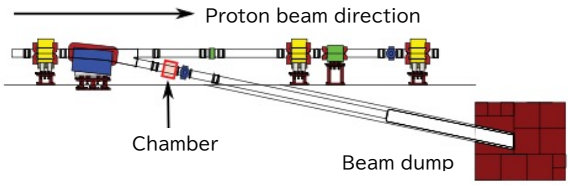

Figure 1: Vertical plane view of the beam dump line at J-PARC.

The proton beam was supplied from the RCS to ^{nat}Pb sample as shown in Fig. 1. The proton energies were 0.4, 1.3, 1.5, 2.2, and 3.0 GeV. For 0.4-, 1.5-, 3.0-GeV protons, the irradiation time and the incident particle number were applied to 75 seconds and 8.6×10^{13}, respectively. Those for 1.3- and 2.2-GeV protons were 100 seconds and 1.1×10^{14}, respectively.

The ^{nat}Pb targets were inserted in the place of "The chamber" in Fig. 1. The target foil, Al, Ce, Pb, and Al in order from upstream, were used for 0.4-, 1.5-, 3.0-GeV protons. For the case of 1.3- and 2.2-GeV protons, the Al, Si, Pb, and Al foil were applied. For both experiments, the size and weight of the Pb target was 25 mm $\times$ 25 mm $\times$ 0.22 mm and 1.4 g, respectively.

After the proton irradiation, the γ-ray spectra were obtained with High-Purity Ge (HPGe) detectors. The measured γ-ray spectrum for 3 GeV proton incidence on ^{nat}Pb is shown in Fig. 2. A variety of peaks were observed in Fig. 2.

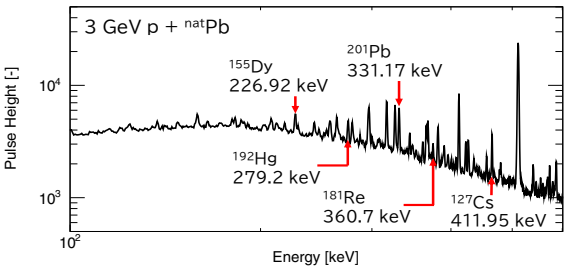

Figure 2: γ-ray spectra by the HPGe detector. The horizontal and vertical axes are γ-ray energy [keV] and pulse height of each γ-ray energy [-], respectively.

3 Results and Discussion

We let references[19, 20, 21] explain the way of data analysis due to the limited space. Heavy nuclides production cross sections obtained in this work are tabulated in Table 1. The statistical error, ambiguity of fitting parameter, projectile proton number, branching ratio of the γ-ray energy used in our analysis, and intensity of the standard γ-ray sources were taken into account as the total uncertainty of present data. In this study, we measured 49 cross sections of 12 nuclides and 5 proton energy points. For ^{192}Hg by 0.4-, 1.3-, 3.0-GeV proton incidence,

^{202m}Pb by 3.0-GeV proton incidence, and ^{203}Bi by 1.3-GeV proton incidence cross sections, the uncertainty about 9%, 13%, and 15%, respectively, are greater than that of the previous results by Yu. E. Titarenko *et al.*[15]. Therefore, we successfully acquired about 90% of the data with smaller uncertainty compared with preceding studies.

Table 1: Nuclide production cross sections of the reactions for ^{nat}Pb with 0.4-, 1.3-, 1.5-, 2.2-, and 3.0-GeV protons. Type "i" and "c" represent independent and cumulative cross sections, respectively. The branching ratio of used γ-ray energy (E_γ) is denoted in the parenthesis below each E_γ. The total uncertainty (1σ) is written in the parenthesis below each cross section.

Nuclide	E_γ [keV]	Type	$T_{1/2}$	Cross section (1σ Uncertainty) [mb]				
				0.4 GeV	1.3 GeV	1.5 GeV	2.2 GeV	3.0 GeV
^{206}Bi	803.1	c	6.243 d	6.20	3.18	3.00	-	3.44
	(99.0%)			(0.22)	(0.11)	(0.11)	-	(0.14)
^{205}Bi	1043.75	c	14.91 d	9.79	4.44	3.71	4.15	3.83
	(7.51%)			(0.37)	(0.19)	(0.14)	(0.32)	(0.51)
^{203}Bi	820.2	c	11.76 h	13.24	5.60	4.28	-	3.90
	(29.7%)			(0.94)	(0.84)	(0.23)	-	(0.29)
^{203}Pb	279.2	c	51.92 h	55.87	32.48	31.78	-	19.08
	(80.94%)			(1.89)	(1.51)	(1.35)	-	(1.18)
^{202m}Pb	786.99	i	3.54 h	17.74	12.45	10.84	9.59	8.73
	(49%)			(1.23)	(0.92)	(0.84)	(2.06)	(1.12)
^{201}Pb	331.17	c	9.33 h	55.59	24.27	22.87	-	14.26
	(77%)			(4.69)	(2.05)	(1.94)	-	(1.37)
^{200}Pb	147.63	c	21.5 h	53.14	20.12	-	-	-
	(38.2%)			(3.21)	(0.98)	-	-	-
^{202}Tl	439.51	c	12.31 d	23.57	16.96	16.80	18.73	13.09
	(91.5%)			(0.85)	(0.58)	(0.59)	(0.84)	(0.88)
^{201}Tl	167.43	c	3.0421 d	81.55	43.45	43.98	-	-
	(10.0%)			(2.95)	(1.59)	(1.52)	-	-
^{203}Hg	279.2	c	46.610 d	2.47	3.58	3.44	3.40	2.91
	(81.56%)			(0.08)	(0.12)	(0.15)	(0.27)	(0.09)
^{192}Hg	274.8	c	4.85 h	54.60	23.98	22.21	-	10.30
	(52%)			(4.56)	(2.02)	(1.86)	-	(1.16)
^{196}Au	355.73	i	6.1669 d	2.93	3.22	3.18	-	2.04
	(87%)			(0.14)	(0.15)	(0.153)	-	(0.15)

Figure 3 shows the excitation functions of ^{206}Bi, ^{203}Pb, ^{201}Pb, ^{202}Tl, ^{203}Hg, and ^{196}Au with INCL/GEM, JENDL/HE-2007, and preceding studies[15, 16, 24, 25, 26]. For overall trends, most of present data is consistent with the preceding results. For ^{206}Bi production, INCL/GEM shows better agreement with present data than JENDL/HE-2007. The average ratio of calculation to experiment (C/E) is 1.01. On the other hand, JENDL/HE-2007 shows an overestimation of the present data by 28% in average.

The chart for average C/E values between INCL/GEM and the present data is shown in Fig. 4. According to Fig. 4, better reproducibility or underestimation by roughly to be 30% is clearly seen for the production of Bi and Pb nuclides. On the contrary, overestimation by approximately twice is confirmed for Tl and Au nuclides production cross sections except for ^{201}Tl. INCL/GEM might have weakness in describing the reactions of several proton emissions compared with those of less than one proton emission. However, it should be noted that further investigation is required to acquire this evidence.

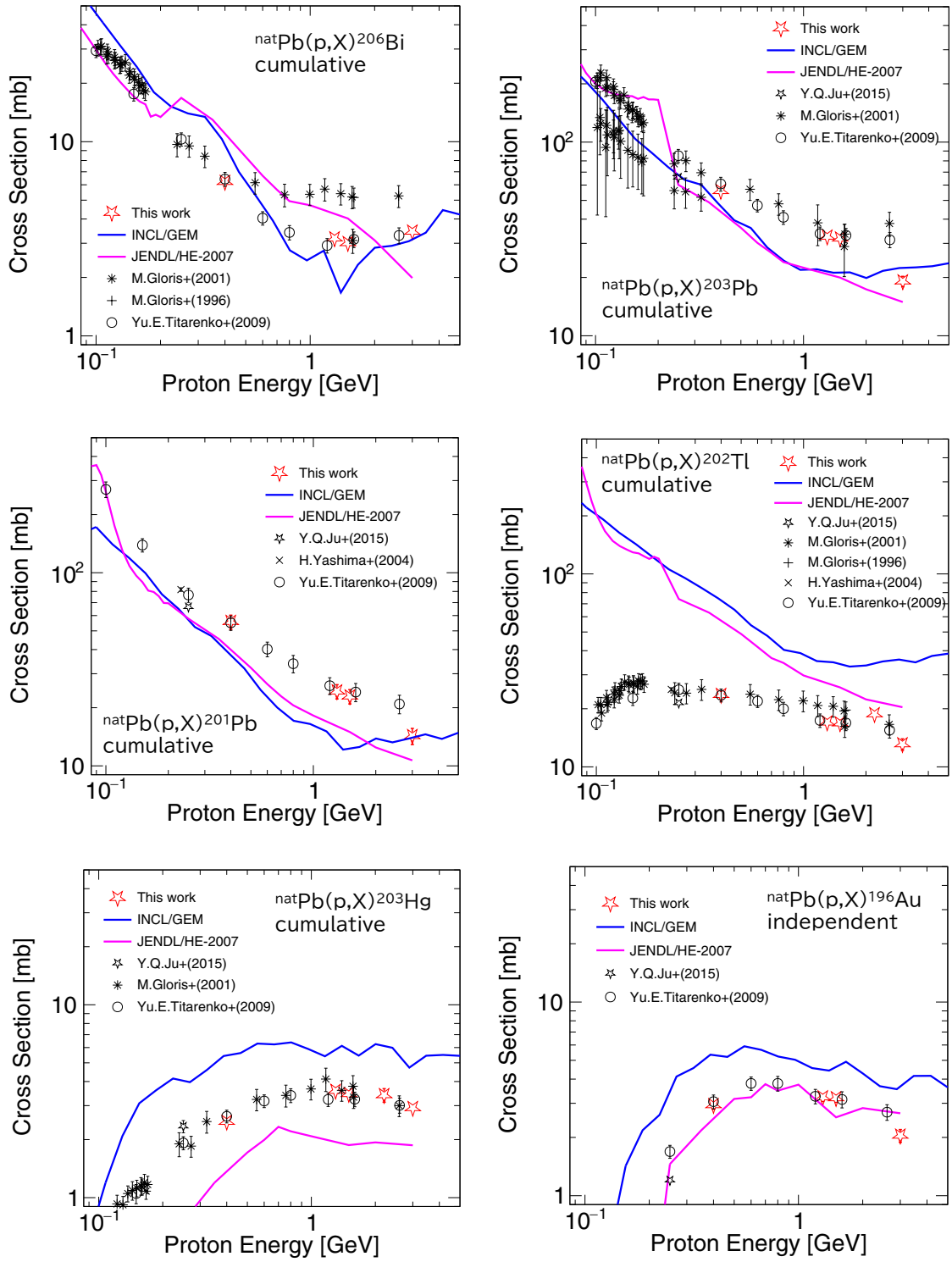

Figure 3: Excitation functions of ^{206}Bi, ^{203}Pb, ^{201}Pb, ^{202}Tl, ^{203}Hg, and ^{196}Au with INCL/GEM, JENDL/HE-2007, and previous results which are taken from EXFOR. The horizontal and vertical axes of all of the graphs represent the proton energy [GeV] and the nuclide production cross section [mb], respectively. The red and black markers stand for present data and preceding results, respectively. The blue and pink lines mean the results of INCL/GEM and JENDL/HE-2007, respectively.

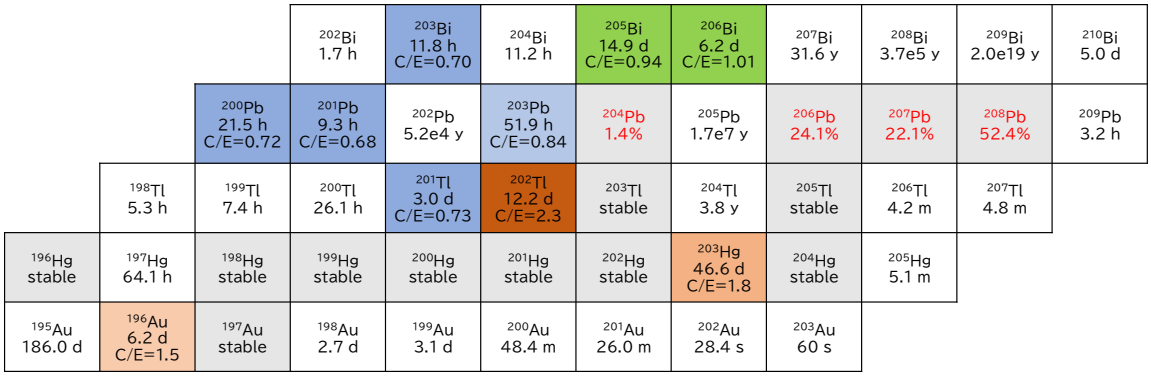

Figure 4: Chart for average C/E values between INCL/GEM and the present data. Red-, green-, and blue-filled boxes represent overestimation, better accuracy, and underestimation, respectively.

4 Conclusion

We measured heavy nuclides production cross sections via the ^{nat}Pb(p,X) reaction for 0.4-, 1.3-, 1.5-, 2.2-, and 3.0-GeV proton incidence at J-PARC. In this work, we successfully obtained the 49 nuclides production cross sections. The uncertainty of most of the present data was smaller than those in the preceding studies. Additionally, present data were compared with INCL/GEM and JENDL/HE-2007 to confirm the prediction accuracy. Through the comparison, it is absolutely found that they have room for improvement.

We will continue the data analysis for lighter nuclides production cross sections. Furthermore, we pursue the key to improve the prediction accuracy of nuclear reaction models.

References

[1] Kumada, H., *et al.*, Project for the development of the linac based NCT facility in University of Tsukuba: Appl. Radiat. Isotope, 88 (2014), pp. 211-215.

[2] Lee, C.L., *et al.*, A Monte Carlo dosimetry-based evaluation of the ^{7}Li(p,n)^{7}Be reaction near threshold for accelerator boron neutron capture therapy: Med. Phys. 27 (1) (2000), pp. 192-202.

[3] Otake, Y., RIKEN Compact Neutron Systems with Fast and Slow Neutrons: Plasma Fusion Res. 13 (2018), 2401017.

[4] Kobayashi, T., *et al.*, Completion of a new accelerator-driven compact neutron source prototype RANS-II for on-site use: Nucl. Instr. Methods A 994 (2021) pp. 1-6, 165091.

[5] Furusaka, M., *et al.*, Activity of Hokkaido University Neutron Source, HUNS: Phys. Procedia, 60 (2014), pp. 164-174.

[6] Baxter, D.V., *et al.*, LENS: 2013 Facility Overview: Phys. Procedia, 60 (2014), pp. 175-180.

[7] Sugawara, T., *et al.*, Conceptual design study of beam window for accelerator-driven system with subcriticality adjustment rod: Nucl. Eng. Des., 331 (2018), pp. 11-23.

[8] Tsujimoto, K., *et al.*, Neutronics Design for Lead-Bismuth Cooled Accelerator-Driven System for Transmutation of Minor Actinide: J. Nucl. Sci. Technol. 41 (2004), pp. 21-36.

[9] Cui, W., *et al.*, Temperature control for spallation target in accelerator driven system: Nucl. Instr. Methods B 448 (2019) pp. 5-10.

[10] Preston, M., *et al.*, Analysis of radiation emission from MYRRHA spent fuel and implications for non-destructive safeguards verification: Annals of Nucl. Energy, 163, (2021), 108525.

[11] Boudard, A., *et al.*, New potentialities of the Liège intranuclear cascade model for reactions induced by nucleons and light charged particles: Phys. Rev. C 87, (2013), 014606.

[12] Furihata, S., Statistical analysis of light fragment production from medium energy proton-induced reactions: Nucl. Instrum. Meth. B 171 (2000), pp. 251-258.

[13] Sato, T., *et al.*, Features of Particle and Heavy Ion Transport code System (PHITS) version 3.02: J. Nucl. Sci. Technol. 55 (2018), pp. 684-690.

[14] Watanabe, Y., *et al.*, Status of JENDL high energy file: J. Korean Phys. Soc., 59 (2011), pp. 1040-1045.

[15] Titarenko, Yu.E., *et al.*, Experimental and theoretical studies of the yields of residual product nuclei produced in thin Pb and Bi targets irradiated by 40 - 2600 MeV protons: INDC(CCP)-0447.

[16] Gloris, M., *et al.*, Proton-induced production of residual radionuclides in lead at intermediate energies: Nucl. Instr. Methods A 463 (2001) pp. 593-633.

[17] Hotchi, H., *et al.*, Beam commissioning of the 3-GeV rapid cycling synchrotron of the Japan proton accelerator research complex: Phys. Rev. ST Accel. Beams, 12 (2009), 040402.

[18] Hotchi, H., *et al.*, Achievement of a low-loss 1-MW beam operation in the 3-GeV rapid cycling synchrotron of the Japan proton accelerator research complex: Phys. Rev. Accel. Beams, 20 (2017), 060402.

[19] Matsuda, H., *et al.*, Proton-induced activation cross section measurement for aluminum with proton energy range from 0.4 to 3 GeV at J-PARC: J. Nucl. Sci. Technol., 55 (8) (2018), pp. 955–961.

[20] Takeshita, H., *et al.*, Measurement of nuclide production cross sections for proton-induced reactions on Mn and Co at 1.3, 2.2, and 3.0 GeV: Nucl. Instr. Methods B 511 (2022), pp. 30-41.

[21] Takeshita, H., *et al.*, Measurement of nuclide production cross sections for proton-induced reactions on $^{\mathrm{nat}}$Ni and $^{\mathrm{nat}}$Zr at 0.4, 1.3, 2.2, and 3.0 GeV: Nucl. Instr. Methods B 527 (2022), pp. 17-27.

[22] Meigo, S., *et al.*, Evaluation of the 3-GeV proton beam profile at the spallation target of the JSNS: Nucl. Instr. Methods A 562 (2006) pp. 569-572.

[23] Meigo, S., *et al.*, Beam commissioning for neutron and muon facility at J-PARC: Nucl. Instr. Methods A 600 (2009) pp. 41-43.

[24] Gloris, M., *et al.*, Production of residual nuclei from irradiation of thin Pb-targets with protons up to 1.6 GeV: Nucl. Instr. Methods B 113 (1996) pp. 429-433.

[25] Yashima, H., *et al.*, Cross sections for the production of residual nuclides by high-energy heavy ions: Nucl. Instr. Methods B 226 (2004) pp. 243-263.

[26] Ju, Y.Q., *et al.*, The production of residual radionuclides by a 250 MeV proton beam: J. Phys. G: Nucl. Part. Phys. 42 (2015), 125102.

Acknowledgments

This paper includes results obtained with the Subsidy for Research and Development on Nuclear Transmutation Technology.

13. Improvement of Benchmark Experiment with Gold foil for Large Angle Scattering Reaction Cross Section at 14 MeV Using Two Shadow Bars

Rio Miyazawa, Sota Araki, Indah Rosidah Maemunah, Shingo Tamaki, Sachie Kusaka, Isao Murata
Department of Sustainable Energy and Environmental Engineering, School of Engineering, Osaka University, 2-1 Yamadaoka, Suita, Osaka 565-0871, Japan
e-mail: miyazawa22@qr.see.eng.osaka-u.ac.jp

Currently, fusion reactors are expected to be future energy resources. And a lot of fusion neutronics related experiments have been conducted so far for the neutronic design. However, improvement of nuclear data is thought to be still needed for the development of fusion reactors. To solve this problem, we established a new benchmark experimental method to verify large angle scattering cross section. However, the previous benchmark experimental system using Nb as a neutron detector by employing ^{93}Nb(n,2n)^{92}Nb reaction required a lot of time for irradiation and measurement. In this study, the feasibility of the benchmark method using ^{197}Au (n,2n) ^{196}Au reaction instead of niobium reaction was examined. The gold reaction has a larger reaction cross section and a shorter half-life, and was expected to become a better method for benchmarking large angle scattering cross section of nuclear data.

In the new benchmark experimental method with gold foil, reaction rates of ^{197}Au (n,2n) ^{196}Au need to be calculated. However, because ^{197}Au (n,2n) ^{196}Au has two excited levels with long half-lives, it is impossible to calculate the exact reaction rates. Therefore, an appropriate experimental procedure using gold foil was examined by numerical simulations. After that, benchmark experiments of large-angle scattering cross section using Au were performed for tungsten, and the results were compared with the performance of the conventionally obtained result with Nb foil.

As a result of the numerical simulations, it was found that benchmark experiments can be analyzed by summing up the ground state ^{196}Au production cross section and two excited levels ^{196}Au production cross sections to be as the total production cross section of ^{196}Au. These apparent reaction rates were confirmed to be almost the same as the theoretically exact values. Also, as a result of the benchmark experiments, it shows that the measurement time required to obtain the same statistical accuracy can be reduced by a factor of at least 2 compared to the conventional method with Nb foil.

1. Introduction

For high energy incident neutrons, the large angle scattering cross section is usually not so important because it is much smaller than the forward scattering cross section. However, in high-intensity neutron fields such as fusion reactors, it cannot be neglected in neutron transport calculation due to gap streaming phenomenon in the blanket and so on. Actually, disagreement between calculated and experimental values has been reported in benchmark experiments at Fusion Neutronics Source (FNS) at Japan Atomic Energy Agency by Ohnishi et al., and uncertainty in the large-angle scattering cross section has been pointed out [1].

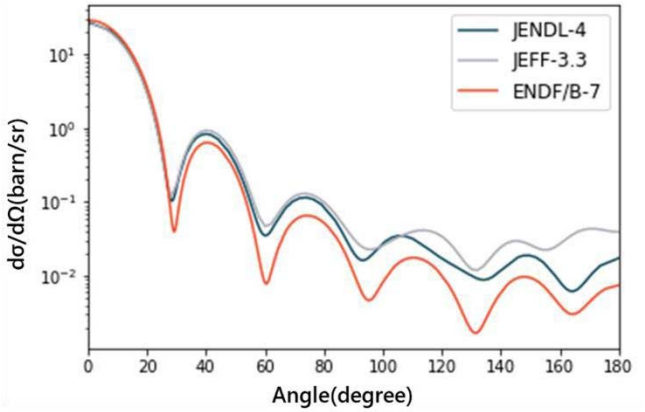

Figure 1 Elastic scattering cross section of ^{184}W

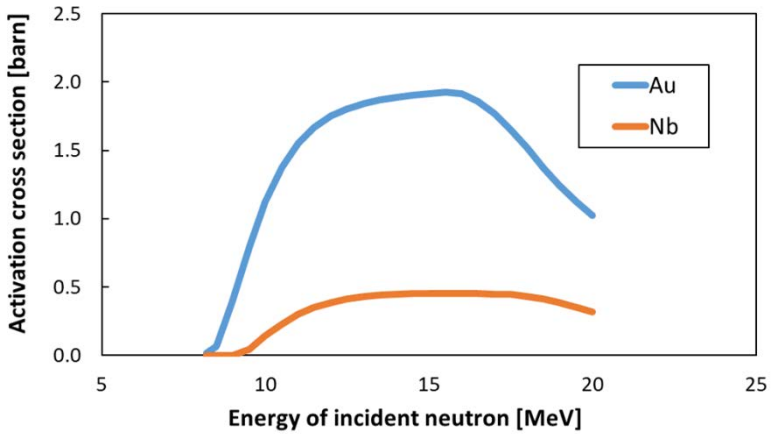

Figure 2 Comparison of Au and Nb activation cross sections

In fact, as shown in Figure 1, the elastic scattering cross sections of tungsten (^{184}W), which is planned to be used in fusion reactor diverters, show different magnitudes especially for large scattering angles [2-4]. Usually, benchmarking of elastic scattering is carried out by integral experiments. However, at backward angles, it is difficult to carry out the benchmark experiment due to small cross sections for backscatter. In response to this problem, the author's group developed a benchmark method for large angle scattering cross sections using shadow bars [5.6]. The benchmark experimental system has so far employed niobium foil as an activation detector by $^{93}Nb(n,2n)^{92}Nb$ reaction. However, in the measurement using niobium foil, it was

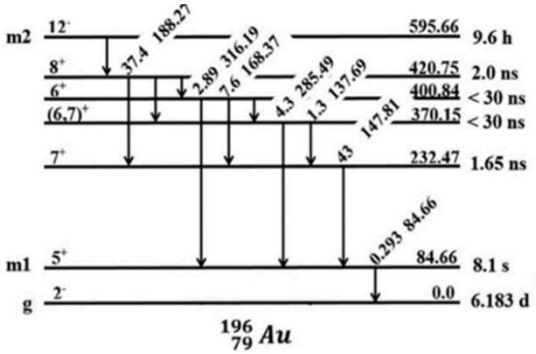

Figure 3 Excited levels in $^{197}Au(n,2n)$

problematic that it takes a very long time to measure and sufficient γ-ray counts for proper evaluation may not be obtained for some experimental systems. To solve this problem, it is considered to use gold foil instead and the activity of ^{197}Au (n,2n) ^{196}Au is used for the evaluation, because this reaction has a larger activation cross section than niobium reaction as shown in Figure 2 and its half-life of ^{196}Au produced by ^{197}Au (n,2n) ^{196}Au is about two times shorter than that of ^{92}Nb produced by ^{93}Nb(n,2n)^{92}Nb [7]. However, ^{196}Au generated in the reaction has two excited levels with long half-lives as shown in Figure 3 and it is impossible to calculate exact reaction rates [8]. Therefore, the objective of the present research is to examine the feasibility of measurement with gold foil. This research is expected to shorten the measuring time for benchmark experiments and to obtain stable γ-rays counts. Benchmark experiments of large angle scattering cross sections of tungsten were also performed using gold foil, and the obtained results were compared with the conventional benchmark experiments with niobium foils to evaluate the feasibility of the experiment using gold foil.

2. Methods and Theories

The present benchmark experimental method using two shadow bars is described in this section. The benchmark experimental system consists of four irradiation experiments, including the two systems shown in Figure 4 and two systems for each in which the target sample is removed. The large angle scattering cross sections are benchmarked by subtracting the reaction rates obtained for each of these four experimental systems. The reaction rate is calculated by Equation (1).

$$\text{Reaction rate(RR)} = \frac{N_A}{V}\int_E \sigma\,\phi dE \qquad (1)$$

N_A is the number of foil atoms, V is the volume of foil, σ is the activation cross section of foil, ϕ is the neutron flux at foil. As shown in Figure 5, the three components of the experimental system are the shadow bar, the wall, and the target, so as in Figure 5 there are seven paths available through which neutrons can transport before reaching the activation foil. Path 3 in Figure 5 is the path of interest, by which neutrons are scattered in the target with a large angle, and the nuclear data libraries can be benchmarked by comparing the obtained reaction rates in this path between experiments and simulations [5]. If the respective four systems are named S1TC, S1C, S2TC, and S2C, the path contributions that neutrons can take in each system can be expressed as described in Figure 6. The reaction rate of path 3 is thus obtained from the reaction rates of these four irradiation experiments by Equation (2).

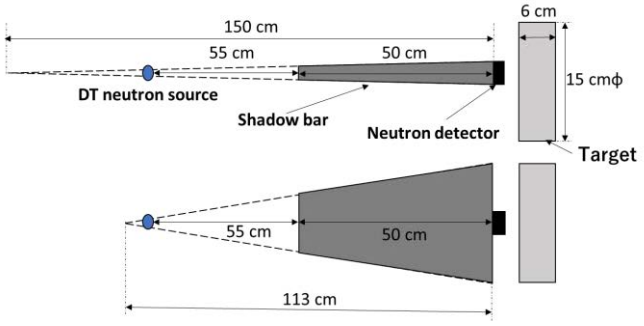

Figure 4 Two types of experimental system for benchmark

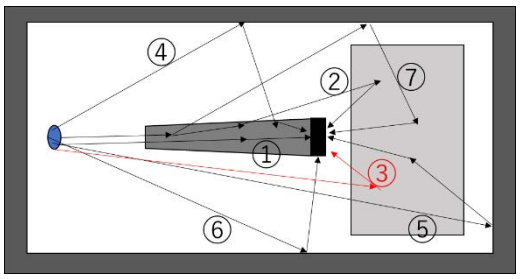

Figure 5 Paths of transporting neutrons in the benchmark system

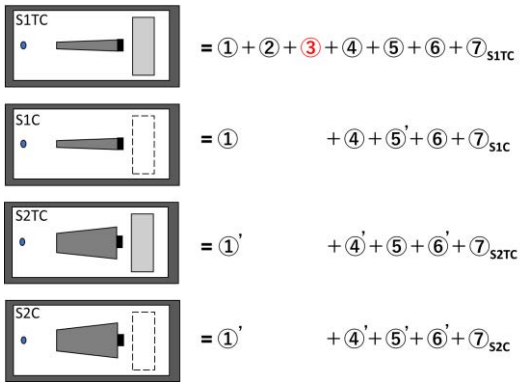

Figure 6 Possible paths in each experimental system

$$S_{1TC} - S_{2TC} - (S_{1C} - S_{2C}) = ③ + (②_{S_{1Tc}} + ⑦_{S_{1Tc}} - ⑦_{S_{2TC}} - ⑦_{S_{1c}} + ⑦_{S_{2c}}) \quad (2)$$

In this case, the reaction rates of paths 2 and 7 are very small compared to path 3, so they are treated as evaluation errors.

Normally, the reaction rate can be expressed by Equation 1, but as described in Section 1, the exact reaction rate cannot be calculated in the benchmark experiment if using gold. Therefore, in the present study we assumed that the gold activity could be evaluated by the apparent reaction rate in Equation 3, and tried to verify whether it could approximate the real value with an acceptably small discrepancy by using MCNP[9].

$$\text{Reaction rate(RR)} = \frac{N_A}{V}\int_E(\sigma_1 + \sigma_2 + \sigma_0)\,\phi dE \quad (3)$$

In the equation, σ_0 is the cross section of ground level production in Figure 3, σ_1 is the cross section of the excited level with the half-life of 8.1 s, and σ_2 is the cross section of excited level with the half-life of 9.6 h. Specifically, the accuracy of this approximation was evaluated by calculating the relative error between the numbers of ^{196}Au excited by the apparent activation cross section in Equation 3 and the exact activation cross section as shown in Figure 3.

3. Results

Figure 7 shows the discrepancy of the number of excited ^{196}Au by the apparent cross section in Equation 3 compared to the result by the exact activation cross section for the irradiation and cooling time. This figure shows that the relative error is less than 0.4% regardless of these times, and is sufficiently small compared to the error in the γ-ray counts. Therefore, it was found appropriate to evaluate the number of excited ^{196}Au by the apparent reaction rate by using Equation 3.

Based on these results, benchmark experiments with a tungsten target were conducted using a gold foil. In the experiments, the dimensions of the foil were 2 × 2 × 0.25 cm^3. A niobium foil was additionally used together with the gold foil to compare the experimental results and performance with that of the niobium foil. The shape of the niobium foil was a cylinder with a height of 0.5 cm and a diameter of 1.5 cm. The experimental results are shown in Table 1. The simulation results were calculated using the nuclear data libraries, JENDL-4.0, ENDF-B/Ⅷ, and JEFF-3.3.

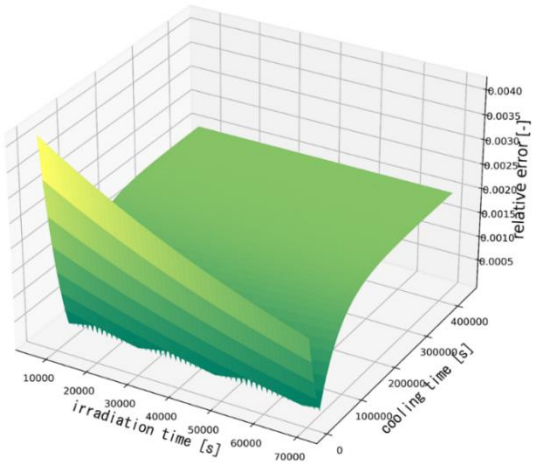

Figure 7 The relative error of the number of ground-state ^{196}Au

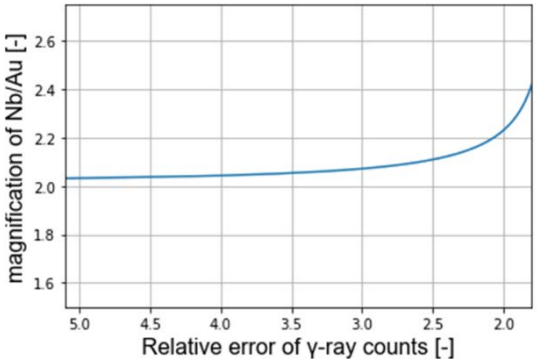

Figure 8 Ratio of the measuring time of Nb foil to Au foil
for given statistical errors for S2TC.

As shown in the results, it is found that C/E values which mean the uncertainty of large angle cross-section data show no significant difference between those using niobium and gold foils. Also, the final experimental results deduced with Equation 1 are larger than the simulation ones. This result suggests possible underestimation of the large angle scattering cross section in the nuclear data libraries. It is also presumed that large difference observed between the experimental and simulation values in the four experimental

Table 1 ^{197}Au (n,2n)^{196}Au and ^{93}Nb(n,2n) ^{92}Nb Reaction rates in the tungsten target experiments
[10^{-9} reaction/source neutron/cm^3]

		S_{1TC}	S_{2TC}	S_{1C}	S_{2C}	S_{1TC}-S_{2TC}-(S_{1C}-S_{2C})	C/E
Au	Experimental Result	51.25	12.44	33.92	20.58	25.48	
	Experimental Relative Error (%)	4.18	2.31	3.93	5.81	11.02	
	JENDL-4.0	27.13	9.95	20.67	16.9	13.41	0.53±0.06
	ENDF-B/VIII	22.62	10.44	20.67	16.9	8.41	0.33±0.04
	JEFF-3.3	28.78	10.25	20.67	16.9	14.76	0.57±0.06
Nb	Experimental Result	9.12	2.51	5.65	3.17	4.13	
	Experimental Relative Error (%)	4.25	3.10	4.51	5.58	12.2	
	JENDL-4.0	4.48	1.45	3.12	2.66	2.57	0.62±0.08
	ENDF-B/VIII	3.19	1.39	3.12	2.66	1.34	0.32±0.04
	JEFF-3.3	4.32	1.39	3.12	2.66	2.47	0.60±0.07

systems are due to the fact that the calculation system does not take desks supporting the shadow bar, accelerator itself, etc. into consideration. Figure 8 shows the ratio of required measurement times of Nb to Au for given statistical errors of γ-ray counts for the irradiation experiment of the S2TC system, which is expected to have the smallest number of counts. It shows that the measurement time required to obtain the same statistical accuracy by gold foil can be reduced by a factor of at least two compared to niobium foil.

4. Conclusion

In this study, improvement of benchmark experimental method for large angle scattering reaction cross section at 14MeV was conducted, because the previously used benchmark experimental method employed a niobium foil with ^{93}Nb(n,2n)^{92}Nb reaction, and in this case, it required a lot of time for the irradiation and measurement. We employed gold foil instead of niobium, because the reaction products by it has a larger reaction cross section and a shorter half-life compared to reaction products by niobium foil. As a result of numerical and experimental analyses, it was found that benchmark experiments could be properly performed using gold foil as a detector regardless of the irradiation and cooling time. Moreover, the measurement time can be reduced by a factor of at least two compared to the conventional method with niobium. In the future, benchmark experiments will be conducted for carbon and other nuclides using gold foil.

References

[1] S. Ohnishi et al.: New integral experiments for large angle scattering cross section data benchmarking with DT neutron beam at JAEA/FNS, Fusion Engineering and Design, 87, pp. 695-699 (2012).

[2] NEA, ” JEFF-3.3”, https://www.oecd-nea.org/dbdata/jeff/jeff33/index.html (accessed 2022-02-06).

[3] K. Shibata, et.al. : "JENDL-4.0: A New Library for Nuclear Science and Engineering," J. Nucl. Sci. Technol. 48(1), 1-30 (2011).

[4] D.A. Brown, M.B. Chadwick, R. Capote, et al., "ENDF/B-VIII.0: The 8th Major Release of the Nuclear Reaction Data Library with CIELO-project Cross Sections, New Standards and Thermal Scattering Data", Nuclear Data Sheets, 148: pp. 1-142 (2018).

[5] Naoya Hayashi, Seiki Ohnishi, Yuki Fujiwara, Sachie Kusaka, Fuminobu Sato, Isao Murata “Optimization of Experimental System Design for Benchmarking of Large Angle Scattering Reaction Cross Section at 14 MeV Using Two Shadow Bars” Plasma and Fusion Research, 13, 2405002, (2018).

[6] Atsuki Yamaguchi, et.al., " Benchmark experiment of large-angle scattering reaction cross section of iron at 14 MeV using two shadow bars – Comparison of experimental results with ENDF/B-VIII –" Journal of Nuclear Science and Technology, 58. pp. 80-86 (2019).

[7] Y. Nakajima, JNDC WG on Activation Cross Section Data: “JENDL Activation Cross Section File,” Proc. the 1990 Symposium on Nuclear Data, JAERI-M 91-032, pp. 43 (1991).

[8] Richard B. Firestone, et al, Table of Isotopes Eighth Edition Volume II, pp. 2453.

[9] Brown, F.B., MCNP-A General Monte Carlo N-Particle Transport Code, Oak Ridge(US): Los Alamos National Laboratory; 2003.

14. The comparison of nuclear data and experimental results for photoneutron spectra on Ta, W, and Bi targets for 17 MeV photons

*T. NGUYEN[1], T. SANAMI[1,2], H. YAMAZAKI[1,2], Y. SAKAKI[1,2], T. ITOGA[3], Y. KIRIHARA[4], K. SUGIHARA[1,2], M. FAIZ[1], S. MIYAMOTO[5], S. HASHIMOTO[6], Y. ASANO[2,7].

[1]SOKENDAI, Shonan Village, Hayama, Kanagawa 240-0193 Japan

[2]KEK, 1-1 Oho, Tsukuba-shi, Ibaraki-ken 305-0801 Japan

[3]JASRI, 1-1-2, Koto, Kamigori-cho, Ako-gun, Hyogo 678-1205, Japan

[4]JAEA, 2-4 Shirakata, Tokai-mura, Naka-gun, Ibaraki 319-1195, Japan

[5] ILE, Osaka University, 2-6 Yamadaoka, Suita, Osaka 565-0871, Japan

[6]University of Hyogo, 1-1-2, Koto, Kamigori-cho, Ako-gun, Hyogo 678-1205, Japan

[7] RCNP, Osaka University, 10-1, Mihogaoka, Ibaraki, Osaka 567-0047, Japan

*Email: ngthuong@post.kek.jp

The photoneutron energy spectra obtained from nuclear data and theoretical calculations were compared with the experimental data for 17 MeV photons on Ta, W, and Bi targets. The results of PHITS code, CoH_3 code, JENDL/PD-2016 nuclear data, and TENDL-2019 nuclear data were included for this comparison.

1. Introduction

High-energy photons are primarily produced as bremsstrahlung by electron accelerators. Secondary neutrons can be emitted via photonuclear reactions from the interactions between these photons and accelerator components. Data of photoneutron yield, energy, and angular distribution are fundamental parameters for the shielding design of electron accelerators.

So far, several studies have been conducted on neutron emission in photonuclear reactions [1 , 2, 3]. Our group recently measured the photoneutron spectra for 17 MeV linearly polarized photons at angles ranging from 30° to 150° on Ta, W, and Bi targets. The results consist of low-energy and high-energy components. The angular distribution of the low-energy component was isotropic, whereas the high-energy component was dependent on the interaction angle between photon polarization and neutron emission.

The measured data are important for benchmarking the nuclear data and theoretical calculations. Thus, in this study, the experimental results on Ta, W, and Bi targets irradiated by 17 MeV photons were compared with photoneutron spectra obtained by the theoretical codes of PHITS [4] and CoH_3 [5], and nuclear data libraries of TENDL-2019 [6], JENDL/PD-2016 [7].

2. Experiment

Our experiment was carried out at NewSUBARU facility, BL-01, Hyogo, Japan. Figure 1 shows the experimental setup of the photoneutron measurement, as mentioned in [1]. The mono-energetic, horizontally polarized photon beam was produced by the collision of a polarized laser source and 1 GeV electron at the backscattering angle. The beam was adjusted to inject into the center of the target. Targets were cylinders with 1 cm thicknesses for Ta and W and 2 cm for Bi. A 5-mm-thick plastic scintillator was placed upstream of the target to estimate the number of incident photons. Six liquid scintillation detectors (NE213, $5^{\phi} \times 5^{L}$ in) were positioned at 30°, 60°, 90°, 120°, and 150° horizontally and 90° vertically to the photon beam direction. Because of the high sensitivity of NE213 to photoneutrons and gamma in the background, the pulse shape discrimination (PSD) technique was used. The time-of-flight (TOF) method was applied for obtaining the photoneutron energy spectra.

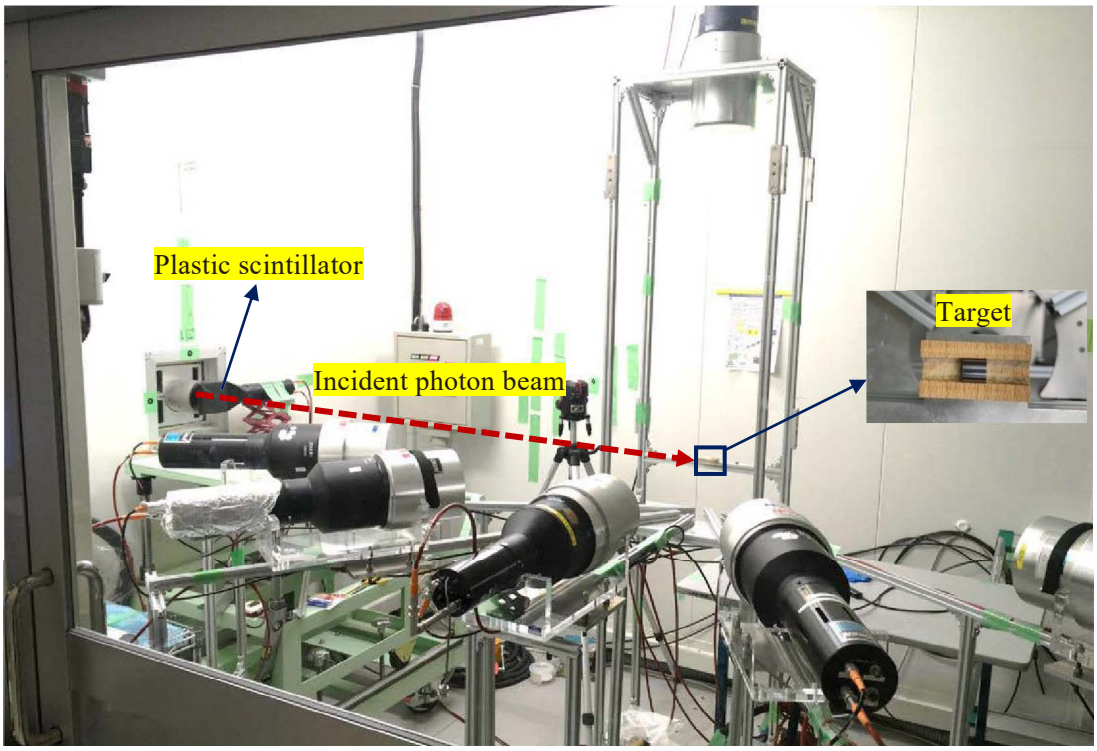

Figure 1: The experimental setup of photoneutron measurement [1].

To acquire data, a system including a charge-to-digital converter (QDC) module, a time-to-digital converter (TDC) module, and a VME controller was prepared, which was identical to that used in previous experiments [1, 2]. The QDC module recorded the tail and total charges of the output signals from NE213, and the TDC module recorded the time difference between the incident photons and signals detected by NE213. A two-dimensional plot of the charge ratio of the tail and total signals, defined as the PSD parameter, and time-of-flight was used to distinguish photoneutrons and background gamma, as shown in Figure 2. Events with light yield greater than 0.25 MeVee - equivalent to half of the ^{137}Cs bias, were selected. Figure 3 shows the neutron-gamma time-of-flight spectra after neutron and gamma separation. The neutron detection efficiency of the detectors was calculated using the SCINFUL-QMD simulation [8] with correction of the neutron measurement from the ^{252}Cf source. The attenuation of the photon beam due to the target thickness was evaluated using the PHITS code.

The experimental data showed the polarization effect of the incident photons same as previous

experiment [1, 2]. Hence, in this paper, we only reported the photoneutron spectra at the vertical 90° position (V90) for comparison, to exclude the polarization effect.

3. Theoretical calculations and nuclear data libraries

In this work, the photoneutron spectra from the theoretical codes of PHITS and CoH_3 and the nuclear data libraries of TENDL-2019 and JENDL/PD-2016 were compared with the measured data. We used PHITS version 3.27 with the default mode and the same geometry as the experiment. The detection regions were simulated as cylinders with a size of 5 × 5 in, without NE213 liquid in volume. The same geometry as that of the PHITS code was used to obtain neutron spectra using TENDL-2019 nuclear data libraries instead of the default reaction models. The neutron spectra from JENDL/PD-2016 were directly derived using the ENDF-6 reader program [9]. Neutron spectra were obtained using the CoH_3 code in the double-differential calculation mode without considering the experimental geometry. Because the results obtained from the CoH_3 code and JENDL/PD-2016 nuclear data library are whole neutrons emitted on a plane perpendicular to the incident photon beam direction, their magnitude must be adjusted for comparison with experimental data.

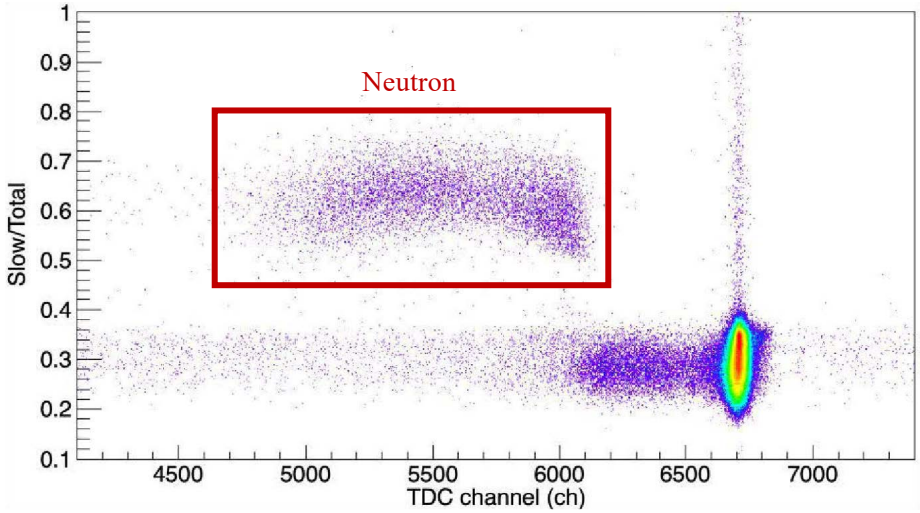

Figure 2: Neutron-gamma separation using the charge ratio between slow and total gates on Bi target at vertical 90° position.

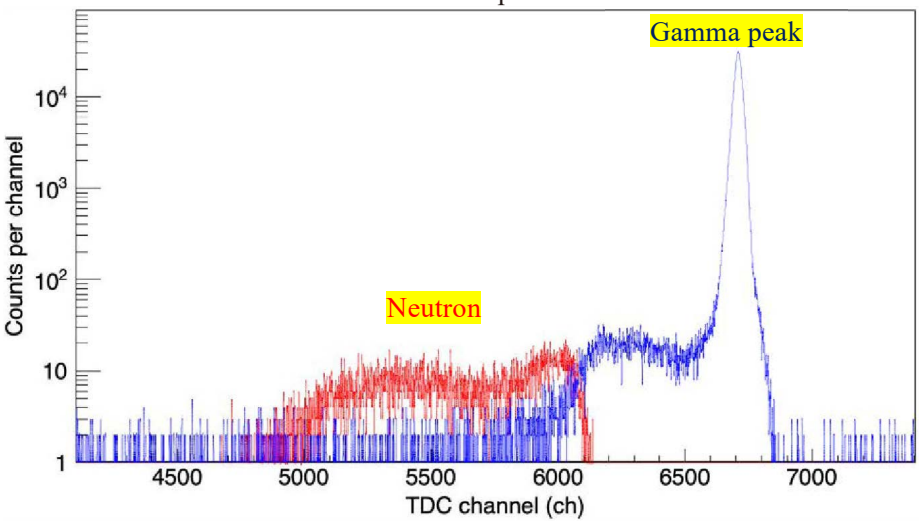

Figure 3: Neutron and gamma time-of-flight spectra on Bi target at vertical 90° position.

4. Result and discussion

Figure 4 shows the photoneutron energy spectra obtained from the experiment, PHITS default calculation, CoH_3 code, and nuclear data libraries of TENDL-2019 and JENDL/PD-2016 for W, Ta, and Bi targets. The red circles indicate the experimental data at a 90° angle perpendicular to the polarization direction with respect to the incident photon. The measured spectra consist of low- and high-energy components.

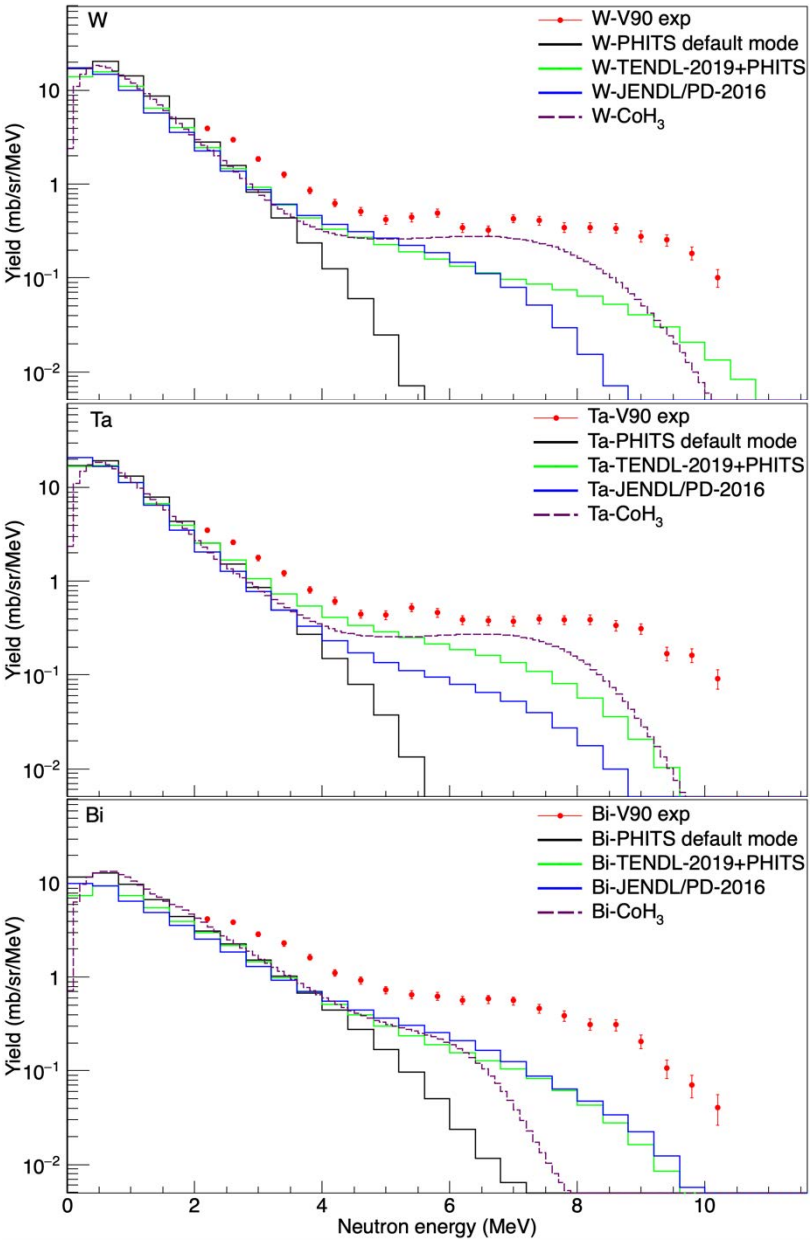

Figure 4: Photoneutron energy spectra for 17 MeV photons on W, Ta, and Bi targets.

All the theoretical calculations and nuclear data underestimate the experimental data. They show approximately identical results below 4 MeV, and a noticeable difference in the region above 4 MeV. The slopes of the PHITS default calculation (black solid lines) are the lowest among all the results. The PHITS results with the default model contain only the low-energy evaporation component that originates from the Generalized Evaporation Model (GEM) [10] for 17 MeV photons. The calculations using the

CoH_3 code are close to the experimental data for Ta and W, but low for Bi. The green and blue solid lines representing the results extracted from the TENDL-2019 and JENDL/PD-2016 nuclear data, respectively, are similar for Bi. However, for Ta and W, the spectra obtained by TENDL-2019 are higher than those obtained by JENDL/PD-2016.

5. Conclusion

We compared the photoneutron energy spectra from the nuclear data libraries of TENDL-2019 and JENDL/PD-2016, theoretical calculations of PHITS and CoH_3, and measurements. The results showed significant differences among the theoretical calculations, nuclear data, and experimental data in the high-energy region. Thus, all theoretical models and nuclear data must be improved to accurately describe the photonuclear reactions.

References

1) Tuyet, T.K., Sanami, T., Yamazaki, H., Itoga, T., Takeuchi, A., Namito, Y., Miyamoto, S. and Asano, Y., Energy Energy and angular distribution of photo-neutrons for 16.6 MeV polarized photon on medium–heavy targets, Nucl. Instrum. Meth. A, vol.989, 2021, 164965.
2) Kirihara, Y., Nakashima, H., Sanami, T., Namito, Y., Itoga, T., Miyamoto, S., Takemoto, A., Yamaguchi, M. and Asano, Y., Neutron emission spectrum from gold excited with 16.6 MeV linearly polarized monoenergetic photons, vol.57, no.4, J. Nucl. Sci. Technol., 2020, pp.444-456.
3) Varlamov, A.V., Varlamov, V.V., Rudenko, D.S. and Stepanov, M.E., Atlas of giant dipole resonances. Parameters and Graphs of Photonuclear Reaction Cross Sections. INDC (NDS)-394, IAEA NDS, Vienna, Austria, 1999, pp.1-311.
4) Sato, T., Iwamoto, Y., Hashimoto, S., Ogawa, T., Furuta, T., Abe, S.I., Kai, T., Tsai, P.E., Matsuda, N., Iwase, H. and Shigyo, N., Features of particle and heavy ion transport code system (PHITS) version 3.02, vol.55, no.6, J. Nucl. Sci. Technol., 2018, pp.684-690.
5) Kawano T., Proc. of the 6th Int. Workshop on Compound-Nuclear Reactions and Related Topics CNR*18, 2019, p. 27.
6) Koning, A.J., Rochman, D., Sublet, J.C., Dzysiuk, N., Fleming, M. and Van der Marck, S., TENDL: complete nuclear data library for innovative nuclear science and technology, Nuclear Data Sheets, 155, 2019, pp.1-55.
7) Iwamoto, N., Kosako, K., Murata, T., Photonuclear Data File, JAEA-Conf 2016-004, 2016, pp. 53-58.
8) Satoh, D., Kunieda, S., Iwamoto, Y., Shigyo, N. and Ishibashi, K., Development of SCINFUL-QMD code to calculate the neutron detection efficiencies for liquid organic scintillator up to 3 GeV, J. Nucl. Sci. and Technol., vol.39, 2002, pp.657-660.
9) Sakaki, Y., Note on Evaluated Nuclear Data Library and a new tool “endf6 reader”, KEK, 2020.
10) Furihata, S., Statistical analysis of light fragment production from medium energy proton-induced reactions., Nucl. Instrum. and Meth. B, vol.171, no.3, 2000, pp. 251-258.

15. Study of GAGG scintillator as a neutron detector

Ren Sakai[1] and Nobuhiro Shigyo[1]

[1]Department of Applied Quantum Physics and Nuclear Engineering, Kyushu University
744 Motooka, Nishi-ku, Fukuoka 819-0395, Japan

*Email: sakai.ren.063@s.kyushu-u.ac.jp

In order to use the GAGG scintillator as a neutron detector, the signatures of neutron detection were investigated. Various conditions were simulated using PHITS to determine the size of GAGG scintillator. The response characteristics when neutrons of some energy are incident on the GAGG scintillator are simulated by changing the thickness of the GAGG scintillator from 0.1 to 100 mm. We also investigated the neutron energy dependence of the GAGG scintillator by changing the incident neutron energy from 1 meV to 10 MeV. Furthermore, the size of the GAGG scintillator was determined from the simulation results, and the response to thermal neutrons was measured.

1. Introduction

In recent years, there is a need for improved nuclear data on high-energy neutron-induced fission of actinides [1]. For example, improving the data of prompt neutrons will contribute to nuclear applications [2]. Even in thermal neutron detection, ^{3}He does not exist naturally and is very expensive and its price has continued to rise due to changes in nuclear security policies in the United States, making it difficult to obtain ^{3}He in recent years [3, 4]. For these reasons, it is necessary to explore for new neutron detectors.

The GAGG scintillator emits a large amount of light and is excellent as a gamma-ray detector, and is used in single-photon emission tomography SPECT, gamma cameras. Gd, a constituent element of GAGG, has isotopes with fairly large capture cross-sections for low-energy neutrons. Among them, ^{155}Gd and ^{157}Gd have particularly large cross sections for thermal neutrons of 60,740 b and 253,700 b, respectively as shown in Fig. 1, and natural abundance ratios of 14.8 % and 15.7 %, respectively. The reaction transition of each isotope can be expressed as follows, and the Q values are 8.1 and 7.9 MeV, respectively. For neutrons above 100 keV, signals due to inelastic scattering can also be expected for neutron detection. For these reasons, it may be used as a neutron detector.

$$^{155}\mathrm{Gd} + n \rightarrow ^{156}\mathrm{Gd}^{*} \rightarrow ^{156}\mathrm{Gd} + \gamma \quad (1)$$

$$^{157}\mathrm{Gd} + n \rightarrow ^{158}\mathrm{Gd}^{*} \rightarrow ^{158}\mathrm{Gd} + \gamma \quad (2)$$

Our purpose is to verify the performance of the GAGG scintillator as a neutron detector. We would like to detect neutrons in the thermal neutron region and neutrons above 100 keV. For that purpose, we first analyzed the response of the GAGG scintillator to various energy neutrons using the 3D Monte Carlo code PHITS [6]. Thermal neutron irradiation experiments were also carried out to investigate the thermal neutron response of the GAGG scintillator.

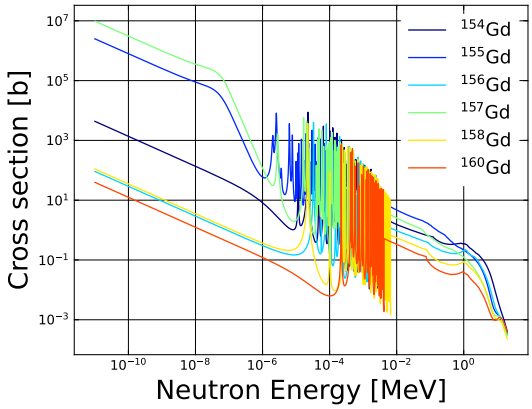

Fig. 1 Neutron capture cross section of Gd isotopes in JENDL-4.0 [7].

2. Simulation of r neutron responses of GAGG scintillator

2.1 Calculation condition

PHITS ver.3.27 was used as the simulation code. JENDL-4.0 [7] was used for neutron reactions, and EGS5 [8] was used for electron, positron, and photon transport. In this section, we discuss the response dependence of the GAGG scintillator on the GAGG scintillator thickness and the incident neutron energy. The area of the GAGG scintillator is fixed at 2×2 cm^2. The number of histories was set to 6×10^6.

The response was simulated for incident neutron energies from 1 meV to 10 MeV and GAGG scintillator thicknesses of 0.1 mm, 1 mm, 1 cm and 10 cm. The obtained calculations are the neutron flux in the GAGG scintillator, the spectrum of neutrons and photons in the GAGG scintillator, and the energy distribution due to particles such as electrons imparted to the GAGG scintillator.

2.2 Results

From neutron flux, the neutron reaction rate was calculated by dividing the neutron flux exiting the GAGG scintillator by the neutron flux entering the GAGG scintillator. The detection efficiency was calculated by taking the sum of electrons imparted when neutrons of a certain energy were incident on the GAGG scintillator from the deposit energy distribution. The neutron flux and the energy distribution of electrons imparted to the GAGG scintillator for 1 meV to 10 MeV neutrons were summarized for each GAGG scintillator thickness, and graphs of the neutron reaction rate and detection efficiency were drawn. These are shown in Figs. 2 and 3. In both figures, it can be inferred that the resonance part of the capture cross section is reflected in the range of about 1 eV to 1 keV.

In addition, from the results shown in Figs. 2 and 3, for thermal neutrons, the thickness of 0.1 and 1 mm shows a certain sensitivity, but compared to 1 cm and 10 cm, the sensitivity to neutrons with energy higher than 1 eV is much lower. Therefore, we determined that the optimum thickness of the GAGG scintillator was approximately 1 cm.

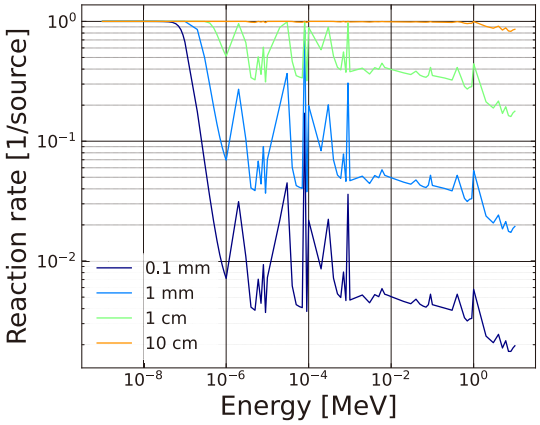

Fig. 2 Neutron reaction rate.

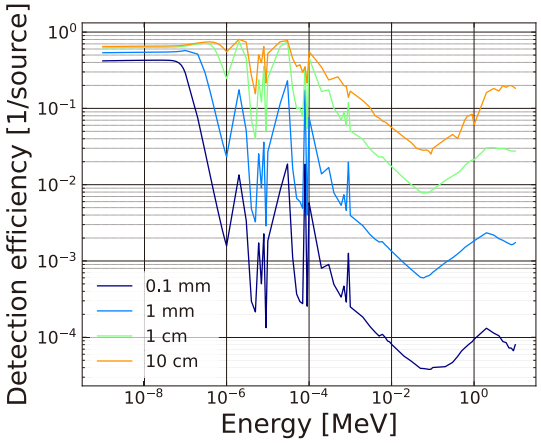

Fig. 3 Detection efficiency.

3. Thermal neutron irradiation experiment

Using the GAGG scintillator, thermal neutrons measured before measuring fast neutrons. Cadmium difference method was used to investigate the response to thermal neutrons.

3.1 Data acquisition and circuit system

The dimension of GAGG scintillator used in this experiment has an area of 2×2 cm^2 and a thickness of 1 cm. This scintillator was wrapped in PTFE tape to improve light collection. The PMT used in this work was a HAMAMATSU H6410. We used four ^{252}Cf neutron sources. At the time of measurement, the total source intensity was 7.1 MBq.

All γ ray and neutron data were acquired with a DT5742 CAEN digitizer. The PMT bias was 2002 V. Logic signals of a CFD were used as fast triggers when recording waveforms. We set the CFD threshold at the lower limit of -30 mV. This circuit system is shown in Fig. 4.

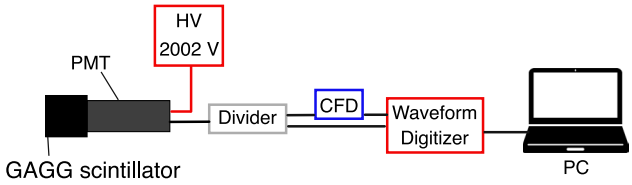

Fig. 4 Circuit system.

3.2 Experiment preparation

The detector was calibrated using the γ rays from ^{241}Am, ^{109}Cd, and ^{137}Cs. The photopeaks of ^{241}Am, ^{109}Cd, and ^{137}Cs are 59.5, 88 and 661.7 keV, respectively.

The neutron sources used in this work were produced from four ^{252}Cf sources discribed above. In order to irradiate the GAGG scintillator with thermal neutrons, the distance from the source to the scintillator was set at 16 cm, and a polyethylene block with a thickness of 10.4 cm was placed between them. In addition, a 5 cm thick lead was placed in front of the scintillator to shield γ rays from the ^{252}Cf sources.

However, in this system, higher energy neutrons above 100 keV came to the GAGG scintillator in addition to thermal neutrons. Therefore, we investigated the response due to thermal neutrons by using the Cd difference method. In this method, measurements were taken for the same amount of time with and without the Cd plate, and thermal neutron data are obtained from the difference. Figure 5 shows a system in which a 10.2 cm thick polyethylene block, a 5 cm thick lead block, and a 2 mm thick Cd plate are placed between the source and the GAGG scintillator. In addition to the two systems mentioned above, we calculated the neutron spectra irradiated to the GAGG scintillator using PHITS, assuming that nothing is placed between the source and the GAGG scintillator, which is shown in Fig. 6. The light blue line is the neutron spectrum when nothing is placed between the source and the detector, the brown line is the neutron spectrum when a polyethylene block and a lead block are placed. The yellow lines represent the neutron spectrum when a Cd plate is added to the brown line system. It can be seen that most of the thermal neutrons have been captured by Cd plate.

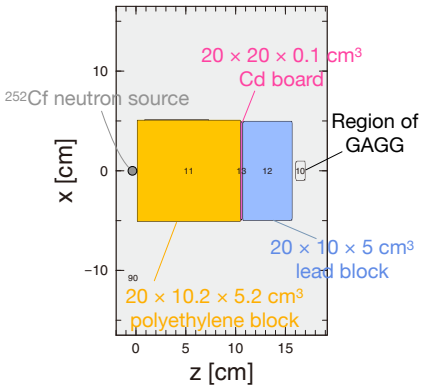

Fig. 5 Simulation system when a 2 mm thick Cd plate is placed between polyethylene and lead

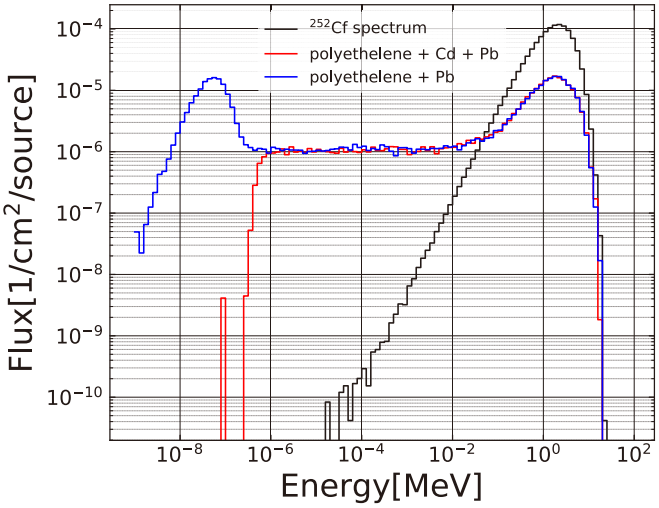

Fig. 6 Comparison of neutron spectra in the GAGG region.

3.3 Results

3.3.1 Energy calibration of gamma-ray sources

Waveform data were collected using gamma-ray sources : ^{241}Am, ^{109}Cd, and ^{137}Cs. Figure 7 shows a comparison of the amount of light yield calculated from each waveform data for each γ ray source. Energy resolution is approximately 22.5 % at 59.5 keV, 19.5 % at 88 keV, and 6.3 % at 661.7 keV. An energy calibration curve is shown in Fig. 8.

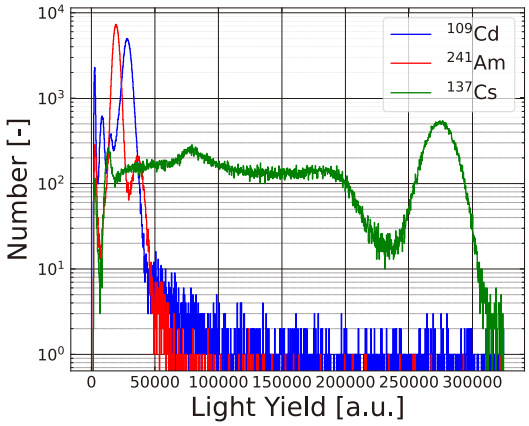

Fig. 7 γ ray source spectra.

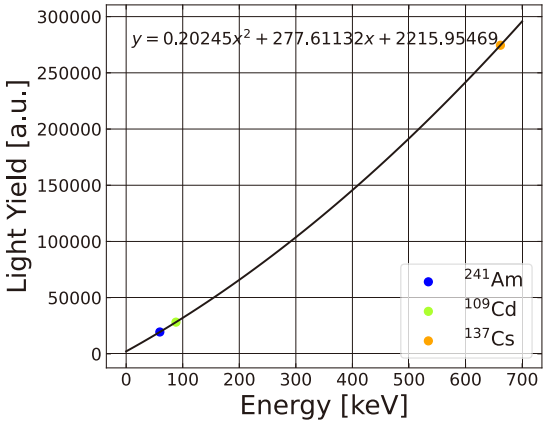

Fig. 8 Energy calibration curve.

3.3.2 Thermal neutron measurements

We acquired the waveform data for 30 minutes for cases with and without the Cd plate. In Fig. 9, the brown line is the data measured in the system without the Cd plate, the yellow line is the data measured in the system with the Cd plate, and the blue line is the data obtained from the difference between them. The combined 1st excited state to ground state transitions for ^{156}Gd and ^{158}Gd at 84.6 keV is the most prominent feature. In addition, two higher energy features are also observed at 263 keV and 454.1 keV.

The 84.6 keV peak is the combination of the 88.9 and 79.5 keV γ rays from the first excited states of ^{156}Gd and ^{158}Gd, which cannot be separately resolved. In Fig. 9, we also observe a γ peak at 263 keV, this is a result of the rotational band structure of both ^{156}Gd and ^{158}Gd in which the 4+ state de-excites in sum-coincidence through the 2+ state to the ground state.

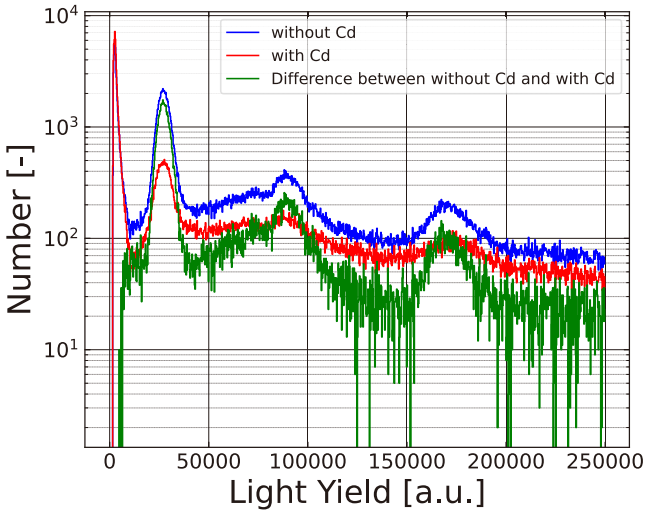

Fig. 9 Light yield spectrum obtained by taking the difference between the data without the Cd plate and the data with the Cd plate.

4. Summary

To investigate whether GAGG can be used as a neutron detector, we calculated the response using PHITS and measured the response to thermal neutrons. From the simulation results, it was found that the optimum thickness of the GAGG scintillator for neutron spectroscopy using the TOF method is approximately 1 cm.

Based on these results, we carried out the thermal neutron irradiation experiment using 1 cm thick of GAGG scintillator. For thermal neutrons, three useful signals for neutron detection were confirmed. In the future, we plan to measure the TOF spectrum using the ^{252}Cf neutron source and verify its performance as a detector for fast neutron components.

References

[1] Neudecker D, Talou P, Kawano T, Kahler AC, et al. Evaluations of Energy Spectra of Neutrons Emitted Promptly in Neutron-induced Fission of ^{235}U and ^{239}Pu. Nucl Data Sheets 2018;148:322–337.

[2] Neudecker D, Taddeucci TN, Haight RC, et al. The Need for Precise and Well-documented Experimental Data on Prompt Fission Neutron Spectra from Neutron-induced Fission of ^{239}Pu. Nucl Data Sheets 2016;131:289–318.

[3] Block T, Gruber M, Gurbuz S, et al. Particle physics readout electronics and novel detector technologies for neutron science. Nucl Instrum Meth A 2023;1046:167753.

[4] Nadeera Hemamali GM, Smith DR, Hobson PR, et al. Europium doped Gd_2O_3 and $GdBO_3$ scintillators for thermal neutron detection. Nucl Instrum Meth A 2023;1048:267918.

[5] Taggart MP, Nakahostin M, Sellin PJ. Investigation into the potential of GAGG:Ce as a neutron detector. Nucl Instrum Meth A 2019;931:121–126.

[6] Sato T, Iwamoto Y, Hashimoto S, et al. Features of Particle and Heavy Ion Transport code System (PHITS) version 3.02. J Nucl Sci Technol. 2018;55(5-6):684–690.

[7] Shibata K, Iwamoto O, Nakagawa T, et al. JENDL-4.0: A New Library for Nuclear Science and Engineering. J Nucl Sci Technol. 2011;48:1–30.

[8] Hirayama H, Namito Y, Bielajew AF, et al. The EGS5 Code System. Stanford Linear Accelerator Center; 2005. (SLAC Report; SLAC-R-730), High Energy Accelerator Organization; 2005. (KEK Report; 2005-8).

16. Characterization of various types of n-γ mixed fields by using a D-D neutron source

Zixu XU[1*], Masaya MATSUKI[1], Kazuma AOKI[2], Yoshihiro ARITOMO[2], Shingo TAMAKI[1], Sachie KUSAKA[1], and Isao MURATA[1]
[1]Graduate School of Engineering, Osaka University
2-1 Yamadaoka, Suita, Osaka 565-0871, Japan
[2]Faculty of Science and Engineering, Kindai University
3-4-1 Kowakae, Higashiosaka, Osaka 577-8502, Japan
[*]Email: Xu.Zixu@qr.see.eng.osaka-u.ac.jp

Abstract: In the treatment field of Boron Neutron Capture Therapy (BNCT), secondary gamma-rays are easily produced during neutron irradiation. In the BNCT project of Osaka University, a material-filtered Radio-Photoluminescence Glass Dosimeter (RPLGD) was developed to measure neutron and gamma-ray doses separately. In this study, to validate the material-filtered RPLGD for BNCT, various types of F-dominant, E-dominant, and T-dominant fields were designed by using a D-D neutron source. This paper provides valuable reference n-γ mixed fields for developing radiation dosimeters for BNCT.

1. Introduction

1.1. Boron Neutron Capture Therapy

Boron Neutron Capture Therapy (BNCT) is a promising and rising technique for cancer therapy. In BNCT [1], boron-10 compounds are concentrated in a tumor by boron delivery agents. After exposing a patient to thermal or epithermal neutrons, the tumor could be destroyed selectively in an effective manner without damaging adjacent normal tissue [1]. In recent years, accelerator-based BNCT systems were widely proposed and developed in many countries [2]. The neutron beams produced by accelerators include contributions of secondary gamma-rays, as well as fast, epithermal, and thermal neutrons [1]. Because neutron and gamma-ray have different biological effects on human bodies [3], it is essential to measure the neutron and gamma-ray doses separately and simultaneously.

1.2. Objectives

Previously, researchers developed and measured different n-γ mixed fields for radiation experiments. F. Ferrulli, et al. [4] developed an n-γ mixed field with an Am-Be source (1.5 mSv/h) and a ^{137}Cs source (up to 60 μSv/h) to characterize a fast neutron dose rate detector. Yi-Chun Lin, et al. [5] measured the gamma-ray and neutron dose rates for BNCT at two reactors (THOR and HFR). Ryo Ogawara, et al. [6] measured the absorbed dose contribution of thermal neutrons, fast neutrons, and gamma-rays at an accelerator-based mixed field (p-Be source, Polyethylene moderator). However, there were few standard

n-γ mixed fields with adjustable gamma-ray to neutron dose ratios, classifications of dominant neutron energy, and wide energy ranges of gamma-ray.

In the BNCT project of Osaka University, a liquid Li based neutron source is now planned to be developed [7], and a material-filtered method of Radio-Photoluminescence Glass Dosimeter (RPLGD) was proposed to separately measure neutron and gamma-ray doses for treatments [8]. However, there was no standard n-γ mixed field for the authors to do validation experiments of the material-filtered RPLGD. In this study, various types of n-γ mixed fields were designed by using a D-D neutron source (2.5 MeV) at OKTAVIAN in the authors' laboratory, as an alternative to cover the energy distribution of the p-Li neutron source (0.6 MeV) [7].

2. Simulation setup and methods

2.1. Irradiation assembly

The irradiation assembly to generate n-γ mixed fields is shown in Figure 1. Source neutrons (isotropic, 2.5 MeV) were produced based on D(d,n)^{3}He reaction. After the source neutrons penetrate the moderator, gamma-rays are produced to generate an n-γ mixed field. The moderator was 40 cm in diameter and 0-70 cm in thickness. The calculations were performed by Monte Carlo N-Particle Code 5 (MCNP5) [9] based on ENDF/B-VIII.0 [10]. The number of source particles was set to 10^9. The radiation fluxes and doses were calculated by F4 and F6 tallies, respectively. Six materials were considered to compose the moderator: Al (2.70 g/cm^3), Fe (7.86 g/cm^3), Pb (11.34 g/cm^3), Polyethylene (PE) (0.93 g/cm^3), CF_2 (2.20 g/cm^3), and AlF_3 (2.88 g/cm^3). By changing the material, combination, and thickness of the moderator, the radiation dose level and energy spectrum of the mixed fields were adjusted.

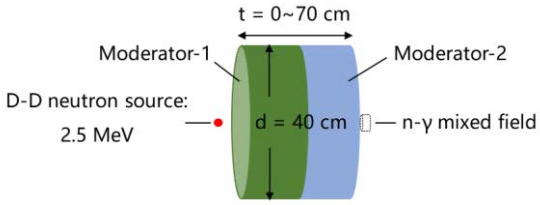

Figure 1. Irradiation assembly to generate n-γ mixed fields.

2.2. Gamma-rays produced at a neutron-generating target

When D-D source neutrons are produced and penetrate a neutron-generating target, gamma-rays are produced by capture and inelastic scattering reactions, which should be evaluated as a contaminant of the total gamma-ray flux. Therefore, the moderator should be thick enough to absorb the gamma-rays produced by the target. As shown in Figure 2, the model of the neutron-generating target at OKTAVIAN [11], in the authors' laboratory, was simulated to examine the behavior of the gamma-rays emitted from the target. The layers of the neutron-generating target were 0.01 cm Ti + 0.1 cm Cu + 0.24 cm H_2O + 0.1 cm stainless steel (304). η_t is defined to evaluate the shielding ability of each material to absorb the gamma-rays emitted from the target:

$$\eta_t = \frac{F_{G_t}}{F_{G_{m+m}}}, \tag{1}$$

where F_{G_t} is the gamma-ray flux produced at the target, and $F_{G_{t+m}}$ is the total gamma-ray flux. When

η_t reaches 0%, the contribution of gamma-rays produced at the target is removed theoretically. The results of η_t of Al, Fe, Pb, CF_2, and AlF_3 are shown in Figure 3. As the thickness increases, η_t of Al, Fe, Pb, CF_2, and AlF_3 declines and saturates at approximately 1%, 0%, 0%, 5%, and 3%, respectively. 19 cm Fe and 12 cm Pb were determined as a minimum thickness to remove the contribution of the gamma-rays emitted from the target.

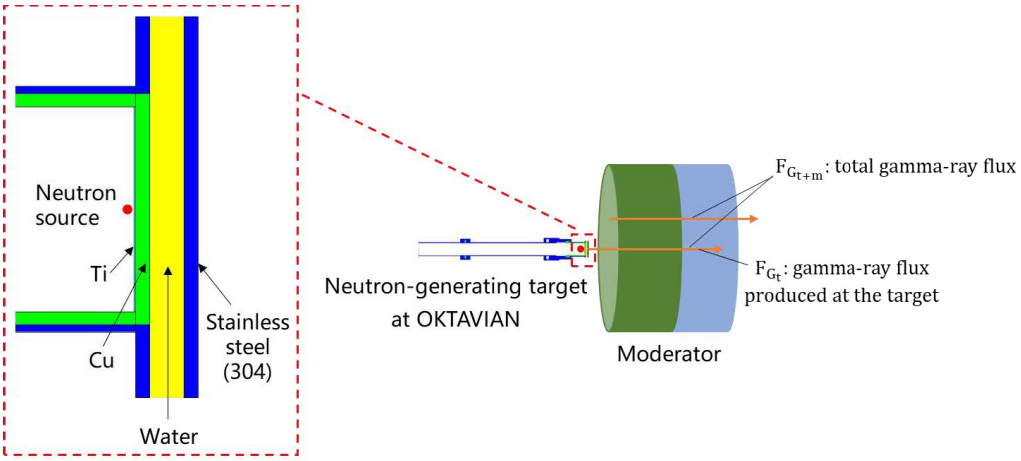

Figure 2. Schematic illustration of calculating gamma-ray flux.

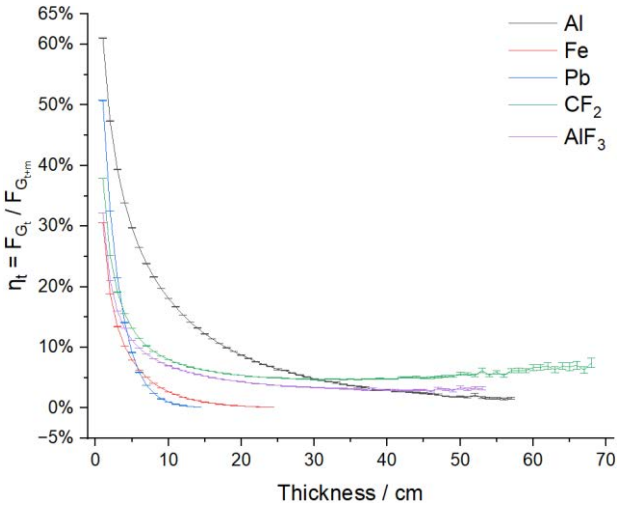

Figure 3. Evaluation of contribution of gamma-rays produced at the neutron-generating target.

3. Results and discussion

3.1. Neutron and gamma-ray doses

The gamma-ray to neutron dose ratio η_d is defined as:

$$\eta_d = \frac{D_\gamma}{D_n}, \tag{2}$$

where D_γ is the gamma-ray dose, and D_n is the neutron dose. In this study, η_d was controlled in between 0% and 200% ($D_\gamma < D_n$, $D_\gamma \approx D_n$, $D_\gamma > D_n$). The combinations and thicknesses of the moderators were set to: Fe (19 cm) + PE (0-8 cm), PE (0-24 cm) + Fe (19 cm), Pb (12 cm) + PE (0-14 cm), PE (0-47 cm) + Pb (12 cm), CF_2 (42-60 cm), and AlF_3 (47-65 cm). The results of D_γ, D_n, and η_d

are shown in Figure 4. In Figure 4 (a), D_n is attenuated, as the thickness of the moderator increases. In Figure 4 (b), D_γ is enhanced with the increasement of the thickness of PE, e.g., Fe (19 cm) + PE (0-7 cm) and Pb (12 cm) + PE (1-10 cm). In Figure 4 (c), η_d ascends rapidly and approaches 200%, by increasing the thickness of PE. Because $^1H(n,\gamma)^2H$ reactions produce more gamma-rays [12], PE is an effective material to increase η_d. For CF_2 (42-60 cm) and AlF_3 (47-65 cm) as a single-material moderator, η_d is below 80.5%.

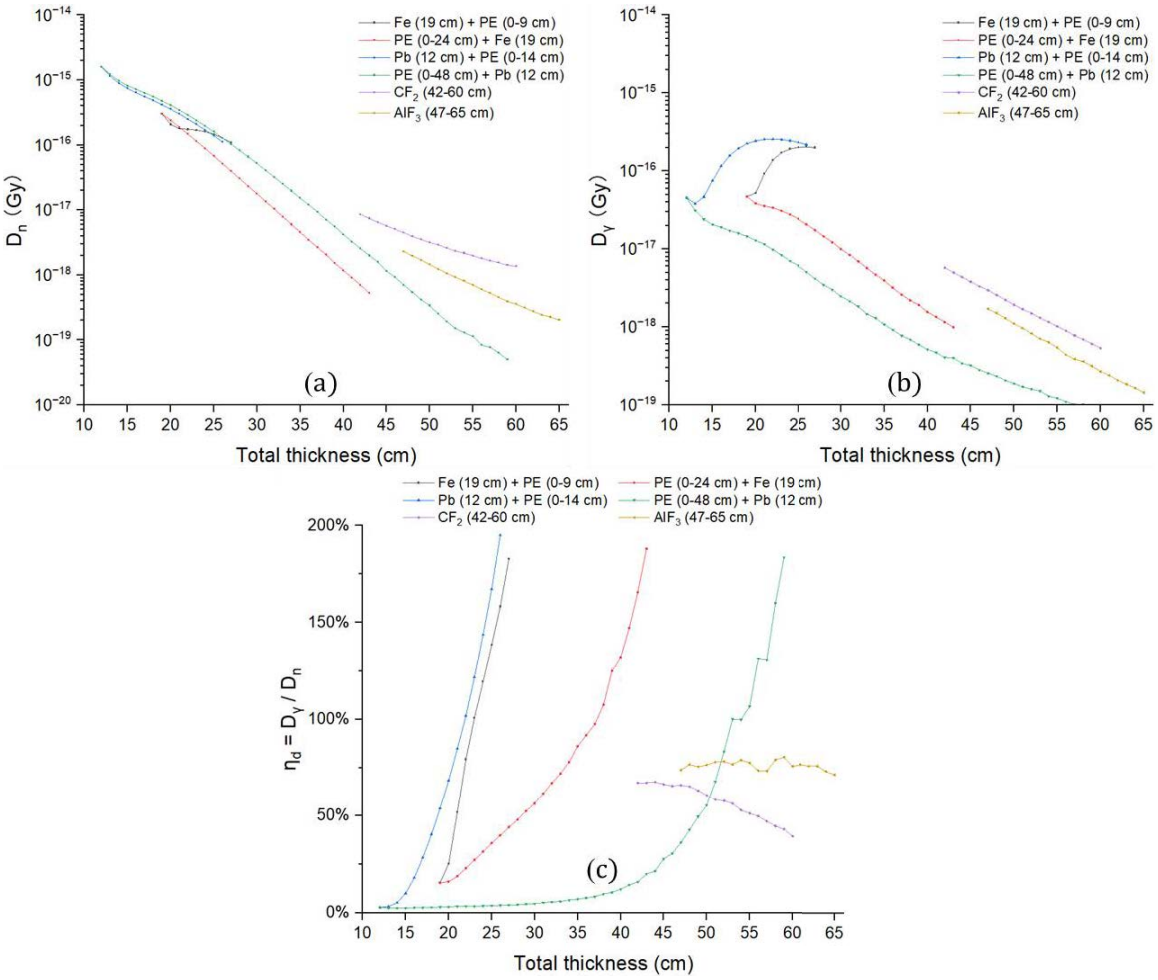

Figure 4: (a) Neutron dose, D_n; (b) Gamma-ray dose, D_γ; (c) Gamma-ray to neutron dose ratio, η_d.

3.2. Mixed field of neutron and gamma-ray

Neutrons produced in the n-γ mixed field were divided into three energy groups: (i) fast (0.01-2.5 MeV), (ii) epi-thermal (5×10^{-7}-0.01 MeV), and (iii) thermal (< 5×10^{-7} MeV) neutrons. Then the n-γ mixed fields were classified into three types: (i) Fast (F) -dominant, (ii) Epithermal (E) -dominant, and (iii) Thermal (T) -dominant fields.

3.2.1. F-dominant field

The results of F-dominant field are summarized in Table 1. η_d ranges from 2.5% to 188.1%. Because Fe has large cross-sections of (n,γ) reaction at thermal energy [12], PE + Fe is a suitable

combination to generate F-dominant fields, and PE (0-24 cm) + Fe (19 cm) provides: η_d from 15.5 to 188.1%, proportion of fast neutron from 88.0% to 99.8%, and gamma-ray energy in 0-10.1 MeV.

Table 1. Characteristics of F-dominant fields

Material	Gamma-ray to neutron dose ratio, η_d	Proportion of fast neutron	Gamma-ray energy, MeV
PE (0-8 cm) + Pb (12 cm)	2.5-3.2%	51.6-100.0%	0-7.3
Pb (12 cm) + PE (0-8 cm)	2.8-68.5%	48.5-100.0%	0-7.3
Fe (19 cm) + PE (0-4 cm)	15.5-100.9%	48.6-99.8%	0-10.1
PE (0-24 cm) + Fe (19 cm)	15.5-188.1%	88.0-99.8%	0-10.1

3.2.2. E-dominant field

The results of E-dominant field are summarized in Table 2. η_d ranges from 39.4% [CF_2 (42 cm)] to 80.5% [AlF_3 (65 cm)], and it is difficult to enhance η_d by increasing the thickness of the material. Besides, the contribution of the gamma-rays emitted from the target remained 5.6% and 3.2% on average for CF_2 (42-60 cm) and AlF_3 (47-65 cm), respectively.

Table 2. Characteristics of E-dominant fields

Material	Gamma-ray to neutron dose ratio, η_d	Proportion of epithermal neutron	Gamma-ray energy, MeV
CF_2 (42-60 cm)	39.4-67.7%	54.4-72.8%	0-7.3
AlF_3 (47-65 cm)	71.3-80.5%	56.0-80.6%	0-9.0

3.2.3. T-dominant field

The results of T-dominant field are summarized in Table 3. η_d ranges from 5.9% to 195.1%. Because Pb has large cross-sections of (γ,absorption) reaction [12], PE + Pb is a suitable combination to suppress η_d to generate T-dominant fields, and PE (13-47 cm) + Pb (12 cm) provides: η_d from 3.8% to 183.6%, proportion of thermal neutron from 49.4% to 66.6%, and gamma-ray energy in 0-6.1 MeV.

Table 3. Characteristics of T-dominant fields

Material	Gamma-ray to neutron dose ratio, η_d	Proportion of thermal neutron	Gamma-ray energy, MeV
Pb (12 cm) + PE (12-14 cm)	143.7-195.1%	48.3-52.8%	0-6.8
Fe (19 cm) + PE (7-8 cm)	158.2-182.8%	49.4-54.6%	0-10.1
PE (13-47 cm) + Pb (12 cm)	3.8-183.6%	49.4-66.6%	0-6.1

3. Conclusion

In this study, various types of n-γ mixed fields were designed to provide standard n-γ mixed fields for validation experiments of the material-filtered RPLGD for BNCT. To remove the contribution of the gamma-rays emitted from the target, 19 cm Fe and 12 cm Pb were determined as a minimum thickness to suppress η_t to approximately 0%. PE was an effective material to adjust η_d between 0% and 200%. The material combinations to generate n-γ mixed fields were recommended: (i) PE (0-24 cm) + Fe (19

cm) for F-dominant fields; (ii) CF_2 (42-60 cm) and AlF_3 (47-65 cm) for E-dominant fields (η_t was not neglectable); and (iii) PE (13-47 cm) + Pb (12 cm) for T-dominant fields. These results indicate that the moderation method by using a D-D neutron source is feasible to generate standard reference n-γ mixed fields for developing RPLGD for a p-Li neutron source based BNCT system.

Acknowledgements

This work was supported by China Scholarship Council (No.202106240024) and JSPS KAKENHI (No. JP19H02648).

References

1. International Atomic Energy Agency. Current Status of Neutron Capture Therapy, IAEA-TECDOC-1223, IAEA, Vienna (2001). pp. 1-2.

2. Kiyanagi Y, Sakurai Y, Kumada H, Tanaka H. Status of Accelerator-Based BNCT Projects Worldwide. AIP Conference Proceedings 2160; 2019, vol.2160, no.05012, pp.1-9.

3. International Atomic Energy Agency, Relative biological effectiveness in ion beam therapy. Vienna, Austria: Technical Reports Series No. 461, 2008, pp. 9.

4. Ferrulli F, Dinar N, Manzano LG, Labalme M, Silari M. Characterization of stilbene and EJ-276 scintillators coupled with a large area SiPM array for a fast neutron dose rate detector. Nuclear Instruments & Methods in Physics Research Section a-Accelerators Spectrometers Detectors and Associated Equipment. 2021; vol.1010, no.165566, pp.1-10.

5. Lin YC, Roca A, Liu YH, Tsai PE, Nievaart S, Liu HM, Moss R, Chou WT, Jiang SH. The dose comparison between the THOR and HFR epithermal neutron beams. Radiation Measurements. 2010; vol.45, no.10: pp.1422-1426.

6. Ogawara R, Kusumoto T, Kobayashi A, Konishi T, Hamano T, Kodaira S. Discrimination of hydroxyl radical yields due to thermal neutrons, fast neutrons, and gamma rays in accelerator-based neutron fields. Radiation Physics and Chemistry. 2020; vol.173, no.108889, pp.1-5.

7. Horiike H, Murata I, Iida T, Yoshihashi S, Hoashi E, Kato I, Hashimoto N, Kuri S, Oshiro S. Liquid Li based neutron source for BNCT and science application. Appl Radiat Isotopes. 2015; vol.106, pp.92-94.

8. Hiramatsu K, Yoshihashi S, Kusaka S, Sato F, Hoashi E, Murata I. Gamma-Ray Dose Measurement with Radio-Photoluminescence Glass Dosimeter in Mixed Radiation Field for BNCT. Epj Web Conf. 2017; vol.153, no.04009, pp.1-9.

9. X-5 Monte Carlo Team. MCNP - A General N-Particle Transport Code, Version 5. 2003, updated 2005. pp. 3-78.

10. Brown DA, Chadwick MB, Capote R, et al. ENDF/B-VIII.0: The 8th Major Release of the Nuclear Reaction Data Library with CIELO-project Cross Sections, New Standards and Thermal Scattering Data. Nucl Data Sheets. 2018; vol.148, pp.1-142.

11. K. Sumita, A.Takahashi, T. Iida, et al. Osaka University 14 MeV Intense Neutron Source for Fusion Studies. (OKTAVIAN Program) Fusion Technology. 1981; 1: pp.675-680.

12. Evaluated Nuclear Data File (ENDF), Database Version of 2022-10-07. [Published: International Atomic Energy, Agency. Available from: https://www-nds.iaea.org/exfor/endf.htm (accessed 2022-02-23).

17. Design investigation of pencil-beam epi-thermal neutron source for validation of low-energy neutron spectrometer

Yu FUJIWARA*, Shingo TAMAKI, Sachie KUSAKA, Fuminobu SATO and Isao MURATA
Graduate School of Osaka University
2-1, Yamadaoka, Suita, Osaka, 565-0871, Japan
*Email: fujiwara21@qr.see.eng.osaka-u.ac.jp

We have developed a spectrometer to measure the energy spectrum in the epi-thermal neutron region (0.5 eV~10 keV). Although the validation experiments of this spectrometer were carried out, there was a discrepancy between the measured and simulated values so the effectiveness cannot be confirmed. We considered that this discrepancy was attributed to neutron incidence from the side of the detector and it was found that a pencil-beam neutron source was required to improve the measurement accuracy.

In this study, we tried to design the beam performance by introducing a "Pre-collimator" to the original beam shaping assembly using Monte Carlo Simulation. Since the previous method could not simulate beam-neutrons, i.e. neutrons generated in a very forward direction, a new method that is separating the calculation into two stages was introduced. As a result, we succeeded in dramatically improving the error of the MCNP calculation from 43% to 2% compared to the previous studies.

Based on this calculation method, design calculations were performed for the pre-collimator to determine four parameters. As a result, the parameters of the pre-collimator were polyethylene as the material, 70 cm in thickness, 1.4 cm as the collimator hole diameter, and 300 cm as the distance from the assembly. Finally, the beam performance was confirmed by calculating the radial and horizontal flux distributions. The results showed that the designed neutron source has excellent performance up to 40 cm from the exit of the pre-collimator.

1. Introduction

Boron neutron capture therapy (BNCT) is attracting attention as a next-generation cancer treatment. BNCT uses epi-thermal neutrons and it is possible to selectively treat only cancer cells. Using this advantage, it is expected to treat refractory cancers such as glioblastoma, and recurrent cancers [1]. Currently, developing an accelerator-based neutron source (ABNS) for BNCT is underway, and evaluating the characteristics of the neutron field generated by the accelerator is one of the issues [2]. One of the characteristics is the energy spectrum in the epi-thermal neutron region (0.5 eV ~ 10 keV). It is necessary to assess treatment effects such as exposure dose. However, there is no accurate method to measure it.

We have been developing a new measurement method with a ^{3}He position-sensitive proportional counter. Figure 1 shows our position-sensitive proportional counter. Using this detector, signals about where neutrons react with the ^{3}He can be obtained [3]. ^{3}He has a large (n,p) reaction cross-section at low energy

and as shown in figure 2, the cross-section is proportional to the neutron energy [4]. Therefore, low-energy neutrons react in the shallow of the spectrometer, and high-energy neutrons are detected in the deeper places of the spectrometer. As a result, we can measure the distribution of the positions where neutrons react with ^{3}He regarding the depth of the spectrometer. We define this information as "Depth distribution, y (r)." Then, we calculate the response rate to monochromatic energy, which is regarded as a "response function, R." The energy spectrum can be obtained based on the following equation (1);

$$y_i = R_{i,j} \cdot x_j \quad (1)$$

y_i is the depth distribution, $R_{i,j}$ is the response function, and x_j is the energy spectrum. To solve equation (1) is "spectrum unfolding," and we apply Bayesian estimation as a method to solve [5].

We confirmed that this method could be used to measure the neutron energy spectrum from the thermal region up to 1 keV [6]. Figure 3 shows the experimental system for the validation by Osawa et al.[6] Figure 4 shows the validation results. y (r) was obtained as shown in Figure 4 (a), and it was converted to the energy spectrum was estimated. Compared to the simulation value (shown in figure 4 (b)), there was a discrepancy and we concluded that the reason was the large influence of neutrons incident from the side surface of the detector. To correctly and accurately validate the spectrometer, a pencil-beam type low-energy neutron source is necessary, and we carry the design in the present study.

Figure 1: Presently employed position sensitive proportional counter

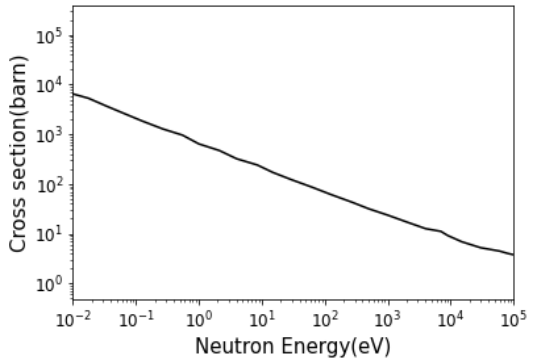

Figure 2: (n, p) cross section of ^{3}He [4]

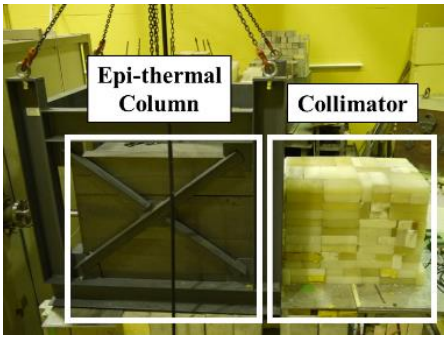

Figure 3: Experimental system of the spectrometer validation [6]

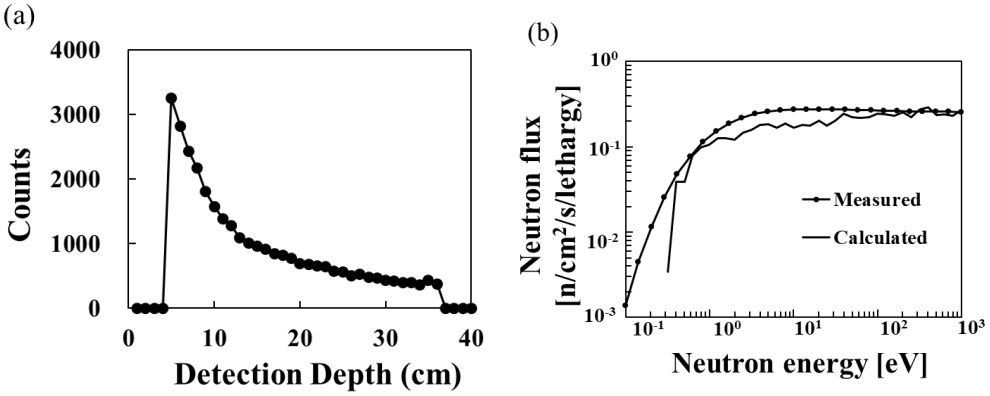

Figure 4: (a) Depth distribution measured in the previous research. (b) Comparison of the experimentally obtained neutron energy spectrum and the calculated one. [6]

2. Methods

2.1. Improvement of calculation Method

Though an attempt to make a pre-collimator was carried out in a previous study, the beam characteristics remained issues [8]. In the previous study, the entire calculation was conducted by SSW/SSR options in MCNP5. The SSW/SSR option can be used to reduce the calculation time substantially for a complex geometry very large system or system in which large particle attenuation is expected. The mechanism is as follows; first, an SSW surface is defined at an exit of the epi-thermal column, and all the transport data of neutrons passing through the exit surface are stored for all the neutron histories. Next, the neutron information obtained by the SSW option is connected to the SSR surface at the entrance surface of the spectrometer (inside the collimator), and calculations between the right-hand side of the epi-thermal column and spectrometer are carried out.

However, under certain conditions, this method has been found to have limitations. For instance, we set a large space between the epi-thermal column and the spectrometer. In this case, only neutrons having very small emission angles at the epi-thermal column surface can reach and contribute to the spectrometer. Figure 6 shows the energy spectrum of neutrons for various emission angles at the column surface. These are made by the transport data stored by the SSW option. As shown in Figure 5, the epi-thermal neutron spectrum in the very forward direction ($\cos\theta > 0.99$) cannot be reproduced well. If the calculation is carried out by this stored transport data in SSW, few neutrons can reach the detector in the design simulation depending on the distance between the epi-thermal column and pre-collimator. Therefore, we employed the following two steps instead of the use of the SSW/SSR option.

Step 1: Calculate the energy and angular distributions of neutrons on the exit of the epi-thermal column.

Step 2: Set the source on the exit surface and carry out the neutron transport calculation through the pre-collimator to the spectrometer under the following source term conditions.

I. Neutron energy distribution: Neutron energy spectrum calculated in Step 1.

II. Emission angle distribution: Precisely calculated emission angle distribution.

III. Set bias in the emission angle. To obtain accurate calculation results without underestimating the reaction rate, the optimum range of emission angle was determined by calculating the reaction rate with ^{3}He in various emission angle.

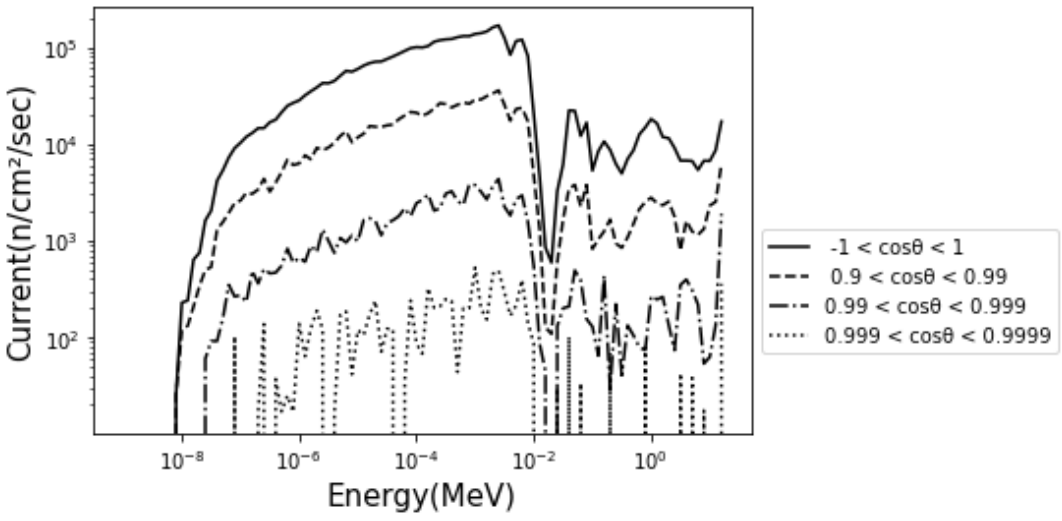

Figure 5: Neutron spectrum at the exit of the epi-thermal column for various emission angles

2.2. Design Model

Figure 6 shows an image of the experimental system for the verification experiment of the present low-energy neutron spectrometer. Compared to the experimental system in the previous study (figure 2), we added a shielding material between the epi-thermal column and the spectrometer with a collimator. We named it a "pre-collimator". Then, we thought of the following four parameters in the design simulation, i.e., (1) material, (2) width, (3) hole diameter, and (4) distance to the epi-thermal column. As a simulation code, MCNP5 [7] was employed. Also, we used JENDL-4.0 [4] as the nuclear data library for the design calculations. In the design, we set three design goals for beam performance;

I. "The ratio of neutrons detected as ***A component*** **(R_A)** should be 99% or higher"

II. "The number of neutrons detected as the *A component* **(N_A)** should be 10,000 counts or higher.

III. "The ratio of neutrons detected as ***B component*** **(R_B)** should be 0.1% or less

In this study, we categorize the neutron detected by the ^{3}He counter into three categories, *A*, *B*, and *C*, as shown in Figure 7.

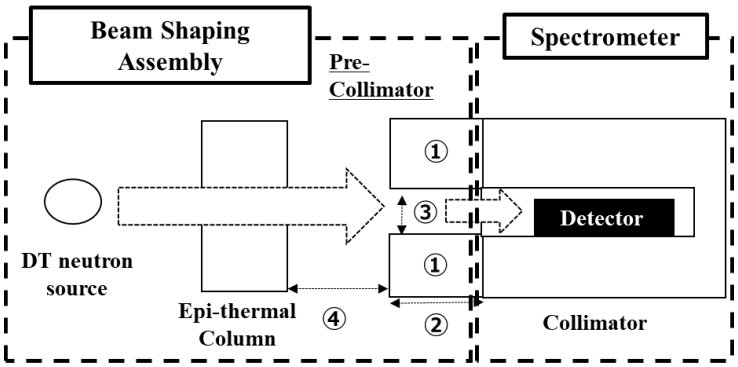

Figure 6: Image of the experimental system

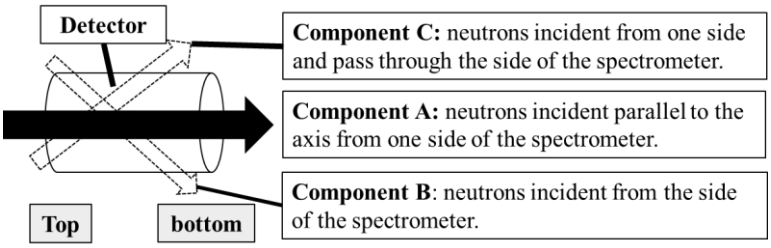

Figure 7: Three possible paths of neutron passing through the detector

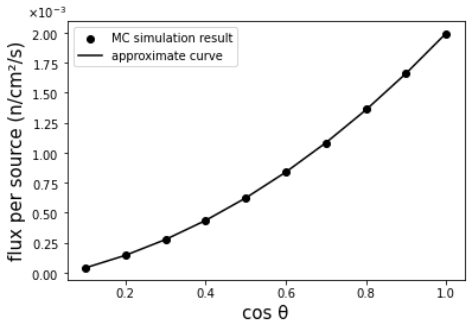

Figure 8: Angular flux at the exit of the epi-thermal column

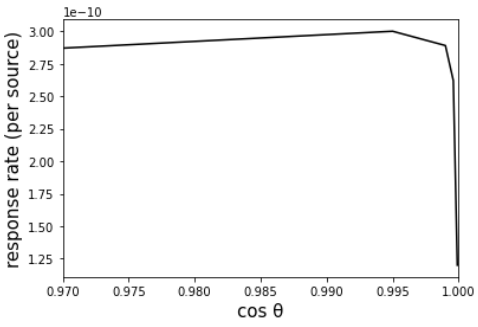

Figure 9: Reaction Rate in the detector with respect to emission angle

3. Results

3.1. Comparison with SSW/SSR

Figure 8 illustrates the angular flux distribution at the exit of the epi-thermal column calculated in MCNP. Third-order Legendre polynomial approximations were performed from this data, and the very-forward emitting neutrons are produced at the exit of the epi-thermal column with this equation. Using this angular distribution and energy spectrum shown in figure 5, the design calculation was carried out. Then, figure 9 shows the reaction rate at the detector for the emission angle under the following conditions: (1) polyethylene, (2) 50 cm, (3) 2.5 cm, and (4) 100 cm. This result meant that while the reaction rate was underestimated in the condition that the emission angle was limited to very forward only, gradually the neutrons no longer affect the reaction rate. In this study, the optimal emission angle was determined the $\cos\theta = 0.995$. To demonstrate the validity of our proposed calculation method, the neutron flux as a function of the distance from the collimator exit was calculated in each case. Typically, in the present result, the neutron flux intensity decreases smoothly as the distance from the source increases. However, the SSW/SSR method shows an unexpected fluctuation in the intensity distribution. This is because the amount of the accumulated transport data with the SSW option is limited, e.g., the number of histories accumulated is not so large compared to the one required in the connecting calculation. Consequently, the reliability of the SSW/SSR method is questionable, especially in the present design case. More practically, we compared the results obtained by our method and the SSW/SSR method for the number of particles reaching the detector and its statistical error with MCNP. While only 3.0×10^2 particles reached the detector assuming 10^{10} particles in SSW/SSR method, 3.3×10^4 particles reached the detector for 10^7 particles in our method. In addition, the statistical error of MCNP calculations is significantly improved to approximately 2% compared to nearly 40% for SSW/SSR. Therefore, this method was thought to be able to perform the current design calculations accurately.

3.2. Pre-collimator design

Table 1 shows the designed four parameters and the performance, the values of R_A, N_A, and R_B of the pre-collimator [9]. The presently designed epi-thermal neutron beam met the design target I and III. However, the design goal II was not met. It would be possible to satisfy the condition by extending the irradiation time.

3.3. Beam performance

In order to investigate the performance of the designed beam, we calculated the horizontal flux distribution from the pre-collimator exit and the radial distribution from the center of the pre-collimator. Figure 11 illustrates the results. X in figure 11 (b) meant the distance from collimator. As for the horizontal flux distribution, this neutron source has good beam performance with little reduction in the range from 10 cm behind the pre-collimator to 40 cm backyards. Sharp reduction by 10 cm behind the pre-collimator was considered that it was attributed to the cadmium sheet set at the exit of the pre-collimator. From the radial flux distribution, the spread of neutron was found. This information should be investigated by the experiment.

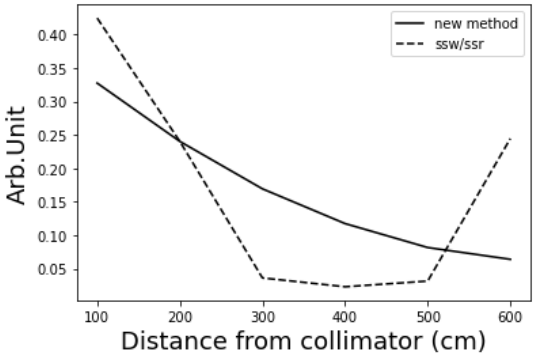

Figure 10: Neutron fluxed as a function of the distance from the exit of collimator

Table 1: Design results and performance [9]

Material	Polyethylene
Width	70 cm
Hole Diameter	1.4 cm
distance to the epi-thermal column	3 m
R_A	99.6 %
N_A	2.6×10^3
R_B	0.04 %

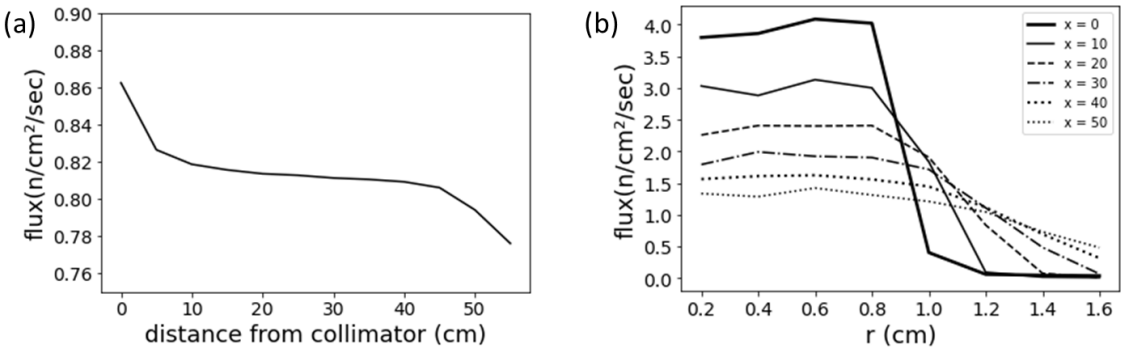

Figure 11: (a) Horizontal flux distribution (b) Radial flux distribution

4. Conclusion

We have designed a pencil-beam neutron source for the validation experiment of the low-energy neutron spectrometer, especially in the epi-thermal neutron region. By installing a pre-collimator, we realized reducing the effect of neutrons incident from the side surfaces of the detector to less than 1%. In the future, we will conduct validation experiments using the designed neutron beam to demonstrate the effectiveness of the new epi-thermal neutron spectrometer. Furthermore, we plan to apply the neutron beam designed in this study to BNCT and a wide range of other fields.

References

[1] Locher, G, L. *Am. J. Roentgenol. Radium. Ther.* 1936; 36: 1-13.
[2] I, Murata, et al. *Plasma and Fusion Res.* 2018; 13: 2501007.
[3] Fischer B. E. *Nucl. Instrum. Meth.* 1977; 141: 173-181.
[4] K. Shibata, et al. *J. Nucl. Sci. Technol.* 2011; 48(1): 1-30.
[5] I, Murata, H. Miyamaru. *Nucl. Instrum. And Meth. Phys. Res. A.* 2008; 589: 445-454
[6] Y. Osawa. *Master-Dissertation*, Osaka University; 2017.
[7] X-5 Monte Carlo Team: MCNP-A General Monte Carlo N-Particle Transport Code, version 5; 2003.
[8] M. Tanoshita. *Master-Dissertation*, Osaka University; 2018.
[9] Y. Fujiwara, et al. *Proceedings of the 37th Workshop on Radiation Detectors and Their Uses in KEK*; 2023: in-press.

18. Estimation of the Total Angular Momentum of Resonances using Low-energy Gamma-rays in ^{181}Ta(n, γ)^{182}Ta Reaction

Shiori KAWAMURA[†1,2], Shunsuke ENDO[1,2], Osamu IWAMOTO[2], Nobuyuki IWAMOTO[2], Atsushi KIMURA[2], Masaaki KITAGUCHI[1], Shoji NAKAMURA[2], Takuya OKUDAIRA[1,2], Gerard ROVIRA[2], Hirohiko M SHIMIZU[1], and Hiromoto YOSHIKAWA[3]

[1]Nagoya University, Furo-cho, Chikusa-ku, Nagoya, Aichi 464-8602, Japan
[2]Nuclear Data Center, Nuclear Science and Engineering Center, Japan Atomic Energy Agency, Tokai, Ibaraki 319-1195, Japan
[3]Research Center for Nuclear Physics, Osaka University, 10-1 Mihogaoka, Ibaraki, Osaka 567-0047, Japan

[†]Email: kawamura@phi.phys.nagoya-u.ac.jp

Abstract

The total angular momentum, J, of resonances is one of the most important parameters in low energy nuclear reactions. In this study, J of resonances were estimated by taking the ratios between low-energy gamma-rays in $^{181}\mathrm{Ta}(n,\gamma)^{182}\mathrm{Ta}$ reaction. This method is based on the Spin-Memory Effect (SME), in which the spin information of the resonance state remains in the lower levels. In this study, J of 17 resonances were estimated with good accuracy from neutron capture reaction measurement at J-PARC MLF ANNRI. Furthermore, the difference in intensity ratios between 270-keV and 403-keV gamma-rays due to J, SME, was confirmed, even though it did not appear in the theoretical value of CCONE. This result suggests that there are unknown transitions.

1 Introduction

A nucleus is a very complex system dominated by strong nucleon-nucleon interactions. In 1936, the compound nuclei model was proposed by Bohr to explain phenomena in neutron capture reactions [1]. A nuclear reaction through the compound nuclei are often understood by a statistical model, especially the Random Matrix Theory (RMT). According to RMT, the distributions of neutron width and partial gamma width of resonances follow the Porter-Thomas distribution [2]. Verifying whether the partial gamma widths follow the Porter-Thomas distribution will give a better understanding of what nuclides and what conditions RMT can be applied to. In order to examine that, the total angular momentum, $J = I \pm 1/2$ where I is the spin of a target nucleus, of s-wave resonances must be determined precisely.

Nuclear data libraries have been used in various fields such as reactor physics and nuclear physics. Thus more accurate data has been required. However, experiments have been associated with difficulty in determining J in many resonances. Since gamma-ray transitions between excited levels are limited by the law of conservation of the angular momentum, the J of the resonances could be directly determined from the primary gamma-ray transitions. However,

in fact, the intensity of primary gamma-rays may be weak or absent in the spectrum of a resonance because of the Porter-Thomas fluctuation for partial gamma width. Therefore, there is the potential for difficulty to identify the selected high-energy gamma-rays and to estimate J of resonances.

Several methods have been proposed to estimate J of resonances from a gamma-ray spectrum without using primary gamma-ray transitions [3–5]. A method was to compare the intensity ratios of appropriately chosen pairs of low-energy transitions in the gamma-ray spectrum of a resonance [5]. This method is based on the Spin-Memory Effect (SME) proposed by Huizenga and Vandenbosch [6]. SME means that the spin information of an initial resonance state remains, even if there are many intermediate excited levels in the cascade transitions. This effect appears as differences in low-energy gamma-ray spectrum. If a transition where SME exits is selected, the intensity ratio of two transitions can be grouped around two different average values corresponding to J of resonances.

Olejniczak et al. [7] suggested that the larger spin difference between two excited levels emitting low energy gamma-rays, stronger SME appears. They also indicated that the SME is stronger for nuclei closer to the atomic number of $Z = 50$, namely magic number. In this study, J of resonances of ^{181}Ta ($Z = 73$) was estimated from the intensity ratio of 403-keV to 270-keV gamma-rays, which are emitted from same spin but different parities, in the $^{181}\mathrm{Ta}(n,\gamma)^{182}\mathrm{Ta}$ reaction. According to Olejniczak et al., SME is predicted to be weak because the atomic number of Ta is far from the magic number and the spin difference between adopted levels is small. Nevertheless, a difference of the intensity ratios was observed, and J of resonances of ^{181}Ta was estimated. The results were compared with Riehs et al. [8] and CCONE [9].

2 Experiment

The experiment was performed with the time-of-flight (TOF) method at the Accurate Neutron–Nucleus Reaction Measurement Instrument (ANNRI) of the Material and Life Science Experimental Facility (MLF) in the Japan Proton Accelerator Research Complex (J-PARC) [10]. At ANNRI, a high-intensity pulsed neutron beam with 6-mm diameter and a Ge-detector array covering a large solid angle with high resolution were used. Metalic natural Ta sample with dimensions of 6 mm × 6 mm × 2 mm was set at a 21.5 m flight path.

3 Analysis

The resonance energy was taken from JENDL-5 [11], and the gamma-ray spectra from resonances were obtained by gating the TOF spectrum at each resonance. Figure 1 shows the TOF spectrum of $^{181}\mathrm{Ta}(n,\gamma)^{182}\mathrm{Ta}$ reaction. The obtained gamma-ray spectrum in the low gamma-ray energy region of 4.28-eV resonance (751 μs in TOF) is shown in Figure 2. The background was determined with connecting both sides of the tail for the gamma-ray peak. The integral of the entire peak minus the integral of the background was defined as net-counts. The value of J was estimated from the ratio of the net-counts between the 270-keV and 403-keV gamma-rays. The ratios of the net-counts between the 270-keV and 403-keV gamma-rays were defined as $R = S_b/S_a$, where S_a and S_b are the net-counts of the 270-keV and 403-keV gamma-rays, respectively. The detection efficiency at 270-keV (403-keV) was defined as ϵ_a (ϵ_b) and the intensity as I_a (I_b), the net-counts was expressed $S_a = \epsilon_a \cdot I_a$ ($S_b = \epsilon_b \cdot I_b$). Since the net-counts depend on the detection efficiencies for each gamma-ray energy, the absolute value of the intensity ratio, R is affected by detection efficiency. However, since only the intensity ratios of two groups, $J = 3$ and 4, defined as $Q = \langle R_4 \rangle / \langle R_3 \rangle$, where $\langle R_4 \rangle$ and $\langle R_3 \rangle$ are the weighted averages of the

net-count ratios for the resonances estimated as $J = 4$ and 3, are considered in this analysis, a correction for the detection efficiency was not required.

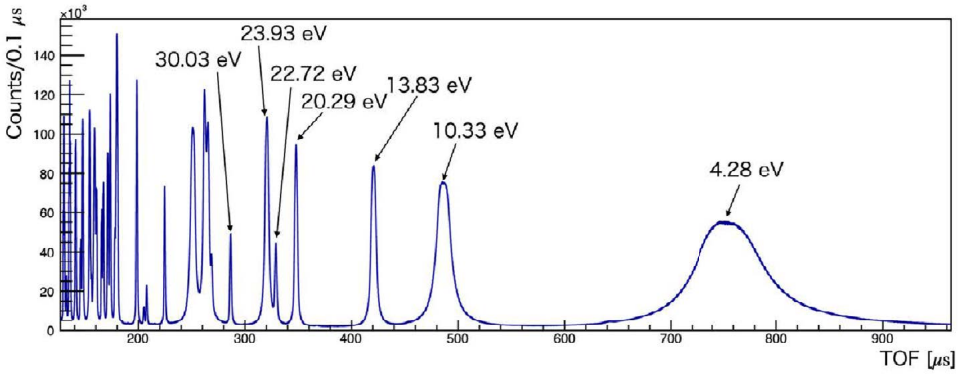

Figure 1: TOF spectrum measured with the metallic natural Ta sample. Many resonances were observed and labeled with the values of their energies taken from JENDL-5 [11].

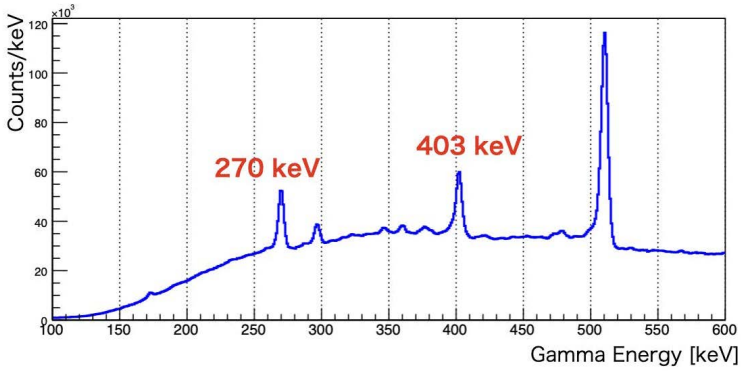

Figure 2: The gamma-ray spectrum in the range of 100 keV to 600 keV emitted from 4.28-eV resonance.

4 Results and Discussion

The ratios of the net-counts between the 270-keV and 403-keV gamma-rays, defined as R, are plotted for each resonance in Figure 3. The red line in Figure 3 indicates the average value of all ratios. The average value $\langle R \rangle$ was 1.24 ± 0.01. The error in $\langle R \rangle$ results from the constant fitting of the ratios. The obtained ratios were clearly separated into two groups. We estimated J of the resonance relative to the average value. This estimation was based on the result that J of the 4.28-eV (10.36-eV) resonance was determined with good precision to be 4 (3) [13]. Table 1 displays the estimated J, compared with evaluated data of JENDL-5 and ENDF/B-VIII.0 and the result of Riehs et al. [8]. Since the errors for 35.9-eV, 57.53-eV, 82.92-eV, and 91.4-eV resonances crossed the average value, J of these resonances could not be fixed. The estimated J was mostly consistent with the study of Riehs et al. [8] and JENDL-5 [11]. However, some differences with ENDF/B-VIII.0 [12] were observed. In this study, J of 17 resonances were estimated with good statistical accuracy and suggestions were given for J of 4 resonances by using the method based on SME.

The weighted averages of the resonances estimated as $J = 4$ and $J = 3$ were defined as $\langle R_4 \rangle$ and $\langle R_3 \rangle$ and shown in Figure 3 with the blue and green lines, respectively. $\langle R_4 \rangle =$

Table 1: Assignment of J for ^{181}Ta+n resonances. Number in parenthesis represents the results from the ratios whose error crosses the average value.

Resonance Energy [eV]	J			
	JENDL-5 [11]	ENDF/B-VIII.0 [12]	Riehs et al. [8]	Present Work
4.28	4	4	4	4
10.33	3	3	3	3
13.83	4	4	4	4
20.29	3	4	3	3
22.72	3	3	(3)	4
23.93	4	3	4	4
30.03	3	4	3	3
34.21	4	3		
35.14	3	4	3	3
35.91	4	3	4	(4)
39.12	4	4	4	4
49.11	3	3	3	3
57.53	4	4		(3)
59.05	4	3		
63.10	4	4	4	4
76.84	4	3		4
77.61	4	4		
78.89	3	3		
82.89	4	4	4	4
85.10	3	3	(3)	(3)
85.60	4	4		
89.58	3	4		4
91.38	3	4		(3)
96.95	4	3		
99.27	3	4	3	3
103.5	3	3		
105.5	3	4	3	3
115.0	4	3	4	4

1.32 ± 0.01 and $\langle R_3\rangle = 1.12\pm0.01$ were obtained. In order to compare the results with theoretical values and to quantitatively describe the strength of SME, $Q = \langle R_4\rangle/\langle R_3\rangle$ was used, and $Q = 1.17\pm0.01$. Furthermore, expressing the ratio of difference $|\langle R_4\rangle - \langle R_3\rangle|$ from their average value $(\langle R_4\rangle + \langle R_3\rangle)/2$ in percentage, SME $= 200|Q-1|/(Q+1) = 15.8\%$ was obtained. This SME value is small, compared to those (27%-32%) of Olejniczak et al. [7]. This may be ascribed to the small spin differences between transition levels. Despite the fact that ^{181}Ta is a nuclide with $Z = 73$, whose atomic number is far from the magic number, and the gamma-rays of 270-keV and 403-keV are transited from the same spin state, a weak SME appears. This result suggests that the SME appears regardless of the atomic number of the nuclide and the spin state of the gamma-ray taking the intensity ratio.

It is interested in comparing the obtained results with the values calculated with a theoretical model. In order to do this, the Hauser-Feshbach statistical model code CCONE was utilized [9]. In the CCONE code, excited level information was taken from RIPL-3 database and gamma-ray strength functions were based on the generalized Lorentzian model for E1 radiation and the Lorentzian model for M1 and E2 radiations. Excited states of $J = 3$ and 4 were generated close

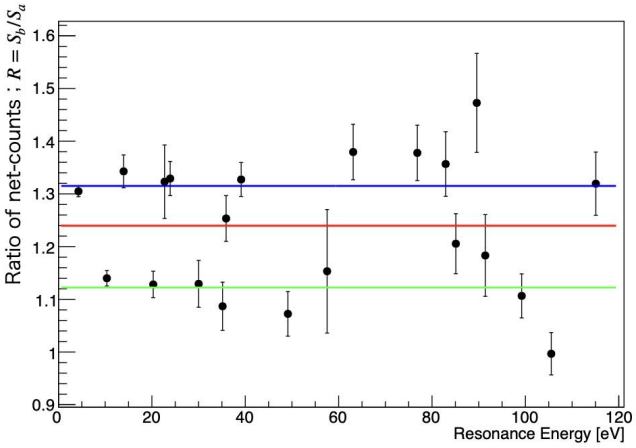

Figure 3: Ratios of the net-counts of 270-keV and 403-keV gamma-ray for each resonance. The red line indicates the average value of all ratios. The weighted average values $\langle R_4 \rangle$ and $\langle R_3 \rangle$ of $J = 4$ and 3 are shown by blue and green lines, respectively.

to the neutron binding energy of ^{182}Ta. Gamma-ray decays from each J-state were calculated. The resulting production cross sections of 403-keV and 270-keV gamma-rays were 23.9 and 42.7 mb for $J = 3$ and 15.3 and 27.5 mb for $J = 4$, respectively. The gamma-ray spectra in a low gamma-ray energy region calculated with CCONE are shown in Figure 4. The ratio of the 403-keV to 270-keV gamma-ray intensities was found to have the same value, 0.57 for both J. Therefore, theoretical results indicate no difference in these gamma-ray intensities. But the clear difference was observed in the present experimental result. This fact suggests that there are unknown transitions to reach the two excited levels which emit 270-keV and 403-keV gamma-rays. In the CCONE calculation the upper excitation energy of ^{182}Ta was chosen to be 817 keV, above which missing levels and transitions increase. The number of adopted excited levels may be too small to follow complicated gamma-ray transitions. This result can help to construct a new validated level scheme.

Before concluding that SME of ^{182}Ta is weak, it is necessary to examine SME with the other low-energy gamma-rays in ^{181}Ta$(n,\gamma)^{182}$Ta reaction. In addition, SME of the other nuclei far from magic number of $Z = 50$ should be examined with the same method.

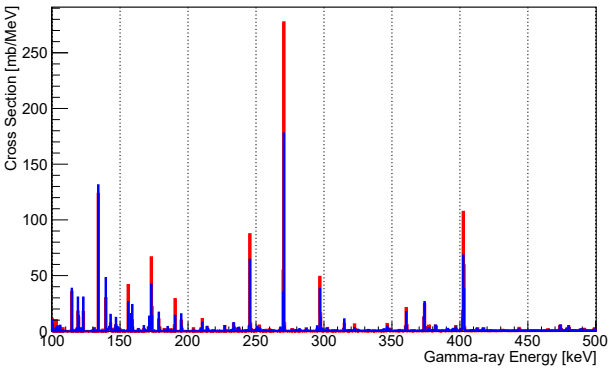

Figure 4: Gamma-ray spectra calculated with CCONE. The red and blue lines represent the gamma-rays from $J = 3$ and $J = 4$ resonances.

5 Conclusion

In this study, we estimated J of 17 resonances with good accuracy and also gave suggestions for J of 4 resonances up to 115 eV in ^{181}Ta$(n,\gamma)^{182}$Ta reaction using the ratio between 270-keV and 403-keV gamma-ray intensities from resonances. The obtained intensity ratios differed from theoretical value of CCONE, and this fact suggested that there are unknown transitions. It is also implied that SME appears independent of the atomic number and the spin state from which the gamma-ray transitions occur. It is necessary to use other low-energy gamma-rays of ^{182}Ta and use other nuclei to verify SME further. The estimated J in this study will be used to verify whether the partial gamma width follows the Porter-Thomas distribution.

Acknowledgments

The authors would like to thank the staff for their efforts in operating the accelerators and the neutron production target of MLF in J-PARC. The neutron experiments at ANNRI of MLF in J-PARC were performed under the project proposal (2022P0301).

References

[1] Bohr N. Neutron Capture and Nuclear Constitution. Nature. 1936;137:344-348.

[2] Porter CE, Thomas RG. Fluctuations of Nuclear Reaction Widths. Phys Rev. 1956;104(2):483-491.

[3] Coceva C, Corvi F, Giacobbe P, Carraro G. A method of spin assignment of neutron resonances based on capture gamma-ray detection. Nucl Phys A. 1968;117(3):586-614.

[4] Reddingius ER, Postma H, Olsen CE, et al. Spins of low-energy neutron resonances in ^{235}U. Nucl Phys A. 1964;218(1):84-94.

[5] Wetzel KJ, Thomas GE. Method for Determining Spins of Neutron Resonances. Phys Rev C. 1970;1(4):1501-1507.

[6] Huizenga JR, Vandenbosch R. Interpretation of Isomeric Cross-Section Ratios for (n,γ) and (γ,n) Reactions. Phys Rev. 1960;120(4):1305-1312.

[7] Olejniczak U, Gundorin NA, Pikelner LB, et al. Resonance-Spin Memory in Low-Energy-Gamma-Ray Spectra from Sb, Tb, Ho, and Ta Odd–Odd Compound Nuclei. Phys. At. Nucl. 2002;65(11):2044–2051.

[8] Riehs P, Axmann HP, Murray J, Thomas BW. Low-energy γ-rays from resonance neutron capture in ^{181}Ta$(n,\gamma)^{182}$Ta. Nucl Phys A. 1972;198(2):430-438.

[9] Iwamoto O, Iwamoto N, Kunieda S, et al. The CCONE code system and its application to nuclear data evaluation for fission and other reactions. Nuclear Data Sheets. 2016;131:259-288.

[10] Igashira M. Kiyanagi Y. Oshima M. Nuclear data study at J-PARC BL04. Nucl Inst Meth A. 2009;600(1):332-334.

[11] Iwamoto O, et al. Japanese Evaluated Nuclear Data Library version 5: JENDL-5. J. Nucl. Sci. Technol. in press.

[12] Brown D, Chadwick M, Capote R, et al. ENDF/B-VIII.0:The 8th Major Release of the Nuclear Reaction Data Library with CIELO-project Cross Sections, New Standards and Thermal Scattering Data. Nuclear Data Sheets. 2018;148:1-142.

[13] Stolovy A. Spin Determinations of Neutron Resonances in Sb, Ta, Re, and Ir, Using Iron-Alloy Targets. Phys Rev. 1967;155(4):1330-1333.

19. Theoretical study of low-excitation fission phenomena in unstable thorium isotopes

Wataru Miyasakai[1], Yoshihiro Aritomo[1], and Shinya Takagi[1]

[1]Faculty of Science and Engineering, Kindai University Higashi-Osaka, Osaka 577-8502, Japan

Abstract

The production yields of fission fragments close to the β stable line cause asymmetric fission with peaks in the heavier and lighter nuclei, but away from the β stable line, fission becomes symmetric. For example, at mass numbers near 226, Thorium (Th) exhibits both symmetric and asymmetric fission [1]. The reason why the fission mode depends on the ratio of neutron to proton number has been investigated by various theoretical models. Even the dynamical models, which have been very successful in the fission of neutron rich nuclei, have so far not succeeded in describing symmetric fission phenomena in proton rich nuclei.

In this study, we use the dynamical model, which can successfully describe the fission of Uraninm (U) and Plutonium (Pu) near the β stable line, to perform calculations for the fission of unstable nuclei away from the β stable line. Based on the results, we will propose a solution policy for the future development and evolution of the model.

1 Introduction

The nucleus is a quantum many-body system consisting of a finite number of nucleons. The various forms of existence and abundant modes of motion exhibited by this quantum many body system have not yet been fully elucidated, and nuclear structure theory, for which model improvements and new models have been proposed, focuses on the static and time-dependent dynamical properties of nuclei. One of the most important research topics is the dynamics of approximate binding conditions of nucleon many body systems. In our laboratory, we have been studying nuclear reactions by following the time evolution of the shape of nuclei with a dynamical model[2].

The dynamical model used in this study defines the shape of nuclei in terms of three parameters: the two center of distance z, the deformation degree δ, and the mass asymmetry α (two center shell model), and uses the Langevin equation, one of the equations of motion. The Langevin equation follows the time evolution of each trajectory by ordinary differential equations based on the fluctuation dissipation theorem, and is able to reproduce the actual width of fission phenomena from the dissipative fluctuation term.

Our previous studies have shown that the dynamical models we use in our theoretical calculations reproduce experimental data for stable fission, such as uranium (Z=92,U) and plutonium (Z=94,Pu), and contribute to the explanation of fission phenomena[1]. However, we cannot reproduce fission yields of experimental data for unstable nuclei[3]. The purpose of this study is to reveal the cause of this problem by analyzing the unstable nuclei thorium (Z=90,Th) in detail.

2 Framework

We use the fluctuation-dissipation model and employ the Langevin equations[4] to investigate the fission process. The nuclear shape is defined by the two center parametrization [5,6], which has three deformation parameters, z, δ, and α to serve as collective coordinates: z is corresponds to the distance between two potential centers, α is a mass-asymmetry parameter defined by (A_1-A_2)/(A_1+A_2) using fragment masses, A_1 and A_2. The symbol δ denotes the deformation of the fragments defined as $\delta = 3(R_{\parallel} - R_{\perp})/(2R_{\parallel}+R_{\perp})$, where $R_{\parallel}$ and $R_{\perp}$ are the half length of the axes of an ellipse in the z_0 and ρ directions of the cylindrical coordinate, respectively, as shown in Figure 1 in Ref. [4].

We adopted the neck parameter ε=0.35 following the empirical relation in Ref. [3]. The three collective coordinates are abbreviated as q, $q = \{z,\delta,\alpha\}$. For a given value of a temperature of a system T, the potential energy is defined as a sum of the liquid-drop (LD) part, a rotational energy and a microscopic (SH) part:

$$V(q,l,T) = V_{LD}(q) + \frac{\hbar^2 l(l+1)}{2I(q)} + V_{SH}(q,T), \tag{1}$$

$$V_{LD}(q) = E_s(q) + E_c(q), \tag{2}$$

$$V_{SH}(q,T) = E^0_{shell}(q)\Phi(T), \tag{3}$$

$$\Phi(T) = \exp\left(-\frac{aT^2}{E_d}\right), \tag{4}$$

Here, V_{LD} is the potential energy calculated with the finite range liquid drop model, given as a sum of the surface energy E_S [6] and the Coulomb energy E_C. V_{SH} is the shell correction energy evaluated by the Strutinski method from the single-particle levels of the two center shell model. The shell correction has a temperature dependence expressed by a factor Φ(T), in which E_d is the shell damping energy chosen to be 20 MeV [7] and a is the level density parameter. At the zero temperature ($T = 0$), the shell correction energy reduces to that of the two center shell model values E^0_{shell}. The second term on the right hand side of Eq. (1)is the rotational energy for an angular momentum l [4], with a moment of inertia at q, $I(q)$.

The multidimensional Langevin equations [4] are given as

$$\frac{dq_i}{dt} = \left(m^{-1}\right)_{ij} p_i, \tag{5}$$

$$\frac{dp_i}{dt} = -\frac{\partial V}{\partial q_i} - \frac{1}{2}\frac{\partial}{\partial q_i}\left(m^{-1}\right)_{jk} p_j p_k - \gamma_{ij}\left(m^{-1}\right)_{jk} p_k + g_{ij} R_j(t) \tag{6}$$

where i =$\{z,\delta,\alpha\}$ and p_i is a momentum conjugate to coordinate q_i . The summation is performed over repeated indices. In the Langevin equation, m_{ij} and γ_{ij} are the shape-dependent collective inertia and the friction tensors, respectively. The wall-and-window one-body dissipation [8-10] is adopted for the friction tensor which can describe the pre-scission neutron multiplicities and total kinetic energy of fragments simultaneously [11]. A hydrodynamical inertia tensor is adopted with the Werner-Wheeler approximation for the velocity field [12]. The normalized random force R_i(t) is assumed to be that of white noise, i.e., $\langle R_i(t)\rangle$=0 and $\langle R_i(t_1)R_j(t_2)\rangle$=$2\delta_{ij}\delta(t_1 - t_2)$. The strength of the random force g_{ij} is given by the Einstein relation $\gamma_{ij}T = \sum_k g_{ij}g_{jk}$

3 Results

In the current situation, as a cause of the strong asymmetric fission, we have explained the fission phenomena by confirming the dynamical trajectories and potential structures of ^{226}Th

nuclides. By looking at the structure of the z-α plane potential in the ^{226}Th calculated in this study as well, we are able to infer some fission phenomena. Figure 1 shows the z-α plane potentials for δ = -0.02, 0.22, and 0.40. When the deformation δ is -0.02, an asymmetric fission valley appears in the direction of the arrow. In other words, if the nucleus is spherical, it causes asymmetric fission, which means that most of the fission trajectories split in a spherical shape in the case of low excitation fission. In addition, when the deformations δ are 0.22 and 0.40, symmetric fission valleys appear, which fission in the direction of the arrow. In other words, fission in the deformed state of the nucleus is symmetric fission.

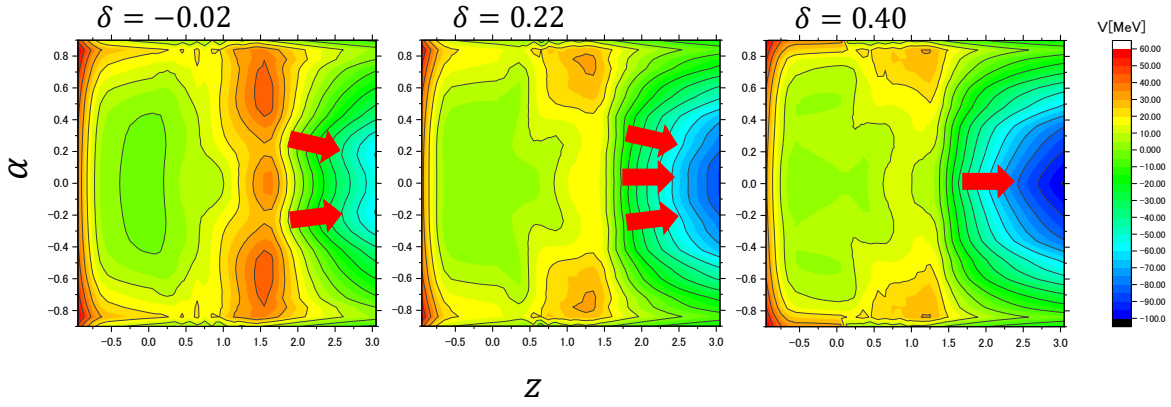

Figure 1: Comparison of z-α plane potentials at ^{226}Th for $\delta = -0.02, 0.22, 0.40$

In the dynamical model calculations, we examined whether the transition between symmetric and asymmetric fission is caused by these features by increasing the initial value of δ_0. By increasing the deformation δ_0 of the compound nucleus, at a certain point we obtain a trajectory in which the nucleus fissions in a deformed state. Figure 2 shows the results of increasing the deformation δ_0. This result confirms that symmetric fission occurs at high deformation, i.e., the structure of the potential plane in Figure 1 determines to some extent the fission event.

4 Conclusion

In this study, low excitation fission of ^{226}Th of nuclides far from β stable line, which experimentally shows the transition between symmetric and asymmetric fission, is calculated with the dynamical model currently being developed to reproduce symmetric fission for proton-rich nuclei, and we analyze to clarify the reason why symmetric fission is not observerd. The results of the present analysis show that the dynamics model is the most suitable for the present study. From the results of this analysis, the reason why symmetric fission phenomena cannot be represented, which is the problem of the dynamical model, is that the z-α plane potential in the absence of deformation has only a structure that causes asymmetric fission, and that two fission fragments split in a spherical shape at fission, in other words, they split without any deformation.

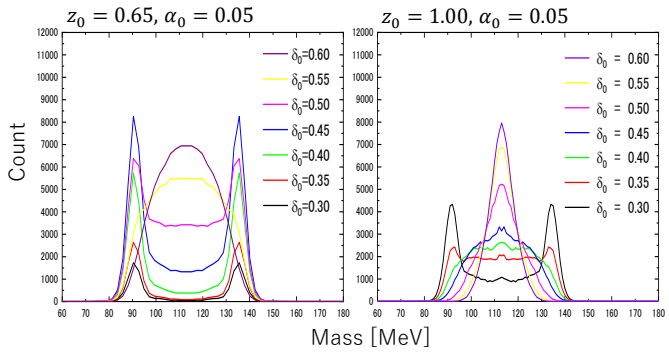

Figure 2: Comparison of mass distribution at ^{226}Th (E^*=15MeV), at two center distance z=0.65,1.00 with deformation δ_0=0.30-0.60 and mass asymmetry α_0 0.05

To solve this problem, we can increase the probability of increasing deformation by making the dynamical model independent[13], in which the two fragments have the same deformation (one more degree of freedom in deformation), to reproduce symmetric fission (fission in the shape shown on the left in Figure 3), or by using a different model for the nuclear structure (potential plane). Alternatively, it is necessary to develop a model that describes a potential structure in which symmetric and asymmetric fission of proton-rich nuclei exist simultaneously by using a different model for the nuclear structure (potential plane) or symmetric fission (fission in the shape shown on the right in Figure 3).

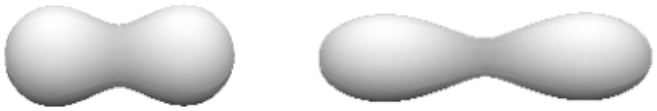

Figure 3: Nuclear shapes at ^{226}Th, the left figure shows the shape of the nucleus when fissioned symmetrically in a spherical shape, and the right figure shows the shape of the nucleus when fissioned in a deformed state as seen in the dynamical model.

References

[1] K-H Schimidt, J Benlliure and A. R. Junghans Nuclear Physics A 693, 169 189(2001).
[2] Y.Aritomo and S.Chiba, Physical Review C 88, 044614 (2013).
[3] Y. Miyamoto et al., Phys. Rev. C, 99, 051601(R) (2019).
[4] Y. Aritomo and M. Ohta, Nucl. Phys. A 744, 3 (2004).
[5] K. Sato, A. Iwamoto, K. Harada, S. Yamaji, and S. Yoshida,Z. Phys. A 288, 383 (1978).

[6] H. J. Krappe, J. R. Nix, and A. J. Sierk, Phys. Rev. C 20, 992(1979).
[7] A. V. Ignatyuk, G. N. Smirenkin, and A. S. Tishin, Sov. J. Nucl. Phys. 21, 255 (1975).
[8] J. Blocki, Y. Boneh, J. R. Nix, J. Randrup, M. Robel, A. J. Sierk, and W. J. Swiatecki, Ann. Phys. 113, 330 (1978).
[9] J. R. Nix and A. J. Sierk, Nucl. Phys. A 428, 161c (1984).
[10] H. Feldmeier, Rep. Prog. Phys. 50, 915 (1987).
[11] T.Wada,Y.Abe, and N. Carjen,Phys. Rev. Lett. 70, 3538 (1993).
[12] K. T. R. Davies, A. J. Sierk, and J. R. Nix, Phys. Rev. C 13, 2385 (1976).
[13] C. Ishizuka, M. D. Usang, F. A. Ivanyuk, J. A. Maruhn, K. Nishio, and S. Chiba, Physical Review C, 96(6), 064616 (2017).

20. Theoretical estimation of synthesizing neutron rich nuclei in superheavy mass region

S. Nishikawa Y. Aritomo, S. Takagi, H. Maekawa, S. Amano, K. Shibata, A. Asami

Faculty of Science and Engineering, Kindai University
3-4-1 Kowakae, Higashiosaka City, Osaka 577-8502, Japan

1. Introduction and Background

The next double magic nucleus after the double magic nucleus lead (^{208}Pb) proton number Z=82 and neutron number N=126 is predicted to be flerovium ^{298}Fl, Z=114 and N=184, and the "island of stability " around this nucleus is predicted in the nuclear chart. In the synthesis of new elements, it was assumed that the incident and target nuclei used in experiments would be stable nuclei. In particular, it was experimentally impossible to use unstable nuclei as target nuclei. Therefore, it was considered difficult to synthesize nuclei on the island of stability because of the insufficient number of neutrons when it came to fusion between stable nuclei. In order to synthesize nuclei around the island of stability, it is necessary to fuse unstable nuclei with an excess of neutrons, but until now there has been no method to achieve this. Recently, however, a new method for colliding unstable nuclei has been devised. This new method is called RUNBA [1]. Using RUNBA, a method to synthesize nuclei located in the island of stability has been developed, and it is expected to clarify whether or not the island of stability exists. If nuclei on the islands of stability can be synthesized and fundamental physical quantities such as lifetime and mass can be determined, this will provide important data for constructing and verifying the ultimate nuclear theory. The goal of this study is to investigate and evaluate the evaporation residue nucleus cross section of a reaction system in which our theoretical calculations using the dynamical model synthesize the island of stability nuclei with unstable nuclei, now that the RUNBA project is underway.

To calculate the evaporation residue cross sections for neutron-rich nuclei, we need to calculate the survival probability. The survival probability is calculated and evaluated using a statistical model. At that time, an error occurred in the statistical model. Currently, the calculation is based on the mass table by P. Moller et al [2], but we found that a problem occurs in the superheavy mass and neutron rich region. In the present work, we have improved the code and mass table to apply the statistical model. We will further analyze the parameters in the code for the calculation and make improvements.

2. Theory and Method

There are several ways to parameterize the shape of the amalgamated system. This two-center parameterization [3] is based on three important parameters are: the distance between two centers z, the mass-asymmetry parameter α, and the neck parameter ε. The dimensionless parameter z is defined as follows,

$$z = \frac{z_0}{BR_{CN}} \quad (1)$$

where z_o denotes the distance between two centers of the potentials, and R_{CN} is the radius of the spherical compound nucleus. B define as $B = (3+\delta)/(3-2\delta)$.

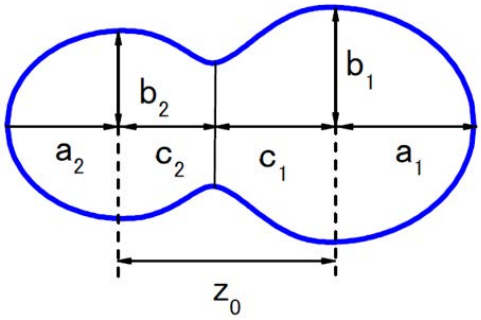

Fig. 1 Nuclear shape the two-center parametrization.

The mass-asymmetry parameter is defined as usual,

$$\alpha = \frac{A_1 - A_2}{A_1 + A_2} \quad (2)$$

The Langevin equation uses potential energy, friction coefficient, and mass of inertia to derive the probability P_{CN}. When the Langevin equation is solved for a large number of trajectories from the coordinates of the contact point, the majority of trajectories go straight down the potential slope to quasi-fission. However, a very small number of trajectories overcome the potential barrier due to fluctuations caused by random forces and reach the compound nuclear region. The probability of not causing quasi-fission, P_{CN} , can be estimated by solving the Langevin equation many times and calculating what percentage of all trajectories will reach the fusion region. In this study, the multidimensional Langevin equation is used.[4]

$$\frac{dq_i}{dt} = (m^{-1})_{ij} p_j$$
$$\frac{dp_i}{dt} = -\frac{\partial V}{\partial q_i} - \frac{1}{2}\frac{\partial}{\partial q_i}(m^{-1})_{jk} p_j p_k - \gamma_{ij}(m^{-1})_{jk} p_k + g_{ij} R_j(t) \quad (3)$$

where q_i is deformation coordinate and p_i is momentum of q_i . V is also the potential, and m_{ij} and γ_{ij} are the inertial mass and friction coefficient, R(t) represents a random force fluctuation, and g_{ij} is the strength of the random force. The shape of the nucleus (q_i) was determined by the two-center parameterization using three variables: z_0, which corresponds to the distance between the centers of distance; δ, the degree of deformation of the left and right fragments; and α, the degree of mass asymmetry.

The third stage is a decay process. In this stage, it is important to know the survival probability P_{sur} and it can be calculated by statistical model [5],

$$P_{sur} = \prod_{i=1}^{N} \frac{\Gamma_n^{(i)}}{\Gamma_n^{(i)} + \Gamma_f^{(i)}} \quad (4).$$

Γ_n and Γ_f are neutron evaporation width and fission decay width, respectively. From all the probabilities in these 3 stages, we obtain the evaporation residue cross sections σ_{ER}

$$\sigma_{ER} = \frac{\pi\hbar^2}{2\mu_0 E_{cm}} \sum_{l=0}^{\infty} (2l+1)\, T_l(E_{cm}, l) P_{CN}(E^*, l) P_{suv}(E^*, l) \quad (5).$$

E_{cm} and E^* denote to the incident energy and excitation energy while μ_0 and l are reduced mass in the entrance channel and angular momentum, respectively.

To calculate σ_{ER}, there are some uncertain parameters in the model in each stage. Here, we focus on the uncertainty in the third stage. In the equation (4) to obtain the survival probability [5], Γ_n/Γ_f is calculated as follows,

$$\frac{\Gamma_n}{\Gamma_f} = \frac{k_{coll}(gr.st.)}{k_{coll}(saddle) \cdot k_{kramers}} A_0 exp\left[2\sqrt{a_n E_n^*} - 2\sqrt{a_f E_f^*}\right]$$

$$E_n^* = E_{int} - B_n \quad , \quad E_f^* = E_{int} - B_f$$

$$k_{kramers} = \frac{\hbar\omega_1}{\sqrt{E_{int}}}\left(\sqrt{1+x^2} - x\right)$$

$$x \equiv \gamma / 2\,\omega_1 \quad (6).$$

$$k_{coll}(\beta_2) = \frac{T}{\hbar^2} J \equiv \sigma_\perp^2$$

$$J = J_0[1 + \sqrt{\frac{5}{16\pi}}\beta_2 + \frac{45}{28\pi}\beta_2^2]$$

$$J_0 = \frac{2}{5} AmR_{cn}^2$$

$$k_{coll}(\beta_2, E_{int}^*) = (\sigma_\perp^2 - 1)g(\beta_2) + 1 \quad for \ \sigma_\perp^2 > 1$$
$$g(\beta_2) = [1 + \exp((0.15 - \beta_2/\Delta\beta_2)]^{-1} \qquad (7)$$

Here, B_n is neutron separation energy. The uncertain parameters include fission barrier height δB_f, friction parameter γ and level density parameter a_f/a_n in eq.(6). In the superheavy mass region, it is no determined which values to be used. We need to know the parameter dependence of the survival probability and to see how these uncertainties influence the survival probability and evaporation residue cross section. The collective enhancement factor k_{coll} can be expressed as a function of the quadrupole deformation parameter β_2.

3. Result and Discussion

In our studies so far, we used the mass table by P. Moller [2]. In this study, however, we created our own mass table, which is named as shiba.dat.

First, we prepared the potential energy surface (map) in two-center shell model and searched the position at the ground state. The shape of its ground state should be taken as the lowest value on the potential energy map around the spherical region, as Moller's table did. However, if the lowest points are selected automatically, the position may jump, sometime. Moller's table shows such a tendency, for example, Z =112, N=194-195. This is thought to be the cause of the abnormal value in the calculation of the survival probability.

In the decay process of the compound nuclei, the position of the ground state is not significantly different among isotopes, that are continuously transferred by neutron emission from the compound nucleus. To search the position of the ground states using the potential energy map, we choose the position of the ground state, which does not change significantly between isotopes. By this method, we create the mass table, shiba.dat. Using this mass table, we calculated the survival probability and the evaporation residue cross section, which are shown in Figs 2 and 3. The results confirm the improvement in survival probability and evaporation residue cross section.

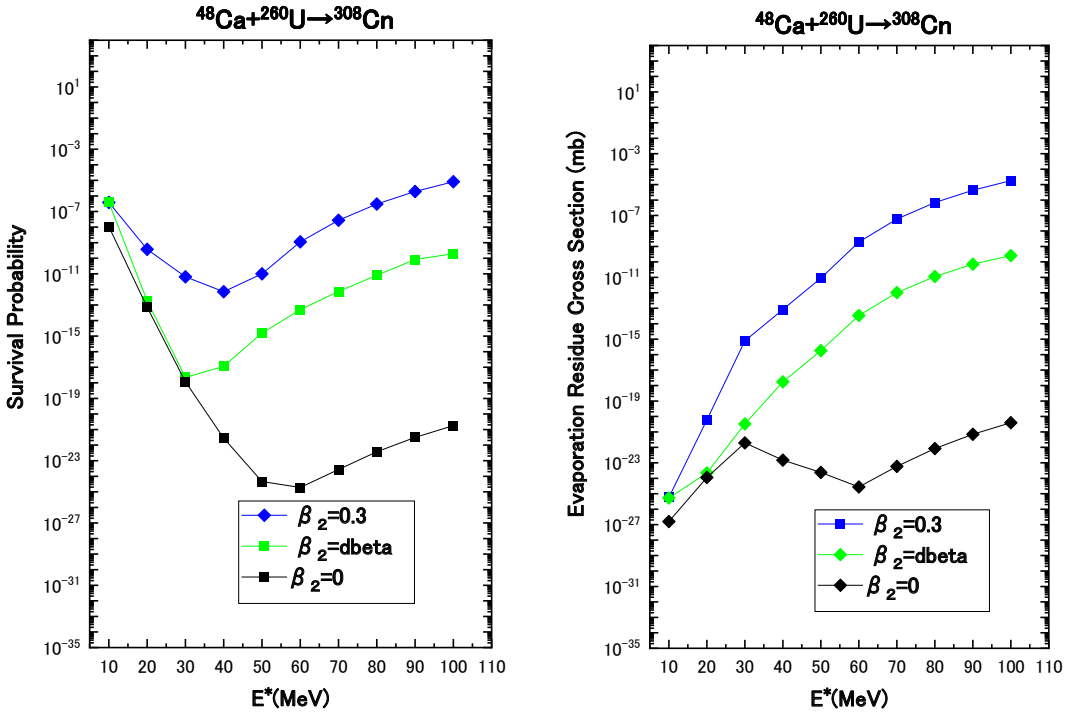

Fig.2 The evaporation residue cross section and survival probability for $^{48}Ca+^{260}U\rightarrow^{308}Cn$ by P.Moller`s mass table. (dbeta is P.Moller`s mass table)

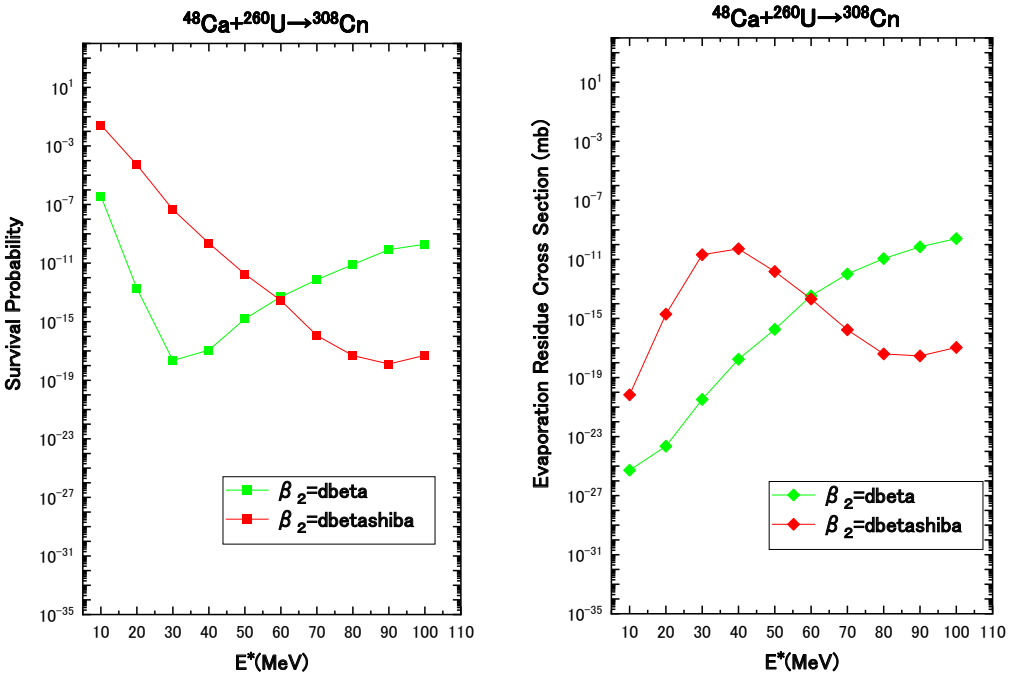

Fig.3 The evaporation residue cross section and survival probability for $^{48}Ca+^{260}U\rightarrow^{308}Cn$ by shiba.dat (dbetashiba is shiba.dat)

We changed the upper limit of neutron emission from 10 times to 20 times in our calculations. Next, ^{286}Cn, we fixed at neutron separation energy (sep1 = 4.87) and β_2 was varied in Fig.4. β_2= +22 is the result of calculating ^{286}Cn to match ^{308}Cn. The results confirm the improvement in survival probability. For fixed β_2= 0.22, the survival probability was found to be abnormal. When fixed to β_2= 0, the survival probability showed improvement. When β_2 of collective enhancement is fixed at 0.22 and β_2 = 0, the survival probability is confirmed to be abnormal. Four results indicate the possible impact of collective enhancement.

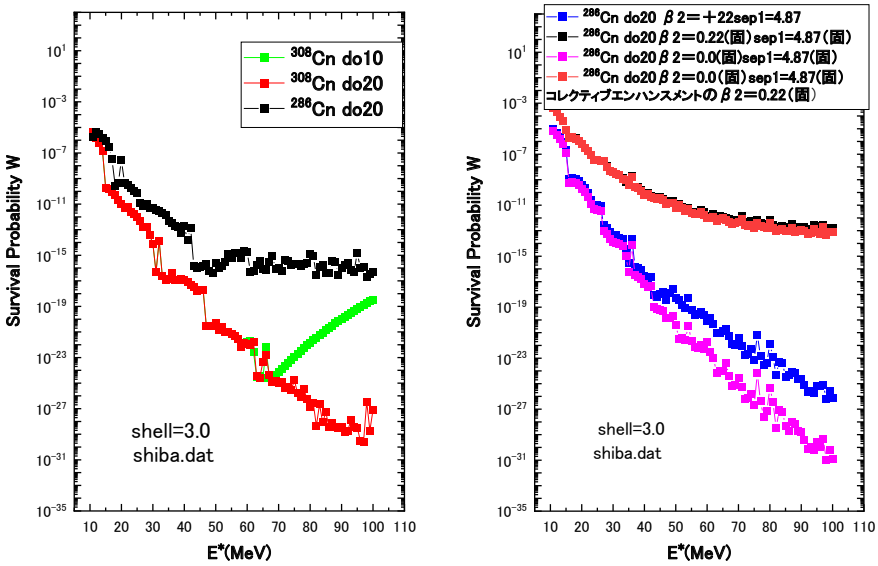

Fig.4 The calculation results of survival probability for ^{48}Ca+^{260}U→^{308}Cn , ^{48}Ca+^{238}U→^{286}Cn (^{308}Cn do10 means 10 times the upper limit of the number of neutrons in ^{308}Cn. ^{286}Cn do20 means 20 times the upper limit of the number of neutrons in ^{286}Cn.)

The anomaly in survival probability is the effect of collective enhancement. In the code, we use the mass table by P. Moller [2], and there are cases where the shell correction energies at the ground state in neutron-rich nuclei are close to zero or even positive. Based on these analysis, we discuss based on these analyses, and discuss the introduction of a dynamical model and the modification of the mass table as solutions to the problem.

References

[1] RIKEN NEWS 2019 September No.459, pp. 6.
[2] P.Moller et. al., Atomic Data and Nuclear Data Tables 109-110 (2016) 1-204.
[3] J. Maruhn, W. Greiner, Z. Phys. 251 (1972) 431.
[4] Yoshihiro Aritomo, Masahisa Ohta, Nuclear Physics A 744 (2004) 3–14
[5] M.Ohta, Proc. Of Fusion Dynamics at the Extremes,100(2001)

21. Fission fragment yields of neutron-rich nuclei evaluated by the Langevin model calculation

Shoya TANAKA[†1], Nobuya NISHIMURA[1,2], and Futoshi MINATO[3]

[1]RIKEN Nishina Center for Accelerator-Based Science, RIKEN, Saitama 351-0198, Japan

[2]Astrophysical Big Bang Laboratory, CPR, RIKEN, Saitama 351-0198, Japan

[3]Nuclear Science and Engineering Center, Japan Atomic Energy Agency, Tokai, Ibaraki 319-1195, Japan

[†]Email: shoya.tanaka@riken.jp

Abstract

Nucleosynthesis by the rapid neutron-capture process (r-process) produces elements heavier than iron via neutron-rich nuclides, observed in the solar system and stars with various metallicities. In the r-process, fission plays a fundamental role through bridging heavy element abundances with light element ones and by shaping the final r-abundance distribution. Nevertheless, due to the difficulty of experimental approaches, most of the fission data available for r-process calculations are based on theoretical predictions with phenomenological models. In this study, we focused on the transition of fission mode from asymmetric to symmetric in neutron-rich isotopes, which has been suggested in recent experiments for fermium isotopes. We investigated the fission of neutron-rich nuclei by a theoretical calculation based on the dynamical model and employed Langevin equations. Furthermore, we calculated fission fragment mass yields and prompt neutron emissions by combining Langevin calculations with a statistical model.

1 Introduction

Nucleosynthesis by the rapid-neutron-capture process, the so-called r-process, represents for cosmic origin of the heaviest elements (e.g., gold and uranium) beyond the iron-group peak. Although several astrophysical scenarios that bring about the r-process have been proposed, the mechanism itself is not completely understood (for a recent review, see [1, 2, 3]. One of the main reasons is large uncertainties arising from the nuclear-physics properties of very neutron-rich nuclei, e.g., neutron capture rates and decay half-lives. To determine nucleosynthesis flows on the r-process ″path″, the β-decay and the neutron capture (strongly depending on theoretical mass prediction) are significant. Nuclear fission plays a key role of the termination of r-process path toward heavier elements if the r-process flow is strong enough to reach actinides or transactinides. Nuclear fission, therefore, plays an essential role under certain r-process environmental conditions [4, 5, 6, 7], in particular, in very neutron-rich environments, e.g., neutron star mergers, where the nucleosynthesis path is able to go into the very neutron-rich trans-uranium region. The effects of fission are also significant to shape the r-process abundances due to the fission recycling in which fission products become seed nuclei ($A < 200$) for the next r-processing during a single nucleosynthesis process. Besides those effects, fission also has a key role as the heating source of kilonovae at late times ($\sim$ 10 days to months), of electromagnetic transients of

neutron star mergers [8, 9]. A sign of fission heating may have been observed in the light curve of the kilonova associated with the gravitational wave, GW170817. The precise understanding of fission becomes much crucial in the era of gravitational astronomy.

Fission product distributions are important for the r-process, but experimental data are not available in the neutron-rich region. From this respect, we calculated in this study the fission fragment mass distributions (FFMDs) of very neutron-rich nuclei. We adopt the Langevin method [10], widely adopted in the study of low-energy fission. In addition, we have combined Langevin calculations with a statistical model implemented in CCONE code [11] that calculates particle evaporation from highly nuclear excited states to estimate post-neutron emission fission product yields. This approach is a more realistic treatment than conventional methods.

2 Model

We use the fluctuation-dissipation model and employ Langevin equations to calculate the evolution of nuclear shape with time [12, 13]. The nuclear shape is defined by the two-center parametrization [14, 15], which has three deformation parameters, z, δ and α to serve as collective coordinates, abbreviated as $q = \{z, \delta, \alpha\}$. The symbol z is the distance between two potential centers, the symbol δ denotes the deformation of the fragments, and $\alpha = (A_1 - A_2)/(A_1 + A_2)$ is the mass asymmetry of the two fragments [12], where A_1 and A_2 denote the mass numbers of heavy and light fragments.

For a given value of the temperature of a system T, the potential energy is defined as a sum of the liquid-drop (LD) part and a microscopic (SH) part:

$$V(q,T) = V_{\rm LD}(q) + V_{\rm SH}(q,T), \tag{1}$$

$$V_{\rm LD}(q) = E_{\rm S}(q) + E_{\rm C}(q), \tag{2}$$

$$V_{\rm SH}(q,T) = [\Delta E_{\rm shell}(q) + \Delta E_{\rm pair}(q)]\Phi(T), \tag{3}$$

$$\Phi(T) = \exp\left(-\frac{aT^2}{E_d}\right). \tag{4}$$

Here, the potential energy $V_{\rm LD}$ is calculated with the finite-range liquid drop model [16], given as a sum of the surface energy $E_{\rm S}$ and the Coulomb energy $E_{\rm C}$. The microscopic energy $V_{\rm SH}$ at $T = 0$ is calculated as the sum of the shell correction energy $\Delta E_{\rm shell}$, evaluated by the Strutinski method [17, 18], and the pairing correlation correction energy $\Delta E_{\rm pair}$ [19]. The shell correction energy has a temperature dependence expressed by a factor $\Phi(T)$ in which the shell damping energy E_d is chosen as 20 MeV [20] and a is the level density parameter [13, 21]. To define the potential of the two-center shell model a neck parameter of $\epsilon = 0.35$ $(0 \le \epsilon \le 1)$ has been regularly used. However, this value is not appropriate for heavier actinide nuclides as pointed out in [22, 23]. To reproduce the experimental data, the value was systematically increased with the mass of fissioning nuclides. A calculation was performed to determine the optimal values leading to the best agreement with each FFMD. We adopt the optimal ϵ values following the empirical relation

$$\epsilon(A_c) = 0.01007A_c - 1.94, \tag{5}$$

where A_c is the mass of the fissioning nuclide.

The multidimensional Langevin equations [12] are given as

$$\frac{dq_i}{dt} = (m^{-1})_{ij}p_j, \tag{6}$$

$$\frac{dp_i}{dt} = -\frac{\partial V}{\partial q_i} - \frac{1}{2}\frac{\partial}{\partial q_i}(m^{-1})_{jk}p_j p_k - \gamma_{ij}(m^{-1})_{jk}p_k + g_{ij}R_j(t), \tag{7}$$

where $q_i = \{z, \delta, \alpha\}$ and $p_i = m_{ij}dq_i/dt$ is a momentum conjugate to coordinate q_i. In the Langevin equation, m_{ij} and γ_{ij} are the shape-dependent collective inertia and the friction tensors, respectively. The wall-and-window one-body dissipation [24, 25, 26] is adopted for the friction tensor. The normalized random force $R_i(t)$ is assumed to be that of white noise, *i.e.*,

$$\langle R_i(t)\rangle = 0, \quad \langle R_i(t_i)R_j(t_2)\rangle = 2\delta_{ij}\delta(t_1 - t_2). \tag{8}$$

The strength of the random force g_{ij} is related to the friction tensor γ_{ij} by the classical Einstain relation,

$$\sum_k g_{ik}g_{jk} = \gamma_{ij}T. \tag{9}$$

We calculated the charge distribution based on the unchanged charge distribution (UCD) assumption. The charge distribution (charge density) remains unchanged during the whole fission process, i.e., the charge density of the compound nucleus is maintained. By combining Langevin calculations with a statistical model implemented in the CCONE [11], we calculated independent yields and prompt neutron emissions. Excitation energy partitions for two fragments are determined by the anisothermal model [27].

3 Results and Discussion

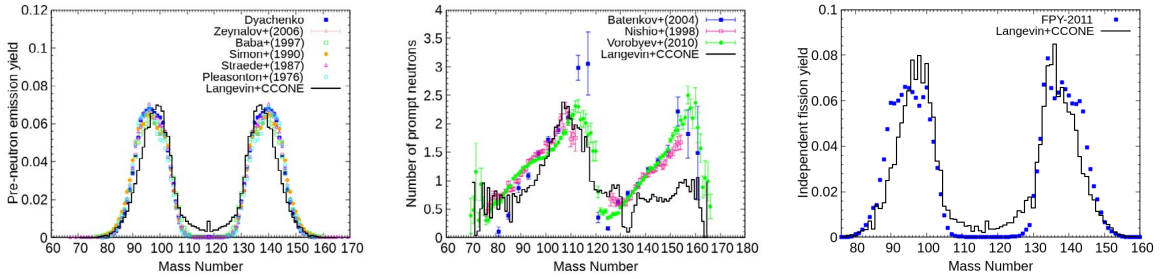

(a) pre-neutron emission yield of fission products

(b) mass-dependent prompt neutron multiplicity

(c) post-neutron emission yield of fission products

Figure 1: (a) The calculated a pre-neutron emission fission fragment mass yield for ^{236}U ($E^* = 15$ MeV) compared with experimental data for the thermal neutron-induced fission on ^{235}U [28, 29, 30, 31, 32, 33]. (b) The calculated mass-dependent prompt neutron multiplicity compared with experimental data [34, 35, 36]. (c) The calculated post-neutron emission fission fragment mass distribution compared with JENDL-FPY/2011 [39].

In this study, we choose the fission of a ^{236}U compound nucleus ($E^* = 15$ MeV), which is easy to obtain enough statistics due to the properties of Monte Carlo calculations, and compare with experimental data of thermal neutron-induced fission. Although the compound systems of the calculation and experimental data are not identical, we think that this comparison is reasonable with respect to the test of our calculation for the moment. In future work, we try to reduce the compound excitation energy of ^{236}U. Figure 1(a) shows the calculated fission fragment mass distribution, compared with experimental data [28, 29, 30, 31, 32, 33]. The calculated result shows a good agreement with the experimental data. However, the positions of the peaks are slightly different and the mass-symmetric fission component is larger than in the experimental data. This may be due to the higher excitation energy of the compound nucleus than thermal

neutron-induced fission in the experimental data. The prompt neutron emission multiplicity was calculated using the CCONE code with the results of the Langevin calculation as input data. It is shown in Fig. 1(b). The result reasonably reproduces the sawtooth structure of experiment data [34, 35, 36]. The calculated average number of the prompt neutron was 1.88, which is lower than the experimental value of 2.43 [35]. This is thought to be due to discrepancies between the calculation result and the experiment data of FFMDs or the calculation accuracy of the charge distribution model (UCD) employed. Figure 1(c) also indicates that the CCONE calculation for the neutron evaporation process successfully reproduces the post-neutron mass distribution. The pre-neutron distribution represented by the double-humped shape is symmetric with respect to mass number, and the symmetry is broken after the prompt neutron emission.

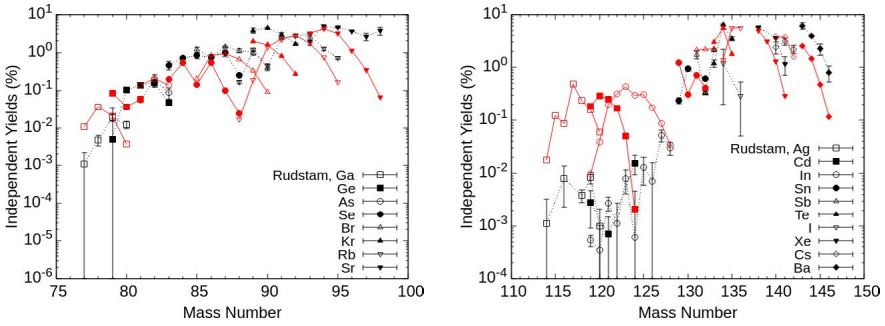

Figure 2: Comparison of the calculated independent yield Y_I(Z, A) with the experimental data.

We compare our calculated independent yield Y_I(Z, A) for several fission products with the experimental data of Rudstam et al. [40] as shown in Fig. 2. This result is extremely important in r-process calculations. Although it is not able to fit the experimental data precisely, especially in the mass region from 115 to 130, the general tendency is well reproduced.

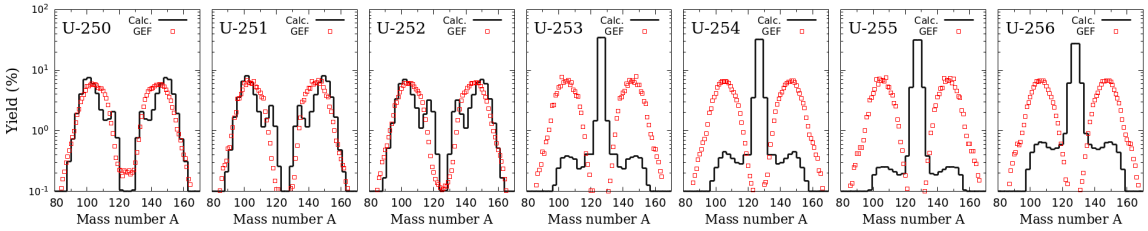

Figure 3: The calculation results of FFMDs for ^{250}U to ^{256}U with the excitation energy of E* = 7 MeV compared with the data from GEF code [38].

We perform a series of fission calculations for uranium (Z = 92) isotopes with 10–20 more neutron-rich from the β-stability line. The calculated FFMDs for ^{250}U to ^{256}U are shown in Fig. 3. We found that the fission fragment distribution changes from the two-peak feature (mass-asymmetric fission) to the one-peak (mass-symmetric fission) with increasing the neutron number. A similar trend which is the dramatic change of FFMDs for fermium isotopes [37] was also observed in uranium isotopes in this calculation. This trend did not appear in the results of the GEF model code [38].

4 Summary

In the presented work, we have performed the fission calculations of ^{236}U and neutron-rich uranium using the dynamical model aiming at its application to r-process simulations. In this study, we have combined Langevin calculations with the statistical model implemented in the CCONE code to calculate prompt neutron emissions, and calculated fission fragment mass distributions of neutron-rich nuclei. The calculated prompt neutron emission multiplicity reproduced the sawtooth structure of experiment data. In the calculated FFMDs in neutron-rich uranium, the dramatic change of fission mode was observed with increasing mass number. Such a systematic behavior can be significant to shape the final abundances of the r-process calculations. Our results, including further improvements, are expected to contribute to understanding the r-process. In future work, the mass number and charge distribution of fission fragments, kinetic energy, prompt neutron number, lifetime, etc., which are necessary for numerical data available for r-process calculations, will be evaluated for each nuclide simultaneously, and a fission database will be constructed.

References

[1] C. J. Horowitz et al. J. Phys. G: Nucl. Part. Phys. **46**, 083001 (2019).

[2] M. Arnould, S. Goriely and K. Takahashi, Phys. Rep. **450**, 97 (2007).

[3] John J. Cowan, Christopher Sneden, James E. Lawler, Ani Aprahamian, Michael Wiescher, Karlheinz Langanke, Gabriel Martínez-Pinedo, and Friedrich-Karl Thielemann, Rev. Mod. Phys. **93**, 015002 (2021).

[4] S. Goriely, J.-L. Sida, J.-F. Lemaître, S. Panebianco, N. Dubray, S. Hilaire, A. Bauswein, and H.-T. Janka, Phys. Rev. Lett. **111**, 242502 (2013).

[5] M. Eichler et al., Astrophys. J. **808**, 30 (2015).

[6] S. Shibagaki et al., Astrophys. J. **816**, 79 (2016).

[7] Nicole Vassh et al., Astrophys. J. **896**, 28 (2020).

[8] Y. Zhu et al 2018 Astrophys. J. Lett. **863**, L23 (2018).

[9] Shinya Wanajo, Astrophys. J. **868**, 65 (2018).

[10] S. Tanaka, and Y. Aritomo, Y. Miyamoto, K. Hirose, K. Nishio, Phys. Rev. C **100**, 064605 (2019).

[11] O. Iwamoto, N. Iwamoto, S. Kunieda, F. Minato, K. Shibata, Nuclear Data Sheets, Volume **131**, pp. 159-288 (2016).

[12] Y. Aritomo and M. Ohta, Nucl. Phys. A **744**, 3 (2004).

[13] Y. Aritomo, S. Chiba, and F. Ivanyuk, Phys. Rev. C **90**, 054609 (2014).

[14] J. Maruhn and W. Greiner, Z. Phys. **251**, 431 (1972).

[15] K. Sato, A. Iwamoto, K. Harada, S. Yamaji, and S. Yoshida, Z. Phys. A **288**, 383 (1978).

[16] H. J. Krappe, J. R. Nix, and A. J. Sierk, Phys. Rev. C **20**, 992 (1979).

[17] V. M. Strutinsky, Nucl. Phys. A **95**, 420 (1967).

[18] V. M. Strutinsky, Nucl. Phys. A **122**, 1 (1968).

[19] S. G. Nilsson, C. F. Tsang, A. Sobiczewski et al., Nucl. Phys. A **131**, 1 (1969).

[20] A. V. Ignatyuk, G. N. Smirenkin, and A. S. Tishin, Sov. J. Nucl. Phys. **21**, 255 (1975).

[21] J. Toke and W. J. Swiatecki, Nucl. Phys. A **372**, 141 (1981).

[22] K. Hirose, K. Nishio, S. Tanaka, R. Léguillon, H. Makii, I. Nishinaka, R. Orlandi, K. Tsukada, J. Smallcombe, M. J. Vermeulen, S. Chiba, Y. Aritomo, T. Ohtsuki, K. Nakano, S. Araki, Y. Watanabe, R. Tatsuzawa, N. Takaki, N. Tamura, S. Goto, I. Tsekhanovich, and A. N. Andreyev, Phys. Rev. Lett. **119**, 222501 (2017).

[23] Y. Miyamoto, Y. Aritomo, S. Tanaka, K. Hirose, and K. Nishio, Phys. Rev. C **99**, 051601(R) (2019).

[24] J. Blocki, Y. Boneh, J. R. Nix, J. Randrup, M. Robel, A. J. Sierk, and W. J. Swiatecki, Ann. Phys. **113**, 330 (1978).

[25] J. R. Nix and A. J. Sierk, Nucl. Phys. A **428**, 161c (1984).

[26] H. Feldmeier, Rep. Prog. Phys. **50**, 915 (1987).

[27] T. Kawano, P. Talou, I. Stetcu, M. B. Chadwick, Nucl. Phys. A **913**, 51 (2013).

[28] PP. D ' yachenko, BD. Kuzminov, and MZ. Tarasko, Soviet J. Nucl. Phys. **8**, 165 (1969).

[29] S. Zeynalov, W. Furman, and FJ. Hambsch, ISINN-13. (2006).

[30] H. Baba, T. Saito, N. Takahashi, and et al., J. Nucl. Sci. Technol. **34**, 871–881 (1997).

[31] G. Simon, J. Trochon, F. Brisard, and et al., Nucl. Instrum. Methods Phys. Res. A **286**, 220–229 (1990).

[32] C. Straede, C. Budtz-Jørgensen, and HH. Knitter, Nucl. Phys. A **462**, 85–108 (1987).

[33] F. Pleasonton, RL. Ferguson, and HW. Schmitt, Phys. Rev. C **6**, 1023–1039 (1972).

[34] Oleg I. Batenkov, Vilen P. Eismont, Mikhail J. Majorov, Andrey N. Smirnov, Kjell Aleklett, Walter Loveland, Jan Blomgren, Henri Condé, Marieke Duijvestijn, and Arjan Koning, AIP Conference Proceedings **769**, 625 (2005)

[35] K. Nishio, Y. Nakagome, H. Yamamoto, I. Kimura, Nucl. Phys. A **632**, 540 (1998).

[36] A.S. Vorobyev, O.A. Shcherbakov, A.M. Gagarski, G.V. Val ' ski and G.A. Petrov, EPJ Web of Conferences **8**, 03004 (2010).

[37] D. C. Hoffman, J. B. Wilhelmy, J. Weber, W. R. Daniels, E. K. Hulet, R. W. Lougheed et al., Phys. Rev. C **21**, 972 (1980).

[38] K.-H. Schmidt, B. Jurado, C. Amouroux, and C. Schmitt, Nucl. Data Sheets **131**, 107 (2016).

[39] K. Shibata, O. Iwamoto, T. Nakagawa, N. Iwamoto, A. Ichihara, S. Kunieda, S. Chiba, J. Katakura, and N. Otuka, Journal of Korean Physical Society **59**, 1046 (2011).

[40] G. Rudstam, P. Aagaard, B. Ekström et al., Radiochimica Acta. **49**, 155–192 (1990).

Acknowledgments

This study is financially supported by JSPS KAKENHI (19H00693, 20K04003, 20H05648, 21H01087, 22K20373). Parts of computations are performed on computer facilities at CfCA in NAOJ and at YITP in Kyoto University.

22. Extension of R-matrix code AMUR toward analysis on actinide nuclei
-A feasibility study on ^{233}U-

Satoshi KUNIEDA[†1]

[1]Nuclear Data Center, Japan Atomic Energy Agency (JAEA)
[†]Email: kunieda.satoshi@jaea.go.jp

Abstract

The extension of an R-matrix code AMUR is now under progress for analysis of neutron cross-section on heavier nuclei. This paper shortly summarizes recent updates in the code for the theoretical calculation of the resonant cross-sections. In this work, with the preliminary version of AMUR, let me also demonstrate a feasibility analysis to experimental neutron cross-sections on ^{233}U which are stored in the EXFOR database. It was confirmed that the values of the resonance parameters were successfully obtained through the fitting procedure, together with their covariance data. It was also found that some characteristics of nuclear reactions could be seen in correlation matrices of the cross-sections.

1 Introduction

The AMUR code [1, 2] is under development in JAEA for the cross-section evaluation in the resolved resonance energy region. The code is based on the R-matrix theory [3] for calculation of cross-sections and the Kalman filtering method [4] for the data-assimilation, which enables us to obtain resonance parameter set from the measured cross-sections with its covariance matrix. The code was initially designed for the analysis of the light-nuclei to narrow large differences of cross-sections among evaluations in the world (e.g., on n+^{16}O [1]). Indeed, it was applied to the development of JENDL-5 [5] for a number of light-mass isotopes. It may be a positive idea to extend applicability of the code toward the analysis of heavier nuclei including structural materials, major and minor actinide nuclei.

The cross-sections of the radiative neutron capture reaction are very important for medium-and heavy-mass nuclei in a number of practical applications. Those of the fission reaction are also highly important for actinide isotopes in design of the reactors. However, it is unrealistic to fully apply the R-matrix theory to calculation of those cross-sections due to lack of fundamental information and huge number of the explicit channels. Therefore, we need to use an approximated theories/formulae of R-matrix (such as of the Breit-Wigner or Reich-Moore types) to calculate those cross-sections. The AMUR code is now being in progress to have a flexibility which allows those approximated calculations for the resonance analysis. In this work, a test analysis is performed for neutron cross-sections on ^{233}U to see feasibilities of the updated version of AMUR. The scope of this study includes estimation of covariance data both for the resonance parameters and the cross-sections.

2 Updates toward analysis of heavier nuclei

AMUR was initially developed for the analysis of the light-nuclei to narrow large differences among the evaluated cross-sections, by making use of the theoretical constraints [1] from the R-matrix theory. The code was also designed to analyze covariance data of the resonance parameters and cross-sections, where both the experimental and theoretical knowledge were reflected to the nuclear data evaluation [2]. We thought such an idea/approach could also be applied to analysis of the heavier nuclei with AMUR, learning a number of experiences on the other codes such as SAMMY [6] and REFIT [7].

Recently, the authors extended capabilities of the code toward the analysis of medium- and heavy-mass nuclei to fully cover range of isotopes required for nuclear science and engineering. In the theoretical part, AMUR is able to read a resonance parameter set stored in the ENDF-6 format (MF=2, LRU=1) files, then it performs reconstruction of cross-sections with the Breit-Wigner (LRF=1,2) or the Reich-Moore type formulae (LRF=3,7). That means the code is able to calculate the radiative neutron capture and fission cross-sections with approximated/reduced R-matrix formulae. The code is also able to perform the Doppler broadening with the free-gas approximation. Therefore, AMUR is getting equivalent to the other resonance analysis and the processing codes in terms of basic capabilities for calculating/reconstructing the cross-sections.

3 Test analysis on ^{233}U and preliminary results

3.1 Resonance analysis

The ^{233}U isotope was selected in this study because,

- Experimental data of the resonant neutron cross-sections compiled in the EXFOR database are very limited for a number of the medium- and heavy-mass nuclei. Fortunately, a few of data-sets were available for ^{233}U in which the transmission, (n,γ) and (n,f) cross-sections were given in the same energy range, which allowed us to perform a consistent resonance analysis in terms of the reaction channels.
- Until now, AMUR had not been applied to analysis on the actinide isotope. Thus it was a good practice for AMUR to analyze fission cross-sections for the first time, as the ^{233}U isotope is one of the well-known fissioning nuclei.
- It is physically interesting to see correlation matrices of cross-sections amongst all the reactions involved, including the fission channel.

The experimental data analyzed in this work were those by Guber et al. [8] for transmission and by Berthoumieux et al. [9] for the (n,γ) and (n,f) cross-sections. According to literatures of those data, all they were the time-of-flight measurements with very high energy-resolutions. Furthermore, corrections for the multiple-scattering and self-shielding effects had also been made at least for the (n,γ) and (n,f) cross-sections. Therefore, in this test/preliminary analysis, only the temperature effect was considered for the experimental correction in AMUR, viz., the experimental corrections are to be performed in forthcoming in-depth studies.

The initial values of resonance parameters were taken from ENDF/B-VIII.0 [10] where all the parameters were defined in the Reich-Moore formula (MF=2/LRF=3) for this isotope. The parameter search was performed simultaneously for all the reactions up to E_n = 20 eV. Figure 1 illustrates fitting results for the transmission, (n,γ) and (n,f) cross-sections. We have not yet made thorough comparisons with other codes, however, this figure visually suggests AMUR is getting equivalent with the other resonance analysis codes in terms of basic capabilities for the reconstructing cross-sections and the fitting to those experimental data.

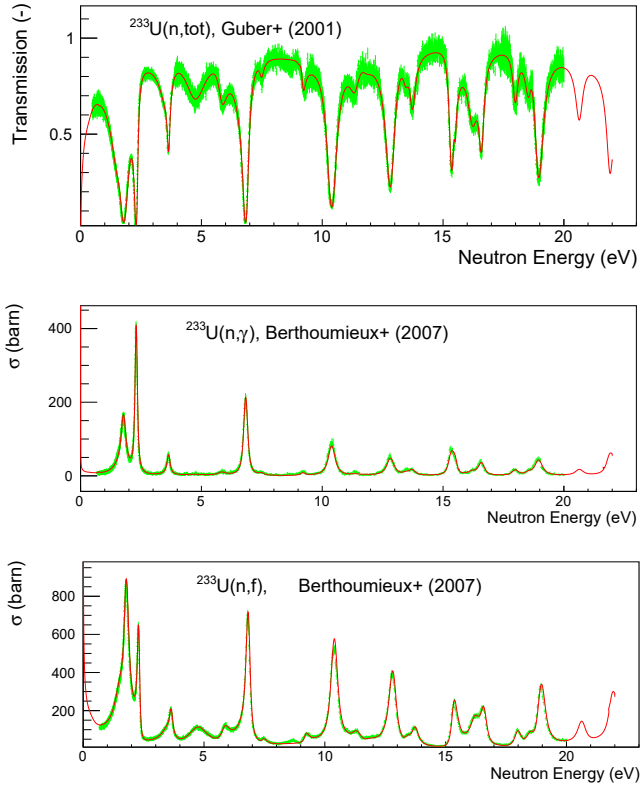

Figure 1: Fitting results of AMUR to experimental data of the neutron transmission [8], (n,γ) and (n,f) cross-sections [9].

3.2 Resulting correlation matrices and uncertainty of cross-sections

The covariance matrix of all the resonance parameters was obtained during the fitting procedure with the Kalman filtering method. Once we calculate sensitivity matrices of the parameter to cross-sections, covariance/correlation matrices of cross-sections are deduced by the propagation law. Figure 2 illustrates correlation matrices obtained in this analysis for the total, elastic scattering, (n,γ) and (n,f) cross-sections. We see overall features of those plots are complicated because of the interference effects on the resonant nuclear reaction. A very strong long-range correlation is seen in the elastic scattering cross-sections. It is because that the shape elastic scattering process, which is calculated by the hard-sphere model in R-matrix, always occurs over the energy range. More in-depth discussion may be possible if we perform experimental corrections in the fitting procedure.

Figure 3 illustrates preliminary results on uncertainty of cross-sections which were propa-gated from those of the resonance parameters. The values are around 1% on average, but they are fluctuated due to constraints from the resonance t heory. Because there were no data points below 1 eV in the measurements I analyzed, uncertainties resulted in very large values for all the reactions.

4 Summary

The extension of an R-matrix code AMUR is now under progress for analysis of neutron cross-section on heavier nuclei, in which approximated R-matrix theories are incorporated to

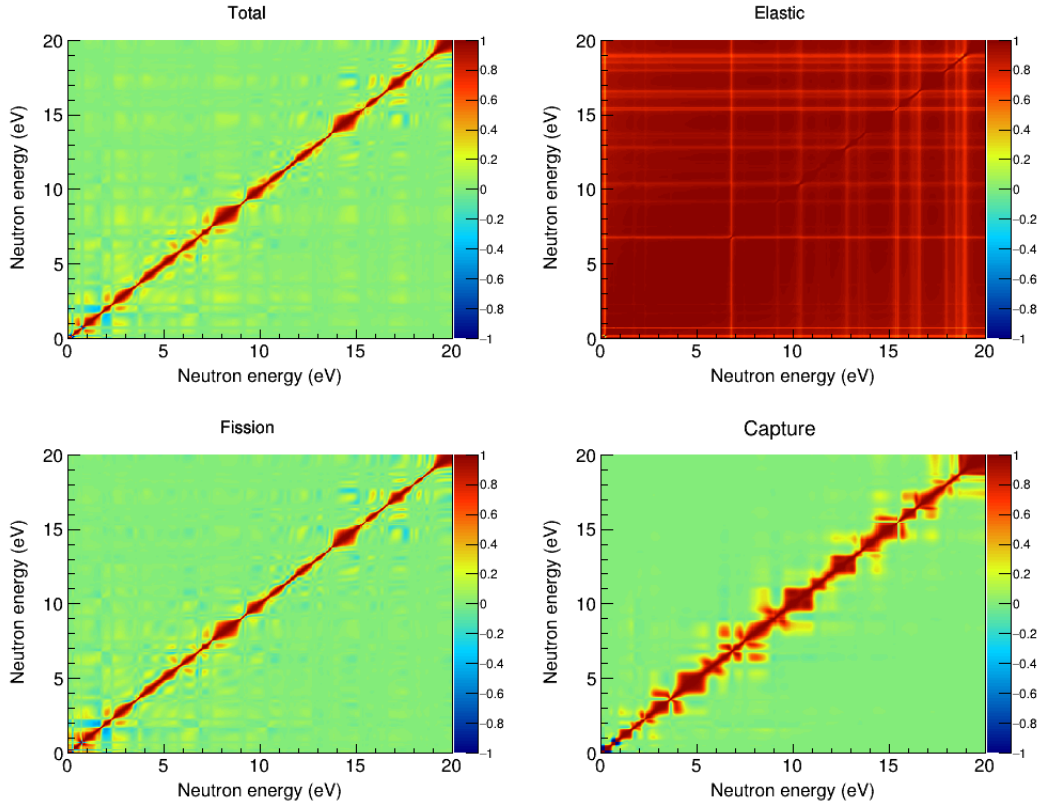

Figure 2: Correlation matrices obtained in this analysis for the total, elastic scattering, (n,γ) and (n,f) cross-sections.

the code. Such an update enables us to perform resonance analysis of the neutron capture and fission cross-sections, as a test analysis was demonstrated for the ^{233}U isotope in this work. Development of the code will be continued to have enough options for experimental corrections, which may allows us in-depth studies not only for the evaluation of cross-sections but also for estimation of their covariance data.

References

[1] Kunieda S, Kawano T, Paris M, et al. R-matrix analysis for n +^{16}O cross-sections up to E_n=6.0 mev with covariances. Nucl Data Sheets. 2014;118:250.

[2] Kunieda S, Kawano T, Paris M, et al. Covariance of neutron cross sections for ^{16}O through matrix analysis. Nucl Data Sheets. 2015;123:159.

[3] Lane AM, Thomas RG. R-matrix theory of nuclear reactions. Rev Mod Phys. 1958;30:257–353.

[4] Kawano T, Matsunobu H, Murata T, et al. Simultaneous evaluation of fission cross sections of uranium and plutonium isotopes for JENDL-3.3. J Nucl Sci Technol. 2000; 37:327.

[5] Iwamoto O, Iwamoto N, Kunieda S, et al. Japanese Evaluated Nuclear Data Library version 5: JENDL-5. J Nucl Sci Technol. 2023; 60:1-60.

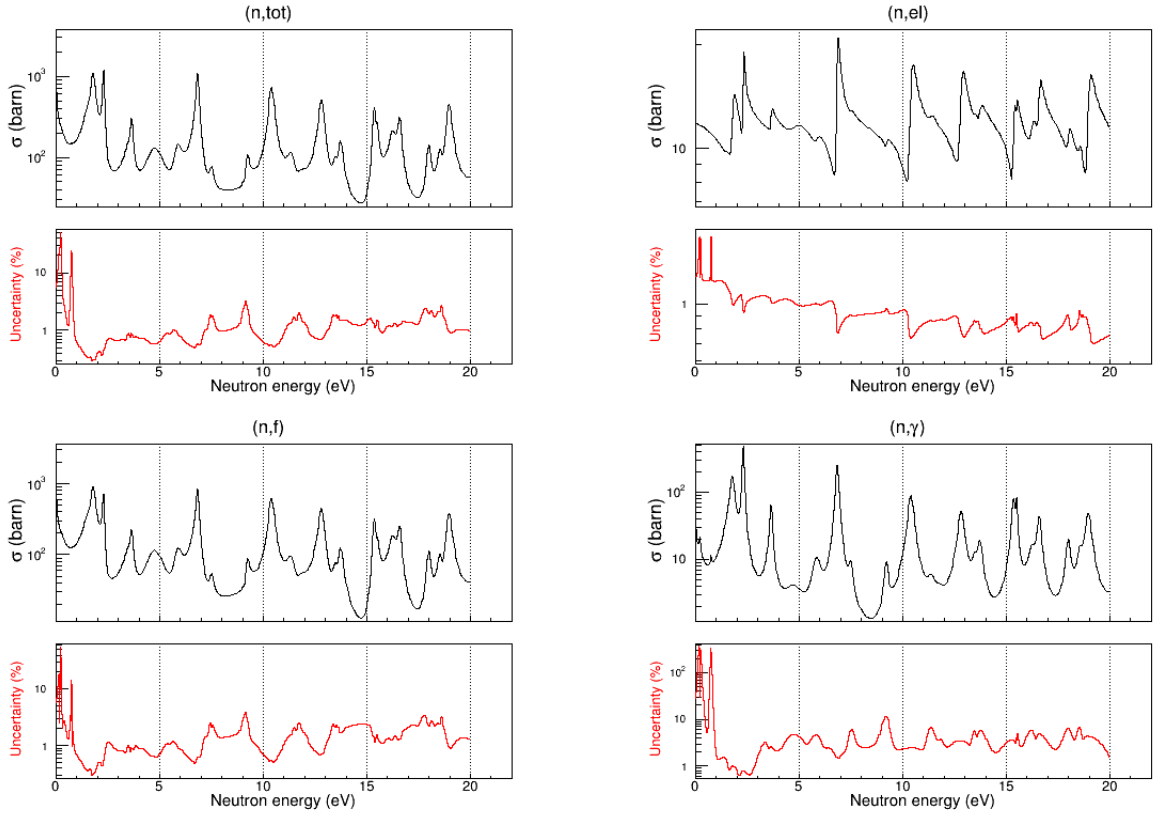

Figure 3: Uncertainty of cross-sections obtained in this analysis for the total, elastic scattering,(n,γ) and (n,f) cross-sections.

[6] Larson MN. Updated user's guide for SAMMY: Multi-level R-matrix fits to neutron data using Bayes' equations ; 1998. ORNL/TM-9179/R4. Oak Ridge National Laboratory; 1998.

[7] Moxon MC, Ware TC, Dean CJ. Users' guide for REFIT-2009-10 ; 2010. UKNSF; 2010 April. pp. 243. UK Nuclear Science Forum.

[8] Guber KH, Spencer RR, Leal LC, et al. High-resolution transmission measurements of ^{233}U using a cooled sample at the temperature T= 11 K. Nuclear Science and Engineering. 2001; 139(2):111–117.

[9] Berthoumieux E, Abbondanno U, Aerts G, et al. Simultaneous measurement of the neutron capture and fission yields of ^{233}U. In: International Conference on Nuclear Data for Science and Technology; 2007. pp. 571–574.

[10] Brown DA, Chadwick MB, Capote R, et al. ENDF/B-VIII.0: The 8th major release of the nuclear reaction data library with CIELO-project cross sections, new standards and thermal scattering data. Nuclear Data Sheets. 2018;148:1–142. Special Issue on Nuclear Reaction Data.

23. Processing of JENDL-5 Photonuclear Sublibrary

Chikara KONNO*
Japan Atomic Energy Agency
2-4 Shirakata, Tokai-mura, Naka-gun, Ibaraki-ken 319-1195, Japan
*Email: konno.chikara@jaea.go.jp

I modified NJOY2016.67 to produce photonuclear ACE files which can be used in MCNP6.2 and PHITS3.27 and produced the ACE file of the JENDL-5 photonuclear sub-library. Simple test calculations with the produced ACE file revealed that the produced ACE file had no serious problems.

1. Introduction

In order to use JENDL-5 [1], which was released in 2021, in MCNP [2] and PHITS [3], its ACE file should be produced. The ACE file of the JENDL-5 neutron sublibrary was produced based on FRENDY [4] and those of the JENDL-5 charged particle and photoatomic sublibraries were generated based on a modified version of NJOY2016.65 [5], which is described elsewhere [6]. The remaining issue is to produce an ACE file of the JENDL-5 photonuclear sublibrary. The current FRENDY cannot process the JENDL-5 photonuclear sublibrary. The latest NJOY, NJOY2016.67, can produce the ACE file of the JENDL-5 photonuclear sublibrary, but MCNP6.2 and PHITS3.27 cannot use the produced ACE file because of an unsupported format. I have produced the ACE file of the JENDL-5 photonuclear sublibrary which can be used in MCNP6.2 and PHITS3.27 by modifying NJOY2016.67.

2. Problems of NJOY2016

NJOY2016.67 converts the energy-angle distribution data of LAW=1 (continuum energy-angle distribution) and LANG=1 (Legendre coefficients are used) in ENDF-6 files [7], which are adopted in most of the nuclei in the JENDL-5 photonuclear sublibrary, to the energy-angle distribution data of LAW=61 (tabular energy distribution) in ACE files. However MCNP6.2 and PHITS3.27 do not support the LAW=61 format in photonuclear ACE files and cannot use it (The next version of MCNP, MCNP6.3, will be able to use it but has not been released yet.). The conversion of the energy-angle distribution data of LAW=1 and LANG=1 in ENDF-6 files to the energy-angle distribution data of LAW=61 in ACE files was introduced in NJOY2016.66, which also includes other important revisions for photonuclear data (Example : Some photonuclear libraries have MF6/MT18 with a neutron multiplicity equal to 1 instead of nubar. In this case the neutron multiplicity is replaced with the nubar data.). NJOY2016.65 converts the energy-angle distribution data of LAW=1 and LANG=1 in ENDF-6 files to the energy distribution data of LAW=4 (angular distribution should be defined separately) with an isotropic angular distribution in ACE files, which MCNP6.2 and PHITS3.27 can use, but it cannot produce complete ACE files of the JENDL-5 photonuclear sublibrary because of any bugs.

3. Modification of NJOY2016

I modified NJOY2016.67 only in the conversion of the energy-angle distribution data of LAW=1 and LANG=1 in ENDF-6 files on the basis of NJOY2016.65 to produce the ACE file with LAW=4 of the JENDL-5 photonuclear sublibrary, which can be used in MCNP6.2 and PHITS3.27. I also modified NJOY2016.67 to fix the following problems. The details of the modification are described elsewhere [6].

- The problem that NJOY2016.65 cannot produce the complete ACE file with LAW=4 of the JENDL-5 photonuclear sublibrary still remained in NJOY2016.67. This problem occurred in the conversion of the energy-angle distribution data of LAW=1 and LANG=1 in ENDF-6 files to the energy distribution data of LAW=4 in ACE files.
- Zero division in normalization of the probability density distribution in ^{245}Bk, ^{244}Cf, ^{253}Cf, and ^{251}Fm.
- No support of the multiple interpolation in MF6/MT5 data in ^{3}He, ^{6}Li, ^{7}Li, ^{9}Be, ^{10}B, and ^{11}B.
- Negative heating numbers in a lot of nuclei were set to 0.0 as shown in Figs. 1 and 2. This modification was based on IAEA photonuclear processing [8].
- Double counting problem of heating number for LAW=2 data of MF6/MT5 in ^{3}He.

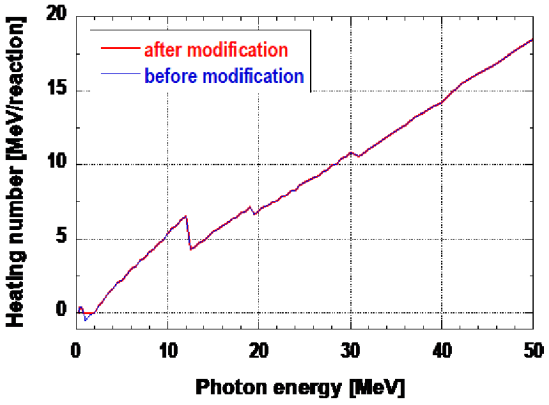

Fig. 1 Heating number of ^{49}S (whole).

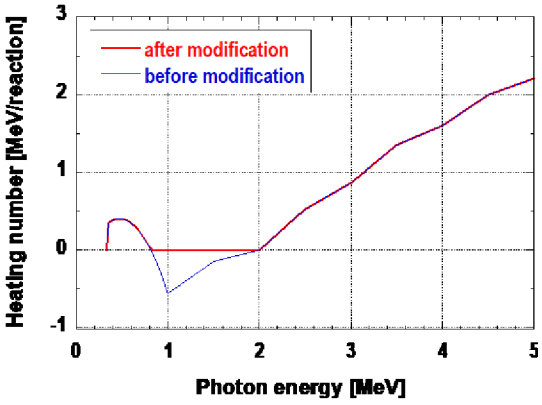

Fig. 2 Heating number of ^{49}S (expanded).

The following NJOY2016 processing problems pointed out by IAEA [8] remain in the present processing. Note that IAEA used the ACEMAKER code [9], which solves the problems but produces ACE files with LAW=61 data, for processing IAEA photonuclear data library (IAEA/PD-2019) [10].

- The photofission delayed fission neutron data were neglected.
- Relativistic conversion between the center of mass system and the laboratory reference framework was not applied.
- Inadequate treatment of LAW=4 data for MF6/MT5 in ^{2}H.
- Inadequate treatment of LAW=2 data for MF6/MT5 in ^{3}He.

The first issue is not responsible to NJOY2016 because the ENDF-6 format does not support photofission delayed fission neutron data. The other issues affect the heating number. While the effect of the second issue is only less than 5% [8], those of the third and fourth issues are very large as shown in Figs. 3 and 4,

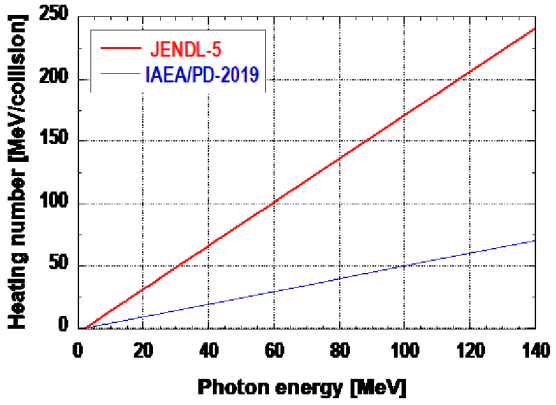

Fig. 3 Heating number of ^{2}H.

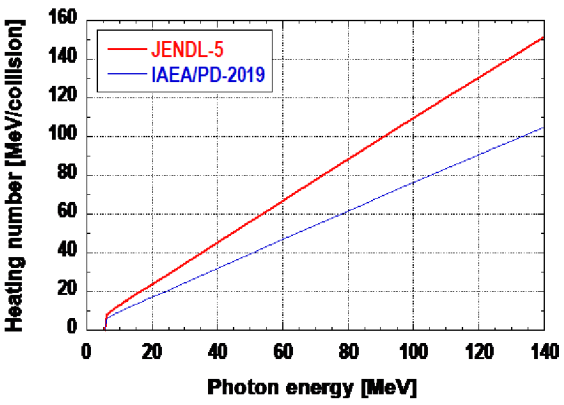

Fig. 4 Heating number of ^{3}He.

where IAEA calculates the heating numbers correctly with ACEMAKER. Note that the ^{2}H and ^{3}He ENDF-6 files in the JENDL-5 photonuclear sublibrary are almost the same as those in IAEA/PD-2019. Thus I manually replaced the heating numbers in the ^{2}H and ^{3}He ACE files of the JENDL-5 photonuclear sublibrary with those of IAEA/PD-2019.

4. Test Calculations

I produced the ACE file of the JENDL-5 photonuclear sublibrary with the modified version of NJOY2016.67. As a test I calculated angular neutron spectra produced from gold (1 cm ϕ, 1 cm thick) bombarded with 25 MeV photons by using MCNP6.2 and the following ACE files.

- JENDL-5 (Present production)
- IAEA/PD-2019 (^{197}Au:JENDL/PD-2016.1 [11], old official ACE file with LAW=4)
- TENDL-2019 (official ACE file) [12]

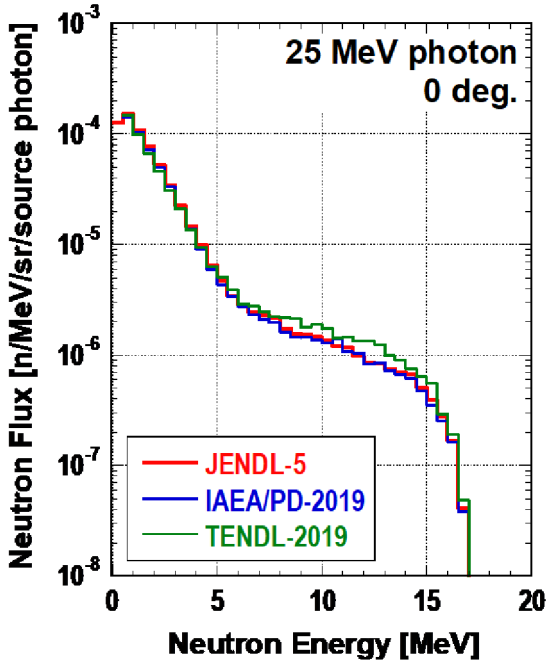

(a) 0 degree

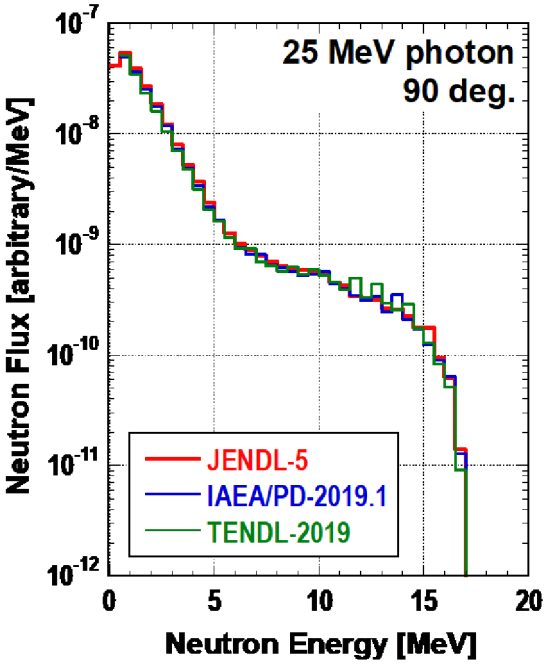

(b) 90 degree

Fig. 5 Calculated angular neutron spectra produced from gold bombarded with 25 MeV photons.

The calculated neutron spectra at 0 and 90 degrees are shown in Fig. 5. The spectra with JENDL-5 are almost the same as those with IAEA/PD-2019, where the ^{197}Au file is that of JENDL/PD-2016.1 which is almost the same as that of JENDL-5. Thus the processing of the JENDL-5 photonuclear sublibrary is considered to have no serious problems.

5. Conclusion

I produced the ACE file of the JENDL-5 photonuclear sublibrary with a modified version of NJOY2016.67. The produced photonuclear ACE files can be used in MCNP6.2 and PHITS3.27. Note that the heating numbers of ^{2}H and ^{3}He were manually replaced with those of IAEA/PD-2019 because they were too large. Test calculations indicated that the ACE file had no serious problems. The ACE file of the JENDL-5 photonuclear sublibrary was released with other JENDL-5 ACE files from JAEA web site [6] as an open source. Users can freely download and use it.

References

1) Iwamoto, O., Iwamoto, N., Kunieda, S., et al., Japanese Evaluated Nuclear Data Library version 5 : JENDL-5, to be published in J. Nucl. Sci. Technol.
2) Werner, C.J. (Ed.), MCNP® USER'S MANUAL Code Version 6.2, LA-UR-17-29981, 2017, 746p.
3) Sato, T., et al., Features of Particle and Heavy Ion Transport Code System (PHITS) version 3.02, J. Nucl. Sci. Technol. vol.55, 2018, pp.684-690.
4) Tada, K., Nagaya, Y., Kunieda, S., Suyama, K., Fukahori, T., Development and verification of a new nuclear data processing system FRENDY, J. Nucl. Sci. Technol., vol.54, 2017, pp.806-817.
5) MacFarlane, R.E., Muir, D.W., Boicourt, R.M., Kahler, A.C., Conlin, J.L., The NJOY Nuclear Data Processing System, Version 2016, LA-UR-17-20093, 2016.
6) JENDL-5 ACE library (neutron induced), https://rpg.jaea.go.jp/main/en/ACE-J50/ (accessed 2022-12-12).
7) Trkov, A., Hernan, M., Brown, D.A., ENDF-6 Formats Manual Data Formats and Procedures for the Evaluated Nuclear Data Files ENDF/B-VI, ENDF/B-VII and ENDF/B-VIII, BNL-203218-2018-INRE Rev.215, 2018, 400p.
8) Aldama, D.L., Noy, R.C., Generating an ACE-formatted photonuclear data library from IAEA/PD-2019 using ACEMAKER, IAEA(NDS)-0858, 2022, 212p.
9) Aldama, D.L., Trkov, A., ACEMAKER-2.0, IAEA-NDS-223 Rev. 2, 2021, 30p.
10) Kawano, T., et al., IAEA Photonuclear Data Library 2019, Nuclear Data Sheets, vol. 163, 2020, pp. 109-162.
11) JENDL Photonuclear Data File 2016 revision 1, https://wwwndc.jaea.go.jp/ftpnd/jendl/jendl-pd-2016.1.html (accessed 2022-12-12).
12) TENDL-2019, https://tendl.web.psi.ch/tendl_2019/tendl2019.html (accessed 2022-12-12).